Cranfield University

G. M. Ashley
2000

High Frequency Thin-Film Bulk Acoustic Wave Resonators for Gas- and Bio-Analytical Applications

CRANFIELD UNIVERSITY
SIMS and IBST

PhD Thesis
Academic Years 2000-2005
G. M Ashley

High Frequency Thin-Film Bulk Acoustic Wave Resonators for Gas- and Bio-Analytical Applications

Supervisors Dr. P.B. Kirby and Dr. D.C Cullen
October 2000
This thesis is submitted in partial fulfilment of the requirements of the degree of Doctor of Philosophy

Declaration

No portion of the work referred to in this thesis has been submitted in support of an application for another degree or qualification of this or any other university or institute of learning.

Copyright

Dedication

To my family, Amanda-Jane and my son Dylan-Marcus-Thomas who have loved me. It is not always easy being the happiest man on Earth.
Also to my friends, Mary-Jane, Adam, Albert and Dimitiri who always have interesting things to show me.

FOR *"the knights"*

Abstract

Thin Film Bulk Acoustic Wave Resonators (FBAR) are mechanical micro scale devices that operate in the UHF/Microwave frequency range. This high frequency of operation potentially offers increased sensitivity to the addition of surface mass loading as implied by the famous Sauerbrey equation. FBAR was shown to be responsive to physical and chemical changes in the environment and was further adapted to act as bio-sensor. Thus indicating a universal platform from which to launch an enhanced sensing technology.

This thesis follows the research and development of a prototype chemical and biological sensor based on FBAR. FBAR devices were fabricated in a clean room and on die RF measurements were made to identify the units with performance characteristics of high enough quality to be useful as sensors. The FBAR design was then adapted so that it could be environmentally isolated, and microwave circuitry was devised to allow the FBAR to remain in electrical contact with the outside world during its isolation. This allowed for controllable environments in which to test FBAR responses to chemical and biological agents free from interfering signals.

A software suite was written to specifically address the requirements for accurate and sensitive data processing of FBAR responses to measured analytes in real time. The isolation assembly and software was tested thoroughly, and the ultimate limits of resolution and sensitivity for the instrumentation were found using temperature change as the variable input parameter.

A gas delivery apparatus was constructed and the FBAR was coated with hygroscopic polymer layers to sensitise the device to water vapour. Changes in the concentration of water vapour in a gas stream were tracked and the range of detection was established along with stability and resolution of the chemically sensitised FBAR.

FBAR device gold surfaces were coated with biological antibodies, these made the devices ultra specific to measurand. Direct experimental comparisons between the FBAR and the relative performance of well established but lower frequency acoustic wave immunosensor technology systems were made and the relative increase in sensitivity was established for the FBAR based immunosensor. Optical methods were used to compliment the acoustic ones in determining the thickness and density of the protein layers adsorbed to equivalent gold surfaces.

The thesis concludes with a section of speculative ideas for future work, with the experimental results for a potential rheological probe device shown. A brief demonstration of the FBAR performance when submerged in semi-infinite liquid environments is shown. Arrays of FBAR devices are software modelled in a novel way and demonstration of their possible applications are presented.

Acknowledgments

Over the course of the work, some technically demanding challenges were encountered, and it was only through interactions with a number of altruistic practical and theoretical specialists, and through extensive trial and error experiments, that the final configuration of a working sensor was possible. There is no doubt, that the overall success of this technically innovative research project was brought about through substantial interdisciplinary teamwork, and as such, the author cannot always take sole credit for the inspiring results that are demonstrated throughout the thesis.

Thanks go to Professor Roger Whatmoore for generous additional funding for the three year practical course of this work. My two supervisors Dr. Paul Kirby of SIMS and Dr. David Cullen of IBST have been invaluable in explaining both the theoretical and practical aspects of this multidisciplinary work, offering careful and thoughtful guidance throughout. Their occasional diametric advice afforded me the opportunity to make my own scientific decisions.

Thanks go to them also for their confidence and open ended approach which allowed me to go my own way, albeit with the occasional sharp nudge. A special thanks also goes to Dr. Kirby for providing me with well paid employment, ostensibly as a gap from my academic studies, this afforded me the opportunity to micro-machine resonators in ample quantity to complete the project and gain invaluable clean room experience.

The assistance of many other people was called upon to complete this work.

Thanks go to;

Dr. Amiel Farrington of Q sensors Ltd. for the initial coating of the FBAR sensing layer, introduction to quartz based resonating technology and the concepts of specificity for gasses based on polymers.

Anthony Lonsdale and the staff of Sensor Technology Ltd and Transense Ltd for assistance in the design and in the machining of the environmental housing chamber for the sensor, and for assistance in development of various aspects of RF PCB design and also for the kind loan of much apparatus as well as a good introduction to development of control software.

To Dr. Sarah Morgan of IBST for assistance in extraction of DNA from living eukaryotes, Dr. Mark Potter for initial support and encouragement as well as an excellent introduction to mathematical modelling techniques of FBAR, particularly in assistance in teaching me to use the MathCad software package and for wiring the elements in the math model that allowed the mass loading and array format models to be created.

Robert Wright and Joe Southin, Ph.D. students at SIMS (nanotechnology group) for assistance in understanding the form and function of FBAR in theoretical, acoustic, electric and physical terms. Thanks also go to Robert for the design and construction of the gas flow delivery apparatus and for sharing his experience in the actual fabrication of the FBAR devices. Gratitude is also given to Dr. Mai Ling of SIMS for explaining advanced concepts in RF acoustics, and for assisting in the interpretation of some of the results.

Thanks go also to Andrew and Mark, the technicians in nanotechnology for help with day to day practicalities too numerous to mention, and to Chaz and Danny of Cranfield computer centre for the loan of various computer equipment, even if it was full of dust!

To my dear friend and arts teacher, Tim Butler, Ph.D. student at Cambridge University for assistance with the design, development and implementation of the control and analysis software. His philosophical and altruistic approach proved to be invaluable to the success of the project.

THE AUTHOR.

Greg graduated with honours (2.1) as a classically trained Microbiologist in 1996 from Liverpool University, his honours project was *independent*, looking at fungal spore morphogeneis in electric fields. He went on to gain an M.Sc in Biosensors from Manchester University in 2000, where he was involved in developing thick-film amperometric enzyme electrodes for clinical diagnosis. The past four years have been devoted to pursuing Ph.D. level research developing MEMS scale piezoelectric thin-film resonating sensors for enhanced sensitivity in chemical and biological analysis. Greg would like to be involved in biomedical nanotechnology in the future.

CONTENTS

CHAPTER ONE
1.0 INTRODUCTION AND LITERATURE REVIEW

1.1. Preamble

The multidisciplinary research topic of this thesis is primarily focussed on developing a prototype, bulk acoustic wave (BAW) chemical and biological sensor[1] with substantially increased mass loading sensitivity. This PhD topic follows in the tradition of the original pioneering work of Sauerbrey (1959) [1] on micro-weighing of thin metal films on resonating quartz crystals and the *chemically-sensitised* version of this developed by King (1964)[2] [2] and the *immuno-sensitised* version subsequently developed by Shons (1972).[3] The work in this project exploits some of the relatively recent advances that have been made in the improved performance characteristics of BAW thin-film resonators (TFR) through the use of established modem microfabrication techniques [4] and the associated emerging technologies, for example the work of Lakin (1991) on the fundamental properties of thin film resonators.[5]

For the purposes of micro-gravimetric sensing, increasing the mass loading sensitivity of resonating transducers is a highly desirable function and it is obtained primarily by increasing their natural or fundamental operating frequency (f_0). Mass sensitivity (M_s) of a BAW is related to fundamental frequency as f_0^2. Simply put[3], this means that there will be an increase in the absolute negative frequency change ($-\Delta f$) per-unit-of-mass (in grams (g)) deposited on the surfaces of devices that are resonating at higher frequencies (in Hertz (Hz)) The time-honoured Sauerbrey theory [1] indicates that a relatively small increase in the f_0 of a micro-gravimetric resonant sensor can lead to a rather substantial increase in device sensitivity to thin-metallic "ideal" mass loads[4] on its surface.

---

[1] Physical sensing was also explored as a subsidiary topic.
[2] King's 1964 prototype could deliver a sensitivity of 10^{-9}g with a response time of 0.05s
[3] Neglecting the increased interfering noise and lower resonator quality factors typical at high frequencies.
[4] The relationship can significantly deviate from linearity when encountering "non-ideal" viscoelastic mass loads as opposed to "ideal" perfectly elastic loads such as thin metal films.

It is the *thickness* of a piezoelectric plate that is the predominant factor determining the natural resonant frequency of a BAW device. Thinner plates of the same type of piezoelectric material will resonate at higher frequencies. ((*See equation* 1.2). TFR technology is typified by piezoelectric membranes with thicknesses in the micron (μm) range, whilst piezoelectric quartz plates usually have thicknesses in the millimetre (mm) range. The piezoelectric microelectromechanical systems (MEMS) used in this work were TFR devices in the form of *thin-film bulk acoustic wave resonators* (FBAR) that were designed to operate at resonance frequencies some orders of magnitude higher[5] than the current state of the art quartz based BAW sensors, and as such, FBAR based sensors were expected to deliver greatly enhanced sensitivity to mass loads placed onto their resonating surface(s). The concept of exploiting the high natural resonance frequencies of TFR devices to gain substantial increase the M_s of micro gravimetric devices for selective recognition of analyte was first demonstrated by O'Toole *et al* (1990 - 1992)[6,7].

By depositing a so called "sensing layer" onto the surface of a BAW resonator, a specifically targeted analyte or measurand[6] can be isolated i.e., selectively bound, out of an ad-hoc mixture of materials which can be either chemical or biological in nature. In the simplest of cases, the increase in the mass load on the resonator surface that is generated from this selective interaction can be used to quantitatively analyse the chemistry of the resonator's close proximity environment. However, even though mass loading dominates the responses in the form of $-\Delta f$, it is not the *only* factor to be considered, because changes in the acoustic properties[7] of the sensing materials during their interaction with target analyte(s) may also contribute to the final output response in the form of electro-acoustic signal attenuation. These types of acoustic interactions can change an output parameter of the acoustic resonator known as the Quality factor (Q factor) and they are explored briefly in this thesis to show the potential use of the FBAR and associated instrumentation in probing material rheology.

It is shown in this work that FBAR devices are innately responsive to physical environmental changes such as temperature variation, but also, that the deposition of sensing layers (organic

[5] Typically operating in the UHF or microwave frequency range in this project, (~300 MHz to ~1.8 GHz),
[6] Analyte or measurand are roughly equivalent terms, indicating the target quantity to be measured.
[7] Important acoustic properties of materials are (i) density, (ii) thickness (iii) stiffness and (iv) acoustic loss.

partitioning polymer films) onto FBAR surfaces simultaneously sensitises them, and makes them *partially selective*, to the presence of chemical moieties in a gas stream. Also, the FBAR was engineered to act as an immunosensor by coating its surface with a sensing layer of biological antibodies which have *ultra-specific* binding affinities for target molecules. In this way, a prototype reagentless immuno-sensor delivering greatly enhanced responses over lower frequency BAW sensors to the antibody/target binding event was unambiguously demonstrated.

A number of traditionally separate scientific disciplines were combined during the course of this multidisciplinary work, and as such, it is neither possible nor desirable to discuss the minutia of every topic, instead they are discussed at the level where the details remain relevant to the development and continued optimisation of the prototype FBAR sensor. It is subjectively considered that it is the overall hybridisation and the successful synthesis of the separate disciplines that is pertinent to this work. However in taking this conscious and deliberate approach, and with finite development time as a limiting consideration, a number of potentially fruitful research avenues could not be explored with significant depth. Hence, for some of the studies[8] the cursory experiments performed, and the interpretations of the results subsequently obtained, are perhaps rather lacklustre, even if technically correct. But on the other-hand, they do offer significant opportunities for future work since proofs-of-principles have been demonstrated, and in some cases new discoveries have been made.

Figure 1.1 below, represents the author's subjective interpretation regarding nature of the instrumentation requirements and the amalgamation of the separate scientific disciplines that were encountered during the creation of the FBAR prototype sensor.

[8] Referring to (i) Overall material rheology studies, (ii) FBAR responses to DNA irradiation, (iii) FBAR responses to ambient light photons, (iv) FBAR complete submersion in semi-infinite liquid loads, (v) Suppression of FBAR spurious modes of resonance with the addition of hygroscopic polymer loads. (vi) Interpretations of the mass loading results from the mathematically modelled FBAR arrays.

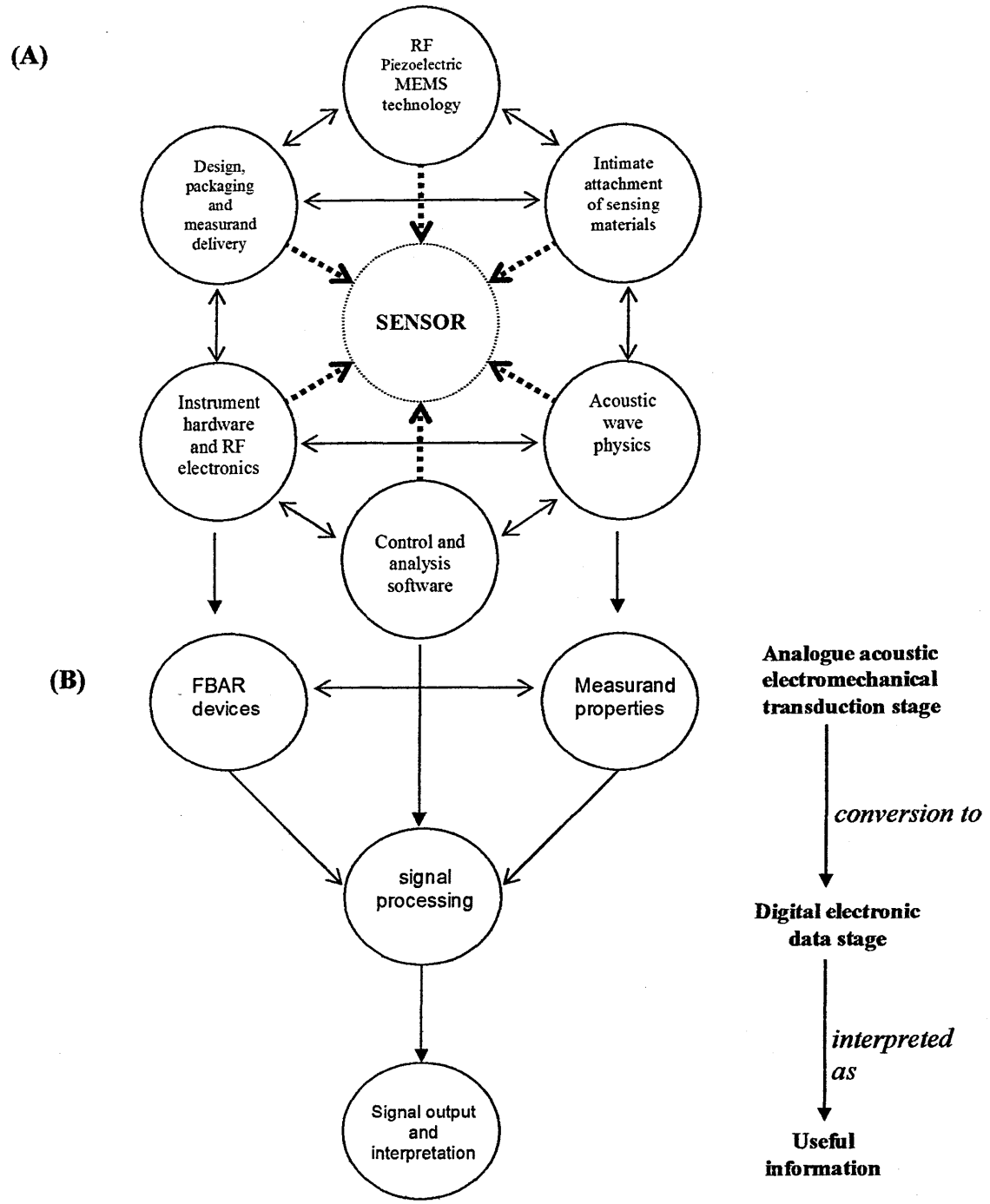

Figure 1.1 **(A)** The *core* principles of mutual dependence involved in FBAR prototype sensor development.**(B)** The path used the for acquisition of useful information which describes the sensing event on the FBAR

1.2 A brief chronological overview of the work presented in this thesis.

In planning, developing and evaluating the performance of the FBAR prototype sensor, the work was necessarily compartmentalised into separate systematic investigatory components which were eventually merged together. Broadly speaking, the results of these investigations are presented chronologically in the thesis. They involved the initial planning phases of the prototype unit but much of the detail involved in the planning phases is omitted for the sake of clarity since they become obvious by default. The actual microfabrication of the FBAR devices themselves and the subsequent physical adaptations that were made for the best performing FBAR devices selected for use in sensing experiments were shown along with the results generated when the prototype was fully operational.

The thesis is split into six chapters, the present chapter, which is in the form of a literature review, introduces the concept and scope of chemical and biological sensing technology in general and shows the operational principles of BAW devices with the main focus being on quartz based systems since they are so well researched and referenced.

The second chapter starts by giving a brief historical background of the work leading up to the emergence of piezoelectric TFR technology, and describes the science behind the electro-acoustic operation of FBAR devices specifically with focus on how they can be adapted for use in sensing. It also reviews the scant literature available on existing TFR technology when applied to chemical and biological sensing. Chapter two also gives the details of the microfabrication stages involved in manufacturing of the FBARs on silicon wafers and continues on to show the methods that were already in place to electrically characterise them upon completion. It highlights the serious limitations existing in the established characterisation methods when attempting to use FBARs as sensors. The novel methods that were devised to circumvent these limitations, namely in the design and construction of an environmental isolation chamber for the FBAR and its associated microwave electronics are described. The chapter concludes with a section following the major steps involved in replacing the existing FBAR characterisation software with new measurement and control software that was developed to give superior real-time access to the wealth of data that the

FBAR could deliver relating to its acoustic interactions with measurand on its resonating surface.

Chapter three describes the main phase of the beta testing and evaluation of the new software and prototype FBAR environmental isolation chamber. The associated microwave electronic components of the chamber were also characterised. Temperature changes were used as the main variable parameter with which to monitor the computer-controlled automated FBAR responses in real-time. Here, the nuances of the interplay between the new software and the hardware are learned and the ultimate limits of resolution for the prototype apparatus are discovered. The methods that were used to reduce system noise and to increase system accuracy are clearly demonstrated. Along with frequency changes, (Hz), the use of alternative FBAR output parameters such as Q factor (or its reciprocal, the dissipation factor (D)) and power transmissions (dB) are introduced.

Chapter four describes the construction of a gas flow delivery apparatus to connect to the FBAR isolation chamber is clearly described. The chapter gives the details appertaining to how the FBAR could be sensitised to the presence of moisture in a gas stream through the addition of a sensing polymer layer on its surface, in essence creating a "model" chemical gas sensor system. The FBAR characteristic responses to changes in relative humidity are then evaluated and interpreted with various thicknesses and various concentrations of the sensitising polymer layer used during the analysis. Some unexpected results, mainly in the complete suppression of FBAR spurious modes of resonance when coated with the polymer layer are presented. The results of this chapter should be considered as a *qualitative* assessment of a FBAR based "model" chemical gas sensor.

In chapter five, the FBAR is demonstrated for the first time as a class of biosensor known as an immunosensor. The FBAR surface, coated with biological antibodies, is shown to behave in an ultra-specific manner toward measurand, and the subsequent immuno-accumulation of mass is measured. Additionally, the immuno-sensitised FBAR is experimentally compared directly against quartz immunosensors of the same type; the relative sensitivities of the two BAW immunosensor systems are evaluated. Surface plasmon resonance techniques are used

to estimate the thickness of the antibody layers and the results for these are shown. Mathematical modelling of the estimates of the thickness of the antibody layers on the FBAR surfaces are calculated based on experimentally deduced frequency changes and estimated protein density. The results of this chapter should be considered as a *quantitative* assessment of a FBAR based "model" biosensor.

Chapter six offers suggestions for future work after discussing and considering the overall nature of the results. The sixth chapter also shows the results of two FBAR experiments that were not placed into the main experimental body of the thesis. The first of these shows the unexpected responses of the device when it was completely submerged in a semi-infinite liquid environment and the second shows the results from the FBAR when it was used to probe changes in the physical state of an intimately attached DNA layer brought about by irradiation with UV light[9]. The results generated by mathematical modelling of FBAR devices strapped into different types of array formats are shown and discussed. Suggestions for future-work in the development of a multi-analyte capable "in the field" sensor based on FBAR technology conclude the thesis.

1.3 Literature Review

1.3.1 Authors note

In the literature that was reviewed relating to the phenomenon of mass loading onto BAW devices, the equations that were presented in the various review papers to describe the most simple case scenario, the so-called "ideal" mass loading onto resonators did not appear standardised. In over twenty three theoretical and/or practical research papers studied during the literature review, on the main, no two papers used the same equation, although they were all based on the original Sauerbrey term, to describe ideal mass loading even when attempting to describe the same type of experiments on quartz. When the more complicated cases of so-called "non-ideal" or non-gravimetric loads were encountered in the literature, the terms used to describe the phenomenon were always extremely complicated and often seemingly speculative.

[9] This experiment was not performed with enough experimental controls to justify a place in the experimental sections, instead is presented as a supplemental "look-see" type test.

During the review, it was not clear how relevant the various extremely detailed arguments presented for mass loading onto resonators given in the literature were to the actual thrust of the thesis, which was of course prototype sensor development, and not theoretical electro-acoustic physics. It was decided to note that the theoretical understanding of "non-ideal" mass loading onto resonators is *not* completely understood by the scientific community at present, and that this thesis would not attempt to address the problem. This problem was mainly the lack of a universally accepted unified term to describe all of the behaviours of BAW sensors in relation to the various types of mass loads that can be presented to them in both the gas and the liquid phase.

A representative form of the classic Sauerbrey equation is shown, (*See* equation 1.4) while the multiple variants that exist for it along with the more complicated non ideal loading terms are presented in a supplemental review section in Appendix 1, this format it is hoped, will serve to keep the fairly complicated topic succinct and relevant to the project while condensing the various aspects of the theory into a single section to assist researchers in the future, but without distracting from the thrust of the main literature review section.

1.3.2 Introduction to the concept of chemical and biological sensors.

A sensor can be defined as "device capable of converting (changes in) the *physical dimension* which is to be measured into (changes in) an *electrical dimension* (voltage, current or frequency) which can be processed or transmitted electronically". A biosensor has been defined by Turner *et al* (1987) [11] as " a compact analytical device incorporating a biological or biologically-derived sensing element wither integrated within or intimately associated with a physicochemical transducer".

The detection and quantitation of biochemcials presents a large market potential, estimated at billions of dollars annually. [8] The increasing attention in chemical sensor research is being driven largely by the increasing technological need to perform analytical measurements remote from a central laboratory.[9] Sensor use is not limited strictly to the chemical laboratory, since medical clinics, industrial processes and bioreactors also rely on these devices. As time goes on, they are to be found more

frequently in the domestic sector such as food freshness monitoring in shops, field analysis of plants and soil, portable air pollution monitors and many more.[10] There is interest in the continued application of biosensors for toxic chemical and pathogenic biological agents of defence interest. [54]

Several microsensor technologies are currently under investigation in an attempt to meet the increase in demand. The microsensors are typically categorised either by their detection mechanism or by the quantity they are measuring (the measurand). Common sensing techniques include potentiometric devices (which are based on ionic charge and chemical potential), chemiresisitve devices (which are based on chemically induced resistivity changes in semiconducting films), calorimetric devices (which measure either the heat of reaction or a change in thermal conductivity), optical sensors (which employ either fluorescence or electromagnetic wave perturbation in the form of absorption) and finally, acoustic wave sensors which measure perturbations of a mechanical wave [11]. In order to realise the full potential of acoustic wave sensors, coordinated efforts between diverse disciplines such as electrical engineering, physics, chemistry, computer science, microbiology and medicine are needed. [12]

A number of different criteria are in use for classifying sensors broadly listed as:

- physical or chemical/effect transduction principle
- measurand
- technology and material
- application
- cost
- accuracy.

The physical sensing dimensions can be classified as magnetic, thermal & mechanical signals, electromagnetic radiation and chemical volumes; these can all ultimately be transduced as an electrical signal[13]

As early as 1969, Lion [14] had suggested grouping the principles into the type of energy the signal received and generated. He distinguished six types:;

- mechanical;
- thermal;
- electrical
- magnetic;
- radiant;
- chemical.

Table 1.1 The physical domains for current sensor technology.

MECHANICAL DIMENSIONS OF SOLIDS	Separation, acceleration, elasticity, density, thickness, torque, speed of revolution, pressure, diameter, shape filling level weight, power, length, height, hardness, mass orientation, through low, tension, distance etc.
MECHANICAL DIMENSIONS OF LIQUIDS AND GASSES	Density, pressure, viscosity of flow, through flow, etc
OPTICAL RADIATION	Intensity, wavelength, polarisation, reflection, absorbance , etc
ACOUSTIC VIBRATION	Sound , pressure, velocity of propagation, absorption, intensity, sound frequency, etc.
NUCLEAR RADIATION	radiant energy, degree of ionisation, radiant flux, etc.
CHEMICAL SIGNALS	Concentration, pH, particle form and size, molecule or ion type, reaction speed, humidity, etc
MAGNETIC AND ELECTRICAL SIGNALS	Inductance, capacitance, resistance, frequency, phase, current, voltage, permittivity, magnetic field strength etc,.
OTHER IMPORTANT DIMENSIONS	Quality, pulse duration, time, etc.

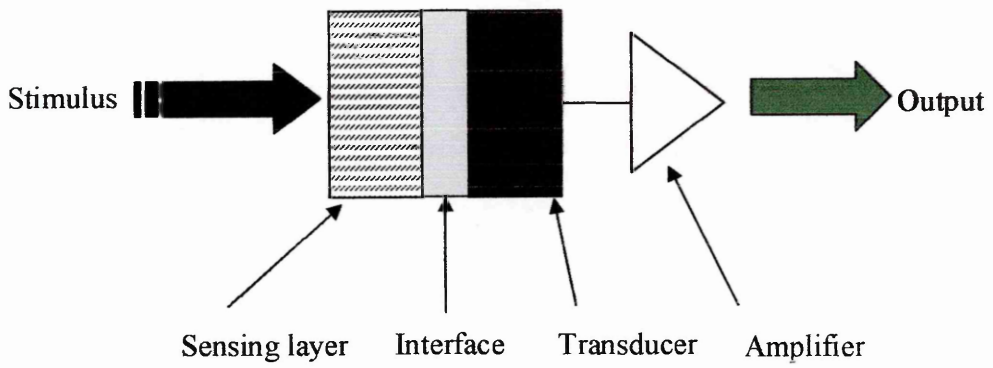

Figure 1.2 (A) Schematic of a Generic Biosensor[10]. (Collings 1997)[15]

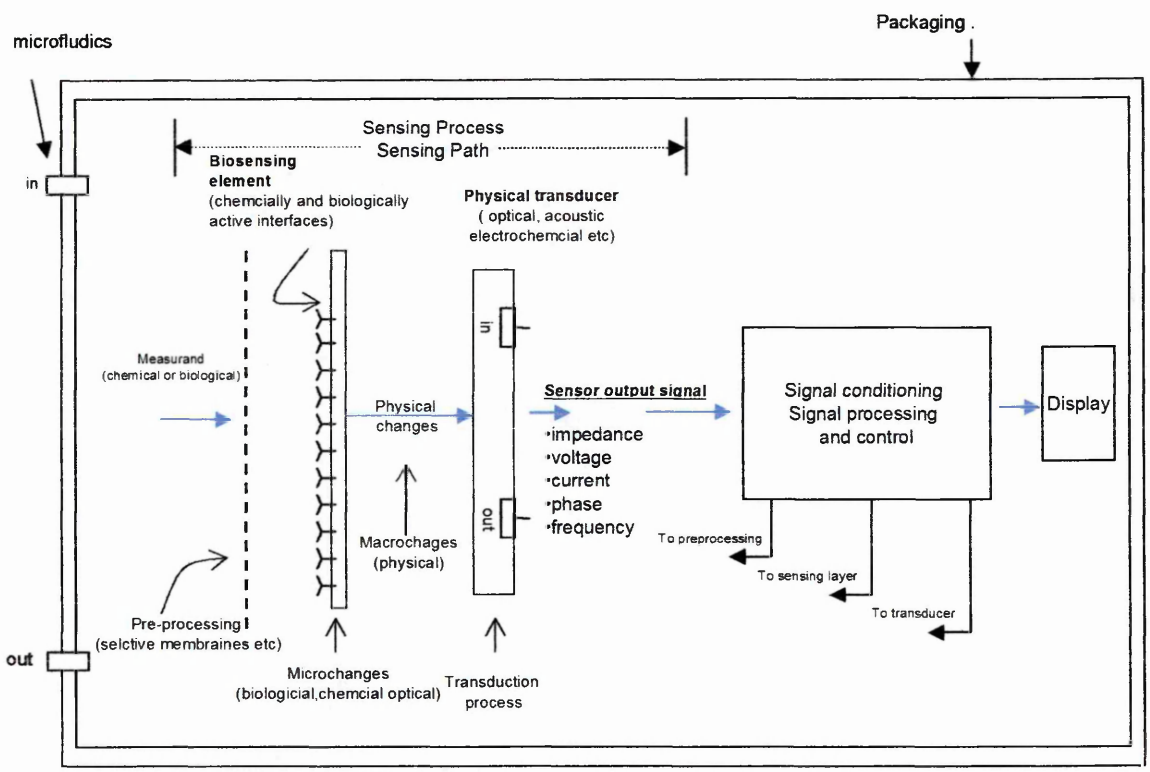

Figure 1.2 (B) General diagram of a biosensor system. Biosensor could be in array format for simultaneous detection of multiple analytes. (Lec 2001) [16]

[10] A biosensor is a special class of chemical sensor, where the sensing layer is originally derived from an animate source, it is also a *misnomer* for a device with an inanimately derived chemical sensing layer used to detect analytes of biological origin.

1.3.3 Types of wave mode and piezoelectric acoustic resonator modules used in sensing

Piezoelectric sensors utilise an oscillating electric field to create a mechanical displacement i.e., an acoustic wave, which propagates *through* the substrate in the case of BAW devices, or *on the surface* of the substrate in the case of Surface acoustic wave (SAW) devices, the mechanical deformation is then converted back into an electric signal for measurement.

The SAW is a combined mechanical and electromagnetic disturbance that is localised to around one wavelength on the surface of a solid. Usually on a piezoelectric substrate generated by interdigitated electrodes and applying RF voltage across them, usually in the range 10 MHz to 2 GHz. SAW devices have seen phenomenal success in sensing mass changes of as little as 100 pg/cm^2 [17] and interpretation of the results from them are increasing in sophistication.[18]

The projection to frequency is equivalent to transferring the information into a time-interval value. Time is invariant to a change from the mechanical to the electrical domain. There is no loss of accuracy by the transfer from a mechanical vibration to the piezoelectrically coupled corresponding electrical signal. The time interval is, with several orders of magnitude-the most accurately measurable quantity of all. [19]

Below are the main categories of acoustic module types used as sensors and based on different acoustic modes.

i) Thickness-shear mode (TSM) sensors
ii) Surface acoustic wave (SAW) and leaky (SAW) sensors
iii) Shear-Horizontal Acoustic-plate mode (SH APM) sensors
iv) Bleustein-Gulyaev wave sensors
v) Love mode sensors
vi) Flexural-plate-Wave (FPW) sensors
vii) BAW compressional or bulk longitudinal extensional mode sensors.

Each wave mode offers its own advantages and disadvantages in acoustic sensor applications, however in this project only (i) and (vii) are used experimentally in sensing applications.

1.3.4 The quartz crystal microbalance in acoustic sensor applications.

There are strong analogies to be drawn between FBAR and QCM principles of operation, and understanding the principles of QCM form and function will help develop an understanding of the principles involved in arranging for the FBAR to function as BAW chemical and biological sensor.

After Sauerbrey, who in 1959 employed the QCM to measure rigid metallic films, W. H. King in 1964, then developed the application of the technology further to make small and selective chemical mass measurements. Here the QCM was employed as a sorption detector, which only became possible when it was understood that QCM coated with gas chromatographic substrates could act as gas chromatographic detectors. This work was in essence, the birth of the electronic nose. King's prototype could deliver a sensitivity of 10^{-9}g with a response time of 0.05s. [2]

QCM's have been used to detect gasses, ions, microbes, biopolymers, and electrochemical mass change.[20] studies with QCM in liquids have been reported [21] and detailed models have been developed to describe the behaviours involving viscoelastic mass loading. Recently (2001), it has also been shown that a weak longitudinal wave can also be generated by a modified QCM known as the electrode separated piezoelectric sensor (ESPS) where one of the metal electrodes is separated from the main body of the piezoelectric by a few mm in a conductive solution. These are interesting devices and bear some resemblance to the wave motions in FBARs but they can not be given deserved attention in this thesis. For review see (Yang. M., et al. 2001) [22] A form of the QCM, the so called electrochemical quartz crystal microbalance (EQCM), where the electrodes are under potential control in an electrochemical cell, can work in a liquid and can deliver sub-nmol sensitivity. For a review see, (Bruckenstein 1995).[23]

1.3.4.1 Thinning of quartz plates to increase frequency and sensitivity

Hung (2003) [24] has attempted to exploit the frequency to thickness and sensitivity relationship by decreasing the thickness of quartz plates by deep reactive ion etching (DRIE). Hong reported a substantial increase in Q factor, from (Q~100) for 1 mm diameter plate 82.3 μm to (Q~30,000) when the plate thickness was reduced to 17.8 μm, f_0 for these plates was reported as 20.3 MHz and 94 MHz respectively, but they do not say how it was calculated, or offer a suggestion as to what could underpin this increase. However, the trend finds some agreement with Osbond *et al* (1999) who observed the influence of ZnO and electrode thickness on the performance of FBARs and noted that with thinner depositions of piezoelectric plate, both the resonance frequency and the Q factor of the FBAR increased [25] The highest fundamental thickness vibration to date for quartz a crystal resonator is 2.074 GHz with a thickness of 0.6 μm and a Q factor of 1037 by Iwata (2004)[55]. Iwata concluded from observation on the characteristics of the admittance spectra of the device that it could not be expressed adequately with the BDV model.

Interestingly, Hung [24] attempted to use the DRIE method to create arrays of high frequency individual resonators within a single quartz plate, with some success. but discovered that there were limits to the minimum thickness achievable with this method[11] due to the inherent fragility of quartz and its subsequent difficulty in handling.

1.3.4.2 QCM immunosensor technology

Shons *et al* (1972),[3] were the first to endow immuno-specificity to the QCM by depositing antibodies that were specific for a target analyte and observing mass changes due to the immuno-accumulation of the target bound by the antibody. After this, over 100 papers devoted mainly to the detection of gasses and particulates appeared in the

[11] In this project, rather than thinning the piezoelectric bulk from the top-down like Hung, the piezoelectric was instead built from the bottom up by means of physically depositing the piezoelectric onto a gold electrode surface from an RF plasma of piezoelectric (ZnO) in a vacuum - and in this way, very thin (~ 0.5 - 4 μm) piezoelectric membranes with natural resonance frequencies in the microwave range could be crafted.

literature with scant attention given to biosensor applications. In 1983, work on QCM as biosensors remerged.[26] The main workers in the field were, G.G. Guilbault, M. Thompson and Y. Okahata. Between them producing some 40 papers mostly confined to antibody-antigen interactions on QCM over about a decade. Kobliner *et al* (1992) [56] adapted the QCM to allow for immunological detection of anti-human immunodeficiency antibodies, but their tactic was to coat the crystal electrode directly with a synthetic HIV peptide and follow the subsequent immuno accumulation of the antibodies from solution. Over the last decade, numerous studies have been conducted on QCM transduced immuno accumulation with the bulk of them being in the field of clinical analysis, but more recently interest has been focussed on environmental pollutants and biowarfare agents.[57]

In this thesis, the antibody-antigen interactions are used as a model system for validation of FBAR as prototype biosensor based on affinity recognition principles.

1.3.4.3 QCM based humidity sensing.

.Mecca et al (1994)[52] reported that when a quartz-crystal resonator is coated with a hygroscopic material it becomes a "very" sensitive moisture sensor, saying that the Du Pont company had exploited this knowledge to manufacture QCM sensors with ability to detect 0.1 ppm moisture changes in non-corrosive gasses.[52] In chapter three of this work, the FBAR was coated with such a hygroscopic material and observations on the response of the device to changes in relative humidity were made.

A variety of studies employing the coated QCM as humidity sensor are available in the literature. For a good review, the reader is directed to (Grate 2000) [27] By far the most humidity sensitive layer yet to be discovered for QCM is the C_{60} buckyball structure giving sensitivity threshold responses of 0.01% changes in relative air humidity when used as a surface coating .[28] It would be interesting to attempt to repeat this work using FBAR devices, but it was not possible due to time constraints.

1.3.4.4 QCM based temperature measurements

The anisotropy of piezoelectric single crystals allows different angles of cuts (different orientations of the resonator shape with respect to the crystallographic axis) AT-cut quartz resonators provide a shear wave vibration with a resonance frequency that is extremely stable over a wide temperature range, BT- cuts also display vanishing temperature coefficients.[29]

The first systematic approach to promoting the temperature sensitivity of the frequency from an unwanted side effect to an attractive temperature sensor was published by Wade and Slutsky (1962). [30] This field of work culminated in the discovery of the so called LC cut (linear temperature coefficient cut) of quartz by workers at Hewlett Packard with an accurate measurement range from -80 to 230 ^{o}C with a calibration accuracy of 0.02^{o}C, and in 1984 Ziegler [31] introduced the HT cut with a sensitivity of 90 ppm $^{o}C^{-1}$.
Since the quartz crystal is an anisotropic medium, the resonance frequency of the plate is highly dependant on the crystallographic orientation, e.g., angle of the cut. A systematic study was performed by Bechmann in 1962,[32] on the temperature dependencies of alternative cuts of quartz.

1.3.5 Fundamental sensor requirements and noise considerations

Table 1.2 below, shows most of the key issues associated with sensor output requirements. The electronics and packaging must be considered when developing a new sensor. In the case of the microwave (RF) frequency sensors such as those used in this project, the additional complications of impedance matching and the subsequent transmission line calculations involved needed to be considered carefully when designing the electronics involved in the packaging for the FBAR sensor.

The highly desirable functions of a low noise output signal, a low power requirement and ultimately, a computer bus-compatible[12], output signal are fundamental requirements of any modern sensor. In addition to this, the sensor should show substantial insensitivity to interference and to ambient environmental influences, or that these types of interferences

[12] In this project this was a General Purpose Interface Bus (GPIB) enabled communication link.

are compensated. It should also have a relatively long life expectancy without significant signal drift due to ageing and it should be problem-free when replacement of the module is required.

Table 1.2 BAW sensor performance considerations

TERM	EFFECT
ACCURACY	A measure of how closely sensor output approximates the true value. (Usually mass loading)
PRECISION	Describes how exactly and reproducibly an unknown value is measured. (best for "ideal" mass loads)
RESOLUTION	Smallest increment in the value of the measurand that results in a detectable increment in the output.
SENSITIVITY	Absolute change in frequency per unit of measurand
SELECTIVITY/SPECIFICITY	How susceptible the system is to additive interference from erroneous non target analytes.
MINIMUM DETECTABLE SIGNAL	Determined by the noise performance of the transducer. and the associated oscillator circuitry.
THRESHOLD	Smallest initial increment in measurand that results in detectable output.
NON-LINEARITY	A measure of deviation from linearity of the sensor (Presents as a problem when the mass load is not perfectly elastic)
DISTORTION	Deviation from the expected output
CONFORMITY	Closeness of experimental curve to theoretical curve.
HYSTERESIS	Difference in output of sensor for given input from opposite directions.
REPEATABILITY	Difference in output readings from same quantity of measurand and also batch-to-batch reproducibility. Major source of calibration issue.
SPAN	Range of input variable giving meaningful sensor output.
NOISE	Random fluctuation in the value o the measurand that causes random fluctuation in the output. i.e. Allen deviations.
INSTABILITY AND DRIFT	Change in sensitivity or base line over time. (Often due to ageing of a device)

Whilst it is true that higher frequency resonators produce larger frequency changes per unit of measurand than their lower frequency counterparts (*See* equation 1.4), it is also

true that higher frequency can result in lower accuracy and in a lesser ability to resolve small changes in the measurand. Vig (2000) [33] states that noise will limit the accuracy with which one can determine the frequency of an oscillator and therefore seriously limits the minimum quantity of measurand that can be calculated with a specified uncertainty.

Vig also shows the known causes of noise or short-term instabilities as random fractional frequency fluctuations, and states that they are also known as Allan deviations;

- Johnson noise due to motional resistance of the resonator and within the oscillator circuitry.
- Phonon scattering noise in the resonator.
- Changes in external load.
- Thermal responses of the resonator
- Temperature fluctuations.
- Random vibrations
- Fluctuations in the number of adsorbed molecules.
- Stress relief and fluctuations at interfaces.

As a consequence of this, Vig [33] states that higher frequency sensors will provide;

- Larger frequency change per unit of measurand.
- Higher noise – offsetting the larger frequency change per unit measurand; decreasing the ability to resolve small changes in the measurand.
- Higher hysteresis –offsetting the larger frequency change per measurand unit, and resulting in poorer reproducibility.
- Increased aging rates, hence inferior long term stability and accuracy.
- Higher power consumption.
- Smaller devices

1.3.6 Theory of BAW operational principles applied to sensing

For the purposes of this description, the *quartz crystal* is taken as a "model" BAW system because it is well covered in the literature and because electromechanical principles of operation are similar enough to FBAR devices to be considered as roughly equivalent, and differ primarily in their frequency of operation. This is due to the thicknesses of the respective piezoelectric plates, not changes in the physics, indeed the electrical equivalent circuits for FBAR and for QCM are identical. The operational principles of FBAR, specifically focussed on sensing applications are covered in detail in Chapter two of the thesis.

Almost all acoustic wave devices utilise a piezoelectric material to generate the mechanical vibration. The piezoelectric effect was first observed and recorded by The Curies in 1880, they showed that an electric dipole could be developed in anisotropic crystals under stress, it was named by Hankel in 1881 and a remained a scientific curiosity for two decades until Cady discovered the quartz resonator for stabilizing electronic circuits. [34]

When a crystal structure lacks a centre of inversion symmetry, the application of strain changes the distribution of charge on the atoms and bonds so a net electrical polarisation of the crystal results. There are seven different crystallographic systems (cubic, hexagonal etc) and 32 different crystallographic point groups, 20 of these are piezoelectric and are spread across the seven systems. The coupling between strain and electrical polarisation that occurs in many crystals provides means for generating acoustic waves electrically. Materials of this type also undergo piezoelectric stiffening; this is the result of the increase of elastic modulus in the crystal due to the presence of piezoelectricity.

As well as acting as a dielectric, a piezoelectric crystal placed in an electric field will experience strains proportional to the electric field strength. If the resonant frequency of the applied field is equal to the mechanical resonant frequency of the crystal, then the

strain can become large. Since the electric conductivity of quartz is very low at room temperature, the quartz plate can be represented by a pure capacitance.

$$C_o = k\varepsilon_o \frac{A}{d} \qquad \text{(Eq 1.1)}$$

Where A is the area of the electrodes, d is the thickness of the plate, $k\varepsilon_0$ is the dielectric constant.

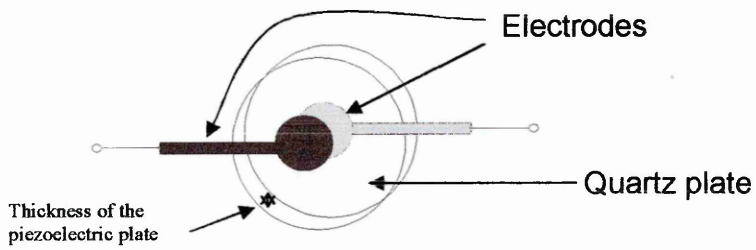

Figure 1.3 Quartz crystal resonator with electrodes contacting opposite faces.

Near the mechanical resonant frequencies, the strain associated with the vibration results in a further polarisation through the piezoelectric effect. The current passing through the device consists of the dielectric displacement and piezoelectric displacement currents which will lead or lag the applied voltage depending on whether the applied frequency is greater or less than the resonance frequency. The acoustic resonance frequencies of an unloaded plate occur when the plate thickness is an odd multiple of a half wavelength. The operation of the QCM relies on the excitation into mechanical resonance induced by an electrical field across the quartz crystal with two metal (usually gold) electrodes sequentially polarised on opposite faces of the piezoelectric quartz plate.

The fundamental resonance frequency of quartz plates is usually between 5 MHz and 20 MHz but is entirely dependent on the thickness of the plate because resonance will occur by means of coherent reflections at the top and bottom boundaries of the plate [35] Therefore at the resonant frequency, a *standing wave* is formed between the two electrodes and the wavelength of the standing wave is simply twice the thickness of the plate, and the frequency is given as (Schmit et al 2001) [36]

$$f = \frac{v}{2h} \qquad \text{(Eq 1.2)}$$

where h is the plate thickness, v is the mode velocity of the acoustic wave.
Resonance also occurs at each harmonic of the fundamental frequency, forming a sequence of resonance frequencies.

$$f = \frac{Nv}{2h} \qquad \text{(Eq 1.3)}$$

where N is a positive integer.

For a piezoelectric disk, there exist two sets of resonant frequencies, these correspond to the two possible electric boundary conditions. The first set corresponds to a disk with an open-circuit boundary condition i.e., where the electrodes are unconnected and is called either anti-resonance or parallel resonance. The other set of resonant frequencies corresponds to a disk with a short-circuit boundary condition i.e., the electrodes are connected, and it is termed "resonance" or series resonance. For both the series and parallel resonances, only odd harmonics occur and each parallel and series resonant frequency will typically lie close together for crystal orientations with a large coupling factor. [37]

In the majority of acoustic sensor applications an approximation of the series resonant frequency is obtained by measuring the frequency of an oscillator circuit that incorporates the resonating transducer in a two-port (e.g., S_{21} or S_{12}) device configuration as the frequency-determining element in the feedback loop of an amplifier. The oscillation frequency, is the point where the phase shift across the entire feedback loop is $2\pi N$, where $N = 0,1,2....$ [38]

For sensor applications, a clean resonance spectrum clear from spurious modes is obligatory[13]. This is because the resonance utilised for the sensor function shifts within a

[13] The concept of spurious modes of resonance, and unexpected methods found to suppress them are discussed in chapter four of this thesis.

certain frequency range depending upon the measurand. If there are spurious modes, or any other modes with different dependencies upon the measurand, resonance-frequency crossings and mode couplings may occur within the measurement frequency range. Such mode couplings not only produce significant deviations from linearity, but sometimes even produce frequency jumps and activity dips. [39] If the unwanted sources of frequency variation and energy loss can be made small relative to the amplitude of the analytical response, then approximate resonant series frequency generated by this method is an acceptable measure of response. Accurate measurements require specialised electronic test equipment such as vector network analysers with precise frequency synthesisers.

The velocity of an acoustic wave in a solid is dependent upon the material used, but usually is in the range 5000 to 10,000 m/s. for longitudinal waves, while shear waves have velocities typically 3000 to 6000 m/s. Any physical changes in the properties of the wave propagation medium will lead to changes in the wave velocity and/or amplitude which can be monitored and subsequently interpreted as a measured sensing response. [8] A thorough review of the exact analysis of the propagation of acoustic waves in piezoelectric systems has been performed by Stuart and Yong (1994) [40]

Piezoelectric mass sensors are passive solid-state electronic devices that respond to temperature, pressure and the physical properties of the interface between the resonating surface and the contacting attached film. Changes such as interfacial mass density, elasticity, viscosity and sorbed layer thickness can be monitored by corresponding changes in the acoustic wave.[7] As the wave propagates through or on the surface of the material, any changes to the characteristics of the propagation path affect the velocity and or the amplitude of the wave. [41] The acoustic wave travels into the adjacent film and deforms the film, thereby probing its mechanical properties.[42]

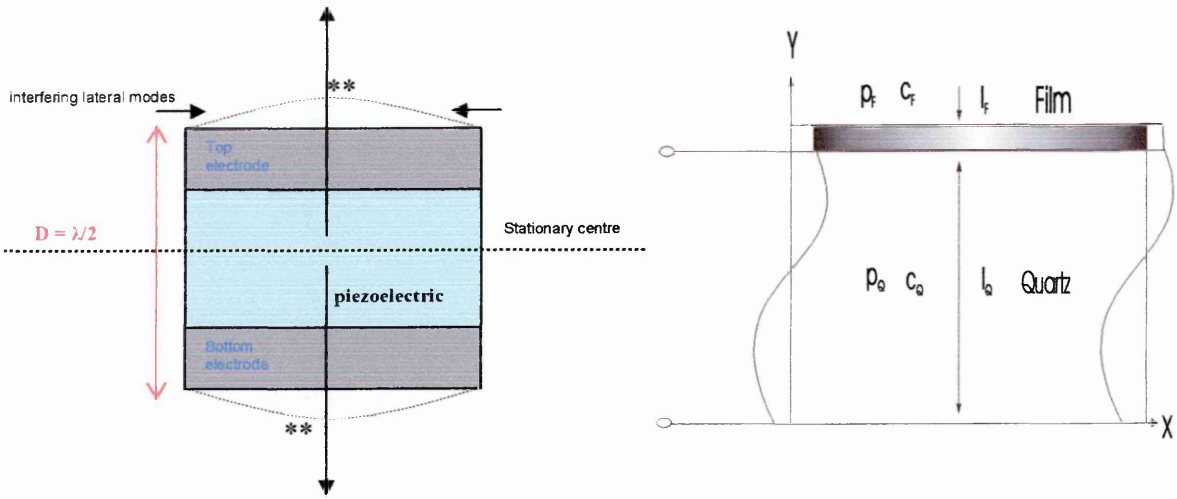

(A) [Bulk longitudinal mode] **(B)** [Thickness-shear mode]

Figure 1.4 (A and B)

(A) Bulk longitudinal direction of motional wave propagation typical of FBAR. The physical displacement of surfaces at resonance (**) is in the order of 5-10 nm. (not to scale) Lateral interfering manifestations are indicated.

(B) TSM mode typical of AT cut Quartz. p_Q, p_F are the densities, c_Q, c_F are the effective elastic constants and l_Q an l_F are the thickness.(not to scale) It is a one dimensional model (section of an infinite plate) of a thickness shear resonator crystal (e.g., AT-cut) loaded with a foreign film and excited at the fundamental resonance.

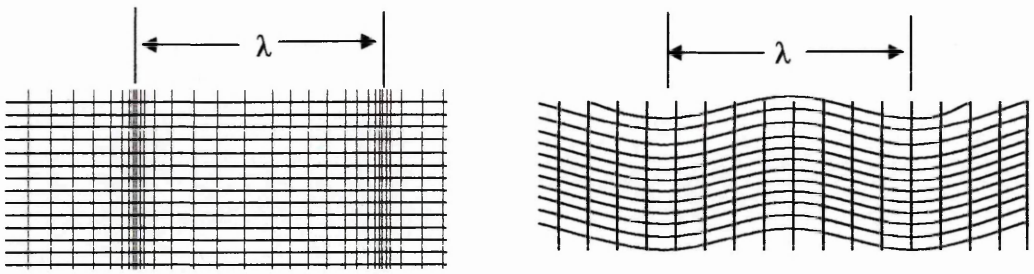

(C) **(D)**

Figure 1.4 (C and D) Schematic of shear and compressional mechanical (acoustic) waves in solids.

(C) Bulk Longitudinal (compressional) wave in unbounded solid – e.g. FBAR. – The displacement is running parallel to the wave vector.

(D) Bulk Transverse (Thickness Shear) wave in unbounded solid –e.g. Quartz crystal, the displacement is perpendicular to the wave vector.

As in the case of the simple clock pendulum, the resonant frequency is inversely proportional to the square root of the oscillating mass. An "ideal" mass layer is assumed to be infinitesimally thick yet impose a finite mass per area on the resonator surface. This condition is approximated by a layer that is sufficiently thin and rigid so that negligible acoustic phase shift occurs across the layer thickness and represents the simplest case scenario for acoustic analysis. For chemical and biological sensors, an adsorbent that selectively interacts with the analyte is coated on the electrode surface of the resonator and the mass increase upon adsorption decreases the oscillating frequency of the crystal.

The *classic* Sauerbrey equation[14] (1959) (Equation 1.4) describes the relationship between the frequency change and the mass accumulated in the gas phase.

$$\Delta f = \frac{-2f_0^2 \Delta m}{A(\rho_q \mu_q)^{1/2}} \qquad \text{(Eq 1.4)}$$

Where f_0 is the unloaded frequency, f is the loaded frequency and $\Delta f = f_0 - f$. μ_q and ρ_q are the shear modulus and the density of the quartz respectively. A is the area of the plate and m is the deposited mass.

and more recently the frequency shift per mass attachment for a simple piezoelectric resonator can be given by: Gabl *et al* (2003) [53]

$$\frac{\partial f}{\partial m} = \frac{f_0}{M} \propto -f_0^2 \qquad \text{(Eq 1.5)}$$

Where f_0 is the fundamental frequency, M is the mass of the oscillator.

It is often found that in liquids or with certain viscoelastic loads the induced frequency shift of a (quartz in this case) resonator is not as expected from the mass of bound analyte. In some cases not only is the magnitude in error, but also the frequency shift Δf

[14] There are a large number a variants of this term and to keep the literature review succinct, the alternative forms are placed into Appendix 1 as a supplemental literature review topic. The Sauerbrey term becomes invalid for large loads, liquid loads or viscoelastic loads, and this concept is reviewed also in the supplemental review section.

is positive rather than negative[15]. [43] This lack of correlation with the Sauerbrey equation prevents confident development of a device with obvious potential as a sensor and it is clear that a fresh appraisal of the underlying physical and chemical operation is required.[44]

Mass sensitivity (Ms) of a BAW (quartz in this case) can be described in equation 1.6 which is the quadratic function of the fundamental frequency. (Su 2000) [45]

$$Ms = \frac{2f_0^2}{(\rho_q \mu_q)^{1/2}} \qquad \text{(Eq 1.6)}$$

But this term is *idealised* since it disregards the potential increases in noise highlighted by Vig (2000) [33] and it also disregards the effect of the change in the quality factor (Q) of a device. A more realistic term would be that of *useable sensitivity* (e.g., lower mass detection limits) which is related to the product of sensitivity and Q factor (See appendix 1 Eqn A25) The electro acoustic physics which underpins the Q factor of a device is complicated and can not be discussed with significant depth in this work. For review see. Su, Kirby and Whatmoore (2001) [46] For the purposes of sensing , Q can be understood simply as: Q = 2π.(maximum energy stored/energy dissipated per cycle)

In this project, the simplest possible measure of the Q factor is used, one that is related to the width of the resonance curve, it is the ratio of the centre frequency of the resonant circuit to its 3 dB bandwidth, most often referred to circuit Q.

$$Q = \frac{f_0}{f_2 - f_1} \qquad \text{(Eq 1.7)}$$

Where f_1 and f_2 are the 3 dB bandwidth on the resonance curve and f_0 is the resonance frequency.

From this it can be seen that higher Q factors therefore allow higher resolution when attempting to measure incrementally smaller shifts in Δf.

[15] Figure 4.7 from humidity experiment 1c showed a response where there was an increase in frequency when a fall in frequency was expected.

Equation 1.7 is effective in measuring any signal attenuation of the resonance curve due to damping since it monitors the "narrowness" of the tip. Also, it was fairly straightforward to write computer code to represent this for incorporation into the FBAR analysis software that was developed during the project.

The graphic below represents the basis of the acoustic sensor transduction pathway.

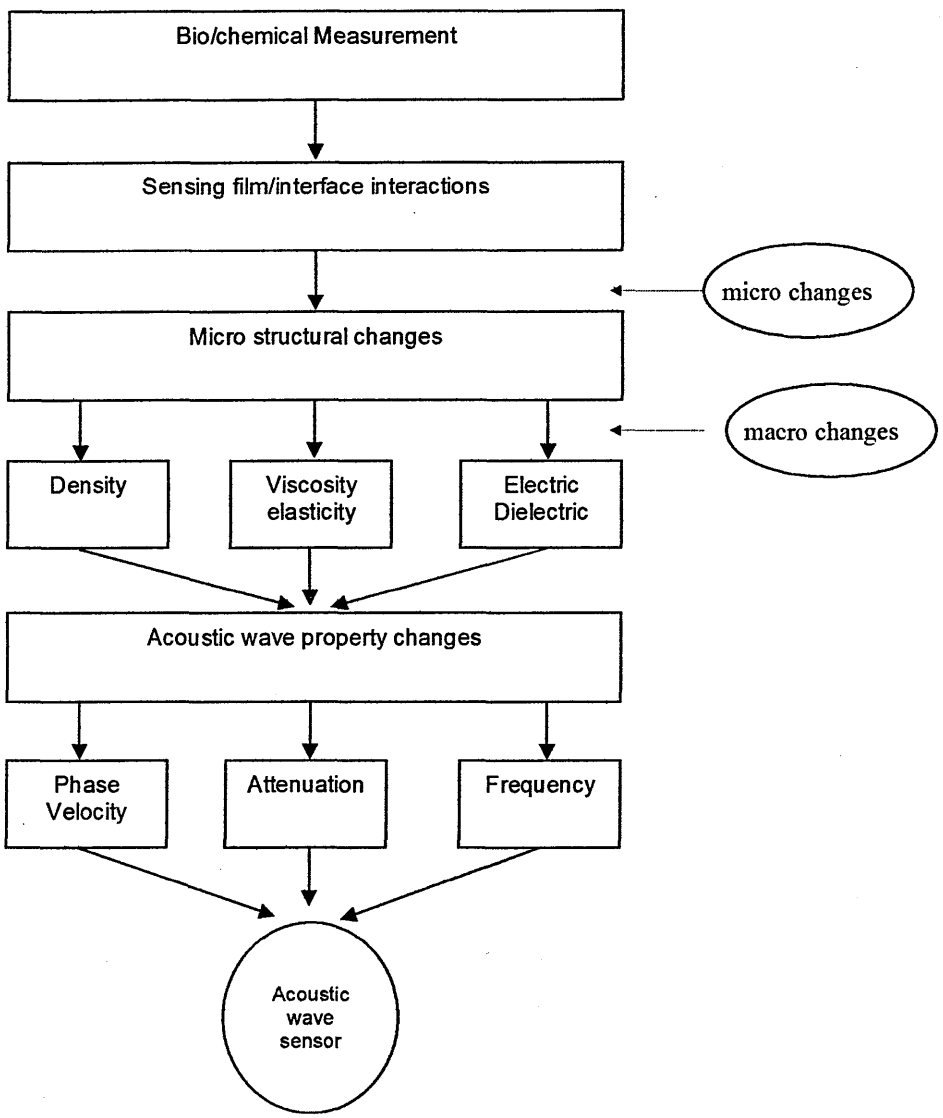

Figure 1.5 A typical acoustic/piezoelectric sensing process. (Generic)

1.3.7 Electrical equivalent circuitry for BAW resonators.

A BAW resonator can be represented by an equivalent electrical circuit. There are at least two equivalent electrical circuit diagrams commonly used to describe the electrical behaviour of quartz and FBAR resonators, these are the so called Butterworth Van Dyke (BVD) circuit and the more complicated Mason equivalent circuit.[47] The powerful mathematical FBAR model that has been constructed by researchers in our department is based on the Mason circuit, but for the purposes of this argument, and the description of FBAR sensor in chapter two, the simpler BVD circuit is invoked because it is easier to understand, and in *most* cases completely adequate in describing mass loading onto BAW resonators. In its simplest form, the BVD circuit only describes the behaviour of the piezoelectric layer, whereas the Mason model also takes into account the other layers present in the acoustic path, for instance the electrode layers. It contains two acoustic ports connected by a transmission line[16] that represents the phase shift undergone by an acoustic wave propagating across the piezoelectric thickness. A transformer, representing the electromechanical coupling between the applied voltage and the piezoelectric displacement couples the acoustic port into an electrical one.

[16] Transmission lines are conductive tracks that transfer energy efficiently at high frequencies by matching input impedance (Z) which was 50Ω in this project.

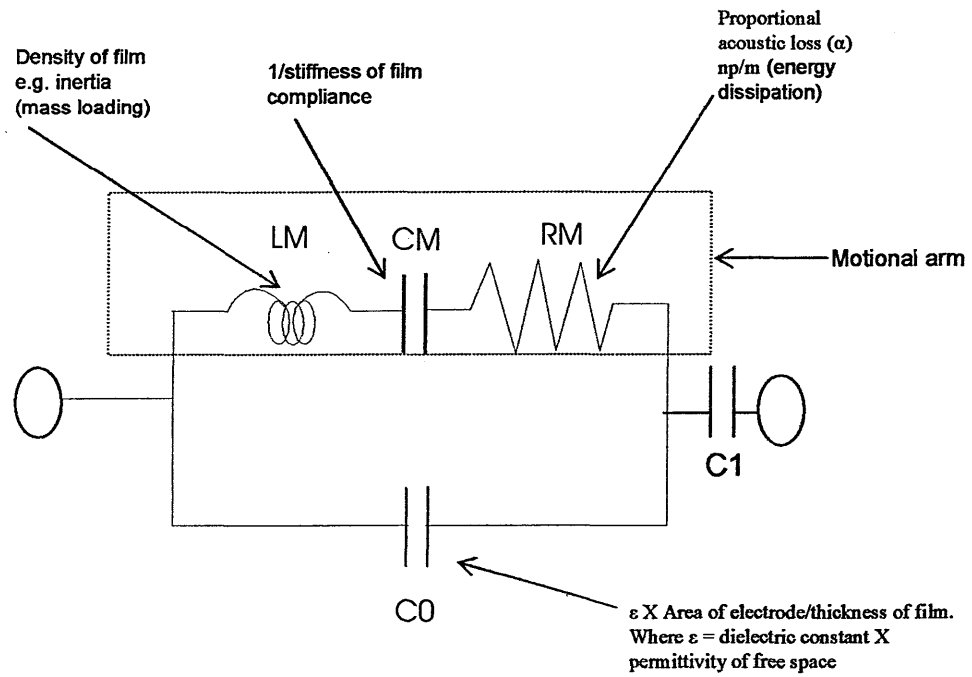

Figure 1.6 (A) Shows the equivalent Butterworth Van Dyke (BVD) circuit for a resonator at resonance. The circuit is acceptable for describing simple ideal mass loads onto a resonator in the gas phase.

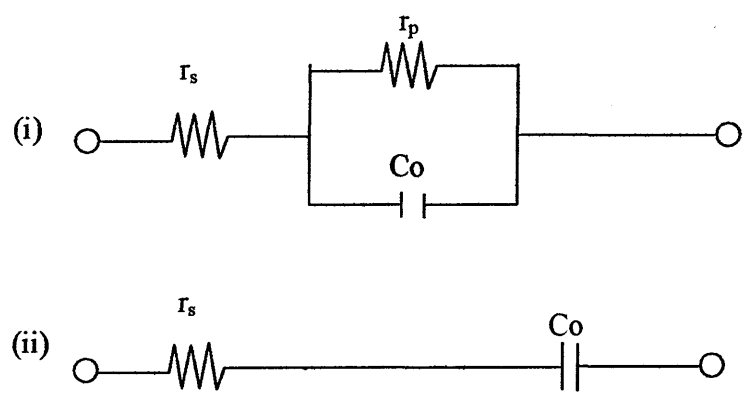

Figure 1.6 (B). Shows equivalent circuit of resonator at frequency (i) much lower than resonance frequency (ii) much higher than resonant frequency.

$$C_o = k\varepsilon_o \frac{A}{E} \qquad \text{(Eq 1.8 A)}$$

$$R_m = \frac{e^3 r}{8A\epsilon^2} \qquad \text{(Eq 1.8 B)}$$

$$L_m = \frac{e^3 \rho}{8A^2 \epsilon_0} \qquad \text{(Eq 1.8 C)}$$

$$C_m = \frac{8A\epsilon^2}{\pi^2 ec} \qquad \text{(Eq 1.8 D)}$$

Where ϵ = Piezoelectric stress constant, ϵ_0 = the susceptibility of space, r = damping coefficient, k = dielectric constant, c =elastic constant, e.

Each of the components in the BVD circuit has an equivalent representation; L_m by the mass of the vibrating body, C_m by the mechanical elasticity of the vibrating load and R_m the resistance. *Co* simply represents the capacitance of the BAW device. The ***motional branch*** of the BVD circuit arises from the electrically excited mechanical motion in the piezoelectric crystal and is explored in detail by (Arnau 2002) [48] These parameters can be evaluated from the conductance (G) frequency and susceptance (B) frequency spectra which can be obtained through impedance measurements. Conductance and susceptance are the real and imaginary parts of the reciprocal of impedance respectively, and impedance is V/I, where V and I are alternating voltage and current respectively. Several factors affecting the resonant frequency can be separated by the impedance measurements.[49]

Thompson and Yang (1993) [50] concluded that for mass sensing applications, the BVD circuit was satisfactory in simulating the impedance characterisations of TSM QCM in all cases, except where the device was completely submerged in a liquid. However, Bandy *et al* (1997) have argued that there are constraints on the applicability of the BVD model representing large loads in the gas phase and *any* load in the aqueous phase.[51]

REFERENCES
CHAPTER ONE

1. . G. Sauerbrey, (1959) Verwndung von schwingquarzen zur wagung dunner schichten und zur mikrowagung (Use of oscillator quartz crystals for weighing thin layers and micro-weighing) Translated by technical information and library services. Ministry of Aviation in 1962 *Z. Physik.* 155 206.
2. W.H. King Jr, (1964) Piezoelectric sorption detector, *Anal. Chem.* **36** pp 1735-1739.
3. Shons, A., Dorman, F., Nagarian, J. (1972) An immunospecific microbalance. *J biomed. Matter. Res.*, **6** 565-570.
4. Madou. M. (1997) Fundamentals of microfabrication. Boca Raton, FL : CRC press. Inc., ISBN 0-8493-9451-1
5. Lakin. K. M. (1991) Fundamental properties of thin film resonators. *Forty-fifth annual symposium on frequency control.* IEEE.
6. O'Toole. R., Burns S. G., Shanks. H. R., D'Silva. A., Weber. R. J., Porter D. M . (1990) Microwave frequency oscillators based on AlN: Toward integrated chemical sensors. *Optical and piezoelectric sensors symposium of the electrochemical society.*
7. O'Toole. R., Burns. S., Bastiaans., G., Porter. M. (1992) Thin aluminium nitride resonators: Miniaturised high sensitivity mass sensors. *Anal Chem.* **64** 1289-1294.
8. Knight, P.(1989) Harnessing Biomolecules for Sensing. Biotechnol, 7 175-176.
9. Madou. M. J., Morrison. S. R. (1989) Chemical sensing with solid state devices. Academic press, New York
10. Jones, B. E (1987) Chemical and Biological Sensors. Ch 13 pp 133. *Current Advances in Sensors.* The Adam Hilger Series on Sensors IOP Publishing
11. Turner, A., Karube, I., Wilson, G. (1987) Biosensors: Fundamentals and Applications, Oxford University Press, London.
12. Andle. J., Vetelino, J. (1994) Acoustic Wave Biosensors. *Sensors and Actuators* A **44** 167-167
13. Hauptmann, P. (1991) *Sensors Principles & Applications.* Prentice Hall

14. Lion, K. S.(1969) "Transducers: Problems and Prospects" *IEEE Transactions IECI-16* 2-5
15. Collings . A. F., Caruso. F. (1997) Biosensors:-Recent advances. *Rep. Prog. Phys.* 60 1397-1445
16. Lec. R. M (2001). Piezoelectric biosensors: Recent advances and applications. *IEEE international frequency control symposium and PDA exhibition.* pp 419-429
17. Ricco, A, Frye, G, Martin, S. (1988) Determination of BET surface areas of porous thin films using surface AW devices. *Langmuir*, **5** 273-276
18. Ricco, A., Martin, S. (1993) Multiple-Frequency SAW devices for chemical sensing and materials characterisation. *Sensors and Actuators* B, **10** 123-131.
19. Benes, E. Groschl M, Seifert F, Pohl (1998) A. Comparison Between BAW and SAW sensor Principles. *IEEE Transactions on Ultrasonics, Ferroelectrics, and Frequency control.* **45**, 5. pp 1314-1330
20. Muramatsu. H., Suda. M., Ataka. T. (1990) Piezoelectric resonator as a chemical and biochemical sensing device. *Sensors and Actuators*, A **23** pp 362-368.
21. Kanazawa. K., Gordon. J. (1985) The oscillation frequency of a quartz resonator in contact with a liquid. *Anal Chim Acta.* **67** pp175 99.
22. Huang. M., Shen. D., Yang. (2001) M. Effects of longitudinal wave on the resonance behaviour of an electrode-separated piezoelectric sensor in liquids. *Analytica Chimica Acta.* **440**.109-118
23. S. Bruckenstein and A. R. Hillman,(1995) in *Handbook of Surface Imaging and Visualization*, ed. A. T.Hubbard, CRC Press, Boca Raton, FL, p. 101.
24. Hung. V., Minh. P., Abe. T., Esashi. (2003) M. High-Frequency one-chip multichannel quartz crystal microbalance fabricated by deep RIE. *Sensors and Actuators* A **108** 91-96
25. Osbond. P., Beck. C. M., Brierley. J. C., Cox. R. M., Marsh. P. S., Shorroks. (1999) M. N. The influence of ZnO and electrode thickness on the performance of thin film bulk acoustic wave resonators. *IEEE ultrasonics symposium. 911.*
26. Roedereer, J., Bastiaans, G. (1983) Microgravimetric immunoassay with piezoelectric crystals. *Anal Chem*, **55** pp 2333-2336.

27. Grate. J. W. (2000) Acoustic wave microsensor arrays for vapour sensing. *Chem. Rev.* 100 pp 2627-2648

28. Radeva. E., Georgiev. V., Koprinarov. N., Kanev. (1997) S. Humidity adsorptive properties of thin fullerene layers studied by means of quartz crystal microbalance. *Sensors and Actuators* B. **42**. pp 11-13.

29. Lack, F., Willard, G., Fair, I. (1934) Some improvements in quartz crystal circuit elements. *Bell Syst. Tech J.* **13** 453-463.

30. Wade. W. H., Slutsky. L. Quartz crystal thermometer, *Rev. Sci Instrum.* **33** (1962) 212-213)

31. Ziegler H. (1984) A low-cost digital sensor system, *Sensors and Actuators* **5** 169-178

32. Bechmann. R., Ballato. A. D., Lukaszek. (1962) Higher order temperature coefficients of the elastic stiffness and compliances of alpha quartz. *Proc IRE*, 50 1812-1822

33. Vig, J. Walls F. (2000) A Review of Sensor Sensitivity and Stability. *IEEE/EIA International Frequency Control Symposium and Exhibition.*

34. A. Ballato (1996) Piezoelectricity: History and new thrusts. *Proc. Ultrason. Symp.* Vol **1**, pp. 575-583

35. Auld. B. (1990) *Acoustic fields in waves and solids*, 2nd Edition. Vol I & II, Krieger Malabar, Florida, USA

36. Schmit. R., Allen. J., Vetelino. J., Parks. J., Zhang. C. (2001) Bulk acoustic wave modes in quartz for sensing measurand-induced mechanical and electrical properties. *Sensors and actuators* B **76.** pp 95-102

37. Salt. D. (1987) *HY-Q Handbook of quartz crystal devices*, Van Nostrand Reinhold, New York

38. Smith. W. (1985) Precision frequency and control, Vol 2, Oscillators and standards. Academic Press: New York Chapter 8.

39. Benes. E., Groschl. M., Burger. W., Schmid. M. (1995) Sensors based on Piezoelectric resonators. *Sensors and Actuators* A **48** 1-21.

40. Steward. T. J., Yong. Y. (1994) Exact analysis of the propagation of acoustic waves in multilayered anisotropic piezoelectric plates. *IEEE transactions on ultrasonics, ferroelectrics and frequency control.* **41**. 3.

41. Bill Drafts. (2001) Acoustic Wave Technology Sensors. *IEEE Transactions on Microwave Theory and Techniques.* **49**. No 4.

42. Lucklum R., Hauptmann.P (2000) The quartz crystal microbalance: mass sensitivity, viscoelasticity and acoustic amplification. *Sensors and Actuators* B **70** pp 30-36

43. M. Thompson, G. K. Dhaliwal, C. L. Arthur and G. S. Calabrese (1987) The potential of the bulk acoustic wave device as a liquid phase immunosensor, *IEEE Trans. Ultrason., Ferroelectr. Freq. Control* UFFC-34 127-135.

44. R. Schumacher (1990) The quartz microbalance: a novel approach to the in situ investigation of interfacial phenomena at the solid/liquid junction, *Angew. Chem., Int. Ed. Engl.*, **29** pp 329-343.

45. Su. X., Chew. F., Li. S. (2000) Piezoelectric quartz crystal based label-free analysis for allergy disease. *Biosensors and Bioelectronics* **15** pp 629-639.

46. Su. Q., Kirby. P., Komuro. E., Imura. M., Zhang. Q., Whatmoore. R. (2001) Thin-film bulk acoustic resonators and filters using ZnO and lead-zirconium-titanate thin films. *IEEE transactions on microwave theory and techniques*, Vol 49 4. pp 469-777

47. Rosenbaum. (1998) Bulk acoustic wave theory and devices, Artech house, Boston

48. Arnau. A., Sigorb. T. (2002) Circuit for continuous motional series resonant frequency and motional resistance monitoring of quartz crystal resonators by parallel capacitance compensation. *Review of Scientific Instruments.* **73** 7 pp 2724-2737

49. Yamaguchi, S., Shimomura, T. (1993) Adsorption, Immobilization and Hybridisation of DNA Studied by the Use of Quartz Crystal Oscillators. *Anal. Chem.* **65,** 1925-1927.

50. Yang. M., Thompson. M. (1993) Acoustic network analysis and equivalent circuit simulation of the thickness-shear mode acoustic wave sensor in the liquid phase. *Analytica Chimica Acta.* **282.** pp 505-515.

51. Bandey. H., Hillman. A., Brown. M., Martin S. (1997) Viscoelastic characterisation of electroactive polymer films at the electrode solution interface. *Faraday Discussions*. **107** pp 105-121

52. Mecea. V. M. (1994) Loaded vibrating quartz sensors. Review paper. *Sensors and Actuators A*. **40**. 1-27.

53. Gable R., H.-D. Feucht, H. Zeininger, G. Eckstein, M. Schreiter, R. Primig, D. Pitzer, W. Wersing (2004) First results on label-free detection of DNA and protein molecules using a novel integrated sensor technology based on gravimetric detection principles. *Biosensors and Bioelectronics* **19** 615–620

54. Paddle. B. (1996) Biosensors for chemical and biological agents of defence interest. *Biosensors and Bioelectronics*. **11**. No 11. pp 1079-1113

55. Iwata. H. (2004) Measured resonance characteristics of a 2-GHz fundamental quartz resonator *IEEE transactions on ultrasonics, ferroelectrics and frequency control*. **51**. 8. pp 1023-1029

56. Koblinger. C., Drost. S., Aberl. F,. Wolf. H., Koch. S., Woias. P. A quartz crystal biosensor for measurement in liquids. *Biosensors and Bioelectronics*. 7 (1992) pp 397-404.

57. Corry. B., Uilk. J., Crawley. C.(2003) Probing direct binding affinity in electrochemical antibody-based sensors. Anal Chim Acta. **496** pp 103-116

CHAPTER TWO
2.0 ADAPTATION OF THE EXISTING FBAR DESIGN FOR THE DETECTION AND MEASUREMENT OF CHEMICAL AND BIOLOGICAL AGENTS.

2.1 Introduction

This chapter gives the main details of the strategies that were devised to specifically address the problems that were encountered, and the solutions that were developed, in adapting the existing Cranfield FBAR design for use in chemical and biological sensing procedures. The recent advances that have already been made using FBARs in chemical and biological sensing are presented along with the relevant American patents that were already in existence prior to the start of this work in relation to FBAR based sensing.

The microfabrication procedures involved in the manufacture of FBAR devices on silicon wafers in a clean-room environment are shown along with the methods that were already in place to electrically characterise them upon completion. The important electro-acoustic principles of FBAR operation are described.[17] The limitations of the existing FBAR characterisation methods in relation to chemical sensing are explained and the methods that were devised to circumvent these limitations are described. The design and fabrication procedures that were involved in the construction of a novel housing chamber in which to isolate the FBAR from the ambient laboratory environment are shown along with the main experiments that were performed to develop high quality, low loss, microwave frequency electrical connectors which allowed the FBAR to remain in relatively efficient electrical contact with the outside world whilst being environmentally isolated from it.

The main points involved in the coding and in the initial implementation of a new software suite that was specifically developed to meet the exacting requirements of the FBAR sensing project are summarised, along with a very brief description of the key abilities and advantages that it had over the existing FBAR characterisation software in

[17] These descriptions are more specific to FBAR than the general overview of BAW operational principles given in Chapter 1

place at the department. A more detailed consideration of the functionality of the software is shown in Chapter 3 where its performance is critically evaluated during preliminary FBAR based sensing experiments.

The specifics of the additional sensing layers that were used to coat the FBAR top surface electrode to bestow selective chemical, gas, or biosensor type abilities upon it are not addressed in this chapter, but are considered in detail in Chapter 4 (*chemical sensing*) and Chapter 5 (*biosensing*).

2.1.1 Background to microsystems

Micromachining and MEMS technologies (also known as Microsystems) can be used to produce complex electrical, mechanical, fluidic, thermal, optical and magnetic structures, devices and systems whose size is in the micron range. This miniaturisation ability has enabled MEMS to be applied in many areas of biology, medicine and biomedical engineering. In the literature, this field is generally referred to as BioMEMS and is possibly the correct term to describe the FBAR based immunosensor prototype development demonstrated in this work.

MEMS is a technology that has been taken from the developments in miniaturisation that were made by the integrated circuit (IC) industry e.g., Intel® and applied to the miniaturisation of various types of other systems not just limited to IC. This miniaturisation is accomplished with microfabrication processes such as micromachining, which typically but not exclusively employ some form of photolithography. The classical and seminal papers of the early stages of this research field can be found in [REF = W. Trimmer. Micromechanics and MEMS: classic and seminal papers to 1990. IEEE press, New York. (1996). Methods on MEMS fabrication procedures are comprehensively covered by Kovacs 1998 [1] and Madou 1997 [2]

The goal of MEMS technology is the merging through solid state microdevices of the functions of sensing, computation, communication and actuation. MEMS technology is already quite well developed offering low-cost, small, light weight and increasingly

reliable devices through durability and redundancy, and its perspective integration with nanodevices is strongly attractive as a near-term technology for a multitude of applications.[3]

2.1.2 Background to the emergence of thin film resonator technology

The emergence of thin film resonator (TFR) technology *per se* can be traced back to the work of Lakin and Wang (1981) who built further on the earlier pioneering work of Sliker and Roberts.[4] TFR devices are different from quartz in that the metal electrodes can be a substantial fraction of the total thickness and of a large lateral extent compared to resonator thickness.[5] There is considerable interest in the development of FBAR for front-end filters for applications in communications systems, radar and electronic warfare applications.[6, 7] The commercial impetus for developing these frequency selective devices is to replace surface acoustic wave (SAW) and ceramic front-end RF filters in mobile telephones with a higher performance, lower weight and size and power handling and consumption properties. FBARs can also be used as resonators for oscillators.

Originally designed for use as frequency filters for microwave enabled communications, and missile RF receivers, FBARs are devices that can generate acoustic waves in the UHF and microwave frequency spectrum. The FBAR is a MEMS TFR device based on a thin (micron range) piezoelectric slab[18], and it is designed to considerably increase the fundamental resonant frequency (f_0) of bulk acoustic wave (BAW) devices.

MEMS technology dimensions allow for the fabrication of electrical circuits that are comparable with the wavelengths of electromagnetic microwaves. In their 1992 paper [8] on applications of film bulk acoustic wave resonators, Horowitz and Milton fail to consider that FBARs could be used in chemical and biological sensing applications, perhaps indicating that it is not immediately obvious to RF engineers The UHF and microwave frequency is typical of the acoustic frequency that was used to probe the analytes that were measured in this project, but the desire was always to use higher

[18] The terms piezoelectric slab, film or plate are used interchangeably in the thesis..

frequencies where possible because in theory higher frequencies should give greater sensitivity to the presence of the measurand in contact with the resonator.

2.1.3 Previous reports of FBAR chemical and biological sensing

The use of FBAR devices as a transduction element in chemical sensing applications can likely be considered a concept that was first described by O'Toole *et al* (1990,1992) [9,10] where demonstration of TFR as a gas-phase sensor was demonstrated. Thiolate monomers (fluorinated or carboxylic acid terminated) were used to generate basic selectivity toward methanol and they that showed that FBARs operating at ~1 GHz could easily detect 2.5 ng/cm^2 methanol with uncertainties due to noise ~0.3 ppm. The results of O'Toole followed the expected theoretical response of a well behaved "Sauerbrey" type resonator. Xia *et al* (1995) [11] showed that FBAR with piezoelectric substrate of AlN operating nominally at 1 GHz can be used to detect the mass loading effects from the lightest of the elements as gaseous molecular hydrogen, H_2. Using a thin PdNi alloy which was known to irreversibly bind hydrogen gas as H-Pd, Xia showed that the additional mass of the H_2 *and* the changes in the viscoelasticity of the layer due to the hydrogen adsorption will change three key parameters in FBAR outputs namely, (i) series resonant frequency, (ii) series resistance, and (iii) the Q factor. From this understanding Xia deduced that it was possible to use an extended version of the one dimensional Mason equivalent circuit to model the wave propagation in the additional layer. The model they use predicts that the changes in viscosity do not affect the series resonant frequency, but that they do affect series resistance and the Q factor. The mass loading effect was shown to be linear with the square root of hydrogen concentration, and this mass loading effect dominated the FBAR output response. As little as 5 ppm H_2 could be detected using this method.

Zhang *et al* (2003), [12] showed for the first time that FBAR devices could still support bulk longitudinal standing waves, *especially overmodes*, when submerged in a semi-infinite liquid layer, although there is significant damping of the response. They also showed that an *uncoated* FBAR device[19] could respond 10^{-9}g\cm^2 of isopropanol vapour

[19] A FBAR device with no chemical or biological sensing layers attached to its resonating surface(s).

on its surface. They point out that high mass sensitivities are related to the high fundamental operating frequency and that both of the sides (top and bottom electrodes) can be used for sensing applications[20]. It is known that reactance is linearly related to the series and parallel resonant frequency in BAW devices. Using reactance as inferred from parallel and resonant frequency spacing, Zhang *et al* have reported the ability to detect resonant frequency changes via reactance as small as 0.3 ppm if the Q factor of the FBAR is 200-300. They suggest that using this method can improve the minimum detectable signal resolution by an order of magnitude because the level of uncertainly in their measurement of reactance approximated to ~ 400 mΩ, and they had previously calibrated this to approximately ~400 Hz. They report a 0.3 ppm uncertainly in the signal, and 400 Hz was modelled to approximately 10^{-9}g cm^2, the minimum measurable detected mass change was therefore comparable to the best QCM.

However in this study, S parameters were not converted to reactance values and the pertinent measurement values (i) series resonance frequency, (ii) power transmission, and (iii) Q factor were investigated as the variables in the output response of the FBAR during its interaction with measurand/analytes. The level of uncertainty in the FBAR response in this work was reduced by fitting polynomial smoothing curves to the measured FBAR output data.

Webber *et al* (1992) [13] showed that FBAR could be used as a gas and chemical sensor with nanogram sensitivity. The sensitivity and selectivity was inferred by coating the TFR surface with organic, selectively adsorbing monolayer films. Interestingly, Webber *et al* also show that the level of hydrophobicity and hydrophilicity existing on the FBAR surface significantly alters its S_{21} series resonance response to methanol vapour. This finds agreement with Absolom's (1987)[29] work on the hydrophobicity and hydrophilicity of QCM surfaces in sensing applications..

[20] This is a useful observation, since the etch hole that is made through the silicon substrate could likely be used as a reaction vessel with which to hold liquids.

Workers at Siemens AG of Munich under R. Gabl (2003) [14] have demonstrated the feasibility of detecting DNA and protein with FBAR and reported that the higher fundamental operating frequencies of FBAR give higher mass sensitivity and resolution than QCM. They also note the expense of quartz and the difficulties involved in forming arrays with it. Furthermore, they show that mass detection is not dependent on the resonator's working area, but on the mass per unit area. They suggest that in the future, FBAR devices with working areas of 20 μm X 20 μm are likely to be microfabricated by downscaling. They conclude that an FBAR with an operating frequency of ~ 2 GHz will give mass sensitivity ~ 2500 times higher than that of a QCM operating at 20 MHz.

A search for Patents exploiting TFR and FBAR as applied to chemical and biological sensing has revealed a few interesting American inventions [28]

2.1.4 FBAR design and principles of operation

First generated artificially by Hertz and Marconi in the year 1888 by spark generators, the RF or microwave signal is often designated as the electromagnetic frequency range from 300 MHz to 300 GHz having wavelengths of 1 mm to 1m. FBARs operate within the lower end of this spectrum up to ~10 GHz, but the range of ~300 MHz[21] to ~1.8 GHz is considered in this project. FBAR is an *acoustic device*, slowing down the near-light propagation velocity of an incident microwave photon in its electromagnetic form and serving to transduce the frequency to an acoustic or mechanical wave[22], and in doing, so decreases the wavelength whilst maintaining the frequency of the microwave signal. This property is a mechanical function of the piezoelectric substrate excited by microwave frequency voltages, the electro-acoustic conversion takes place at *all* frequencies, but the amplitude of the acoustic vibration is small except at the natural resonance frequency and the harmonic overmode frequencies (n =1,3...) of the device where the mechanical displacement becomes large.

[21] This is actually in the UHF range, but for simplicity, the term microwave frequency range is used throughout the thesis

[22] Acoustic waves are in fact mechanical waves of displacement/disturbance through a material.

The generic concept of an FBAR is of a piezoelectric layer, usually AlN, ZnO or PZT in between two thin (~100 nm), usually Au but sometimes Mo, conducting electrodes to make a metal-piezoelectric-metal stack and an isolation layer of a resonant region from a piezoelectric substrate[23]. The isolation layers isolate the propagation of acoustic waves from the piezoelectric layer to the substrate with high acoustic loss. Therefore, the acoustic wave is confined within the piezoelectric layer and this enables a FBAR device to have a high quality factor (Q).[15] The total thickness of the piezoelectric layer the electrodes is frequency determining whilst the planar area of the active device determines its impedance and is dominated by the clamped capacitance (C_0) at most frequencies.

When a high frequency AC potential is applied to across the FBAR top and bottom electrodes, the piezoelectric substrate between the two electrodes expands and contracts, this creates an oscillatory vibration in the membrane structure of which the piezoelectric layer is a part. The amplitude of the contraction and expansion reaches a maximum at the *mechanical* resonance frequency of the membrane. As the AC is applied across the device, the polarisation vector (P) will change in phase with the applied signal frequency. At some voltage (V_s), P will be in phase with the vector (E) created by the applied potential. This corresponds to the series resonance of the device. At another voltage frequency (V_{fp}) the polarisation vector will be 180^O out of phase with E, this corresponds to the parallel resonance. The resonances are associated with rapid changes of the electrical impedance, this behaviour is used to construct frequency selective filters and oscillators.

The resonance frequencies in the microwave range are a very sensitive function of the layer thickness and mass of the membrane, and it is this fact that leads to the consideration of the FBAR device as a chemical and biological micro-gravimetric sensor.

[23] This is the place on the device where the Top and Bottom electrodes, which are separated by the piezoelectric film, overlap each other. (*See Figure* 2.8 completed FBAR device)

The series resonant frequency f_s is given by:

$$f_s = \frac{1}{2\pi\sqrt{L_m C_m}} \qquad \text{(Eq 2.1)}$$

And the parallel resonant frequency f_p is given by:

$$f_p = \frac{1}{2\pi}\sqrt{\frac{1}{L_m C_m} + \frac{1}{L_m C_0}} \qquad \text{(Eq 2.2)}$$

Where R_m, L_m, and C_m are motional resistance, motional inductance and motional capacitance respectively. C_0 and R_s are the clamped capacitance and series resistance respectively.

The elecromechanical coupling constant K_t^2 is a value representing the efficiency of the piezoelectric conversion of input electrical energy to mechanical energy output from the FBAR. It can be shown to be related to the difference between the frequencies of the series and parallel resonances as;

$$k_t^2 = \frac{\pi^2(f_p - f_s)}{4 f_s} \qquad \text{(Eq 2.3)}$$

Su *et al* (2001)[24] [16]state that the presence of additional mass layers loaded onto FBAR devices will result in lower effective electro-mechanical coupling coefficients. therefore k_t^2 will decrease as Z_m increases) This fact is further verified by Zhang and Kim (2002) [17] who have shown empirically that K_t^2 will decrease with the addition of a mass load onto the resonator.

In a FBAR, the thickness of the electrodes, the support film and the optional upper SiO_2 layer is comparable to that of the piezoelectric film. Therefore, these layers must be included in the calculation of the resonant frequencies, and in this work, the thickness of

[24] In this paper, Su *et al* (2000) a much more in-depth analysis of FBAR physical design approaches, along with detailed descriptions of the equivalent circuits used to model Q factor, S parameter derivations and impedance calculations along with its use as applied in microwave filter applications and also descriptions of advanced methods of FBAR measurement techniques and analytical procedures can be found.

these films was used to influence the FBAR resonance frequency. This fact has also been noted by Osbond *et* a (1999) who observed the influence of ZnO piezoelectric substrate and electrode thicknesses on the performance of FBARs [18]

Typically, the characteristic use of a sensing piezoelectric resonator is as a frequency-determining element in a feedback loop of an oscillator circuit.[19] When incorporated into a sensing system, the piezoelectric resonator, which is the frequency-determining element is incorporated into an oscillator circuit.

At frequencies far from the resonance frequency, where the acoustic amplitude is small, The FBAR can be considered as a parallel plate capacitor with a dielectric (the piezoelectric) between two conducting plates (the electrodes). But this is a special case, since the capacitance transforms into a *pure resistance* at series resonance.

The basic operation of an FBAR can be understood simply by the use of the fundamental equation;

$$v = f\lambda \qquad \text{(Eq 2.4)}$$

Which relates the velocity v, of the acoustic wave to the product of frequency and wavelength, for convenience, this can be written as;

$$f = \frac{v}{\lambda} \qquad \text{(Eq 2.5)}$$

If the thickness of the FBAR is say, $2\text{x}10^{-6}$ m, and if the acoustic velocity is ~ $5\text{x}10^{3}$ ms^{-1}, the frequency of operation will be approximately $f = 5\text{x}10^{3}/2\text{x}10^{-6} = 2.5$ GHz. These considerations show that even a change in thickness in the nanometre range will have a measurable frequency change on suitable apparatus.

In the FBAR, like quartz, the resonance condition occurs if the thickness of the piezoelectric thin film (d) is equal to an odd integer multiple of a half wavelength. (λ_{res}).

$$d = \frac{\lambda}{2} \qquad \text{(Eq 2.6)}$$

The fundamental resonant frequency (F_{res} or $f_0 = 1/\lambda_{res}$) is then inversely proportional to the thickness of the piezoelectric material used, and is equal to $V_a/2d$ where V_a is an acoustic velocity at the resonant frequency.

Using this equation, if the acoustic properties of an additional layer are, for the moment neglected, and assumed to be continuous, then the resonant frequency will fall as the thickness of the composite device increases as;

$$F_{res} = \frac{V_a}{2d} \qquad \text{(Eq 2.7)}$$

If the metal electrodes and or the additional sensing layers make up a significant fraction of the total FBAR thickness, then although equations 2.4 - 2.7 are still valid, the velocity of the wave is now determined by its speed through all of the layers. (i.e., the composite) Using this approach, it can be seen how the FBAR can act as an acoustic sensor.

Although the argument presented above is technically correct, it is somewhat simplified since it does not take account of the mechanical nature of the layers that make up the FBAR structure. The simplest model that does take the mechanical properties into consideration is the physical Mason model whose electrical equivalent circuit is the BVD model. Using a Mason model, the electrical impedance (Z) of the FBAR for the case of thin electrodes (which can be ignored) is derived as;

$$Z = \frac{1}{i\omega C_0}\left[1 - k_t^2 . \frac{\tan\varphi}{\varphi}\right] \qquad \text{(Eq 2.8)}$$

Where ω is angular frequency, C_0 is clamped capacitance, k_t *is* the electromechanical coupling coefficient. φ is $kd/2 = \omega d/2v_a$, where d is the thickness of the piezoelectric film. v_a is the longitudinal acoustic velocity of the piezoelectric film.

When the electrodes are thick enough to make a contribution to the impedance, they can be represented as;

$$Z = \frac{1}{i\omega C_0}.\left[1 - k_t^2 . \frac{1}{\varphi.(\cot\varphi - R\varphi}\right] \qquad \text{(Eq 2.9 A)}$$

Where:

$$R = \frac{\rho_t d_t + \rho_b d_b + \rho_m d_m}{\rho d} \qquad \text{(Eq 2.9 B)}$$

ρ is the piezoelectric layer, *d* is the thickness of the layers. In this case R is the mass loading factor as a consequence of the electrodes and is due to inertia. Subscripts t, b, and m are the top electrode, bottom electrode and membrane

Motional Impedance is given as: (Cernosek 2003) [20]

$$Z_m = R_1 + j\omega L_1 + \frac{1}{j\omega C_1} + Z_m^1 \qquad \text{(Eq 2.10)}$$

where motional impedance is due to surface perturbation given by:[20]

$$Z_m^1 = R_2 + j\omega L_2 \qquad \text{(Eq 2.11)}$$

See figure 2.1 below.

The electrical impedance is equivalent to mechanical impedance which is the equivalent extra inertia[25] generated from mass loading. L_2 therefore dominates the response. R_2 is dissipation of energy resulting from the attenuation of the acoustic probing wave when interacting viscous i.e., lossy loadings. If the additional layer is not continuous, the difference in the acoustic properties of the electrode and the additional layer become significant at the interface. A perfect *ideal mass load* could therefore be represented by merely increasing the thickness of the gold that makes up the electrode so that no significant acoustic interface exists[26].

[25] This is why the word **gravimetric sensor** is really a misnomer, it will be recalled that inertia is a function of mass which totally independent of gravity as it is commonly understood at present.

[26] In Chapter 6, future work, math models are shown with increased electrode thickness and the subsequent effect that this had on FBAR resonant frequencies.

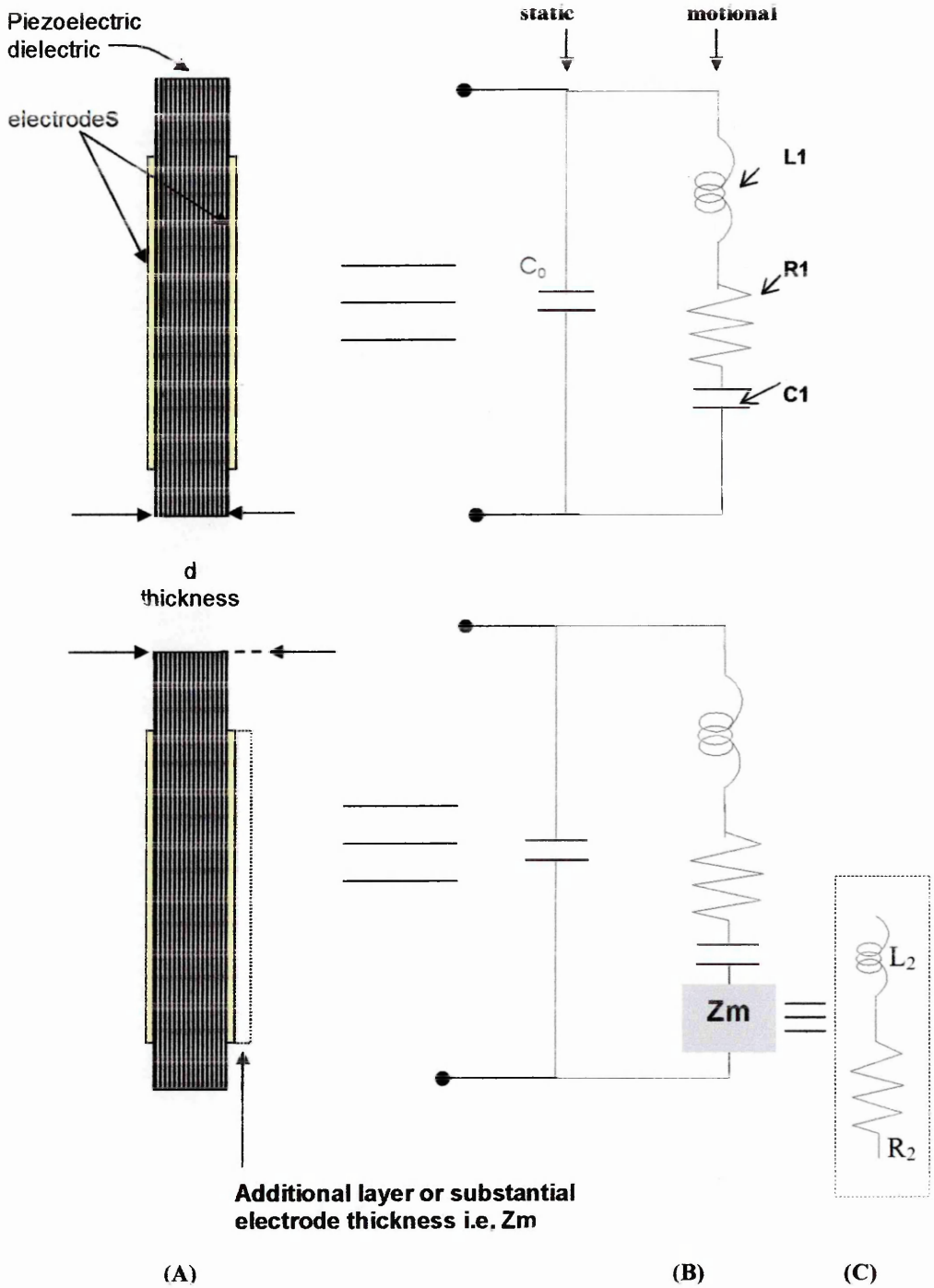

Figure 2.2 (A) is a cross section of piezoelectric resonator, **(B)** is the BVD circuit and **(C)** is the equivalent series L_2R_2 component representing electrical impedance which comes from the addition of a mass load on the resonator. *Adapted* from [21] The BVD model will not predict harmonic overmode responses of the device.

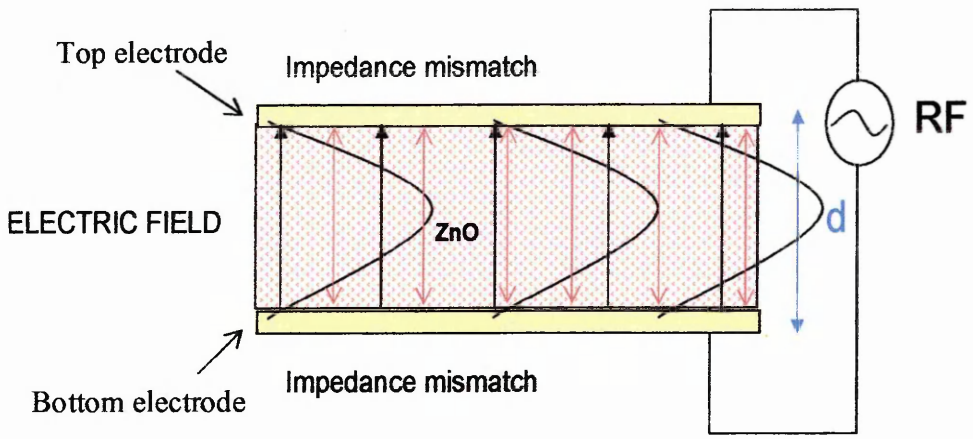

Figure 2.2 Schematic to show longitudinal wave generation (this mode is also known as bulk longitudinal extensional) and propagation in an acoustic resonator by an electric field in the thickness direction.

d = thickness :- piezoelectric (~ 0.5 -3 micron range) Top and Bottom electrodes are usually gold. (~100 nm.)

(Taken from *www.mems.usc.edu/fbar.htm*)

2.2 FBAR microfabrication procedures.

2.2.1 Materials and Methods

FBARs were fabricated in a clean room[27] of 100 square meters with class 1000 filters and locally 100 under the lamina flow hoods. FBARs were coated with metallic and oxide in a Coatings laboratory with a semi-clean environment. Upon completion, the devices were interrogated in the Measurement room on the HP 8753D network analyser. The list of chemicals and the various apparatus used in the processing of the blank wafers is given in Appendix 2. A summary of the main processing stages is given before the details of the microfabrication procedures involved are described.

2.2.2 Fabrication of FBARs with micromachining techniques

The FBAR devices were created on silicon wafers using a thin film semiconductor sputtering process to make an unsupported metal-piezoelectric-metal stack. The fabrication was completed in 23 to 26 processing stages involving 10 main steps, the steps are outlined as a schematic below in figure 2.3

2.2.2 1 Wafer handling

Wafers were handled with tweezers 45° relative to the main flat as this is where the wafer possesses most mechanical strength. Care should be taken when handling wafers with tweezers because wafers are brittle and prone to breakage most especially if the wafer had notches or chips in it.

Wafers were assumed to be as clean as possible when immediately removed from the packaging supplied by the manufacturer. Table 2.1, shows the common sources of wafer contaminants. The required number of wafers were taken and their thickness measured with a micrometer. They were then inspected with the naked eye (bringing the eye almost horizontal to the wafer) under a very bright light to check for flocculent contamination. Records were taken with the batch cards on the number and positions of any visible

[27] This is a highly controlled environment where the presence of particulates in the air is minimised. Particulate contamination of the devices during their development can deleteriously influence their performance.

particles. Micron sized particles were visible using this method. If heavy contamination was observed over the wafer it was first washed with Acetone /IPA spinning, if heavy flocculent contamination remained, especially over the areas that would later be supporting the devices (i.e., towards the centre of the wafer) then it was rejected as part of the quality control procedure. Contamination at the edges of the wafer was not seen as overtly critical to continued processing. Repeated working of wafers after mistakes or unavoidable processing failures would inevitably increase particulate/chemical contamination and since certain particles would become electrostatically bonded to the surface; they were difficult, if not impossible to remove. Wafers were diamond scribed for identification if not already possessing a serial number and placed into the PTFE spider boxes which were also marked for identification and tracking purposes.

Table 2.1 Common wafer contaminant sources From Madou (1997) [2]

Wafer transfer box.
[illegible]
Process equipment
Residual photoresist or organic coating
Metal corrosion
Solvents and chemicals
[illegible]
Clothing/lint
Electrostatic charge (cleanroom should have a conductive floor)
Humidity and temperature variation
Unclean room furniture
Operator – smoker or non smoker.

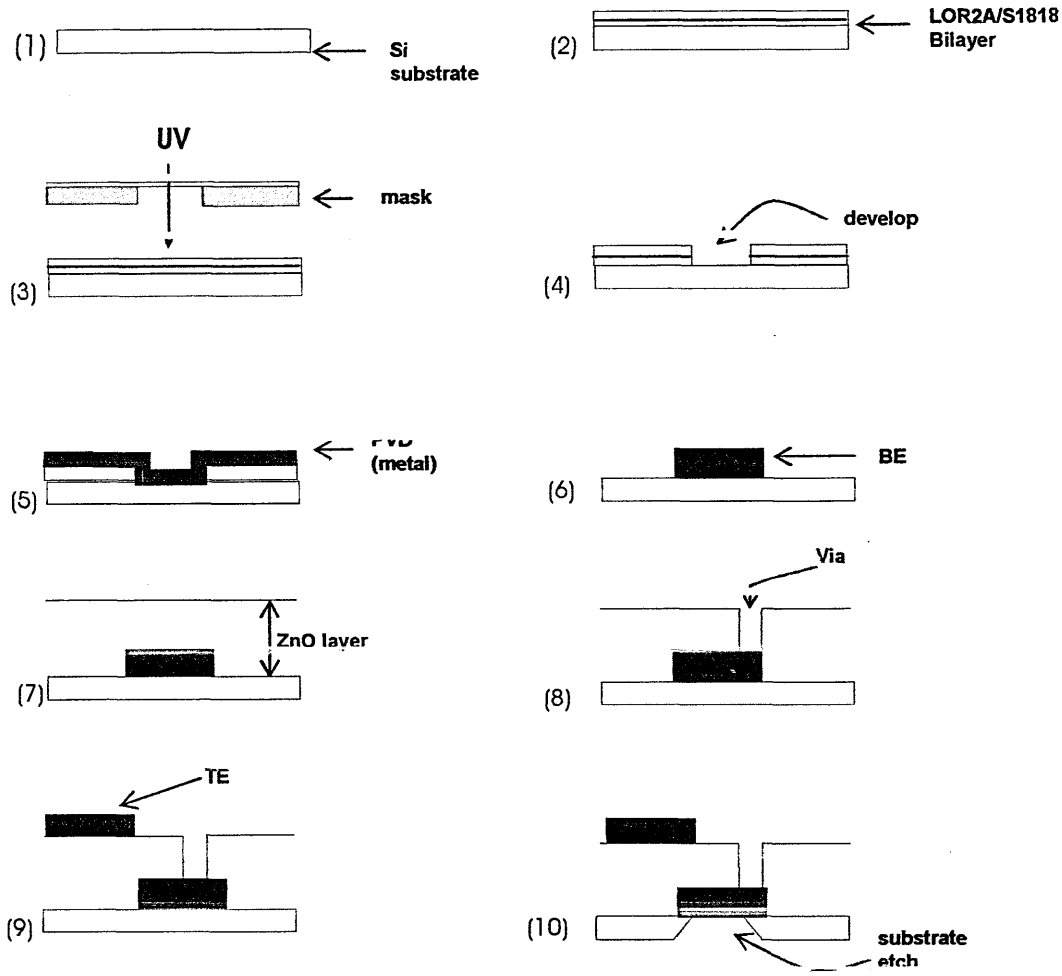

(1) Represents the bare wafer (Silicon substrate)	(2) Coated with LOR2A & S1818 photo resist. (Bilayer formation)
(3) UV exposure through mask for patterning and developing.	(4) Represents the patterned and developed wafer
(5) The patterned wafer is then PVP sputtered with Ti/Au	(6) Represents the acetone "lift off" process, leaving BE bound to the substrate
(7) Represents the PVD deposition of the ZnO film over BE.	(8) Further photoresist (S1818) spin coating, UV exposure and developing to etch via contact to BE
(9) PVD deposition of TE over the surface of the ZnO film.	(10) Final substrate etch to release the membrane. This represents the finished FBAR.

Figure 2.3 Schematic of the major steps in the microfabrication procedures involved in construction of the FBAR device on 4 inch silicon wafers

2.2.2.2 Bottom electrode deposition

2.2.2.2.(A) General and safety considerations

All wafer photoresist depositions were performed under the protection of a fume hood. The dark-field mask that was used for the patterning of the bottom electrode (BE) was the QQBASE mask. It was deemed to be good practice to clean the spinner chucks in sonic acetone bath to remove any residues on them left by previous users before attempting all of the following procedures.

The spinner collecting bowl was always covered with absorbent papers to collect spin residues that could clog up the apparatus rendering it unavailable for use until servicing. These resist laden papers were disposed of in plastic bags which were sealed under the protection of the fume hood to avoid solvent vapour contamination of the clean room working environment since the solvent vapours were noxious. It was also good practice to remove these photoresist contaminated papers from the spinner before attempting any further solvent cleaning procedures as the solvent spray did, on occasion, back contaminate the wafer depositing residues of photoresist upon evaporation.

Mask aligners were powered up for at least 10 minutes for a warm up period and if nitrogen cooled, nitrogen line was left running for 30 minutes *after* the lamp has been turned off to minimise explosion risk. Care should also be taken not to over expose the photoresist in the aligner as UV light leakage will interfere with the immediately adjacent non-pattern area and cause an etch profile with rough edges and hence decreased precision of the micro components Care should be taken also not to over bake the Photoresist as this will cause cracking since too much solvent will be removed and flexibility will be lost. It was noted that if the photoresist was applied using a plastic pipette, then in certain and unpredictable cases the liquid photoresist would form small droplets and "skate" across the wafer surfaces often contaminating the edges and hence the underside of the wafer. It was conjectured that this effect could have been due to static charge carried from the inside of the plastic pipette and may have given rise to the poor adhesion of the initial LOR2A photoresist layer. For this reason, it was deemed good practice to only use glass vessels to hold and to deliver the photoresist.

2.2.2.2.(B) Photoresist bilayer formation

A photoresist LOR2A/S1818 bilayer of was made by and an undercut developed to ensure good lift-off was created with the procedures that are described below.

Photoresist was taken from the refrigerator where they were stored at 4^{O}C and poured into small (25 ml) glass bottles, which were allowed to stand for ~30 minutes to warm to room temperature 24^{O}C – 28^{O}C as cold photoresist likely possessed a viscosity other than that specified by the manufacturer and hence alter its layer thickness upon spinning. Photoresist containers were not agitated unnecessarily as this could introduce air bubbles into the solution.

The wafers were pre-baked at 175^{O}C for 5 minutes on the EMS hotplate which had previously been washed with acetone. This allowed any moisture adsorbed onto the surface of the wafer to evaporate. The wafer was centred onto the EMS spinner chuck, the vacuum was engaged and the spin was manually examined for balance by spinning at a reduced speed and looking for "wobbles" during the turns. When centred, HDMS adhesion promoter was carefully pipetted onto the centre of the clean wafer and spun at 3000 rpm for 30s to produce a monolayer of the adherent on to which the later photoresist could stick. If HDMS was not used, problems could occur with the adhesion of the LOR2A and an excessive halo effect could be seen at the next inspection stage. This indicated poor adhesion of the LOR2A and in these cases, the wafer would need to be reworked by acetone bath and acetone/IPA spin.

LOR2A liquid photoresist was deposited onto the centre of the wafer and the spin was engaged at 3000 rpm for 30 seconds. Immediately after, the coated wafer was removed from the spinner and placed onto the pre-warmed hotplate at 175^{O}C for 5 minutes to bake the LOR2A by evaporating off its solvents. Once pre-baked, the wafer was centred onto the spinner, and the S1818 photoresist at equilibrated to room temperature was poured in a smooth motion from its glass container onto the centre of the wafer and the spinner engaged at 4000 rpm for 60 seconds. Care was taken to ensure the resist did not reach the edge of the wafer before spinning as this could result in resist contamination on the back

side face of the wafer. A pre-bake (also known as a soft bake) at 115°C for 1 minute completed the formation of the photoresist bilayer. At this stage it was not practical to confirm the film thickness of the bilayer.

Spun photoresist film thickness is a function of the spin speed, solution concentration, and molecular weight of the photoresist polymer measured by intrinsic viscosity.

$$T = \frac{KC^{\gamma}\eta^{\beta}}{\omega^{\alpha}} \qquad \text{(Eq 2.12)}$$

Where K is an overall calibration constant, C is the polymer concentration in grams per 100 ml of solution, η is intrinsic viscosity and ω is the number of rotations per minute. β, γ and α are exponential factors. T is thickness of the spun layer.

The wafer was then inspected for any obvious problems. Flocculent could cause streaking of the resists and in certain cases, flocculent not noticed in the first inspection stage could manifest as streaks in the resist. In cases where streaking was obvious and centred over the proposed device locations, the wafer would be need to be reworked by dissolving the bilayer in (i) acetone bath (ii) developer (iii) acetone/IPA spin clean and repeating the procedure from the start. This situation was not desirable as it increased the chances of wafer contamination from chemical and particulate entities.

2.2.2.2.(C) Bilayer exposure alignment and undercut development procedure.

The appropriate mask was acetone/IPA spin cleaned in its dedicated holder, then visually inspected for any obvious streaks or residues. If any remained, then "micro-clean" cloths were used to mechanically agitate any persistent residues. The MA56 single sided aligner was powered up; and its nitrogen supply and vacuum pump were engaged. The UV intensity meter was placed under the exposure window of the MA56, its UV source switched on left to warm and UV intensity readings were taken. If the reading was lower than expected, then the UV exposure time was increased accordingly. The reading for this work was somewhat low due to the age of the bulb (7.1 mW/cm^2). Incident energy of the exposure J/cm^2 is W/cm^2 x exposure time (s). On occasion certain functions of the MA56 were taken not available due to servicing issues, specifically the semi-automated

flat aligner, in which case the flat of the wafer and some arbitrary visible horizontal on the mask needed to be matched by eye and the alignment made by manual rotational adjustment of the wafer. Care was taken at this stage as if too great a degree of misalignment was obvious after development, then the wafer would need to be reworked.

The clean mask was inserted into the mask holder of the MA56 with its metallic side facing the wafer. Contact mode was set, that is the mask was firmly clamped onto the wafer and then the appropriate exposure time, in this case 18 seconds, was set. The UV light exposure at both the G and I line induced chain scission[28] frequencies of the resist was performed when the eyepieces of the MA56 moved out of place. Immediately after the photoresist bilayer had been exposed for the set time, the wafer was removed from the MA56 and inserted into a dedicated development holding wand, then placed into fresh developer (MF319) which had been poured into a dedicated square beaker previously rinsed with developer.

Development times were somewhat variable, and although the mean range time was around 60s, it was helpful to visually examine the dissolution of the exposed photoresist (as a purple evolution) from the wafer during it immersion in the developer solution. Once the purple evolution was no longer visible, the wafer was removed from the developer solution and washed copious distilled water and then the wafer was blow dried in nitrogen stream taking care to move the remaining liquid to the wafer's edge so as to leave little or no tarnish marks on it

For the purposes of float off as opposed to lift off [29] an undercut formation was a necessary prerequisite in the photoresist bilayer. Inspection of the developed wafer was made for the presence of an undercut. The undercut was not visible directly though the focussed microscope, instead a faint somewhat blurred halo around the edge of the top of the developed structure was sought and it was only made visible by slight adjustment of

[28] The reaction scheme for the photoresist material property chnages is shown in Appendix 2

[29] Lift off was method to remove the layer that involved sonicating the water whilst in acetone, but this was considered as a harsh treatment that should ideally be avoided and a passive longer lasting float off procedure was preferred.

the micrometer on the microscope to bring the objective just slightly out of focus. Some further manipulation of the contrast facilities of the microscope made this feature visible. If the undercut was not visible, further development time was required. If the undercut was not visible after a further two minutes of development, then it was assumed that the procedure had failed, and the wafer was reworked by complete removal of bilayer in acetone bath, acetone/IPA spin.

If undercut was visible, a further inspection was made to ensure the complete removal of photoresist down to the wafer surface. Since the lower parts of the of the bilayer are, by default, less exposed than the resist surface, partially exposed resist residues can persist and these will not dissolve in the developer. The removal of these types of residues was achieved by RF plasma barrel ashing the wafer in the Biorad® barrel etcher for 10 minutes in a process known as de-scumming, but this stage is was not performed until immediately prior to the deposition of the Ti/Au layer in the Nordiko RF sputtering apparatus since it also removed oxide films.

2.2.2.2.(D) Bottom electrode metal sputtering procedure.

Magnetron sputtering of thin films by plasma or physical vapour deposition (PVD) was the method of choice for the deposition of both the thin au metal electrodes and the ZnO piezoelectric substrate of the FBAR[30]. In the basic sputtering process which is performed under vacuum, the target (or cathode) plate is bombarded by energetic ions generated in a glow discharge plasma placed in front of the target. The bombardment process causes the removal, i.e., "sputtering" of the target atoms, which may condense on a substrate as a thin film.[22] The technical details of magnetron sputtering and recent advances that have been made in physical vapour deposition methods are reviewed by Kelly (2000)[23]

The N_2 level supplying the Nordiko was checked as the chamber would not open if it was exhausted. The high vacuum was switched off by closing the "High vac" and "throttle" valves. The chamber was vented and care was taken not to attempt to open the chamber

[30] A dedicated PVD apparatus (a Nordiko) was used for metallic depositions and another sputtering apparatus was used for the oxide depositions (a Balzers). This was done to ensure that there was no cross contamination of metallic and oxide films during the sputtering procedures.

until fully vented as this can damage the lifting assembly, it was deemed good practice to wait until an air flow could be felt on the skin from the rim of the chamber before lifting the chamber, this usually took around three minutes of waiting time. After raising the lid, the appropriate targets were checked or loaded. The wafers were placed by screw fittings onto the Nordiko sample holding plate which was placed back into the Nordiko chamber and the chamber lid closed after wiping the seals of the chamber with an IPA soaked cloth to remove any particles that could interfere with the seal, and hence the vacuum of the apparatus. Immediately prior to this, the glass slide in the view window was replaced or the Au particulate cleaned from it to allow for later visualisation of the plasma ignition in the chamber. The shutter was tested for operation since it was prone to stick, and the marker flags for each sample holding were checked for visibility.

The initial rough vacuum was engaged via the Rotary pump, and pumped down to about (0.01 Torr), this took about 3 minutes, with the rough valve open. The rough valve was then closed, and the Hi Vac and Throttle valves were opened. The Rotary pump was switched off and the cryo-pump only engaged. After three hours was the system was checked for good vacuum (8×10^{-7} Torr was a working vacuum). The vacuum gauge was then turned off and the Throttle valve was closed. The RF power unit was turned on and allowed to warm for about 10 minutes. The gas inlet was opened and the appropriate target electrode selected. After 15 minutes of gas flow, the RF was engaged and turned up to (0.1 kW), using the view window it was possible to see if the plasma had ignited by the presence of diffuse pink/purple glow. If the plasma had not ignited, the shutter could be manually adjusted and failing this the gas flow rate could be increased. Once ignited, the RF power was turned up to (0.3 kW) and the reflected power tuned to zero. The appropriate pre sputtering times were observed, and then the power was altered and the sample was coated with the metal simply by opening the shutter underneath the target for the appropriate time. With a chamber vacuum pressure of 0.01 mB, the sputtering times for a 15 nm thickness of the Ti adhesion layer was 27 seconds at 300 watts, and for a 100 nm thickness of gold, the sputter time was 3.5 seconds at 100 watts.

The next sample was then rotated over the sample using the target pro computer program on dedicated Nordiko computer. This process was repeated for the next target using the specified settings. When sputtering was completed, the RF was turned to zero and then turned off. The gas supply was turned off, and the throttle valve opened. 20 minutes was given to allow the RF supply to cool. The power supply to the RF unit was finally turned off, the High vac and throttle valves were then closed and the vent valve opened. After three minutes the chamber lid was opened and the samples were removed and quickly placed into their holding boxes. The seal of the chamber was IPA wiped the viewing window slide cleaned and then chamber was lowered. The Nordiko was pumped down ready for the next operator. The appropriate run sheets were completed during operation.

To save time, it was on occasion necessary to share the Nordiko run with another user. On one occasion, the other user required a platinum layer and the run was performed under the same vacuum session. It was noted later that the quality of the gold layer on the wafer was poor, and it was also observed that if the wafer needed to be reworked for some reason, that the Ti/Au layer could not be removed by the normal process of potassium iodide + iodine rinse ($KI + I_2$) this may be indicative some contamination of the gold layer by residual platinum ions in the chamber. After this observation was made, it was decided that good practice was to only share the Nordiko vacuum runs with other users' employing the *same elements* in their run. Also, although it was not done during these runs, experience has taught that an initial XRD trace should be obtained for both the Titanium and Gold layers as these may influence the orientation of of the ZnO deposition and its subsequent C axis orientation. More XRD studies are required to discover the optimal conditions required for a the Ti/Au layer intended for as the nucleation site for the ZnO coating. The effects various of bottom electrodes metals e.g., Al, Cu, Ti and Mo have on the *c*-axis preferred orientation of another type of piezoelectric substrate for FBAR, aluminium nitride (AlN) has been researched by Lee *et al* (2004) [24] AlN deposited on bottom electrodes made from Mo were shown to give superior FBAR characteristic responses.

The Ti/Au layer contacting the unexposed "sacrificial" photoresist layer was floated off by immersion in acetone for an hour or until the float off procedure was complete. After half an hour or so, the surface layer of the wafer would start to bubble and this was indicative of good float off initiation . Ti/Au Residues would be mechanically agitated by means of forcefully spraying acetone from a container directly onto the wafer surface taking care not to let the acetone dry on the surface, this was to avoid residues. A final immersion in developer for ~2 minutes removed any residual photoresist, a final acetone/IPA spin clean would complete the process. After inspection and surface profile with DEKTAK the wafer would be plasma cleaned and this step concluded the formation of the bottom electrode of the FBAR device and this is shown on whole wafer. (*See Figure* 2.4) below.

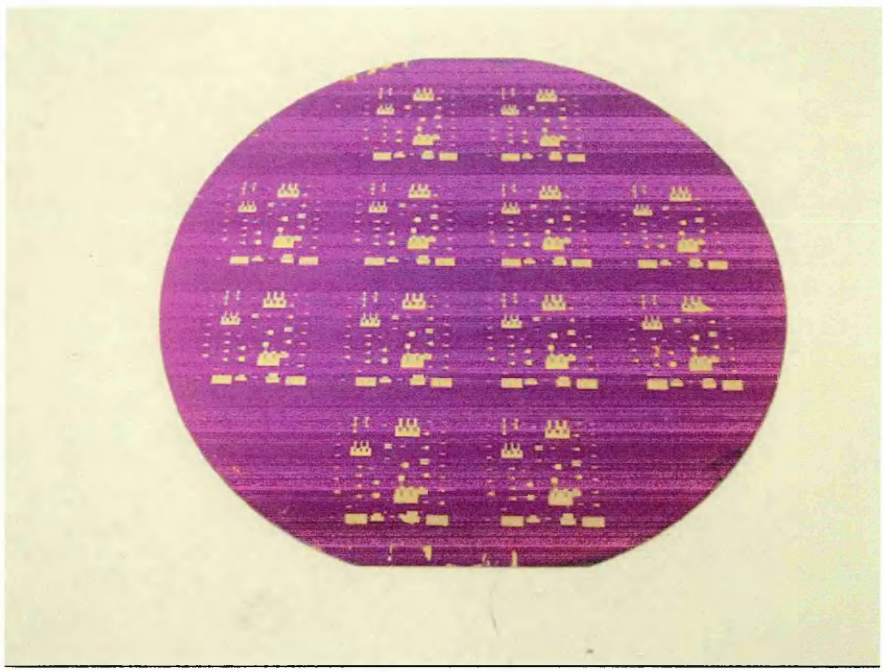

Figure 2.4 (A) Bottom electrodes deposited by PVD onto the Si wafer. 12 Die each with numerous individual FBARs visible. Some of the structures visible are destined for use as RF filters. The sensors project used only individual resonators.

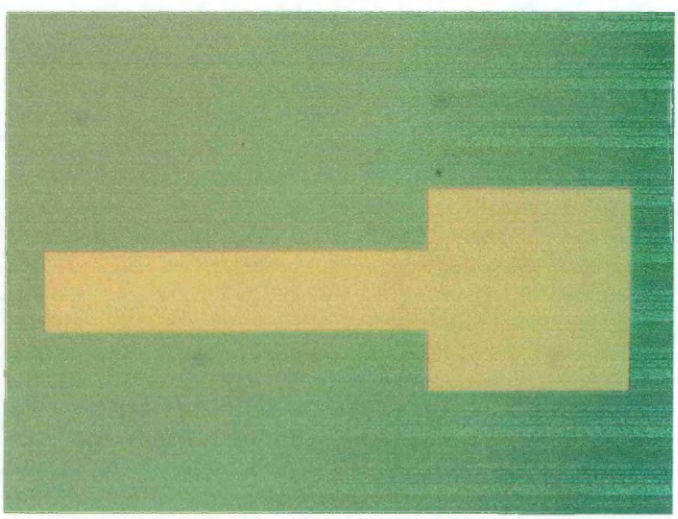

Figure 2.4 (B) Shows a fairly well formed Bottom electrode. Good clean edges are apparent. Bottom electrodes were designed to be ~100 nm thick with ~8 nm Ti adhesion layer Dektak profiling scans would confirm this thickness. (Results not shown). (Magnification 50X with 2X optical zoom)

2.2.2.3 Deposition of piezoelectric zinc oxide films

The Balzers sputtering system which was used exclusively for the deposition of oxide films would be found under a high vacuum state, The "Hi Vac" valve was closed and the switch moved from "pump" to "vent". A few minutes allowed the chamber to depressurise and when the side hatch could be easily removed, the chamber was known to be depressurised. The chamber hood was raised and the sample holder was taken out of the chamber with gloved hands and the sample wafer with BE was placed into the holding tray, this was then rotated manually so as to face the ZnO target a fully facing as possible. The chamber was then lowered, when completed, the side panel would be removed and the thermocouple moved into place by means of a metal rod. Good contact should be made between the thermocouple and the back of the sample holder to ensure accurate heating. The side panel was replaced, and the switch was turned fro m" vent" to "pump". The "Foreline" valve was then closed and the Bypass valve opened until pressure reached (0.075 Torr) at which point the bypass valve was closed. The "Foreline" and " High Vac" valves were opened and the system was left to pump down to a value below (1.5×10^{-6} Torr). The time taken to reach this value was extremely variable, but if not reached after 4 hours, it should be assumed that there is a problem with the vacuum seals or oil back contamination, in any case the procedure should be abandoned and time spent on examination the sputter system itself. The throttle valve was then turned on, and the (Ar/O_2 (20%)) gas flow let into the chamber for at least 10 minutes. A typical value would be (40.8SCCM) and a pressure of around (20 mT). The sample heater was turned on usually about 150°C and the thermocouple temperature value checked. After a further 10 minutes, the RF was engaged and the power increased *slowly* to 300W, reflected power dropping rapidly would indicate plasma ignition, and this value was then tuned to zero using the power matching box.

The ZnO target was left to pre sputter for 8 minutes. The power was the decreased to 250W and after readjusting the tuner box to reflect zero power, the target was left for another 2 minutes for pre sputtering. This time period was used on the advice of other users who had found that the additional pre sputter time usually resulted in a better quality ZnO film. The sample was then exposed to the ZnO plasma and left for deposition

for the appropriate time, the ZnO deposition rate of the Balzers was about 0.5μm/per hour.

At the set time period, which was dependent upon the ZnO thickness desired the shutter would be closed and the sputtering procedure stopped by reducing the sputtering power to zero. then after 1 minute the RF switch breaker would be turned off. At least half an hour should be given for the samples to cool before closing the "Hi Vac" valve. All the pressure reading panels were then switched off and the chamber vented. After 5 minutes, the vented chamber side panel would be loose, the chamber was raised and the ZnO coated wafer samples would be removed. The chamber was left for other users' under high vacuum by closing shutter, and lowering the lid, the chamber was pumped and the "Foreline" closed, at (0.075 Torr) the bypass valve was closed and the "Foreline" and "Hi Vac" valves were opened and chamber left to depressurise.

Si wafer samples (not devices) were also studied to examine the quality of the ZnO deposition and for thickness measurements. This was to gain understanding of deposition rates in relation to temperature and pressure variations in the Balzers system in attempts to optimise the sputtering deposition processes for ZnO films. Dektak thickness measurements would be taken by dissolving the ZnO in Acetic acid around a photoresist painted circle and XRD traces would be obtained to give an indication of the c-axis orientation of ZnO crystal lattice.

The ZnO coated samples would be examined with the SEM to look for any obvious aberrations such as the common "sharks tooth" type formations in the ZnO film. The ZnO coated samples were then passed on to other technicians for X-Ray diffraction (XRD) analysis of the films by using an X-ray beam to obtain a full-wave-half-maximum value from a rocking curve. This was done to gain insight into the quality of the ZnO films in terms of its C-axis orientation, this orientation was in part but not exclusively indicative of the piezoelectric responses that could be expected from the ZnO film; these would become a major factor in the characteristic responses of the FBAR devices when they were completed. A representative example of the XRD and SEM results for ZnO

films are shown below with a poor sample and an acceptable sample shown. (*See figure* 2.6)

When the Balzers apparatus was eventually optimised for reproducible good quality ZnO piezoelectric films, e.g. with a good vacuum and with stable and accurate temperature and constant gas flow, the real device samples as opposed to wafer test fragments would be sputtered with ZnO. However, the process was not always successful and this was point for failure of FBAR devices, indeed many samples were lost at this stage. There were no wafer samples obtained from the Balzers system where the thickness of the ZnO layer was homogenous across the wafer. (*See Figure* 2.5 (A))

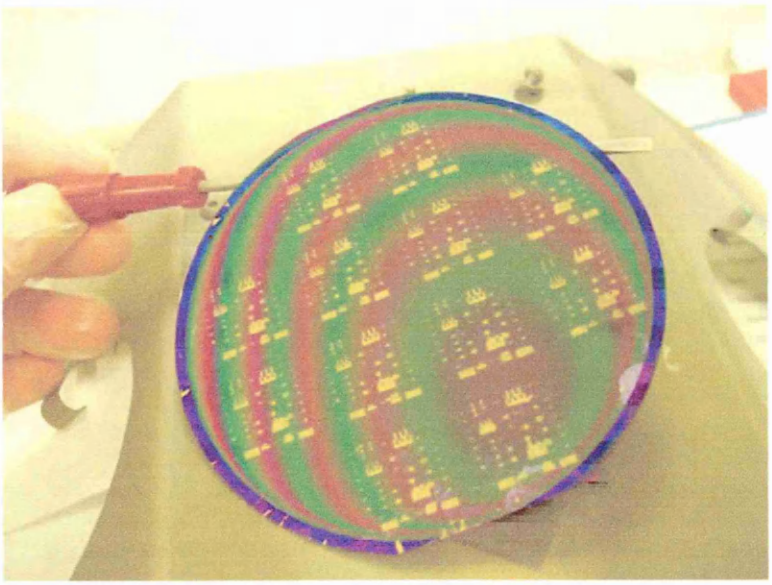

Figure 2.5 (A) ZnO coated wafer.

Shows wafer after RWU deposition of ZnO thin film onto wafer with bottom electrodes. Note the light wave interference patterns due to wedging formation of increasing ZnO thickness over the entire wafer. The bottom electrode of the FBAR is clearly visible under the transparent piezoelectric crystal. Because the thickness of the ZnO was variable, at this point it was necessary to map the device die over the surface of the wafer as show in the figure below.

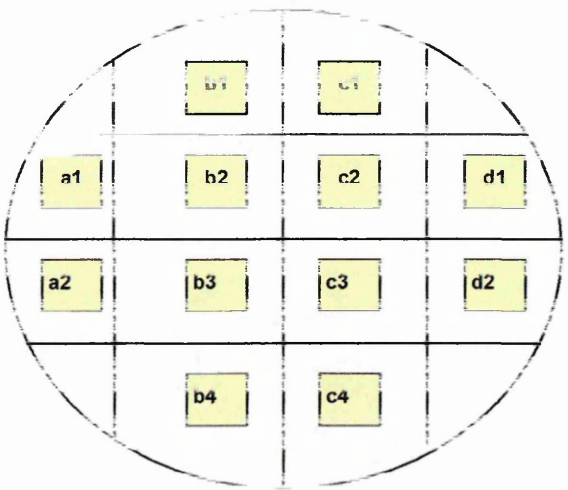

Figure 2.5 (B) An example of Die wafer mapping to accommodate for variations in the ZnO thickness.

In future testing, the device die would be recalled to look for any obvious performance changes over the wafer. From the banding sizes, it can be seen that there would be no steep gradient over any given individual FBAR device but there were ZnO film thickness variations from one die to the next.

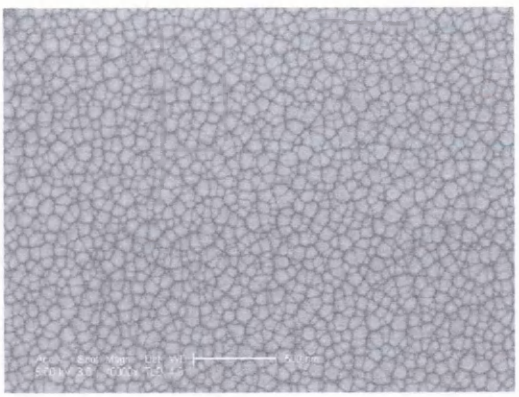

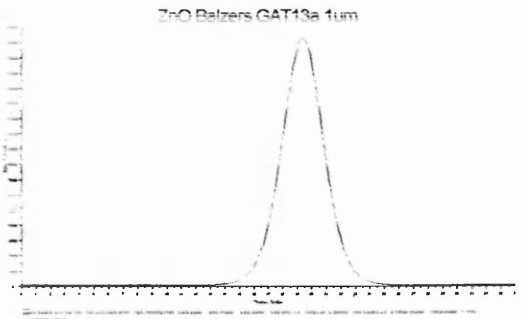

(i) (ii)

Figure 2.6 (A) SEM image of ZnO film. (b) Shows XRD trace for crystal. (Sample GAT -13A.)

This figure represents a fairly good example of a ZnO sputtering. The film in (i) (1µm) is smooth and the XRD rocking curve trace of the full width half maximum (FWHM) value is narrow indicating good c-axis orientation. The settings used to obtain ZnO results at this quality would be employed in real FBAR fabrication.

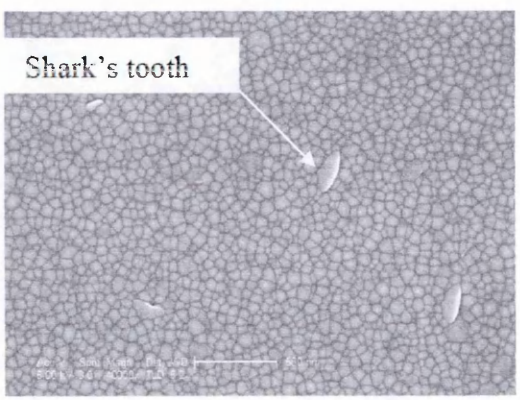

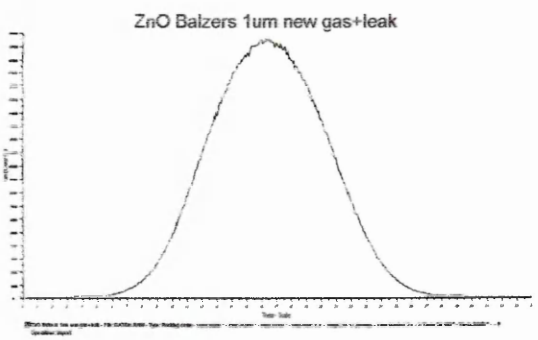

(i) (ii)

Figure 2.6 (B) SEM Image of ZnO film (b) Shows XRD trace for crystal. (Sample GAT 6 -14A)

This Figure (B) represents an example of a relatively poor ZnO sputtered film. There are sharks teeth clearly visible in the film (iii) (1µm) and the FWHM is wide - indicating poor c-axis orientation of the ZnO crystal.

Poor c-axis orientation is *one of* the contributory factors leading to poor piezoelectric responses of ZnO films This poor film deposition result may be attributed to a vacuum leak during the run or the implementation of a new gas flow line. A film such as this would not be used for FBAR fabrication. For more information on the formation and responses of ZnO piezoelectric films - See Kirby *et al* (2003) [25].

2.2.2.4 Top electrode deposition

The wafers were visually inspected for any obvious defects and these were noted on the relevant batch card. The wafer was pre baked for 5 minutes at 175 °C. LOR2A was spun as previously described and pre-baked for 5 minutes at 175 °C. The S1818 was deposited and spun as previously described and pre baked for 3 minutes at 115 °C. "QQ" Maintop mask was cleaned as previously described and placed into the MA56 aligner. The wafer was inserted to the exposure stage and the mask aligned over the features using manual dexterity. Exposure was for (18s ~ 100 mJ). The wafer was post baked at 115 °C and then developed in MPF319, rinsed in copious distilled water and blow dried in a fast flowing N_2 stream. The developed wafer was then plasma cleaned for 10 minutes at (20W) RF. Finally the wafer was inspected for complete removal of photoresist at under the microscope at 5X mag. The wafer was taken to the Nordiko sputtering apparatus and PVD metallic sputtered with 8 nm Ti and 100 nm of Au as previously described. The wafer was then immersed in acetone bath for float off as previously described. Observations at 5_X magnification were made for complete removal of the metal.

2.2.2.5 Photolithographic procedures for developing BE via contact.

It was necessary to make a hole "via" through the ZnO film giving access to the bottom electrode for proper functionality of the FBAR device. The entire wafer was protected by spinning on photoresist layer (S1818). The mask QQZNOETCH was cleaned as previously described and placed into the MA56 aligner. The wafer was placed into the exposure stage and the features aligned with the mask using dexterity. Exposure was for (18s ~100 mJ) and the wafer was post baked for 115°C for 90s. The wafer was then submerged in developer MPF319, rinsed in distilled water and N_2 dried. The wafer was inspected for defects and the complete development of the resists. This gave an unprotected area over the bottom electrode where the ZnO could be dissolved away. It was important to align the mask precisely as misalignment could mean exposure of pattern over Si wafer rather than gold resulting in unwanted edge dissolution.

2.2.2.5.(A) BE contact hole (Via) wet etch.

The wafers were immersed in 10% glacial acetic acid for about 2 minutes or until the cloudy formation of ZnO dissolution was no longer visible and had gone clear. The resist

was dissolved in with acetone and IPA and then examined for quality of pattern definition. A Dektak scan would reveal the etch depth of the removed ZnO after removal by development of the S1818 photoresist layer. Since the thickness of the ZnO varied across the wafer, where the ZnO was thinner, the via etch would be completed before the thicker regions. To ensure overdevelopment of the thinner regions did not occur, periodic complete scans of the wafer were made under low magnification (5X) to see what zone of the wafer had its etch completed. This would be noted and the wafer would be placed on an angle in the acetic acid bath ensuring only the non-completed via were exposed. Some problems could occur at this stage of the processing, in that the acetic etch could begin to attack the lateral dimensions of the devices, if the erosion contacted the top electrode surface, then the devices were rendered useless and great care was taken to avoid this as some otherwise perfectly good devices were lost to the project in this way. ZnO via etches to Bottom electrode are shown. (*See Figure* 2.7)

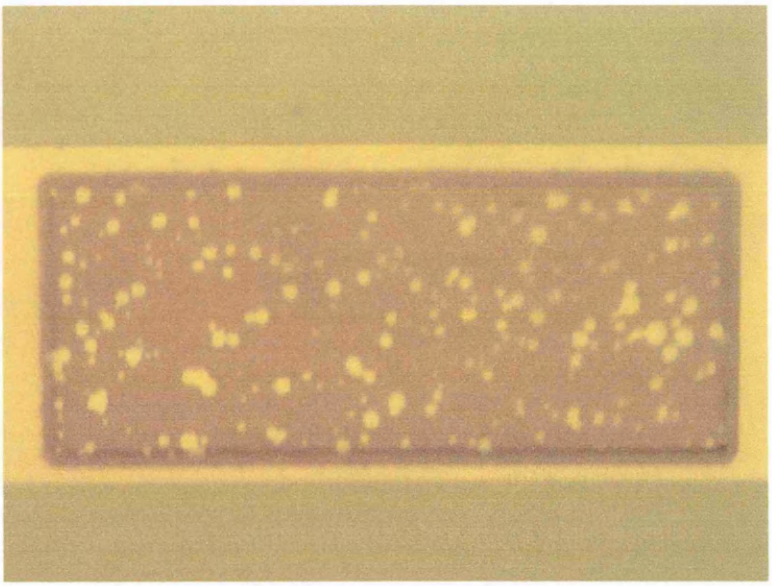

Figure 2.7 (A) Via formation nearing completion.

~~is almost completed. The alignment was good as the etch hole remained true over the Au Bottom~~ electrode and there was no breaching of the edge to the surrounding area. Mag 50x This represents an almost perfect BE ZnO via.

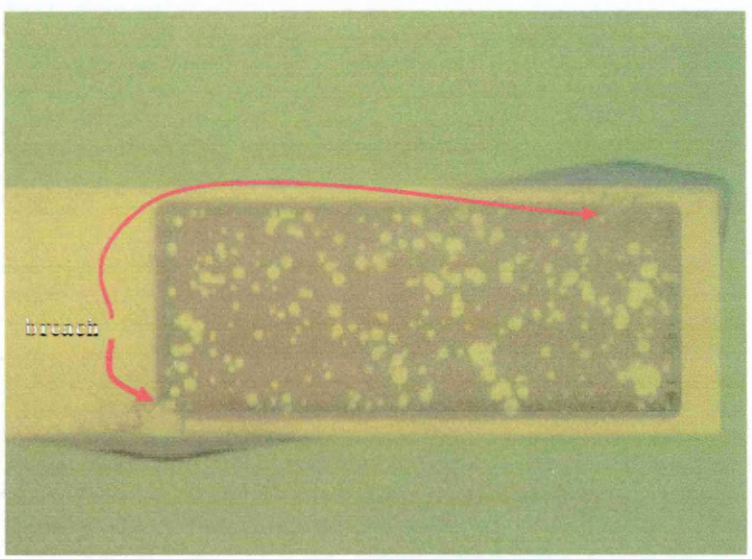

Figure 2.7 (B) Shows effect of breaching in BE via formation.

~~shows the effect of breaching from Au surface to non Au Surface. The Via is well aligned, ZnO etch is not~~ complete, over-exposure is likely to be the cause of this. Mag 50x

A device with this level of breaching was acceptable for use as FBAR resonator device.

2.2.2.6 Back-side photolithography

It was of *utmost importance* to ensure good device and mask alignment at this stage and care was taken as a mistake at this vulnerable stage in the FBAR microfabrication process could render all the previous processing steps invalid if not corrected.

A thicker, more viscous type of Photoresist (AZ4562) was spun onto the rear of the wafer. (1500 rpm for 40s) and pre-baked for 5 minutes. This process left a thick bead of resist around the edge of the wafer which was removed with fine acetone spray. This was done because it would lead to problems with unwanted mask adhesion in the double sided aligner. There were problems with this manual fine spray method, and the AZ4562 needed to be reworked usually 3 to 5 times before the edge bead removal was neat enough to proceed. Alignment at this stage was considerably more difficult than previous alignments because the double sided aligner MJB21 movement tables were not as accurate as the MA56 single sided aligner tables.

A mask usually "Main Top" would be aligned with the "QQDIREETCH" mask. When alignment was complete, the wafer would be inserted into the aligner and the features from the top face aligned with the top loading mask. Here it was assumed that exposure would be true for the bottom mask since both were previously aligned. It was particularly important to focus on the *orientation* of the alignment in this case. When alignment was thought to be complete, the wafer would be scanned over distant edges to confirm that there was no drift in orientation. When satisfied with correct orientation of the wafer, the back face would be exposed for 18s – 30s (~100 mJ) A post bake of 115 °C for 90s was given before immersing in developer (AZ351B (40 ml in 160 ml H_2O)) for ~3 minutes. The wafer was washed in copious distilled water and blow dried in fast N_2 stream.

A plasma cleaning in Biorad® was performed at (12W) for 3 minutes. With shorter exposure periods, partially exposed photoresist residues at the bottom of the development hole would be visible. A balance between over exposure and persistence of the residual resist needed to struck as a compromise. This time period was variable. 18s-30s. A Dektak profilometer scan would reveal that the AZ4562 layer to be approximately 10 μm

thick and this proved to provide sufficient protection for the rest of the wafer from unwanted etching in the DRIE stream. Wafers were then mounted onto backing wafers at first using Glyseal but this was found to leave a contamination residue, so alternatively a photoresist, unbaked and unexposed, was used as the adherent instead. The wafers were co-joined by clamping a vacuum seal over the MA56 and closing over the two masks ensuring a tight fit. This method proved to be relatively effective and did not suffer from residual contamination at the end of the etching process.

2.2.2.7 Silicon substrate etching

Wafers at this stage of development were then passed on to other process technicians for SiO_2 etching in the RIE80 or with HF. (DRIE will not etch SiO_2). Then for DRIE ($SF_6C_4F_8$) substrate etching up to the SiO_2 top layer (device layer). The rate was about ($3\mu m/min^{-1}$). The etched wafers were returned and the backing wafer removed by immersion into acetone solvent and the two wafers would be gently horizontally slid apart. A final acetone /IPA spinning rinse would be performed on both sides and the wafer would be left to dry naturally as it now possessed an unsupported working membrane which was exquisitely delicate and could easily be destroyed by the N_2 stream previously used for drying. With this stage complete, the devices were ready for testing on the network analyser.

Figure 2.8 below, is a schematic representation of the completed FBAR device. There is a top electrode (d = ~100 nm), a piezoelectric, usually ZnO, (~1-3 μm) the thickness of the piezoelectric can be used to modify the resonant frequency of the FBAR. and a bottom electrode (d = ~100 nm). The via allows electrical contact to the bottom electrode. This is usually made with a signal probe, but in this project, a gold wire was bonded directly to the bottom electrode through the via. The SiO2 layer is used when the device silicon substrate is etch through by DRIE, its thickness can also be used to modify the resonance frequency of the FBAR. The SiN_4 layer is used to protect the devices when the etch is made by KOH wet-etch, again its thickness can be used to modify the frequency of the device. The complete etch through the silicon wafer substrate is performed to release the membrane, leaving it in effect, unsupported. The completed devices were extremely delicate and care was taken whilst handling.

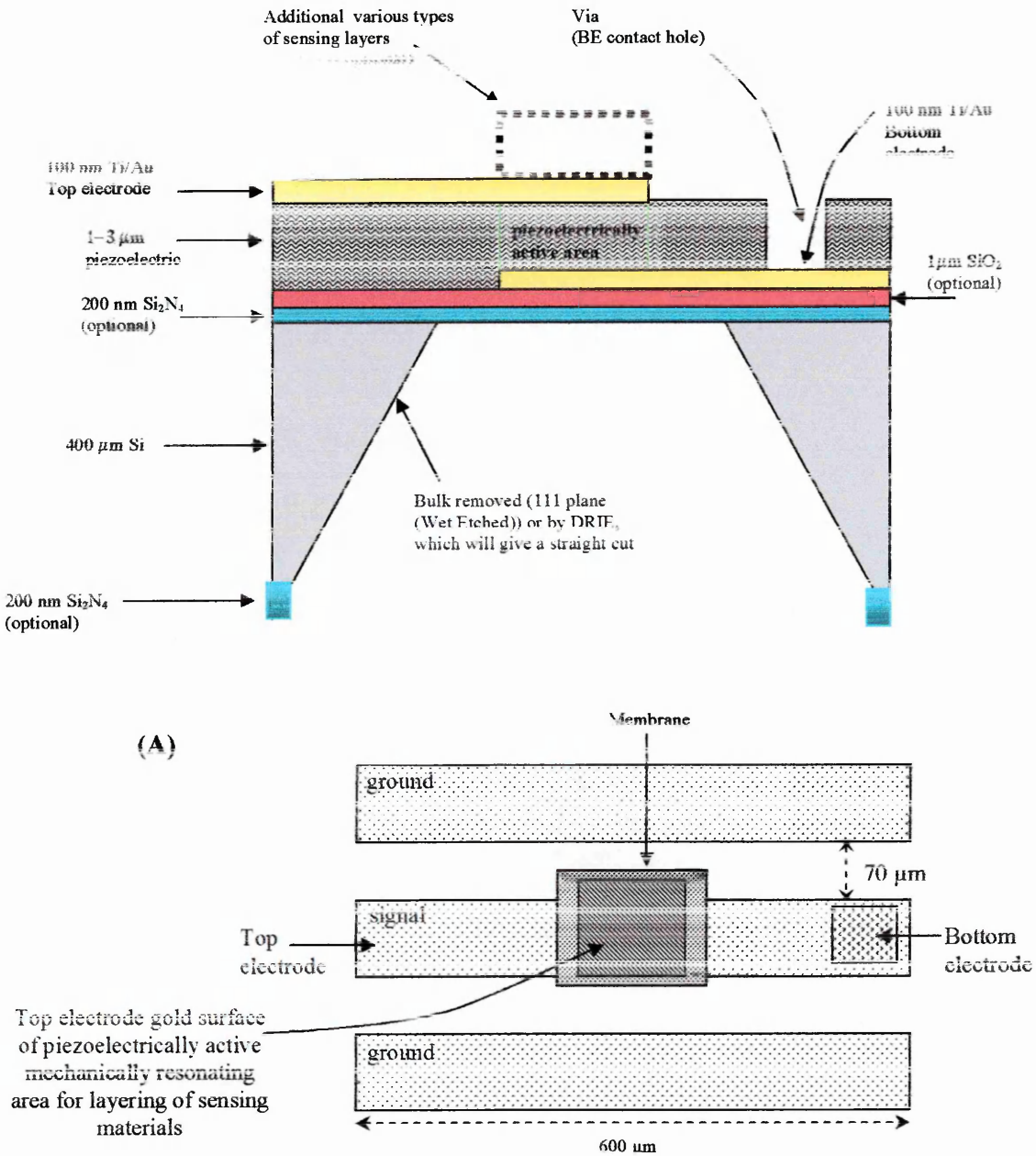

Figure 2.8 (A and B) Schematic of a completed FBAR device **(A)** is the cross-sectional view. The *piezoelectrically active* area is where the Top and Bottom electrodes overlap. (not to scale) and **(B)** is the top view showing the Coplanar waveguide configuration of the device. (approximate dimensions are indicated) The piezoelectric is usually ZnO, with Au electrodes.

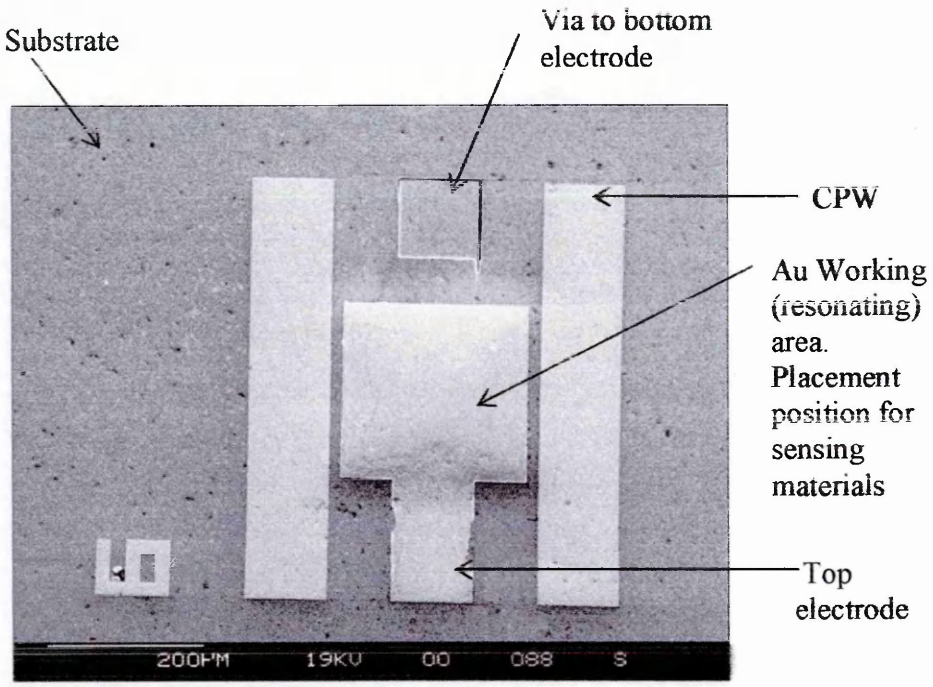

(C) FBAR with 200 μm^2 working area

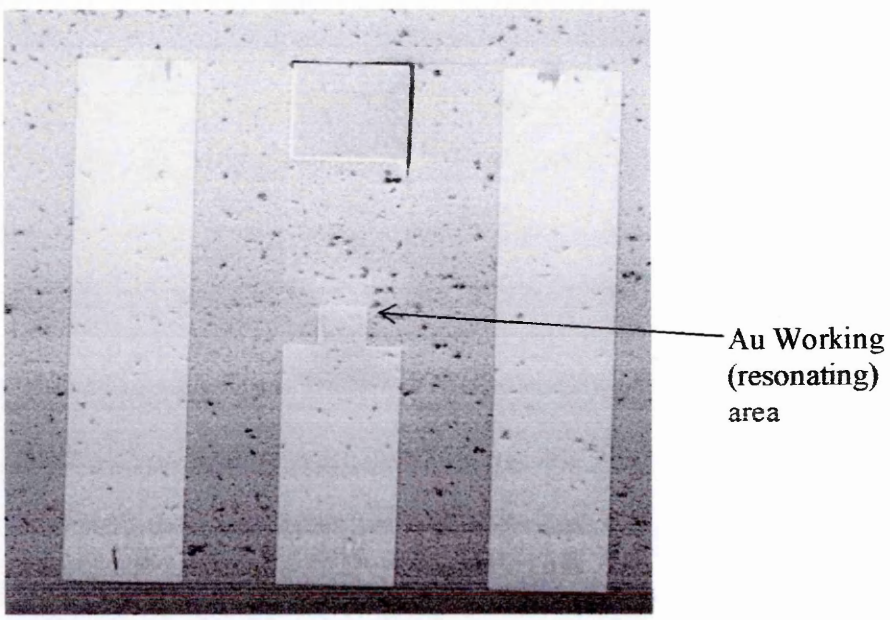

(D) FBAR with 20 μm^2 working area

Figure 2.8 (C and D) SEM of Top side of two FBARs showing the variability possible in the size of the working area of the completed devices. Working areas define the static capacitance of the devices.

2.3 Initial testing of FBAR devices on die with the summit 9000 probe station and the HP-8753D network analyser

2.3.1 Network analyser - basic layout and functions

A vital piece of apparatus used in the project was the Hewlett Packard (now Agilent) network analyser (HP 8753D), it was central to the analysis of FBAR since it both electrical excited the device to piezoelectrical resonance whilst simultaneously recording various electrical characteristic responses from it.

A network analyser applies a signal that is either transmitted through the test device, or reflected from its input, a comparison is then made with the incident signal generated by the swept RF source. The signals are subsequently applied to a receiver for measurement, signal processing and display. The 8753D model could produce a swept RF signal or a continuous signal in the range 30 kHz to 3 GHz. The unit is phase locked to a highly stable crystal oscillator. A built in microprocessor takes the raw data and performs all of the required error correction, trace math, formatting, scaling averaging and marker operations according to the user-input instructions from the front panel, or from a computer through a general purpose interface bus (GPIB) channel. The swept high frequency signal is then translated to a low fixed frequency intermediate frequency (IF) using sampling and mixing techniques, the IF signals are converted into digital data by the on-board analog to digital (ADC) converter.

The GPIB interface between the computer and the network analyser was used to gain control of the analyser during the software development stages of the project and the front panel controls were not used, but they are shown in figure 2.9(D) to highlight the various control options that were available. The software interface that was developed to control these settings is described in section 2.4

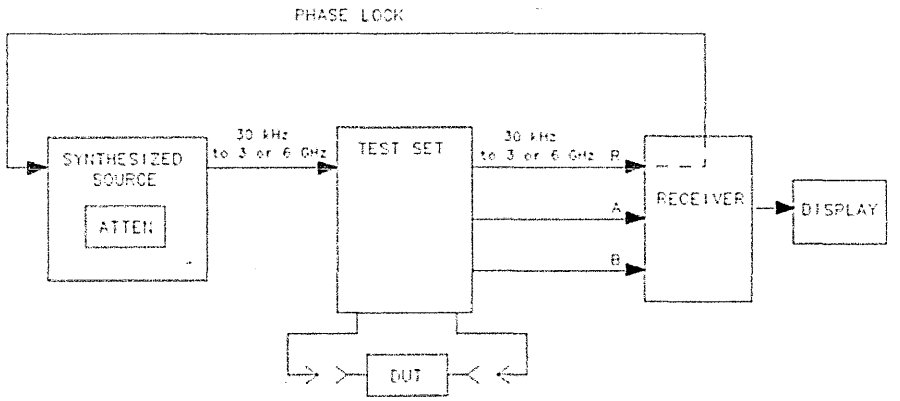

Figure 2.9 (A) Simplified block diagram of the network analyser system[26]

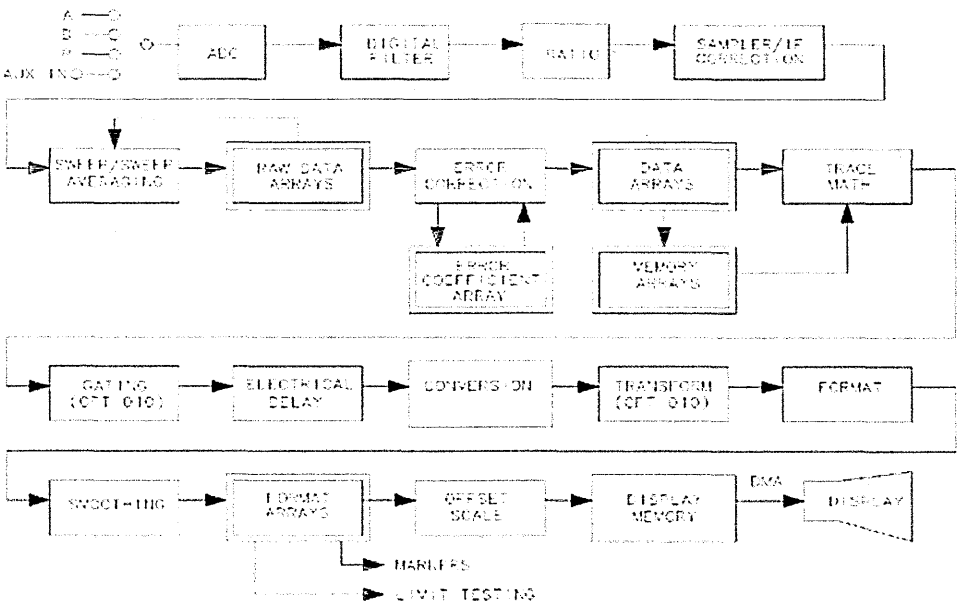

Figure 2.9 (B) The data processing flow diagram of the network analyser. [26]

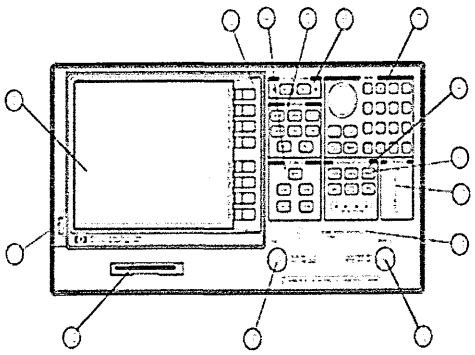

(a) Front panel

(1) Line on/off switch
(2) Display
(3) Soft keys
(4) Stimulus Function Block
(5) Response Function Block
(6) Active Channel Keys
(7) Entry Block
(8) Instrument State Function Block
(9) Preset Key
(10) Port 1 and Port 2
(11) Probe Power Connectors
(12) R channel Connectors
(13) Floppy drive

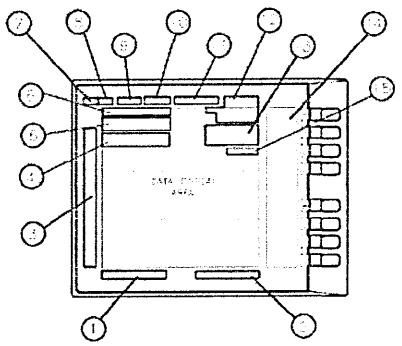

(b) Screen values

(1) Stimulus Start Value
(2) Stimulus Stop Value
(3) Status Notations
(4) Active Area Entry
(5) Message Area
(6) Title
(7) Active Channel
(8) Measured Input(s)
(9) Format
(10) Scale Division
(11) Reference Level
(12) Marker Values
(13) Marker Stats/Bandwidth
(14) Soft key Labels
(15) Pass Fail

Figure 2.9 (C) HP8753D network analyser front panel [26]

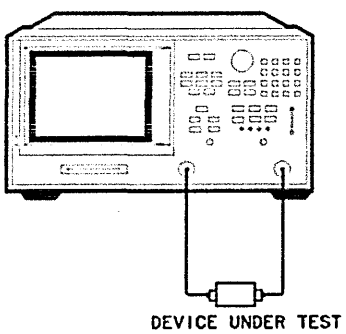

Figure 2.9 (D) The basic network analyser test arrangement [26].

2.3.2 The use of the Scattering Parameters

Impedance and admittance parameters are used by engineers to describe low frequency circuits. However, their measurement is impractical at higher frequencies where S-parameters are used to describe a circuit network and are derived from the travelling waves that enter and leave a network. Incident waves are denoted "a"- waves and exciting waves from the network are denoted as "b"-waves. The S parameter (S_{21})[31] was used almost exclusively throughout this project to follow the series resonance frequency of FBAR devices.

A matrix equation is formed to relate the incident and reflected wave by the S-parameter matrix

$$\begin{bmatrix} b_1 \\ b_2 \end{bmatrix} = \begin{bmatrix} s_{11} & s_{12} \\ s_{21} & s_{22} \end{bmatrix} \begin{bmatrix} a_1 \\ a_2 \end{bmatrix} \qquad \text{(Eq 2.13)}$$

2.3.3 Methods of existing FBAR characterisation and its limitations in relation to chemical and biological testing.

The FBAR devices used in this project were based within coplanar waveguide structures (CPW). (*See figure* 2.8 (B))The use of coplanar waveguides provides a convenient method of making contact with an FBAR device.[27] CPW also provide well-defined ground planes and avoid the introduction of stray inductances which may arise when wirebonding is being used.

At the start of the project, FBAR measurements with the network analyser were typically performed on die with the use of the Ground-Signal-Ground (GSG) coplanar wave probes of a Summit 9000® probe station. This characterisation method was found to be of

[31] S_{21} and S_{12} means the signal that is passed from port 2 to port 1 or port 1 to port 2 of the network analyser respectively– they are **two port** transmitted signals. S_{11}, denotes the signal that is sent from port 1 and returned to port one, this is a **one port** reflected signal, likewise S22 is a single port reflection to and from port 2. (*See equation 2.14*)

limited use for the planned chemical and biological sensing experimental procedures on FBAR because the probe station did not allow for a *controlled environment* in which to test the FBAR responses to various agents. This on die G-S-G probing method (*See Figure* 2.10 (B)) did however allow for the initial characterisation of the newly fabricated FBAR devices, and this showed which individual FBAR devices provided characteristic responses that were of high enough quality[32] to be used for sensing experiments.

It was important to isolate the FBAR from the ambient laboratory environment so that conditions could be controlled and FBAR responses calibrated, clearly the G-S-G probing methods could not deliver this required degree of isolation. It became obvious at this stage that an isolation chamber would be required for the FBAR and that it would not be possible to continue using the well established G-S-G probing methods once the FBAR was isolated. The design and manufacture of the FBAR isolation chamber or FBAR housing assembly (FHA) and the associated microwave electronics is described in Section 2.4 below.

[32] The term "high quality" in this case merely implies FBAR devices with resonance curves that were at least 3 dB and were relatively free from spurious modes of resonance. Devices with good quality responses operating at higher frequencies tended to be favoured.

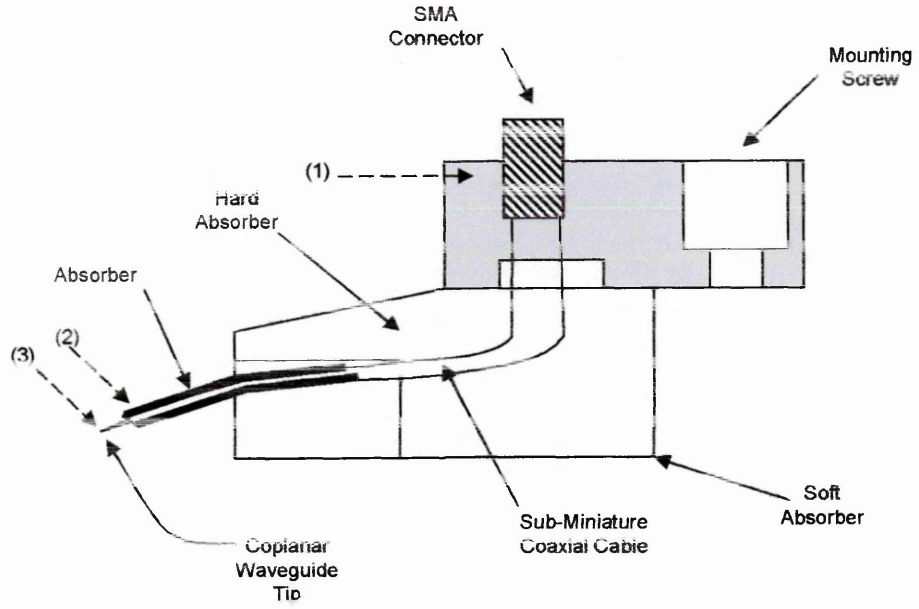

(A)

(1) SMA to 1 mm sub-miniature coaxial cable
(2) Sub-miniature coaxial cable to CPW probe tip
(3) CPW probe tip to wafer/test device probe pads.

Fig 2.10 (A) Schematic of generic CPW probe head

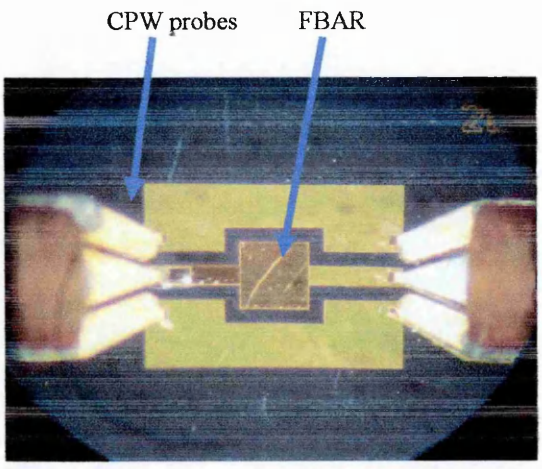

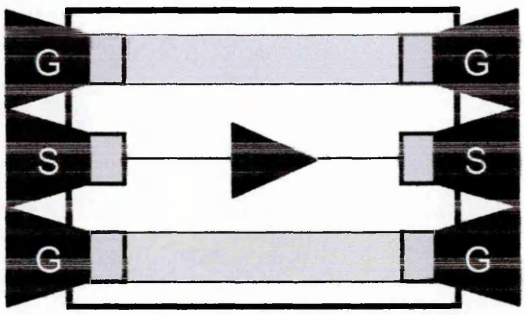

(B) **(C)**

Figure 2.10 (B) Photograph of the GSG 200 tri probes of the summit 9000 probe station making contact with FBAR Top and Bottom electrodes. Mag 100 X 2.5 optical zoom.

Figure 2.10 (C) Schematic FBAR probed on wafer with coplanar probes

2.4 Design and manufacture of an isolation chamber for the control of FBAR environment

The FBAR Housing Assembly (FHA) was designed so that isolated FBAR samples could be conveniently exchanged from the chamber. This was achieved by attaching and wirebonding an FBAR to a printed microwave circuit board[33] (PCB) which was then incorporated into the FHA. In this way, numerous PCB and FBAR samples were available for experiments. This requirement for easy sample exchange meant that the PCB could not be wire-bond connected to the housing connectors. Not using wire bond connections required that the PCB be carefully positioned into the housing so that electrical connectivity was achieved between the conductive tracks[34] on the circuit board and the FHA signal connectors. Poor connection at microwave frequencies can lead to signal losses.

AutoCAD engineering diagrams were drawn by workers at Sensor Technologies Ltd (See Figure (2.11(A)). These were based upon original conceptual design sketches conceived by the author after in-depth discussions with microwave engineers. From two solid blocks of brass, the FHA base and lid were machined out with a vari-turret milling apparatus. SMA microwave connectors were obtained from stores, and these were modified by the removal of most of their dielectric so as to fit securely into the FHA base, this was later sealed with silicone to make the unit air tight. The Base was then further machined to cut in a groove for the addition of a gas seal "O" ring. Plastic screws were obtained for fitting in the PCB to the base of the housing unit. Gas input/output Festo ® seals (5 mm diameter) were inserted into the lid holders and a quartz slide was diamond cut to act as a window for the centre of the lid for use in later UV radiation exposure type experiments. Upon machining, the FHA was tested for snug lid fitting and any roughness was removed where necessary. The entire unit was then gold flash-sputtered, under vacuum, to improve conductivity lost from the effects of surface oxidation. The thickness this gold flash layer was not established.

[33] Capable of handling microwave frequencies
[34] These were actually 50Ω transmission lines.

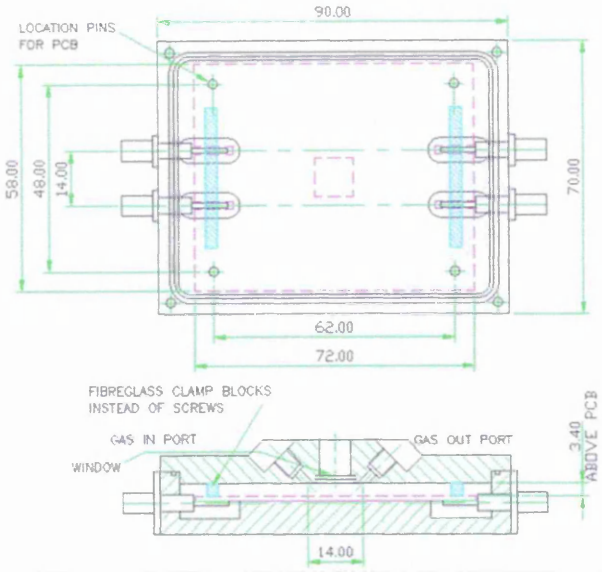

Figure 2.11 (A) Shows the AutoCAD design diagram for the FHA.

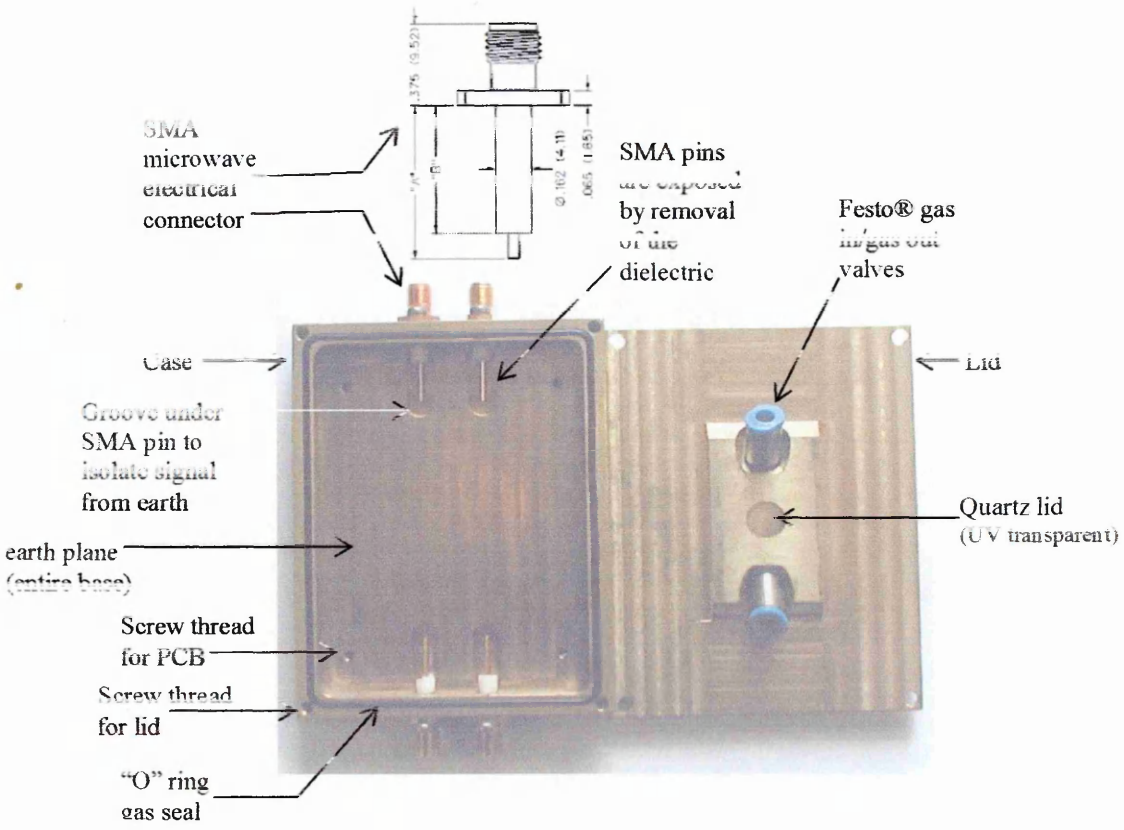

Figure 2.11 (B) Photograph of the completed FBAR Housing Assembly (FHA). The PCB is not inserted

2.4.1 PCB Design.

The purpose of the PCB was to hold the FBAR in place and to allow it to remain in efficient electrical contract with the network analyser once the chamber was sealed. It was therefore necessary to calculate the transmission line dimensions in microstrip configuration to give 50Ω to avoid loss at microwave frequencies. The Microstrip configuration is the transmission line type used in the PCB, whilst the coplanar wave guide is representative of the transmission line configuration of the FBAR. There was some initial concern that swapping from microstrip to coplanar and back to microstrip would cause some problems with loss of signal, but these concerns proved to be unfounded at the frequencies of operation used in this project, but may be of concern if the operating frequencies were increased in post prototype devices.

2.4.1.1 Laminate material choice

The choice of PCB material was based on its physical characteristics its known electrical performance and cost. For the prototype, the RF material laminate "FR4" was chosen because it was known to function without too much loss at the frequencies required and was fairly rigid in form[35]. Some rigidity was required since it was known that the PCB would have to be pressed with some force onto the SMA connectors with screws and should not buckle in at its centre, lifting itself from a good connection to ground.

FR4 Pertinent material parameters are listed below.

- FR4 dielectric constant: 4.2
- Loss tangent:.....0.012
- Thermal conductivity: 0.2
- Copper thickness:.....35µm
- Board thickness: 2.4 mm
- Completed PCB conductors were treated with Immersion Gold Finish

[35] Some microwave material laminates can be quite soft and malleable

Other more expensive laminates were available with characteristics somewhat more suited to requirements but were prohibitively expensive. However, considering the high dielectric constants (up to 9.6) on laminates such as Rogers TMM, these might be employed in post prototype devices.

2.4.1.2 Design and calculations for the 50Ω transmission lines on the PCB

In microwave circuits supporting electrical transmission at microwave frequencies, the signal flow of the current, which can be of very low amplitude, is confined to the surface of the conductor and it will experience inductance when travelling along a wire because the magnetic and electric vectors are resistant to change. Parallel wires may be considered as a transmission line when operating at high frequencies. A transmission line simply means a conductive path that transmits energy efficiently without the significant losses which becomes important at high frequencies. At low frequencies, impedance is the resistance of the wire, but as the operating frequency of the signal increases, the reactance from the induction becomes more significant. At resonance, the values of the inductor and capacitor are equal and opposite, and the resistance becomes capacitive. It should also be noted that capacitors will become inductive and inductors will become capacitive above the resonance frequency of the line, further note that the FBAR which is a parallel plate capacitor becomes a pure resistor at series resonance.

The software package "Aplac" was used to calculate the correct dimensions of the microstrip for a 50Ω signal. Based on the manual input of the pertinent physical properties of the FR4 laminate board; these were thickness of board, its dielectric constant, its loss tangent, the distance of the FHA lid from the transmission line and finally, the centre frequency of the signal over the estimated usage range. (~300 MHz-1.8 GHz). After calculation of the correct transmission line dimensions and sketching of the board layout (top and underside) in a suitable drawing package, it was necessary to import the sketch files into the electronics PCB design software package "Boardmaker" which is capable of converting the image files into a Gerber Text output file. *(See figure 2.12).*

This additional stage was primarily one of cost reduction, due primarily to the costing regimens of the PCB art workers who charge considerably more money if the PCB design layout is not e-mailed to them as a Gerber text file. Upon receipt of the Gerber file, the art work company (Lormay Ltd) delivered the boards as shown in Appendix 2. The boards were immersion gold coated over the copper cladding to ensure good contacts, but this additional process incurred some small additional charge.

There was a design consideration in how to maintain transmission line continuity with the SMA connectors when the FHA was sealed. The placement of the board in relation to the SMA connectors meant that a section of the transmission line needed to be printed on the underside of the board so that it could make physical contact with the SMA pins protruding into the FHA. For this reason, a via needed to be passed through the entire thickness of the board to connect the underside and the top side transmission lines. Since via are known to act as inductors at high frequencies, and since it was not possible to model their presence in the stripline calculation in the Aplac package, a few configurations of via numbers and via sizes were written into the art work, however of all the variable formats devised, none gave better or worse electrical performance than any other at the frequencies used throughout the project, so the results of these initial transmission line tests are omitted from the results sections. It should be remembered however that all of the tests in the thesis are in low end of the microwave spectrum and these via inductor considerations would likely become relevant at higher frequencies.

A number of test strip configurations were used to examine the effect of cross talk in the system. This simply varied the adjacent distance of the parallel strip lines on the PCB. The results of the cross-talk tests are shown in Chapter 3. The continuity of the strip lines were broken with increasing distance to examine the effect of increasing wire bond length in the circuit, because it is of course impossible to tune a wire bond to 50Ω and it was considered shrewd to make allowance for this unavoidable impedance mismatch at this stage. The results of the effect of wire bond lengths are shown in Chapter 3.

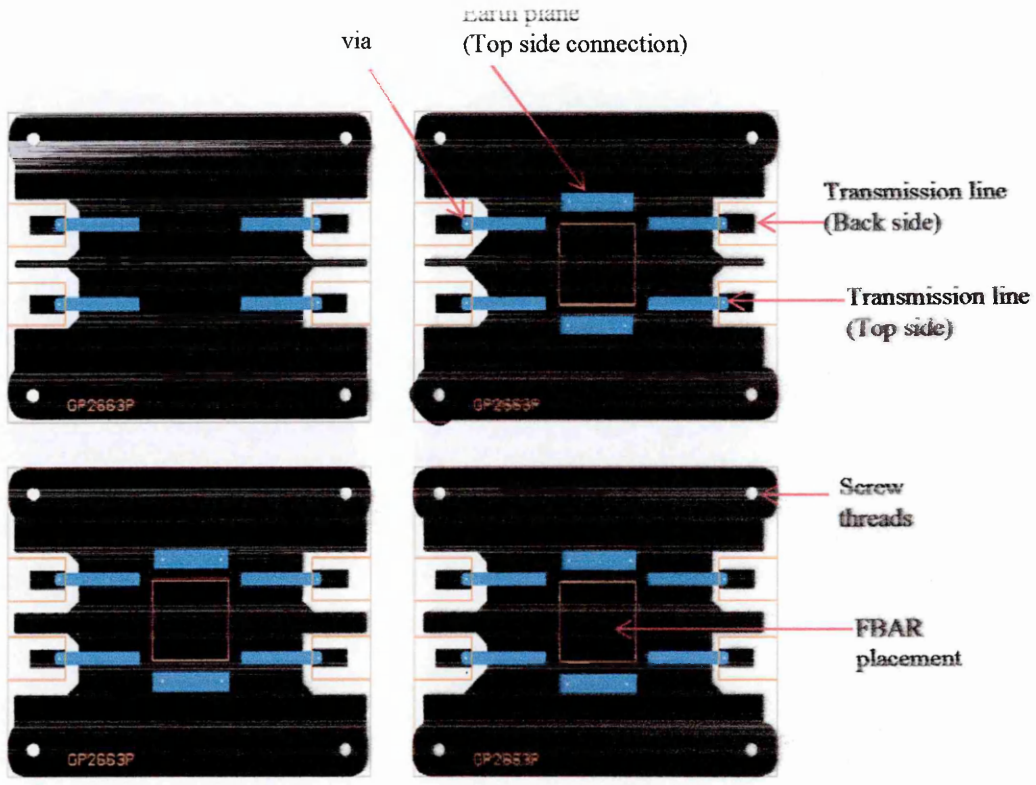

Figure 2.12 .Representative sample of the "Boardmaker" software image files ready for conversation into a Gerber file text output. The underside of the board is gold coated with a large area earth plane to make god ground contact with the earthed base of the FHA - this is not shown in the diagram. The height of the final transmission lines was calculated as 2.9 mm.

2.4.2 Thermosonic ball-wedge wire bonding procedures

Once the PCBs were obtained from the manufacturers and the FHA was constructed, it was then necessary to mount the FBAR die (~1 cm X 1 cm[36]) to the PCB with an adhesive. Then it was necessary make electrical contact to the live (signal) and earth planes of the PCB to the bottom electrode, top electrode and earth wave guides of the FBAR.

The PCB was placed into the holding bay of a Kulike and Soffa Model number 4124 Thermosonic Wire Bonder. Later, a commercial wire-bonders with better equipment would be used due to excessive loss of devices using the 4124 which was outside of the suggested minimum ball size limits when connecting the FBAR bottom electrode through its via. The PCB was first heated to 140 ^{O}C to ensure that it could tolerate the temperature that was required for the initial ball formation of the gold wire bond. FBARs were not tested for temperature tolerance, but stability was assumed based on the high temperature operations used in FBAR fabrication.

The main difficulty here was in placing the initial ball bond into the via contact to the bottom electrode (110 μm). Compressing the ball size too much would force the liquid to move back up the bonder head by capillary action. Were too large a ball size used, then it would cover the via and make direct contact to the top electrode of the FBAR rendering the procedure useless due to a short circuit. After many practice attempts, it was possible to obtain a ball bond size in the region 100μm and this made a clean connection to the bottom electrode. Multiple wedge bonds were then made to the TL's because these are known to be somewhat less strongly adhered to the surface. A simple test with a strain gauge showed these bonds to hold roughly 1 gram before either snapping or becoming dislodged from the surface.

[36] FBAR die were cut from the wafer using a diamond scribe and carefully snapping the scribed wafer over a suitable mount such as a paper clip, this method did on occasion cause the loss of devices.

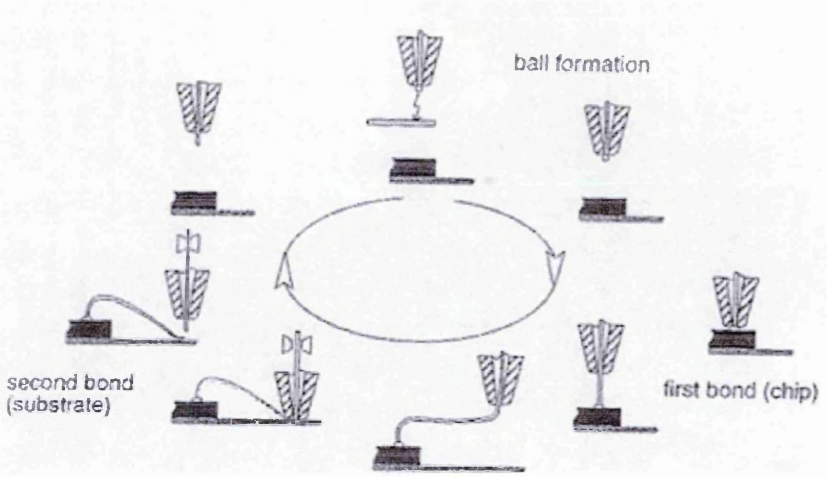

Figure 2.13 (A) The process of the Thermosonic Ball-wedge wire bonding procedure.

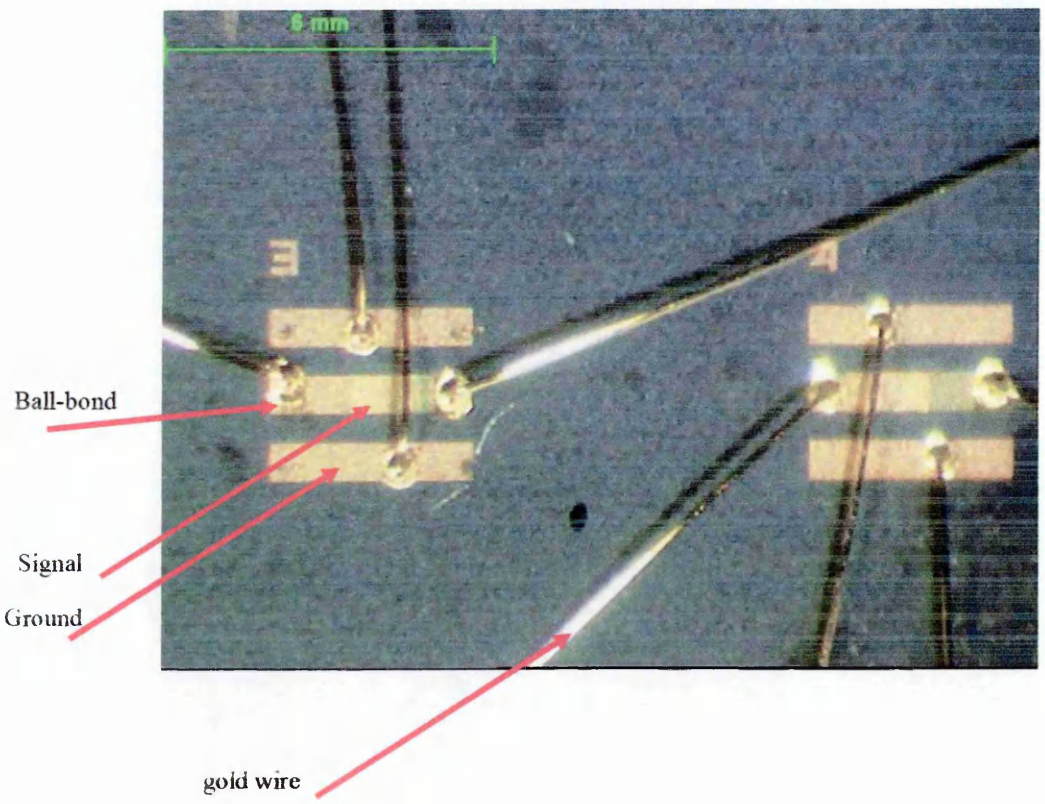

Figure 2.13 (B) Shows wire bonded FBAR devices – only balls are shown (scale is indicated)

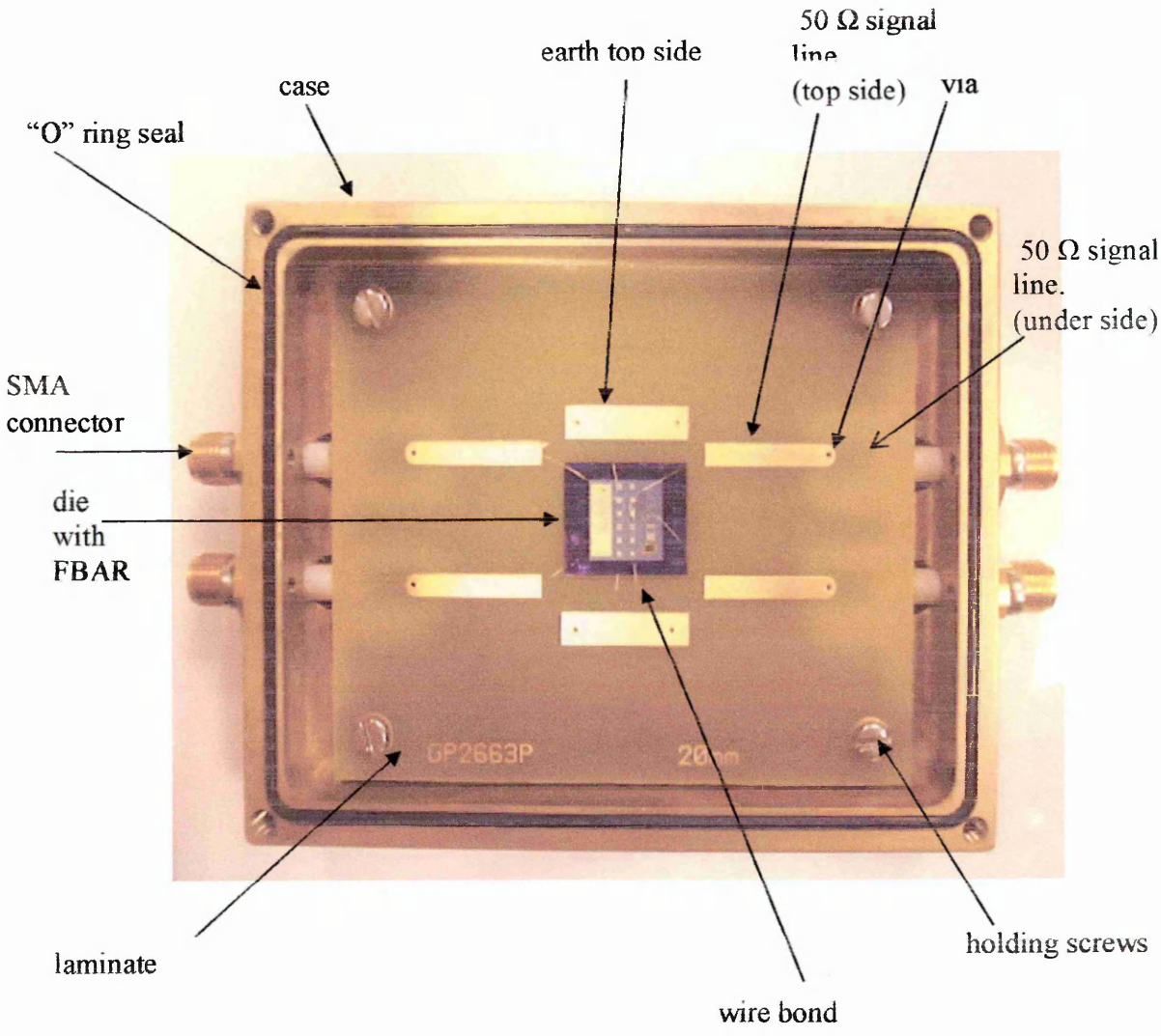

Figure 2.14 Photograph of the final configuration of on-die FBAR devices wire bonded to the PCB and mounted in the FBAR housing assembly. Lid not shown.

Note only two of a possible twelve devices are wire bonded. These devices would have been pre-characterised prior to wire bonding using the traditional G-S-G probing method.

The underside component the transmission line is visible as a shadow through the laminate.

2.4.3 Continuity testing of wire bonded FBAR devices

FBARs were tested for the quality of their characteristic response using the G-S-G on die measurement techniques previously described in section 2.3.3. At this point, many devices were rejected and only the individual FBAR units that delivered the highest quality responses were selected for wire bonding. Quality in this case means a clear resonance peak that was relatively free from unwanted spurious modes of resonance at its tip and with peaks that were at least 3 dB in magnitude so that a Q value could be established for them.

Consideration was also given to the quality of the harmonic overmodes as these were considered equally valid for sensing purposes as the primary modes were. In some cases, there was a severe spurious mode manifest on the primary mode but not on the harmonic overmodes, so decisions based on a balanced consideration of all of the resonance peaks from a given device were made, and this meant that, on occasion, some of the modes from the FBAR trace were not useable in the sensing project. It was quite time consuming analysing each of the resonance peaks from every FBAR used in the project, but since there were no automated routines written to do this, it was necessary to obtain the values manually. In this way, a detailed picture of the characteristic responses of each mode of each FBAR was made, these extra details about the FBAR characteristic responses proved to be very useful later in the project.

The wire bonded FBARs, now mounted on the PCB, were characterised in the FHA on the network analyser to ensure that there were not significant losses and that the signal continuity had been maintained. Comparisons between the characteristic responses of the pre-wirebonded devices that were G-S-G probed and the same devices now wire bonded were made for all of the devices in used.

A representative result which was typical of the pre and post wire bonded samples is shown below in figure 2.15. All of the devices responded in a similar manner, (numerous results not shown) that is, frequency (primary and overmode resonance) remained at the

original G-S-G recorded frequency values, but there was significant signal power loss on the wire bonded FBARs. The 6th overmode at ~1.2 GHz is lost due to this signal damping in the example shown, this was unfortunate since the highest overmodes were expected to deliver the best frequency to measurand responses. Overmodes were not always attenuated in this manner.

The increase in insertion loss was not considered critical to the sensing project, since the responses were to be calibrated exclusively for the wirebonded samples, however it is desirable, or at least considered to be generally good practice by RF engineers to keep signal losses to a minimum in all microwave electronic devices.

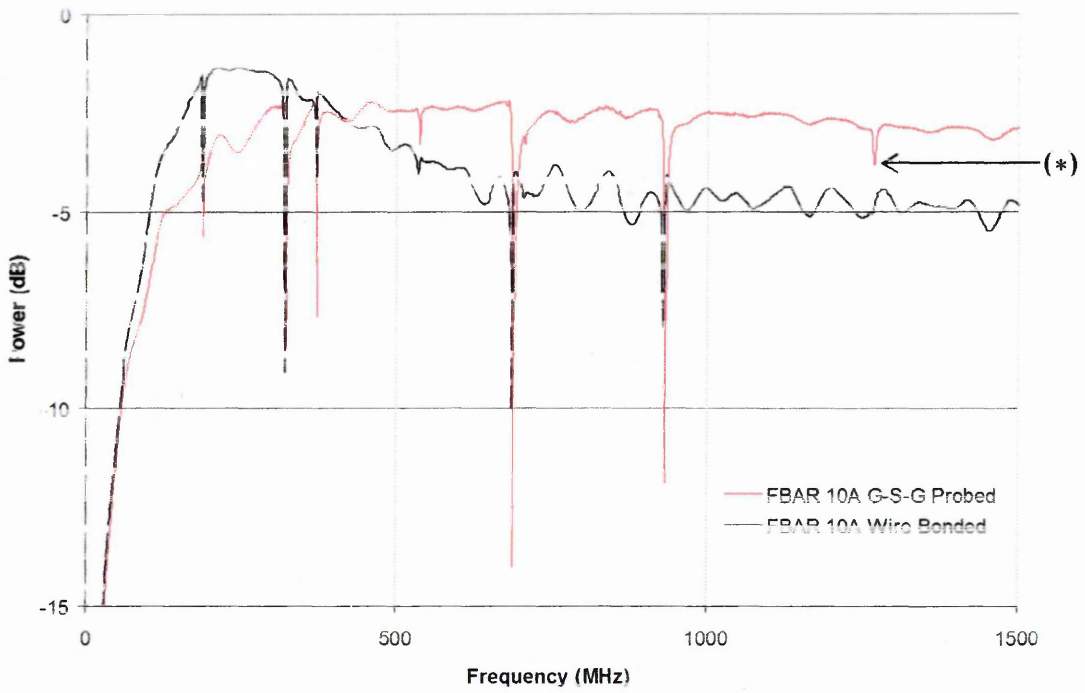

Figure 2.15 is a representative S_{21} trace result from the network analyser. It is typical of pre and post wire bonded FBARs that were characterised by (i) G-S-G on die measurements and then from (ii) within the FBAR housing assembly.

Note the loss of the highest overmode, indicated as (*) harmonic resonance peak due to wirebonding the FBAR to the PCB. This was a relatively unusual effect, and most devices did not suffer from losses such as this.

2.5 Development of the control and analysis software

2.5.1 The limitations of the existing departmental software relating to FBAR sensing experimentation

A new FBAR interrogation software suit was written because the existing departmental software (WinCal 2.3 by Cascade Microtech Ltd) which was already in place and used to process FBAR characterisation data from the network analyser was not flexible enough to be of any real use in interpreting data from the FBAR when it was responding to the presence of measurand. This was because typically, these types of sensing result would ideally be visualised and subsequently interpreted by a set of rapid, sequential FBAR responses[37] over time.

The main problem with the departmental software, was that it required a large degree of manual intervention to extract the pertinent FBAR response data from it, and also because it was not capable of performing multiple network analyser sweeps without substantial user intervention. As such, processing of the FBAR responses to measurand was laborious and this made subsequent interpretations of the FBAR responses rather difficult. This was mainly because not enough raw data could be collected in a reasonable time frame. Ostensibly, by placing reliance on the existing departmental software, it could take up to half of a working day to collect and process a set of just 20 or so network analyser sweeps of the FBAR, and this reliance on manual configuration and processing of the data increased the likely hood of human error.

Another major draw back in the use of the departmental software resided in the fact that it did not have the ability to accept electronic data from environmental measurement tools such as hygrometers and thermocouples. This meant that observations about FBAR responses to temperature or humidity over time were almost impossible to follow with any degree of accuracy. Software that could be purchased for better automated control over the network analyser such as Agilent Technologies IntuiLink VNA series software was prohibitively expensive and still required a some coding in Visual Basic to get it set up. It was therefore desirable to develop new computer code that would automate the data

[37] Usually, but not exclusively FBAR S_{21} series resonance frequency.

acquisition process from the network analyser and from additional environmental monitoring and measurement apparatus.

In order to collate and interpret large amounts of FBAR response data rapidly, it was necessary that multiple sequential frequency sweeps could be performed automatically by the network analyser with minimal user intervention. The information about the FBAR responses then had to be efficiently filtered leaving only the pertinent data for processing. In most cases, less than 0.1% of the network analyser trace information was required for tracking the FBAR resonance responses to measurand, and the remaining data in any given individual frequency sweep was superfluous. The important information required for FBAR sensing analysis was the resonance frequency (Hz) of the single data point, from up to 1601 data points in that sweep, which had the least S_{21} power transmission (-dB) over the bandwidth range of the sweep. In this way a profile of the FBAR resonance frequency responses to measurand over time could be graphically represented as a simple XY scatter plot. This type of X (time (s)) Y (frequency (Hz)) scatter graph makes up the bulk of the results throughout this work.

2.5.2 Software and hardware preliminaries

An IBM compatible X86 computer was built from reclaimed boards. A General Purpose Interface Bus (GPIB) card and cable were loaned from Sensor Technologies Ltd. The GPIB card was in the old "ISA" format and this was a limiting factor on other hardware acquisition since ISA slot main boards were phased out in around 1996/7. A copy of Microsoft® Windows '98 operating system was installed using the FAT 32 format. A new copy of Labview 6 was obtained from stores and installed. There were no network facilities available in the measurement room where the network analyser was situated so an external Iomega ZIP® drive was purchased to back up the data.

The computer was checked for stability by running CPU intensive screen savers for a few days at a time to look for crashes, but the installation of the hardware and respective drivers and the operating system went smoothly. There were occasions when the computer would hang, but this is expected with non-NT versions of windows. NT

versions of windows would not run on the computer given its specifications and therefore there were memory management problems, these are well known problems and do not occur in later versions of the windows operating system. Access to a PCI version of the GPIB card would have solved this, since it would have been possible to use a modern main board for the computer.

The programmers guide and the general user manuals for the network analyser were obtained in PDF format from the Agilent website (www.agilent.com) and the paper versions were obtained from the in-house library.

2.5.3 Software design

A control package was initially written in Labview for the FBAR sensor project by the computer programmers working at Sensor Technologies Ltd. The program that they developed for this project clearly demonstrated to the author the principles that were involved in using GPIB syntax commands to control the network analyser. Ultimately however, this package was not used during sensing experiments because it lacked a number of vital functions that were seen as critical to the sensing project. The main weakness was that it could not track resonance frequency changes in the FBAR automatically and that there were no noise filters written into its code.

External assistance was sought from colleagues during the writing of the controller/analysis software. Firstly, the HP8753D network analyser virtual instrument (VI) drivers were obtained from the internet to allow for a two way GPIB enabled communication protocol to be established between the Labview program and the network analyser. Then the perceived desirable or ideal features of the software were carefully considered and written down in a flow chart on paper. Each additional feature from the flow chart was written sequentially into the core controller program by copying the appropriate GPIB command syntax from the programmers guide into the Labview program. In this way, the suite increased in sophistication and each prototyping stage improved its capabilities until most of the desirable features from the flow chart had been successfully implemented. This took about three months to complete since there were

numerous debugging stages, the completed beta version software revision was called R0.1.

This version (R0.1) was the one that was used throughout the work, some minor modifications were made to the program as bugs in the code appeared during testing but none sufficiently major to warrant a new revision designation. These were mainly problems of instability of the response (severe signal jumps (MHz range)) during the reset stage between successive iterations, the solution to this problem was found by allowing the Labview program to autoscale rather that attempting to force the response to a set centre frequency on successive iterations. There were also memory management problems that were never adequately solved but this was likely to be due to the operating system on FAT32, not the interrogation software. These were non-trivial and much valuable experimental time was lost due to this. It was also necessary to make minor changes R0.1 as unforeseen coding errors only became obvious in the later stages of experiment when certain setting combinations were used that were not covered during the alpha testing phase, especially when attempting to obtain maximum resolutions from the FBAR responses.

An environmental data acquisition hardware board[38] was purchased from (www.drdaq.com). It was able to measure changes in temperature, relative humidity and light levels, and when connected to the parallel port of the computer, these environmental parameters could be recorded directly into the R.01 software with some additional Labview coding. This was extremely useful as it automated the environmental records, saved much time, and greatly simplified the FBAR sensing tests when observing FBAR responses to temperature change and to changes in relative humidity and to changes in light levels. These environmental results are shown in Chapter 3.

Figure 2.16 below, shows the flow chart for the operation of the R0.1 beta version of the software. This was deemed functional enough to use for sensing applications.

[38] Measurement ranges, resolution and accuracy values are given in the relevant experimental sections

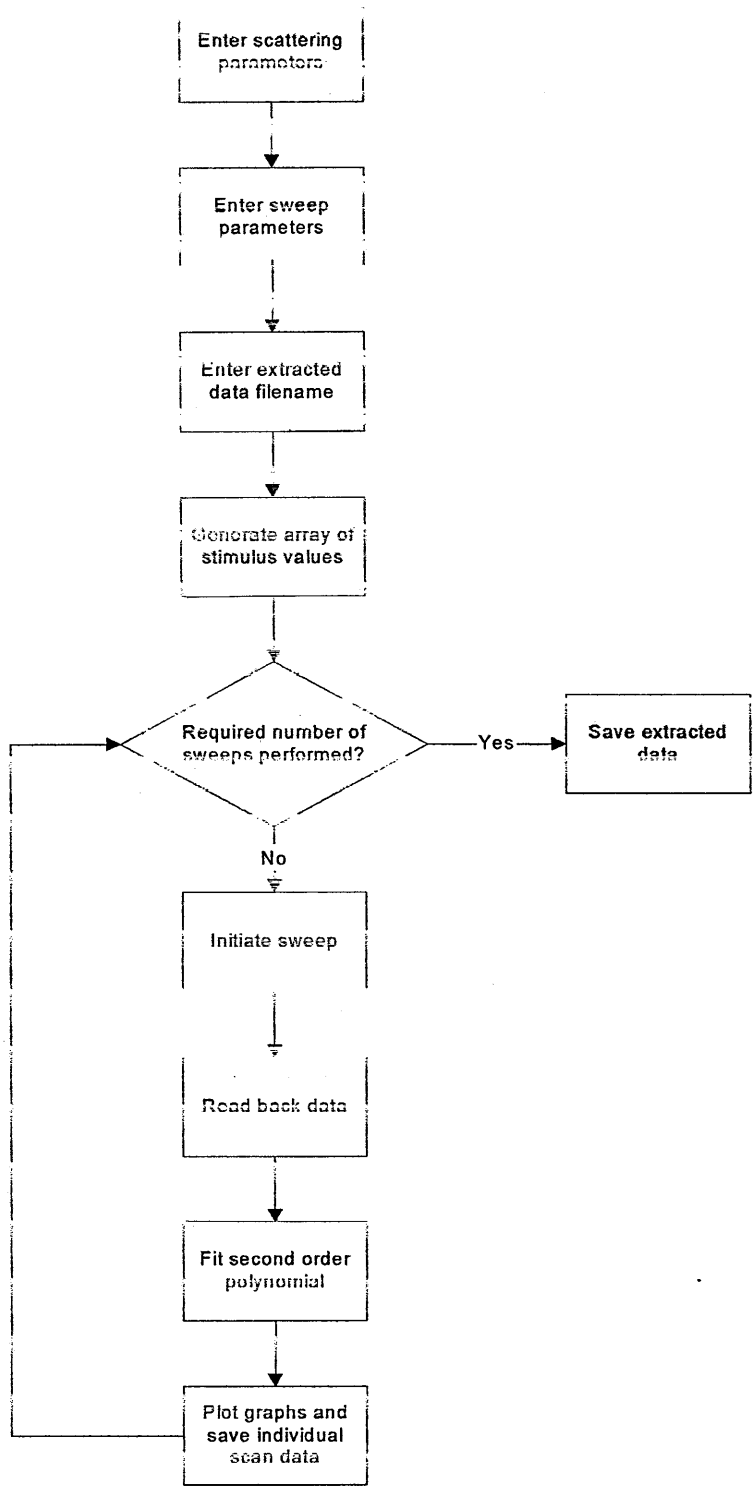

Figure 2.16 The flow chart diagram for the R0.1 software for controlling the HP8753D network analyser.

Table 2.2 The Important VI↔NA control settings

FUNCTION	SETTINGS	USE AND EFFECT	NOTES
S parameters	$S_{11}/S_{22}/S_{12}/S_{21}$	1 or 2 port transmission or reflection signal Send instruction and receive data.	S21 was almost exclusively employed.
Centre Frequency (f_c)	Accurate to 1 Hz	Specifies in Hz the centre frequency point for the scan.	The alternative method of specifying start and stop frequency were not coded into this version of the VI but the outcome was identical
Bandwidth f_1 to f_2	1 MHz to 3 GHz	Spacing on the curve relative to the fixed centre frequency input setting f_1 and f_2 are equidistant from the centre frequency	This function allowed for full range (3 GHz) sweeps or to zoom into the resonance tip at 1 MHz resolution.
Number of data points collected in the entire bandwidth sweep	3 -1601	+/- number of point in the sweep over the specified range.	Point to point raw data spacing over the bandwidth. More points increased accuracy. Was fast enough to use 1601 maximum resolution exclusively
Iteration number. i.e. number of automated sequential network analyser frequency sweeps	1-9999	Number of times a scan would run	Prone to crash if the run took more memory than computer system RAM (256 Mb). Scratch files did not appear to be compatible with VI.
IFBW	10 Hz – 3000 Hz	Random electronic noise floor reduction	Drastically increased time taken for each iteration at high resolutions 1000 Hz was the optimal setting.
dB cut off point for polynomial calculation	+3 dB -0.01d B from tip minimum	Sets Q factor bandwiidth.	This gave unrealistic Q values that needed to be taken into consideration
Memory	On/off	Normalised the circuitry and allowed suitable -10 dB attenuation as calibration solution.	Ultimately found not to be necessary or useable

2.5.3.1 Software implementation overview

As well as controlling and reading the output from the NA as shown in table 2.2. the software when completed at beta stage R.01 performed the following higher processing functions:

- Find lowest point on bandwidth span for frequency (Hz). (X axis).
- Find lowest point on bandwidth span for power (dB). (Y axis)
- Fit polynomial for resonance curve f_2 - f_1/f_0 at specified bandwidth.
- Calculate Q as measured f_2-f_1/fitted f_0.
- Find the lowest point on span for fitted frequency. (X axis)
- Find lowest point on span for fitted power. (Y axis)
- Record and graph environmental (temp, light, humidity) values from DAQ.
- Save each iteration as data file.
- Collate all data files as values in extract file for graphing at iteration end.
- Save (i) span, (ii) IFBW, (iii) frequency settings, (iv) time, (v) iteration number.

The GUI screen shot shown in Figure 2.17 below is set out into three columns showing 11 graphs, from top left to bottom right the interface gives the following real-tine information about the state of the FBAR and of its micro-environment within the FHA.

- **Column 1** – (1) Fitted frequency, (2) Measured frequency, (3) Calculated Q, (4) Measured Q.
- **Column 2** – (1) Measured power response, (2) Fitted power response, (3) Fitted sweep with polynomial (4) actual trace from NA , this should be identical to the green screen output on the physical network analyser.
- **Column 3** This is the environmental column showing (1) temperature, (2) ambient light levels, (3) relative humidity.

The drop-box menus on the far left are the control settings for (i) bandwidth, centre frequency, (ii) IFBW, (ii) S parameter designation, (vi) number of points in the sweep

and (V) number of loops to run. The address settings and the data save paths are also shown. The number of points set for the polynomial fit and the dB range over which to calculate it were set from the drop menus in this sector.

The GUI was useful for real time observation of the FBAR frequency tracking functions, but it also showed the entire characteristic response of the FBAR on any given iteration. This was useful in avoiding resonance peaks that were afflicted by spurious modes. The data acquired for each sweep was usually sent to excel spread sheets for final analysis. The entire data set from the sweep that showed the characteristic response of the FBAR with all of the data points was also saved into the same data path, but as a separate file per individual sweep. This was a very useful function, but it dramatically increased the size in megabytes of the saved experimental data, so it was necessary to archive this regularly to storage devices.

The data that was recorded into the spread sheet contained the following information in an extract file.

From the network analyser

Settings

- The Run number of the sweep in the automated sequence. (1-9999)
- The time in seconds at which the data was recorded, t=0 at start of first sweep.
- The number of data points collected in the sweep (3-1601)
- The type of S parameter used...(S_{21},S_{22},S_{11},S_{22})
- The centre frequency setting f_0
- The bandwidth of the sweep f_2-f_1
- The IFBW value (10-3000 Hz)

Results

- The measured minimum frequency of the FBAR
- The polynomial fitted minimum frequency of the FBAR
- The measured minimum power transmission or reflection
- The polynomial fitted power transmission or reflection
- The recorded Q value at specified bandwidth (-3 dB to 0.01 dB)

From the Environmental Monitoring Hardware,

- Recorded temperature (^{O}C) at start of sweep
- Recorded humidity (%RH) at start of sweep
- Recorded light intensity (% saturation of photodiode) at start of sweep

The investigation now became simultaneously focussed on *both* the software performance and stability i.e., beta testing *and* the FBAR performance as a sensor. These twin components were considered to be of equal importance for the continued prototype development..

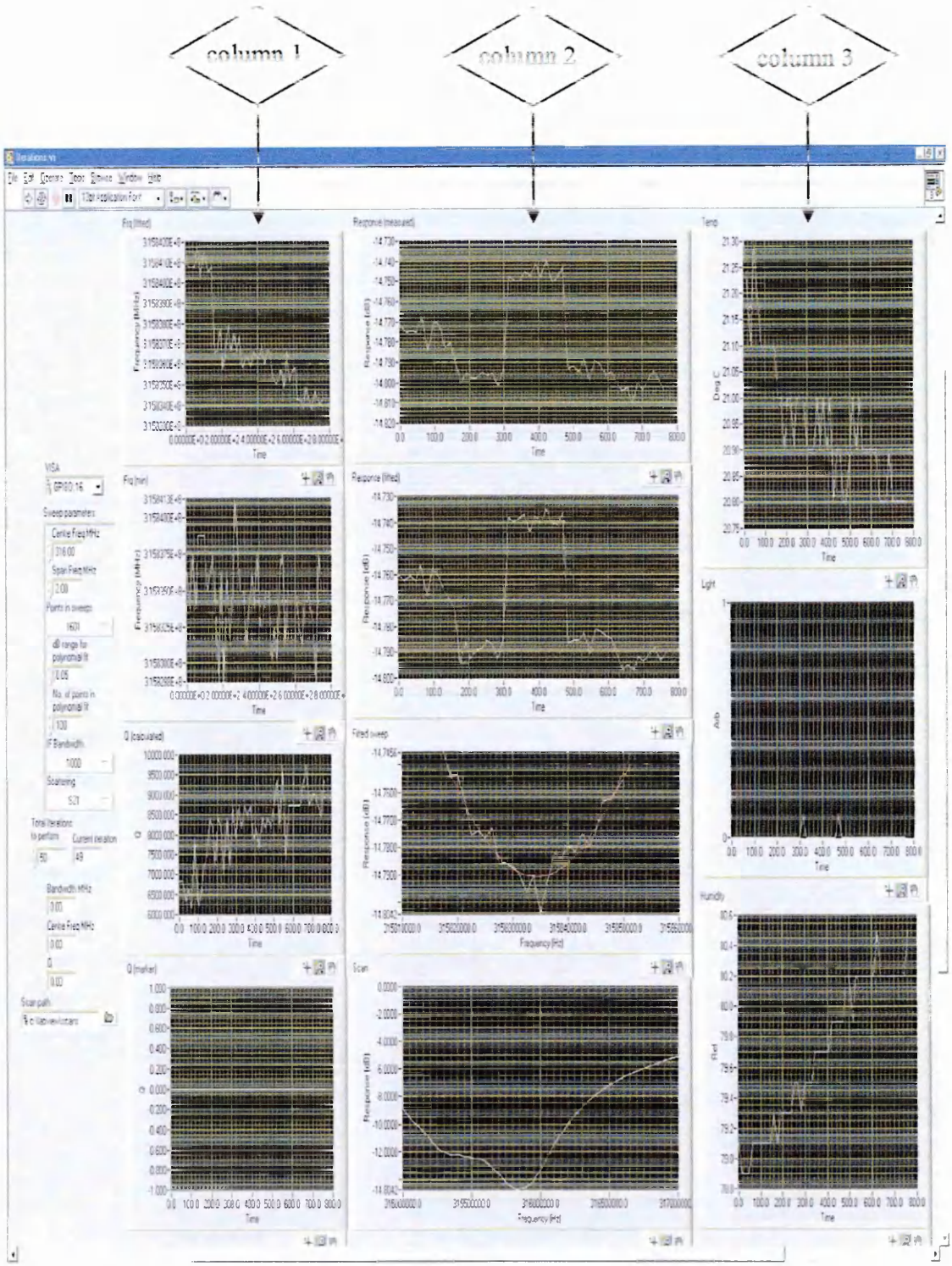

Figure 2.17 A Screenshot of the GUI of the working version FBAR interrogation software revision. version (R.01).

REFERENCES
CHAPTER TWO

1. Kovacs. A. (1998) Micromachined transducers sourcebook. WCB/M^{C}Gaw-Hill. ISBN 0-07-290722-3
2. Madou. M (1997). Fundamentals of microfabrication. Boca Raton, FL : CRC press. Inc., ISBN 0-8493-9451-1)
3. Santoli. S. (1999) Hyper-intersperced nano/MEMS-architecture design for new concepts in miniature robotics for space exploration. *Acta Astronautica.* Vol 44. Number 2. pp 117-122.
4. Wang. J. Lakin, K. M. (1981) *IEEE Proceedings of the Ultrasonics Symposium.* pp 502-505.
5. Lakin K. M. (1993) Numerical analysis of two dimensional thin film resonators. *IEEE international frequency control symposium.* pp 502-508
6. Krishnaswamy. S., Rosenbaum. J., Horowitz. S., Vale. C., Moore. R. (1991) . Compact FBAR filters offer low loss performance. *Microwaves and RF.* 10 pp 127-136.
7. Ruby. R., Bralley P., Oshmyanski. Y (2001), Thin film bulk acoustic wave resonators (FBAR) for wireless applications 2001 *IEEE Ultrasonics symposium,* pp 813-821.
8. Horowitz. S., Milton C. (1992) Applications of film bulk acoustic resonators. *IEEE Marconi Materials Technology-S Digest.* D5
9. O'Toole. R., Burns S. Shanks. R., D'Silva. A., Weber. R., Porter M (1990). Microwave frequency oscillators based on AlN: Toward integrated chemical sensors. *Optical and piezoelectric sensors symposium of the electrochemical society.* October 1990
10. O' Toole. R., Burns. S., Bastiaans., G., Porter. M. (1992) Thin aluminium nitride resonators: Miniaturised high sensitivity mass sensors. *Anal Chem.* 1289-1294
11. Xia. J., Burns. S., Porter M., Xue. T., Liu. G., Wyse R., Thinlen. C. (1995) Micromachined sensor array using thin film resonators. *IEEE international frequency control symposium*
12. Zhang. H., Kim. S. E. (2003) Vapour and liquid mass sensing by micromachined acoustic resonator. *IEEE Proceedings* pp 470-473
13. Weber, R. J., Burns. G. S., Campbel. C. F., O' Toole. R. (1992) Applications of AlN thin film resonator topologies as antennas and sensors. *IEEE D4 MTT-S digest.*
14. Gabl. R., Feucht. H., Zeininger. H., Eckstein. G., Schreiter. M., Primig. R., Pitzer. D., Wersing. W. (2004) First results on label-free detection of DNA and protein molecules using a novel integrated sensor technology based on gravimetric detection principles. *Biosensors and bioelectronics.* 19 615-620
15. Lee. J., Kim. H., Kim. S., Hwang. C., Hong. S., Shin. Y., Lee. (2003) N. Deposition of ZnO thin films by magnetron sputtering for a film bulk acoustic resonator. *Thin Solid Films* 179-185.
16. Su. Q., Kirby. P., Komuro. E., Imura. M., Zhang. Q., Whatmoore. R. (2001) Thin-Film bulk acoustic resonators and filters using ZnO and lead-zirconium-

titanate thin films. *IEEE transactions on microwave theory and techniques*, Vol 49 4. pp 469-777.
17. Zhang. H., Kim. E. (2002) Air-backed Al/ZnO/Al film bulk acoustic resonator without any support layer. *IEEE International Control Symposium and PDA Exhibition*. pp 20-26
18. Osbond. P., Beck. C. M., Brierley. J. C., Cox. R. M., Marsh. P. S., Shorroks. M. N The influence of ZnO and electrode thickness on the performance of thin film bulk acoustic wave resonators. (1999) *IEEE ultrasonics symposium. 911.*
19. .Benes. E., Groschl. M., Burger. W., Schmid. M. (1995) Sensors based on Piezoelectric resonators. *Sensors and Actuators* A 48 1-21..
20. Cemosek. An overview of acoustic wave devices for chemical sensing, biological detection, and materials characterization. **Lecture Notes**. Materials Research and Education Centre, Dept. Mech Eng. Aubum University. US. (2003)
21. Lakin. K (1992) Modelling of thin film resonators and filters. *IEEE MTT-S digest.* pp 149-152.
22. Rossnagel. S. (1995) Sputter deposition. Opportunities for innovation: Advanced surface engineering. Switzerland: Technomic Publishing Co.
23. Kelly. P., Arnell. R. Magnetron sputtering: a review of recent developments and applications. Vacuum 56 (2000) 159-172
24. Lee. J., Jung. J., Lee. M., Park. J (2004). Effects of bottom electrodes on the orientation of AlN films and the frequency responses of resonators in AlN-based FBARs. *Thin solid films*. 447-448, pp 610-614.
25. Kirby. P. B., Potter M. D. G., Williams. C. P., Lim. Y. M (2003). Thin film piezoelectric property considerations for surface acoustic wave and thin film bulk acoustic resonators. *Journal of the European ceramic society*. 23. pp 2689-2692
26. HP 8753D Network analyser user's guide. (December 1997) Hewlett Packard.
27. Krishnaswamy. S. V., Horwitz. S. S., Moore. R. A. (1991) Microwave film bulk acoustic resonator and manifold filter bank. US PATENT 5 185 589

28. Other Relevant Patents
Thin film resonant chemical sensor with resonant acoustic isolator.
PATENT NUMBER: US5936150 (1999)
Lateral field FBAR.
PATENT NUMBER: US5233259 (1993)
Piezoelectric contamination detector.
PATENT NUMER: US4561286 (1985)

29 D. Absolom, W. Zingg, A.W. Neumann (1987) *J. Biomed.Mater. Res.* **21** 161

CHAPTER THREE
3.0 EXPERIMETNAL INVESTIGATION INTO THE RESPONSES OF THE FBAR TO ENVIRONMENTAL CHANGES WHEN ISOLATED WITHIN THE FBAR HOUSING ASSEMBLY.

3.1 Introduction

This chapter describes the procedures that were used to investigate the characteristic responses of the wire-bonded FBAR devices isolated from the ambient laboratory environment within the FBAR Housing Assembly (FHA), up to the point where the responses could be confidently interpreted for chemical and biological acoustic analysis[39]. In this chapter, the first part of the experimental section up to section (3.3.5), examines the electrical performance of the individual FHA components, the circuit board transmission lines, wire bonds and cables and connectors. The remaining experimental sections look at the responses of wire bonded FBARs sealed inside the FHA whilst the environment was controlled and monitored and the network analyser was under the control of the new software. The purpose of these tests was to attempt to track changes in the FBAR characteristic responses to controlled environmental fluctuations with increasing accuracy and increasing levels of resolution using the new software.

In brief, the nature of the work undertaken in this chapter was designed to;

1. Characterise the RF electrical responses of the individual FHA components
2. Seek out and reduce sources of system noise to improve measurement accuracy
3. Use temperature change to follow and interpret responses of FBAR
4. Discover the best practical instrumentation settings for later chemical and biological analysis
5. Discover the highest achievable limits of resolution, sensitivity and accuracy with the FHA apparatus, network analyser and new software
6. Beta test new software throughout 1-5.

[39] Chemical and biological experimentation on the FBAR are described in Chapter 4 and Chapter 5 respectively.

FBAR resonance frequency change[40] (Δf) was *generally* monitored as the sensing parameter in this work. However, a brief study was made of the possibility of using other network response parameters that were also recorded during a frequency scan of and included the Q factor and the minimum S_{21} power transmission value in dB.

RF electrical characterisations of all of the major electrical components of the FHA circuit were made before proceeding to actual sensing experiments[41]. This is because, in general at low frequencies, (< 10 MHz) the environment around electrical connections does not influence transmitted electrical signals. However, as the frequency of the signal increases into the microwave range the characteristics of the propagating signals along electrical conductors is influenced by the electrical environment, which includes nearby conductors, which can alter the impedance of the electrical conductors used for transmitting signals. It was required to take such potentially interfering influences into account during the design and construction of the FBAR housing assembly (FHA) and to check their influence experimentally.

These kinds of checks are normally done by measuring the transmission of signals through the system using the network analyser and assessing the deviation of the transmission line characteristic impedances from 50Ω. Since the input impedance of the network analyser is 50 Ω and the connecting cables are 50 Ω, then any deviation from 50 Ω for the conducting tracks in the FHA will lead to transmission losses[42].

[40] S_{21} series resonant frequency.
[41] Recording the responses over time of the FBAR whilst it was subjected to changes in temperature whilst sealed in its environmental isolation chamber. The FHA
[42] This is also known as insertion loss in microwave engineering

3.2. Materials and Methods

3.2.1 Apparatus

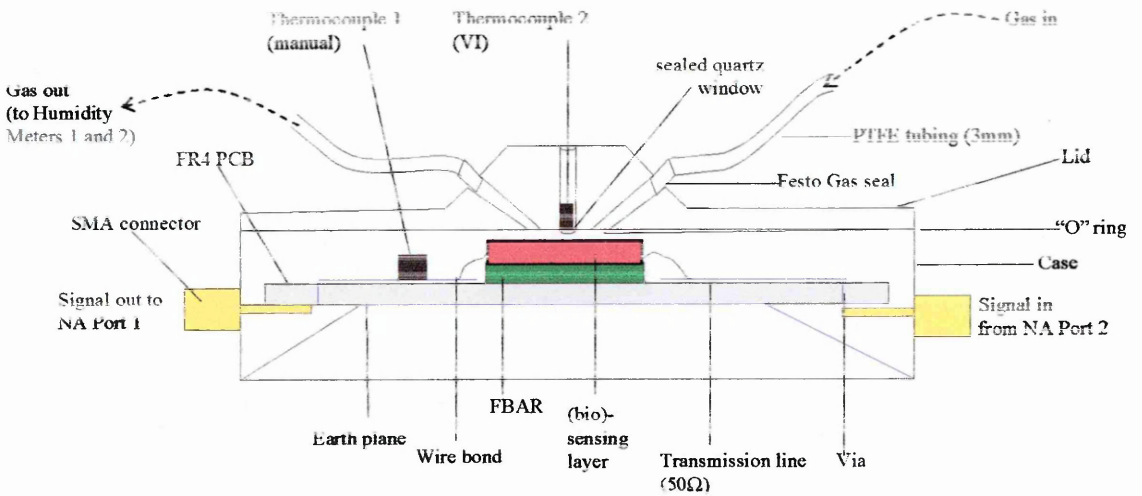

Figure 3.1 Schematic shows the principal components[43] of the FBAR Housing Assembly. (FHA) (Not to scale)

The complete list of the materials that were used to perform the experiments in this chapter can be found in appendix (2) and the methods involved in the design and fabrication of the FHA and its associated electronics can be found in Chapter 2 along with a colour photograph of the chamber (*See Figures* (2.11 (B)) and (2.14)

[43] The gas flow system is not shown here because it does not form part of the present discussion, it is shown in Figures 4.1 and 4.2. The reference to (bio) sensing layer in the diagram relates to the chemical (Chapter 4) and biological (Chapter 5) sensing layers connected to the FBAR surface.

3.3 Experimental procedures

3.3.1 Loading the FHA with FBAR wire bonded to microwave printed circuit board and connection to the network analyser.

FBARs on microwave printed circuit boards (PCB(s)) that were to selected for testing were placed into the FHA and secured in place by tightening the screws, this ensured that there was a good electrical contact between the metallic base of the FHA and the Au layer on the underside of the PCB. In this way, a good ground plane was established as is favoured for stably responsive microwave circuits. It was found that if too much pressure was applied to the screws, then the PCB would arch or buckle slightly and continuity could be lost or become intermittent. PCB 50Ω transmission lines (TL) continuity to both of the SMA connectors of the FHA was confirmed with a multimeter every time the PCB sample was exchanged. The coaxial cables were then firmly screwed onto the SMA connectors of the FHA and the other end of the coaxial cables were attached into the network analyser ports 1 and 2 with sexless N type connectors to finger tightness. It was important to ensure that the coaxial cables in good contact with both the SMA connectors on the FHA and also with the ports of the network analyser, otherwise a distorted signal could result. The FHA would be periodically cleaned inside and out with acetone IPA and blow dried with warm air to avoid residues that may have interfered with electrical contacts.

Wirebonds would be carefully inspected and positions noted to avoid touch or disturbance from the internal thermocouple which required repositioning after each PCB change. For the PCB having printed 50Ω transmission-line structures, continuity between the between input and output SMA could be easily checked as described above, however this was not possible for PCBs holding wire bonded FBARs. However in this case it was possible to compare the signal transmission of FBARs incorporated into the FHA with measurements previously obtained for them by on-wafer probe measurements before the FBAR was wire-bonded so that poor connections could be identified.

There are specifications for how much the high frequency coaxial cable can be bent, or more specifically the minimum acceptable bend radius. This is because static charge can

be generated in the cable and parasitic inductances and capacitances between adjacent bent regimes can occur. So it was good practice to leave the coaxial cabling undisturbed and as far as possible in the same position and curvature radius for each experimental set that did not involve removing the cables from the FHA or NA. To this end, marks were made on the workbench to position the telescopic retort pad on which the FHA was placed and its height, once adjusted for convenience of handling, was left fixed.

3.3.2 Temperature control

Conditions in the laboratory were stabilised, ambient temperature variation was found (empirically) to be smallest when the laboratory door was wedged open. Most of the experiments were performed in the evening when the laboratory was not in use by other workers.

The internal thermocouple was fixed in place on the PCB with sticking tape as close as possible to the Si die of the FBAR positioned within the FHA, whilst avoiding disturbing the four delicate wire bonds connecting the FBAR to the circuit. The external thermocouple was placed into the FHA quartz window socket, resting some 5 mm above the device. This sent temperature data to the computer directly through the environmental data acquisition card. (Range = -10°C to 150°C, Resolution = 0.1°C @25°C and Accuracy 0.3 °C @ 25°C)

To stabilise and to control the temperature of the wire bonded FBAR on the PCB, the FHA was placed on top of a Peltier heating block at set temperature with heat transfer paste on the underside of the assembly to ensure good thermal contact. Once equilibrated, the temperature of the internal thermocouple and hence the FBAR inside the sealed FHA was reasonably impervious to brief unavoidable[44] fluctuations in the room temperature. The thermocouples were accurate to $\pm$ 0.1 °C. Internal (manually read) and external (VI GPIB enabled) thermocouples[45] were periodically compared against each other to ensure that VI temperature data was being correctly reported. Temperature would be increased

[44] A person entering the measurement room (especially coming straight from outdoors) would temporarily alter the recorded room temperature

[45] The positions of the thermocouples are shown in Figure 3.1

or decreased gradually using the Peltier heater settings, if more rapid temperature change was required, the FHA would be warmed with hot air from a heat gun or placed onto ice

3.3.3 Beta testing of software and electrical characterisation of the principal components of the FBAR housing assembly.

Beta testing the software was not mutually exclusive from the apparatus checks such as circuit continuity, scattering parameter and cross-talk tests. The initial testing stages were aimed at discovering the most appropriate settings to be used in future FBAR sensing experiments whilst simultaneously collecting data for the complete characterisation of the FHA and its associated wires, PCBs, transmission lines, coaxial cables and SMA and N type connectors for the purpose of minimising signal loss and reducing random electronic noise from the final output traces.

Once the newly developed software was debugged up to stage version R.01, it was necessary to compare its performance in relation to the established NA data acquisition software which was already in place at the department.[46] It was also necessary to make a direct comparison with the output green-screen values of the NA, this measurement was made by eye. Ostensibly, the green screen and VI graphs should be identical and any significant discrepancies would indicate that the new software was not complete and further code time would be required. Most of the following system checks were performed to ensure that the developed R.01 software was working properly, whilst simultaneously attempting to improve signal to noise ratio, and increase the sensitivity of the recorded responses from the wirebonded FBAR samples. The methods were under a state of perpetual improvement throughout the experimental work in this chapter.

In cases where the software crashed[47] the experiments would be repeated from the last available logical start point if reagents or materials were limiting[48]. Notes were made on the time and date and setting states used during any crashes, this was to attempt to

[46] This established software was called Wincal 2.3 ™ by Cascade Microtech who were the manufacturers of the Summit 9000 probe station.
[47] Failure to perform next iteration in loop, GPIB communication error.
[48] It was time that was the main limiting factor, software crashes, although relatively uncommon were a major set back in the continuity of the experimental sessions. Reagents were only of concern in later chemical and biological testing.

generate a pattern[49] to highlight any obvious serious weaknesses in the software system which was still being scrutinised for flaws occluded during the alpha testing stages.

3.3.3.1 Use of scattering parameters to characterise FBAR

3.3.3.1.1 Methods

All scattering (S)-parameters (S_{11},S_{21},S_{12},S_{22}) were recorded to give a complete characterisation of the FBAR responses and to ensure that each of the four S parameters could be controlled by the new software. S_{21} was nearly always used for the experiments, since it was the established prior art with most departmental historical results being presented in this format. To obtain all of the S parameter responses through the new software, a pre-characterised[50] wire bonded FBAR was loaded into FHA. The VI was set to command the network analyser to perform a full frequency span range (0-3 GHz) for a single iteration[51] with 1601 points. The two port transmission S parameters S_{21} and S_{12} were recorded, along with the reflections from single port measurements S_{11} and S_{22}, these were displayed graphically.

3.3.3.1.2 Results

The results in Figures 3.2 A, C and D are as expected with FBAR primary resonance and harmonic overmodes in S_{12},S_{12} and S_{11} clearly visible. However, the S_{22} signal (*See Figure* 3.2 B) is present as a reflection but the resonance states of the FBAR failed to have manifest as was expected. It was assumed that this signal should have been identical to S_{11}. The second port was known to have continuity since the S_{21} and S_{12} transmissions both used that port to transmit signal. S_{21} was designated the parameter of choice for *all* future tests.

---

[49] No clear pattern for software failure emerged. The only common factor in crashes was a high data density request (and subsequent large memory requirement) over extended (> 30 minutes) time periods, but this did not always occur. Eventually, through experience, the sound of the hard drive making a swap file during an experimental run was generally a good prediction of a failure.

[50] The S parameter responses for this device had been previously obtained using on-wafer measurements with the probe station (Summit 9000 ®) linked directly to the network analyser.

[51] An iteration means the number of frequency sweeps that the software was programmed to command the network analyser to perform. This could be 1 to 9999.

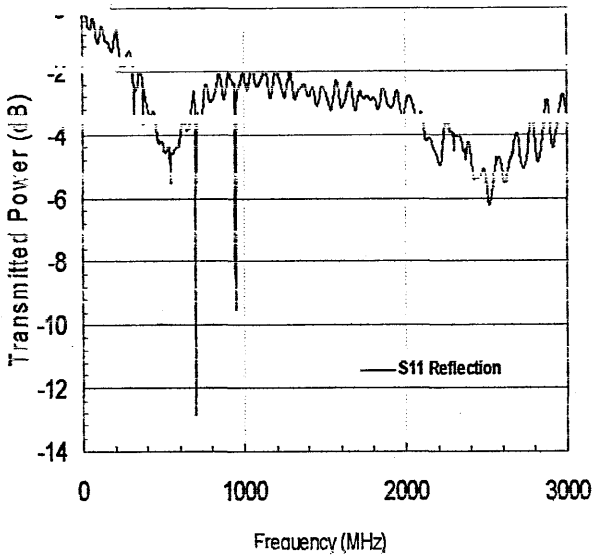

(A) S_{11} Port 1 single port reflected signal

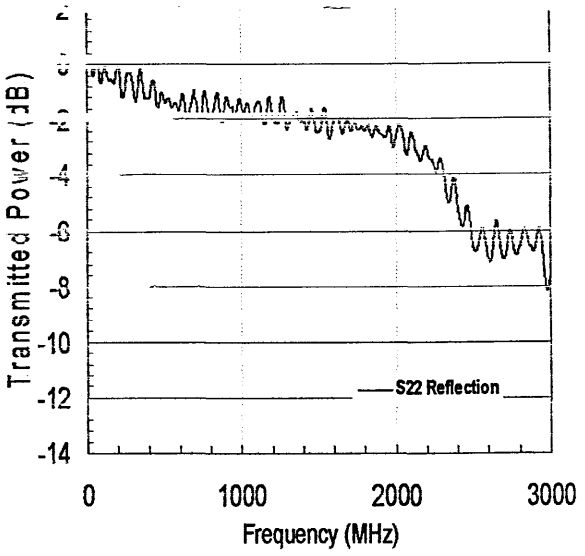

(B) S_{22} Port 2 single port reflected signal

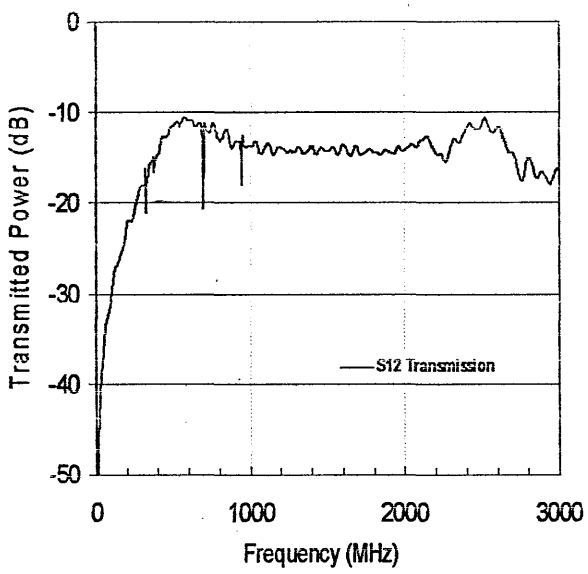

(C) S_{12} two port transmitted signal

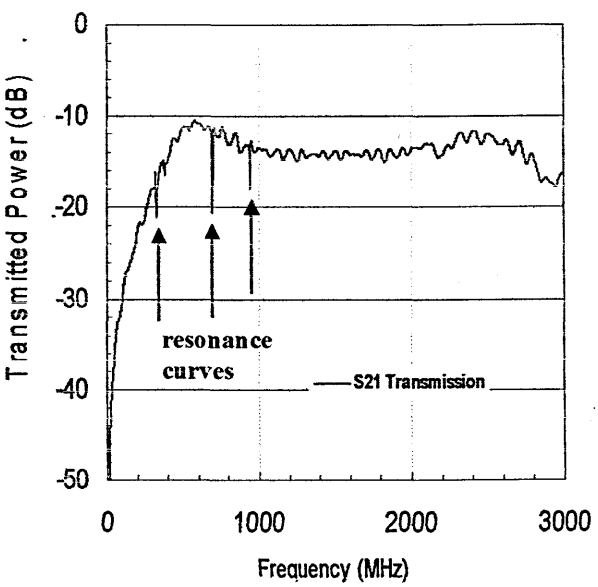

(D) S_{21} two port transmitted signal

Figure (3.2) (A, B, C, D) All S parameters of FBAR with single 0-3 GHz frequency sweep for each S parameter.(1601 data points per trace) Resonances are visible in the graphs as sharp decreases in the S_{21} power transmission.(dB). Representative examples of the FBAR resonance (fundamental and overtones) curves are marked by three arrows in D which shows S_{21} transmission data.

3.3.3.2 Confirming the S_{21} RF signal continuity

3.3.3.2.1 Methods

This experiment was designed to ensure that the S_{21} transmission response was operating as anticipated. This was to confirm a primary and basic yet critical and essential function of the R.01 software - that is specifically, to command the NA to deliver signal at;

- Specified centre frequency (f_c)
- Specified frequency bandwidth[52]. (Frequency 2 (f_2) to Frequency 1 (f_1))
- Set IF bandwidth
- Set number of collected data points over frequency range
- Set number of iterations

It was important to be certain that the VI controllers were truly representative of the actual NA front panel controls and that they would operate in all of the combinations necessary for the flexibility required for later biosensing.

A PCB with intact[53] 50 Ω transmission line was fitted into the FHA and complete electrical continuity was confirmed with a multi meter. The unused electrical path was terminated with 50Ω terminators. (*See Figure* 3.3 A) From the VI, the centre frequency (f_c) of the network was set at 1500 MHz and the bandwidth ($f2$ to $f1$ spacing (Hz)) was set to, f_1 = 300 kHz, f_2 = 2999 MHz,[54] The responses were recorded by the computer and saved to the specified folder path. The coax cable connecting port 1 of the network analyser was then removed from the SMA connector on the FHA and replaced with a 50Ω signal terminator (*See figure* 3.3 B). Full band sweeps (0-3 GHz) with 1601 points were made. Power (dB) over frequency (MHz) was plotted as an XY scatter graph.

---

[52] f_2 to f_1 span range in Hz equidistant from the set centre frequency, also known as measurement range.

[53] Some of the test transmission lines were printed with deliberate discontinuities to test RF effects of wire bonds length increases.

[54] For convenience throughout this thesis, this measurement range or bandwidth value is denoted as 0-3 GHz **not** 300 kHz -2998 MHz

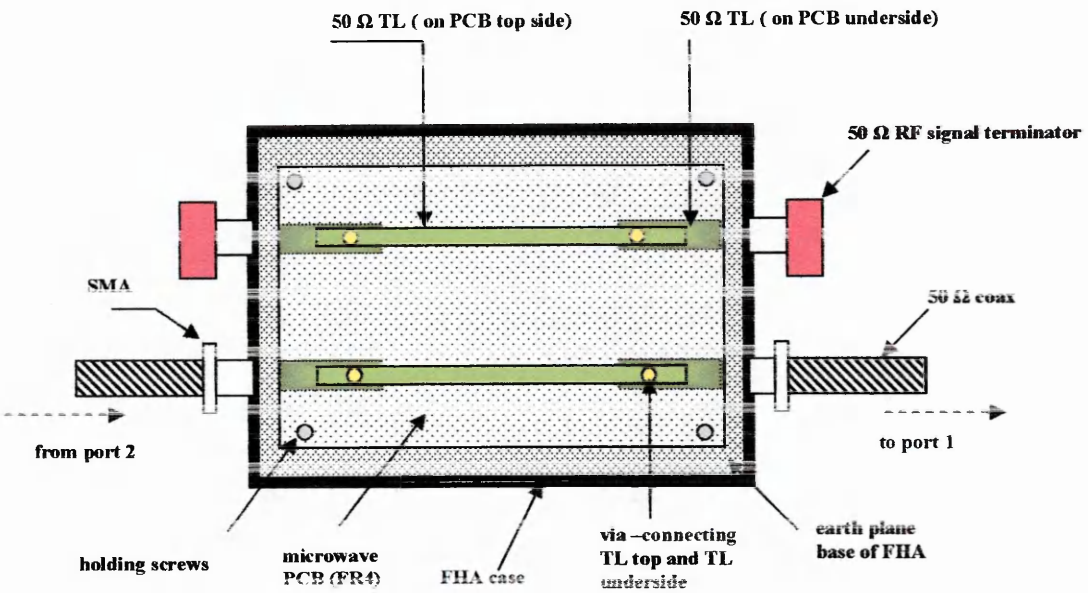

Figure 3.3 (A) Shows FHA with S_{21} continuity arrangement

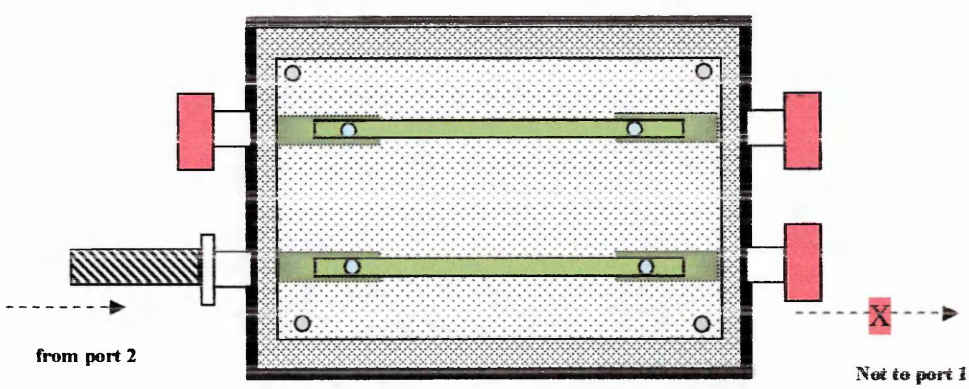

Figure 3.3 (B) Shows FHA with S_{21} termination arrangement

3.3.3.2.2 Results

The continuity trace seen in Figure 3.4 is from data produced by the VI ↔ NA command with the continuity arrangement as shown in Figure 3.3 (A) It shows inconsequential transmission power loss which increases slightly as the signal frequency increases to give a maximum loss of ~5 dB @ 3 GHz. This is indicative of a transmitted signal being very closely matched to 50 Ω and therefore efficiently transmitted. The experiment was repeated but the connection to port 1 was blocked with a 50Ω signal terminator on the SMA connector. This is the termination arrangement shown in Figure 3.3 (B). Signal loss was ~ -100 dB (i.e., no transmission) over the complete frequency spectrum confirming that signal was not transmitted to port 1. The result is as expected, it confirms the successful negotiation of the S_{21} signal command from the VI to the network analyser and the successful receipt and storage of FBAR interrogation data from the network analyser to the VI.

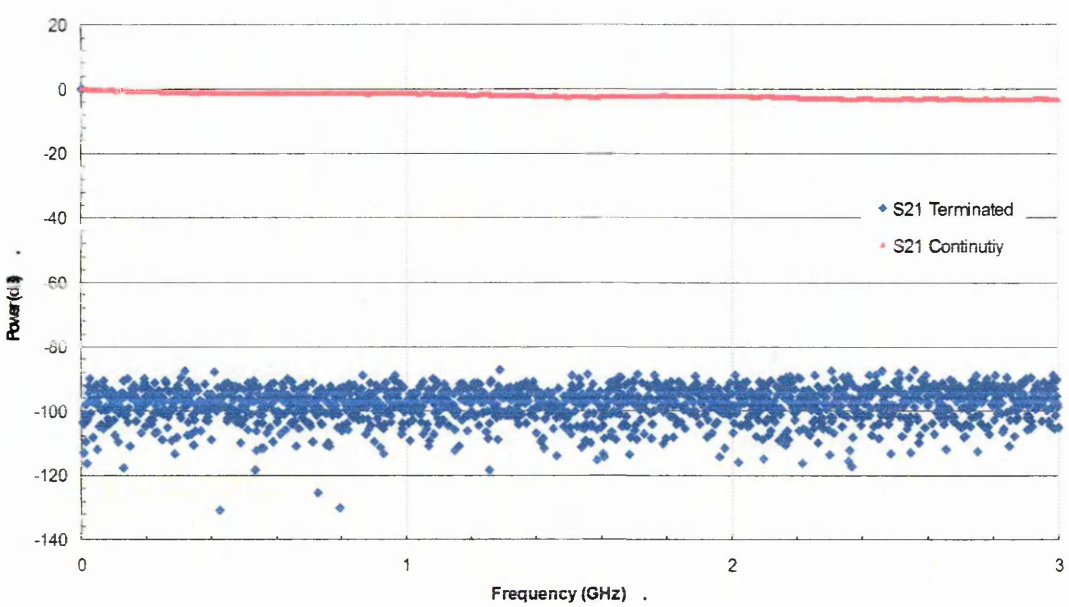

Figure 3.4 Shows S_{21} signal continuity and S_{21} signal termination
Power transmission vs. loss over 0-3 GHz span. Port 1 continuity intact and Port 1 continuity terminated.

3.3.3.3 Effect of RF cross-talk on 50Ω TL spacing gap

3.3.3.3.1 Methods

Since RF signals are known to penetrate 3 dimensionally as electromagnetic fields into space, there can be signal bleed or so called "cross talk" between closely spaced RF components if they are in that field. Tests were performed to examine the magnitude of this effect in FHA assembly between closely spaced but non-touching continuous 50ΩTL on the PCB. The figure below 3.5 (top) shows the experimental arrangement and it is clear that there is no *direct* electrical contact between Port 2 and Port 1 of the network analyser. Any transmitted power would therefore have to be attributed to the phenomenon of cross-talk between the transmission lines.

PCB test structures with parallel TL spacing (10 mm, 7.5 mm and 5 mm) were loaded into the FHA. S_{21} transmitted power over frequency was plotted (0-3 GHz) (1601 data points)

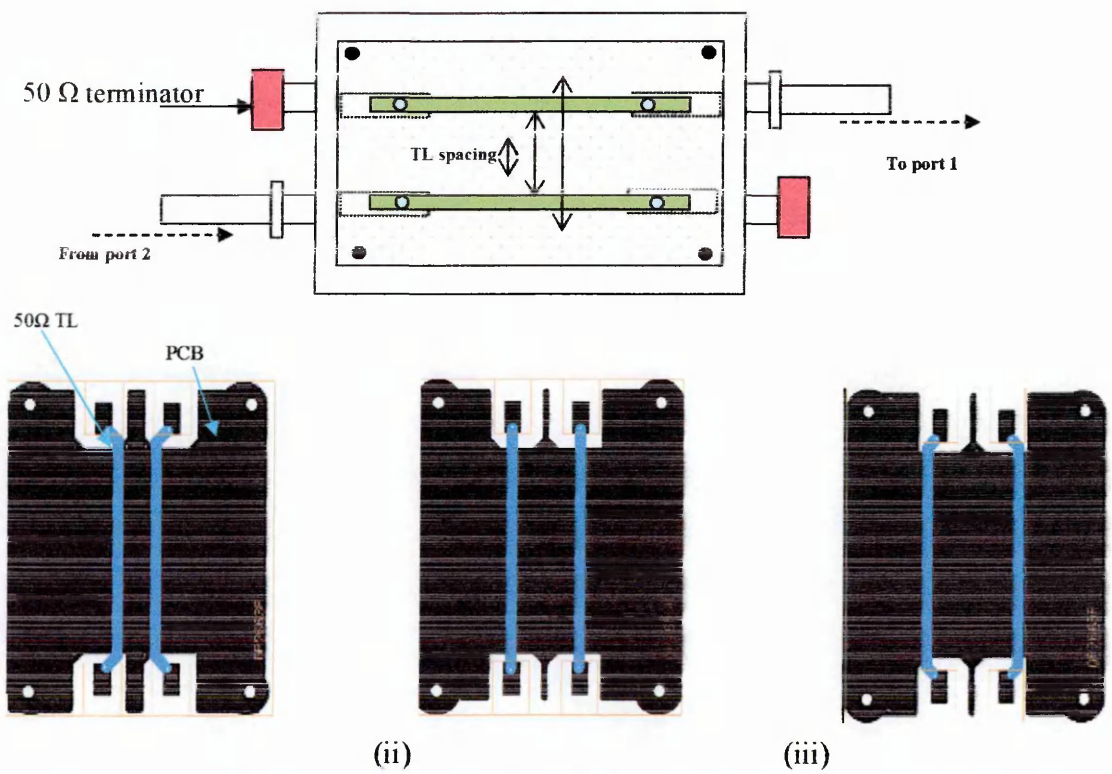

Figure 3.5 (Top) Schematic of PCB TL and FHA configuration for cross-talk determination. (Bottom) shows PCB 50 Ω TL in Gerber type output file images. TL distance = (i) 5 mm, (ii) 10 mm, (iii) 15 mm.

3.3.3.3.2 Results

The results in Figure 3.6 show that there is RF signal cross-talk signal interference between 50 ΩTL at all distances, but the signal fades with increasing TL parallel distances. There is a trend for increasing levels of cross-talk interference as the frequency increases with all TL spacing distances.

Results show values of cross-talk for parallel 50Ω TL spacing @3 GHz were;

- 5 mm -19.5 dB
- 10 mm -29.0 dB
- 15 mm -36.0 dB

There is sharp decrease in cross-talk transmission at ~2 GHz for the 15 mm distance TL and a similar effect is seen but with less cross-talk with the 10 mm spacing TL.

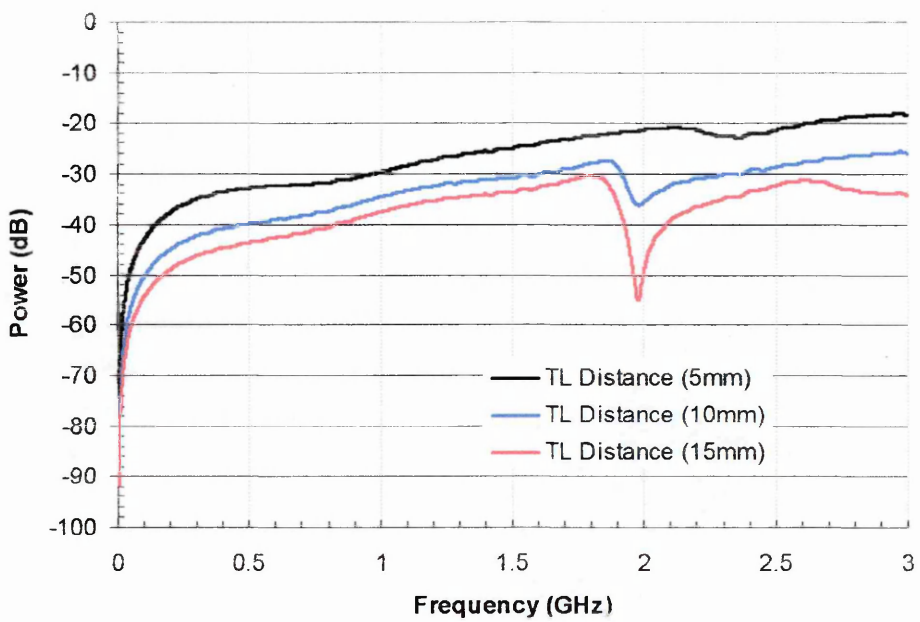

Figure 3.6. S_{21} cross-talk interference on adjacent 50Ω TL separated by distances of 5 mm, 7.5 mm and 10 mm on the PCB.

3.3.4 RF testing of individual FHA components

3.3.3.4 The effect of wirebond length on S_{21} signal insertion loss

3.3.3.4.1 Methods

As previously described, thermosonically induced ball-wedge wire bonds were used to connect FBAR samples to 50Ω TL on microwave PCBs. It is not at all easy to take into account the potentially deleterious electrical influence of wirebonds when designing 50Ω systems. So experiments were designed to assess the influence of wirebonds of different length on 50Ω design TL over the frequency range 0-3 GHz.

Test-structure PCBs with 50 Ω TL discontinuities of 5 mm, 10 mm, and 20 mm were bridged with the standard thermosoncially ball and wedged Au wire bonds of appropriate length, keeping the bond as close as possible to the edges of the discontinuities. A test PCB with unbroken continuous 50Ω TL was used as control.

Also, since wires were prone to failures (snapping or lifting from substrate), the effect of using two parallel wire bonds to introduce redundancy into the system was observed, the change in FBAR S_{21} signal response to single and double wire bond were also examined.

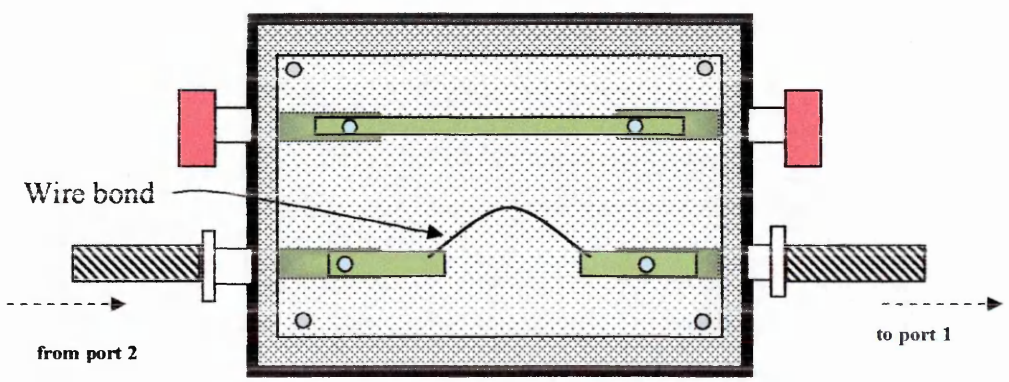

Figure 3.7. Shows an example of a discontinuity purposely written into the artwork of the PCB design to allow the broken 50 Ω TL to be bridged by wire bonds of various lengths. (not to scale)

3.3.3.4.2 Results

The results in Figure 3.8 (A) show that @ 3 GHz, unbroken continuous 50Ω transmission line showed ~ -3 dB attenuation, a 5 mm wire bond attenuated the signal by ~ - 6 dB, and a 10 mm wire bond attenuated the signal by ~ -10 dB, finally, the 20 mm wire on the 50 Ω TL line discontinuity increased signal attenuation to a value of ~ -12 dB.

Figure 3.8 (B) show that when employing an additional wire bond in parallel with the first wirebond to bridge the 10 mm gap, the result showed signal attenuation @ 3 GHz, for (i) Single wire bond = ~ -10 dB and for (ii) Double bond = ~ -6 dB.

This showed that the addition of an extra wirebond lowered the signal insertion loss. It was also useful practically, because it added some redundancy into the system, where loss of a single signal wire bond would not necessarily mean halting experimentation on the given sample. Knowing this fact would have been more useful before bonding the bulk of the devices, as it stood the samples only had a single bond for each of the four separate connections.

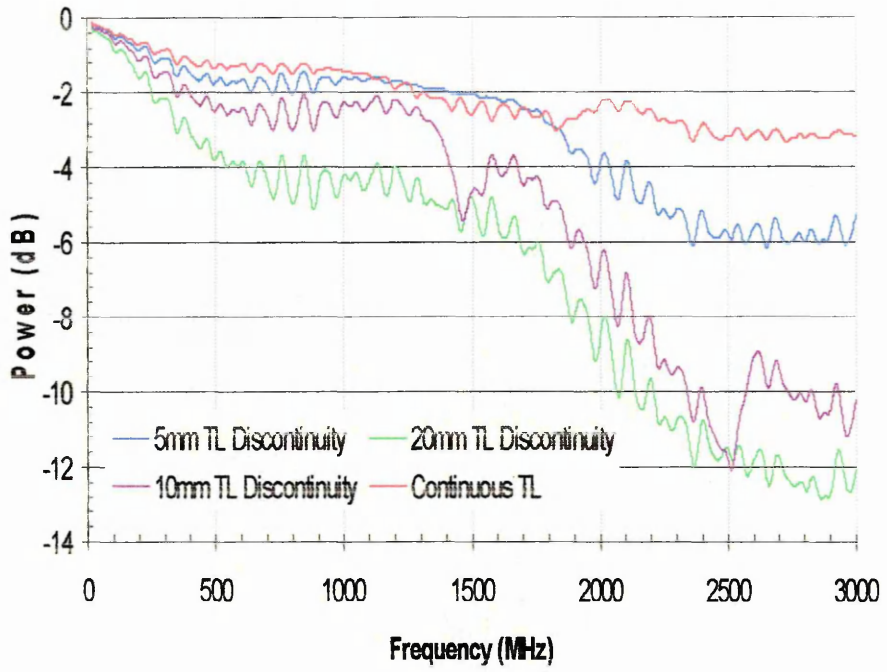

Figure 3.8. (A) S_{21} Frequency (Hz) vs. loss (dB) on wire bonds lengths bridging discontinuities of various lengths on 50Ω TL.

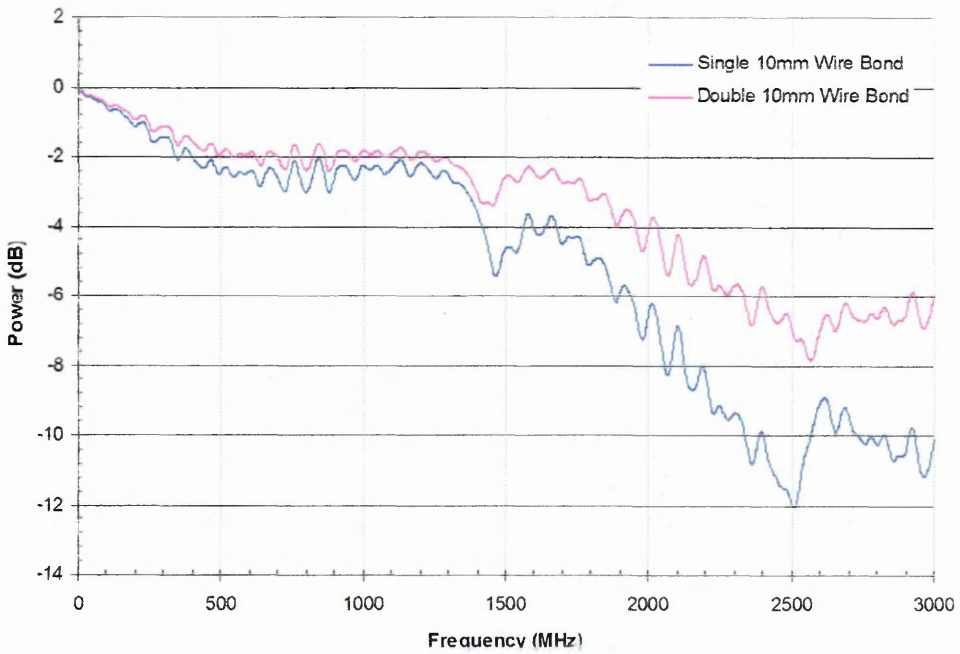

Figure 3.8 (B) S_{21} Frequency (Hz) vs. loss (dB) on 10 mm 50ΩTL discontinuity (i) A single 10 mm Au wire bond and (ii) Redundant double 10 mm Au wire bond.

3.3.3.5. The RF effects of different laminate PCB thickness

3.3.3.5.1 Methods

Two test thicknesses of board were examined both with 20 mm wire bond bridging discontinuities of the same length over the 50 Ω TL. S_{21} (0-3 GHz span) Transmitted power (dB) over frequency (MHz) XY scatter graphs were plotted. The board thickness giving the least amount of insertion loss was found experimentally this was done to compliment the thickness calculator within the APLAC modelling software which had been used during the PCB and TL design stages to estimate the best thickness of board to use for a 50Ω match.

3.3.3.5.2 Results

The Results in Figure 3.9 show that the responses of the boards were very similar up to ~1.4 GHz, above this electrical excitation frequency, increased RF signal attenuation occurred on the thinner (2.7 mm) board. The 2.7 mm board showed insertion loss of ~ -19 dB @ 3 GHz. The 3.4 mm board showed insertion loss of -12 dB @ 3 GHz

The thicker of the two boards (3.4 mm) gave the least loss, and was therefore the thickness ordered from the manufacturer since it was a closer 50Ω match. It was considered likely that FBARs with resonance frequencies greater than 1.4 GHz would be used at some point during the sensing tests.

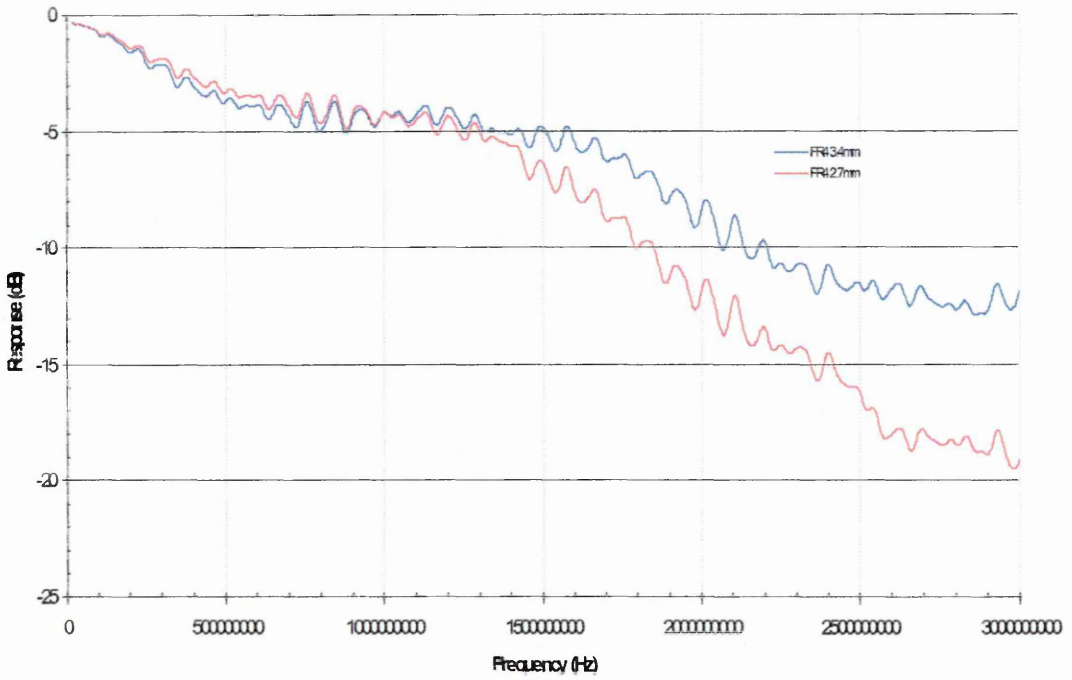

Figure 3.9. S_{21} Frequency (Hz) vs. loss (dB) on 20 mm Au wire bond with a 20 mm discontinuity on a 50Ω TL on PCBs made from FR4 laminate with thicknesses of 2.7 mm and 3.4 mm

3.3.5 Use of the memory normalisation functions of the network analyser.

Normalisations were performed as memory trace subtractions to standardise the starting state of the experiments to a value of 0 dB

1 The test was conducted over a specified frequency range and the response was recorded

2 The recorded response of (1) was saved into network analyser memory[56]

3 Subtract memory (1), (analyser performs vector subtraction on the memory data)

4 Re-Run test on same frequency range as (1) with subtracted memory

[56] stored the data trace in the active channel memory

Performing steps 1 to 3 should give rise to a sweep at stage 4 which gives a normalised response close to 0 dB over the range It was important to keep the initial sweep (1) at the same measurement range as the second sweep (4)

3.3.5.1 Effect of memory normalisation with high frequency 50 Ω flexible coaxial cable

3.3.5.1.1 Methods

Methods to reduce sources of noise in the testing apparatus were explored. The 50Ω high frequency coaxial cable (*See Figure* 3.10 (B)) was considered to be a convenient test structure on which to explore the memory normalisation functions of the NA.

Confirmation was needed at this mid-beta testing stage which unambiguously demonstrated that the VI↔NA command link and all of the associated instrumentation was performing as expected. This was so that later sensing experiments could be conducted with confidence in the RF instrumentation whilst the new software was controlling it.

Figure 3.10 (A) shows the experimental arrangement. Single coaxial cable (100 cm) was firmly attached via N type connectors to Port 1 and Port 2 of the NA. A full frequency (1601 points 0-3 GHz span) S_{21} VI ↔ NA command was sent, and the results were recorded. (ii) A second cable was linked to the first cable with an SMA adapter and the second cable was firmly connected to N adapter on port 2 of the network analyser. This gave a total length of 200 cm of coaxial cable. The S_{21} signal command was repeated. (iii) A "R411810" Radial -10 dB RF signal attenuator was fixed as a bridge between the two separate coaxial lines. The S_{21} signal command was then repeated.

The use of the attenuator as an independent reference source was implemented to confirm that whilst under the control of the software, the network analyser signal had been attenuated by -10 dB, and that the recorded result showed this unambiguously on a graph made up from the automated VI data collection processes. The actual VI recorded data is shown in figure 3.11 (|A) and (B) as an XY scatter plot.

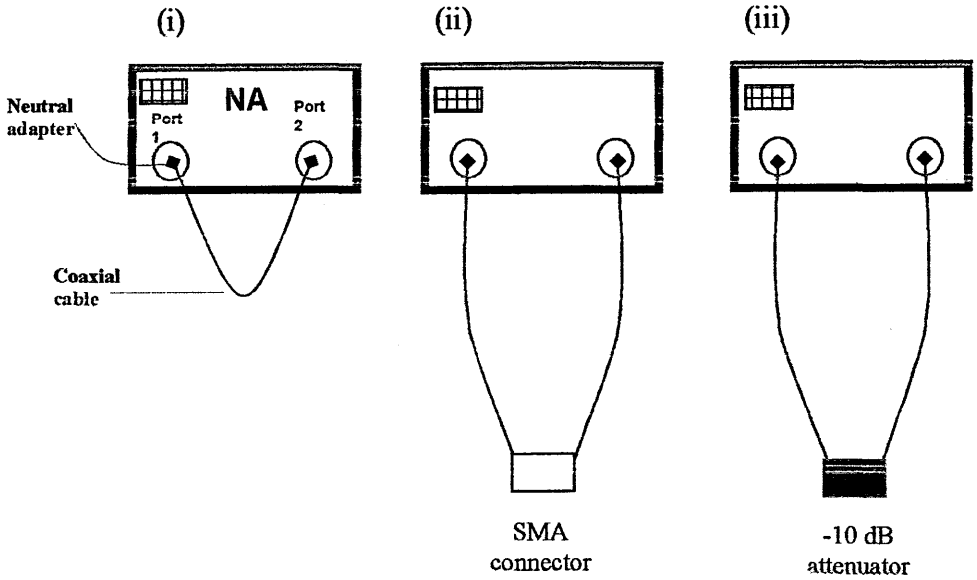

Figure 3.10 (A). Cable arrangements for S_{21} continuity confirmation on 50Ω Coaxial cable. (i) Single coaxial cable. (ii) Two coaxial cables connected with SMA connector. (iii) Two coaxial cables connected through -10 dB signal attenuator.

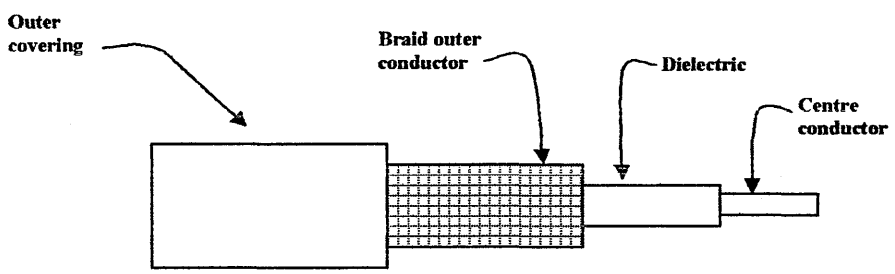

Figure 3.10 (B) Schematic of a typical high frequency coaxial cable.

Attenuation of the S_{21} signal through the coaxial cable with -10 dB signal attenuator was performed, and the attenuated signal was then compared against normalised coaxial responses that were stored in the active memory channel of the network analyser. This was done to confirm that the signal trace delivered the expected -10 dB result. The demonstration served two additional functions; (i) It confirmed the correct software coding of the memory normalisation functions in the VI and; (ii) It provided a convenient method of cancelling out spurious RF modes naturally generated by the FHA circuitry.

3.3.5.1.2 Results

The results in Figure 3.11 (A) show that @ 3 GHz, the signal attenuation in coaxial cable is;

- -1.25 dB attenuation for single cable (100 cm) and,
- -2.4 dB attenuation for two cables (200 cm) plus the SMA connector linking them together.

The results in Figure 3.11 (B) show that the memory subtraction functions can be used to *normalise* the output response data from the S_{21} transmission signal though a double length coaxial cable close to a value of 0 dB (~ $\pm$0.004 dB error range)

The results in figure 3.11 (C) Show traces for (i) Measured data, (ii) Normalised data and (iii) -10 dB attenuated data with normalisation from two 100 cm 50Ω coaxial cables. The signal range is 0-3 GHz span with 1601 data points. A result with a value of -9.8 dB was obtained over the entire range, with slight ($\pm$0.01 dB) signal response perturbation error increasing when the signal was operating above 2 GHz.

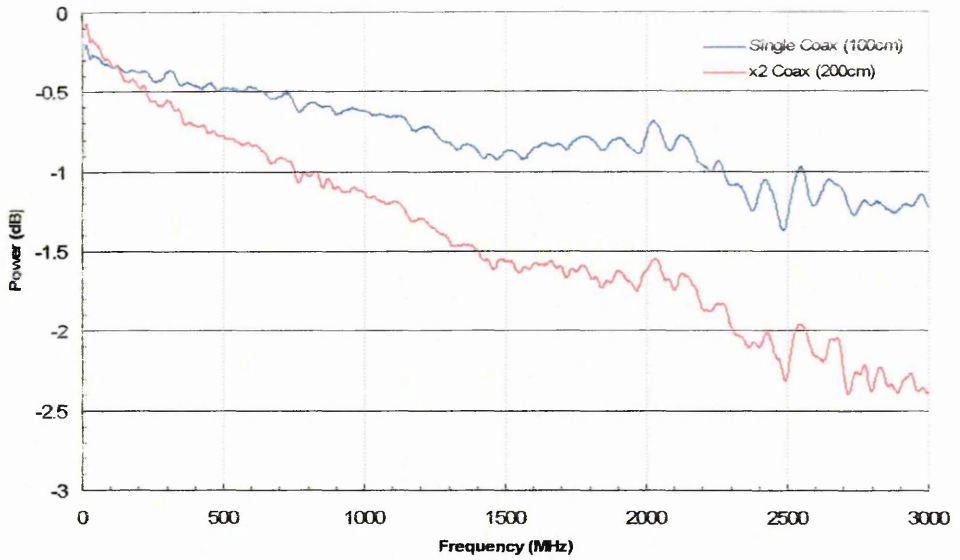

Figure 2.11(A) S_{21} Coaxial cable tests. S_{21} Frequency vs. loss on (i) Single coaxial cable (ii) Two coaxial cable lengths joined with SMA connector. (1601 points)

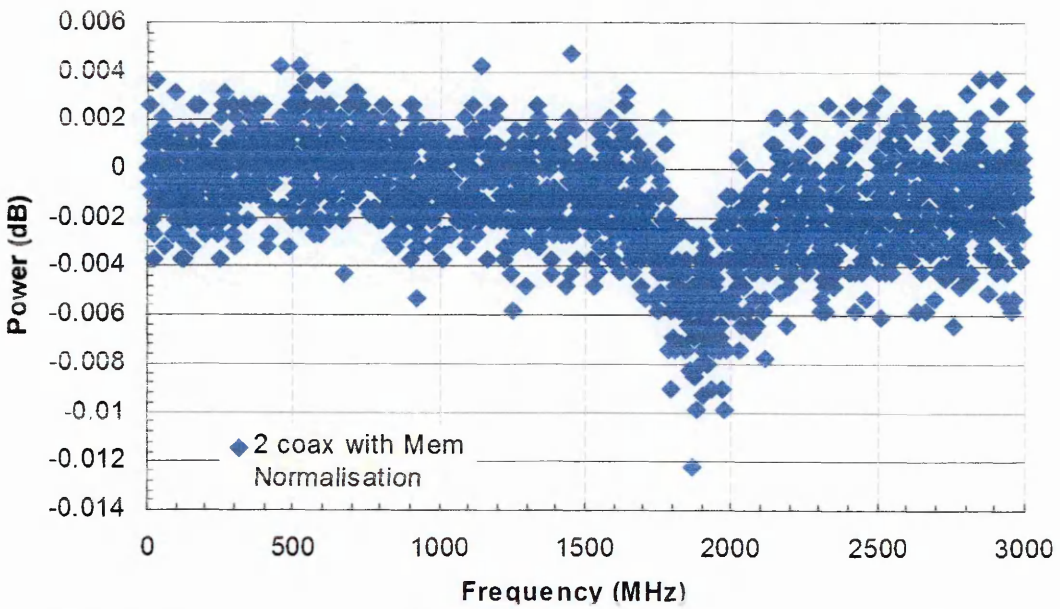

Figure 2.11 (B) S_{21} Signal normalisation on two coaxial cables joined with SMA connector (1601 data points)

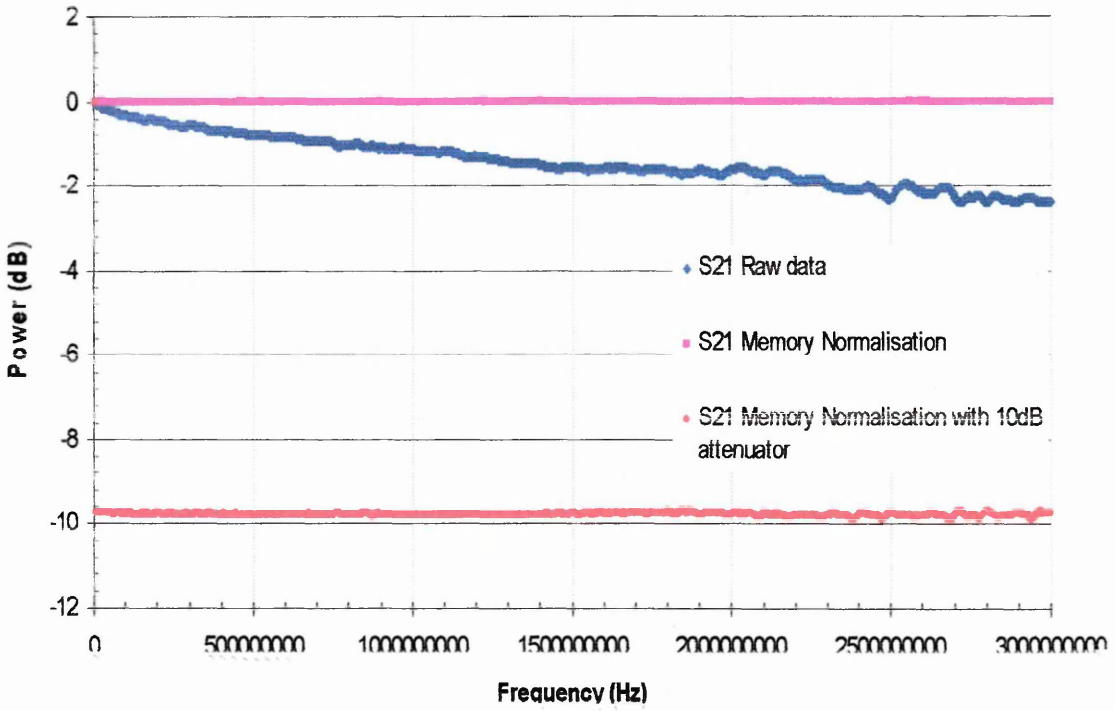

Figure 2.11(C). Signal attenuation on normalised memory trace for 50 Ω coaxial cable. (1601 points). S_{21} Frequency vs. loss on two coaxial cables joined with SMA connector (200 cm total length). (i) Measured (raw data) responses, (ii) Memory normalised response data and (iii) Memory normalised with -10 dB signal attenuation are shown.

3.3.5.2 FBAR normalisation using a de-embedding circuit in conjunction with the memory subtraction function.

3.3.5.2.1 Methods

Wartenberg (2003)[1] discusses that in the past, up to about the 1980's, prior to Coplanar waveguide ground-signal-ground (G-S-G) enabled testing, the characterisation of RF devices was performed in a test fixture. In the past, the test fixture's effects were removed by mathematically deembedding the effects of the fixture.

The FHA. PCB 50 Ω TL and associated cables and connectors could be considered as a test fixture since it possessed many similarities to those used in the past. It was relatively simple to attempt to cancel out RF recorded signal from the FHA leaving only the FBAR resonance signature on the output trace on the NA. To this end, a deembedding circuit was made (See Figure 3.12) that as far as possible approximated all of the components of the FHA circuit except for the piezoelectric resonating working area of the FBAR (replaced by 50Ω signal TL) in attempt to normalise RF response from all FHA associated circuitry with the use of memory subtractions.

The de-embedding circuit was loaded into FHA and interrogated over the frequency range 200 MHz to 2700 MHz with 1601 points per trace. The results were recorded and stored in memory. Sub GHz FBAR was interrogated over same frequency range with memory subtracted for deembedding circuit. Power (dB) over frequency (Hz) was plotted.

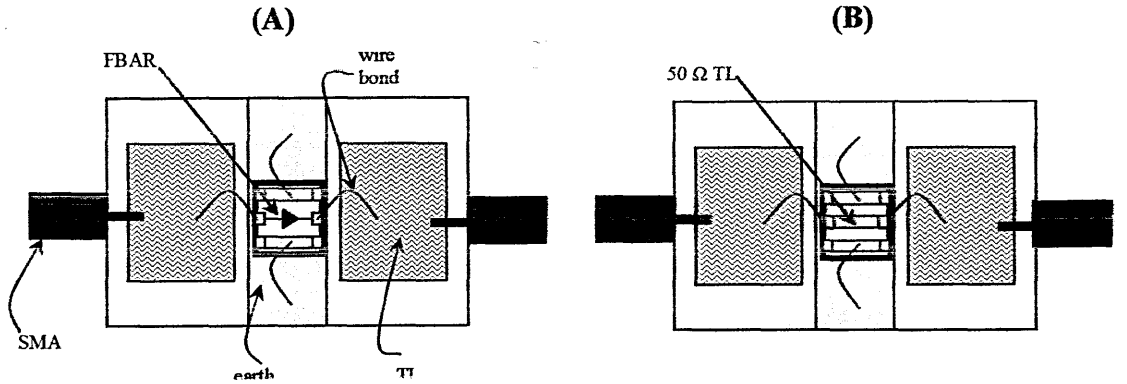

Figure 3.12. Schematic of the de-embedding circuitry created for FBAR normalisation (A) FBAR mounted die in FHA. (B) TL only mounted die in FHA.(de-embedding circuit)

3.3.5.2.2 Results

Results in Figure 3.13 show FBAR device 9 on PCB 1 S_{21} interrogated with 1601 points over measurement frequency range (200 MHz – 2.7 GHz). The primary (f_0) and overmode (f_n) harmonic resonances are visible on the XY scatter graph. It can be seen that there is a steep signal attenuation at operating frequencies greater than 1800 MHz. The device was then re-tested against the deembedding circuit result which was stored in memory in an attempt to normalised all of the FHA circuitry other than the piezoelectric slab and gold electrodes of the FBAR. The memory value of the de-embedding circuit was subtracted for the FBAR test. The responses of the FBAR at frequencies greater than 1800 MHz were not linear and were *not normalised* to ~ 0 dB over range as was anticipated. However, the important part of the trace i.e., the main resonance curves are normalised so that they begin and end at ~ 0 dB.

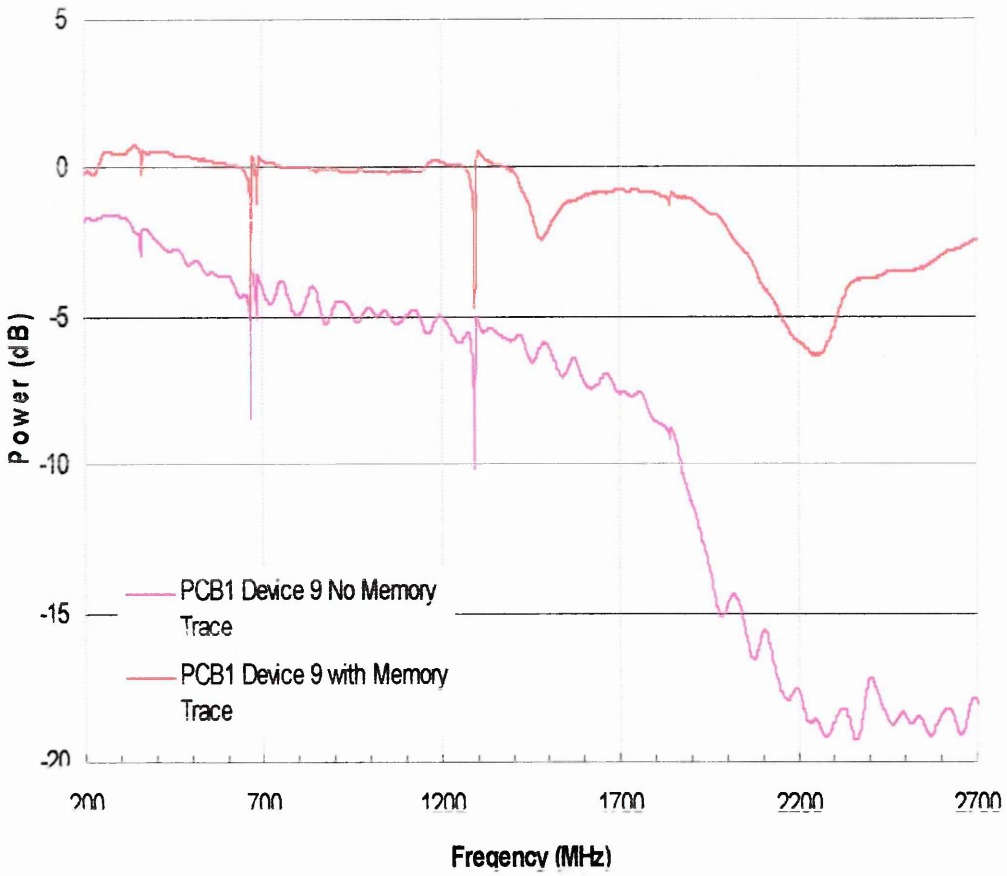

Figure 3.13. Responses of FBAR device 9 on PCB 1 (i) Without normalisation and (ii) FBAR responses normalised by memory subtraction against the deembedding circuit.

3.3.5.3 Reduction of random electronic noise output from the network analyser by manipulation of the intermediate frequency bandwidth settings.

Noises, i.e., perturbations in the generated signal can lead to uncertainty about the definitive lowest point on the resonance tip of the data trace, and this generates a range of indeterminacy directly reflecting the frequency error range measurement uncertainty, so methods were devised to minimise the effect of these non-desirable factors

The two main sources of interference on the resonance trace were from (i) FBAR the laterally generated resonances, but in the case of (ii) the network analyser, they were random electronic fluctuations at the so called noise-floor limits of the equipment. This section addresses only the electronic noise reductions from the network analyser since *at this stage*[57], there was no known method of reducing spurious resonance modes in FBAR.

Network analyser dynamic range is the difference between the analyser's maximum allowable input level and minimum measurable power. For a measurement to be valid, input signals must be within these boundaries. The dynamic range is affected by the following factors.

- Test port input power
- Test port noise floor
- Receiver crosstalk

Since the dynamic range is the difference between the analysers input level and its noise floor, changing the system intermediate frequency (IF) receiver bandwidth with tenfold reduction lowers the noise floor by 10 dB. For example, changing the IF bandwidth from 3 kHz to 300 Hz lowers the noise floor by about 10 dB. [3]

3.3.5.3.1 Methods

Procedures were explored for reducing noise, increasing sensor sensitivity and accuracy whilst paying attention to the time taken by the sensor system to respond, that is to complete and save the data from a single iteration and to initiate the next loop. The limit

[57] Later experiments did serendipitously reveal a method to suppress spurious modes of resonance in the FBAR (*See Figures* 4.15 and 4.16)

of this function being due, on the main, to the processing speed at which the NA can run its inbuilt functions on the specified settings.

The intermediate frequency bandwidth (IFBW) control settings of the NA were written into the VI as a set of GPIB commands and the functionality of these controls was now assessed. Observations on the effect of modifying IFBW settings on the output responses were made with focus on normalised data and its respective noise floor. The time to complete single iterations on the various IFBW settings were noted. The most appropriate IFBW value to use for FBAR sensor experiments later in the thesis were established from these tests.

Double length coaxial cable was connected to Port 1 and Port 2 of the NA with neutral N type connectors and joined together with a SMA connector. The S_{21} trace was obtained for full band frequency span (0-3 GHz) and the result was then normalised to obtain value approximately (0 db) across the entire measurement frequency range. This procedure was repeated with IFBW settings (3000 Hz, 1000 Hz 300 Hz and 100 Hz 10 Hz 30 Hz and 10 Hz) with 1601 data points. To assist in clarity, only the results from the 3000 Hz, 300 Hz and 10 Hz IFBW setting tests are shown

3.3.5.3.2 Results

The effect of decreasing the IFBW span on S_{21} responses of memory normalised coaxial cable is shown . The spread of data points around zero ($\pm$ 0.04 dB range) when the IFBW is set to 3 Hz span is due to the random electronic noise floor of the NA. Decreasing the IFBW bandwidth decreases random electronic noise, but increases the time taken to perform the iteration.

The results in figure 3.13 (A) shows IFBW dependent noise floor reduction for the normalised data and figure 3.13 (B) shows the time taken to perform single iteration grows exponentially when IFBW is constrained to below 300 Hz.

Figures 3.14 (A, B, C, D) show VI screen shots of consecutive interrogations of FBAR with increased IFBW resolution 3000 Hz, 1000 Hz, 100 Hz and 10 Hz. The frequency span was set at 1 MHz around the centre frequency (664 MHz) and 1601 data points were collected. The Q factor bandwidth was set at 0.5 dB. This - value is most often calculated from 3 dB bandwidth, but cutting the value to 0.5 dB for the purposes of this demonstration allowed for a much higher (x6) magnification at the tip of the resonance curve. The fitted polynomial is clearly visible as a red line running through the measured data which is shown as a white line.

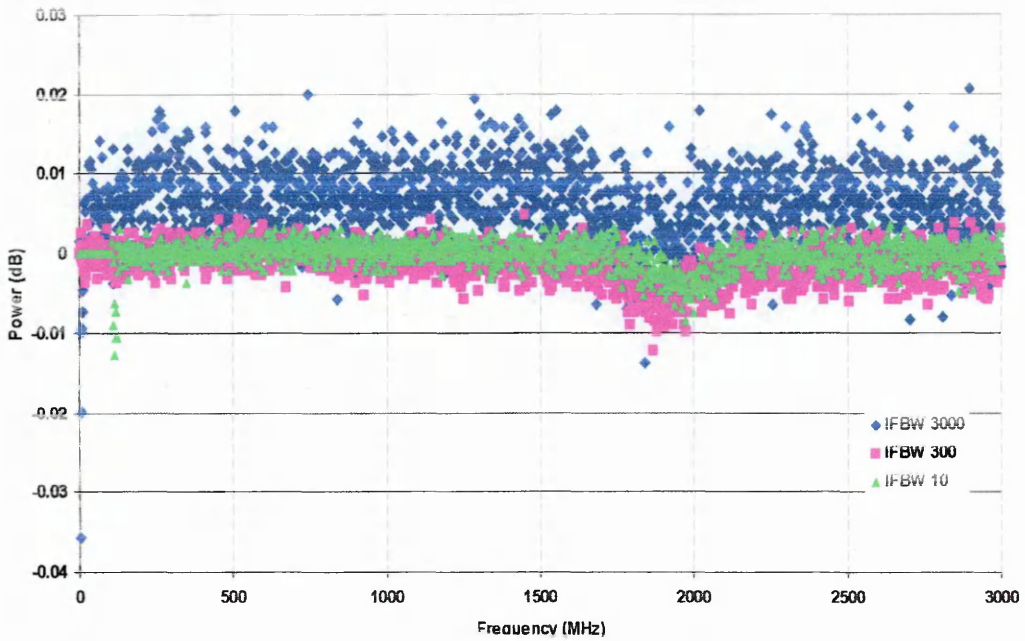

Figure 3.13 (A) Shows the effect of electronic noise floor reduction using IFBW settings S_{21} frequency (Hz) vs. loss (dB) on memory normalised 50Ω coaxial cable with IFBW set at 3 kHz, 300 Hz and 10 Hz. (1601 data points over 0-3 GHz measurement range)

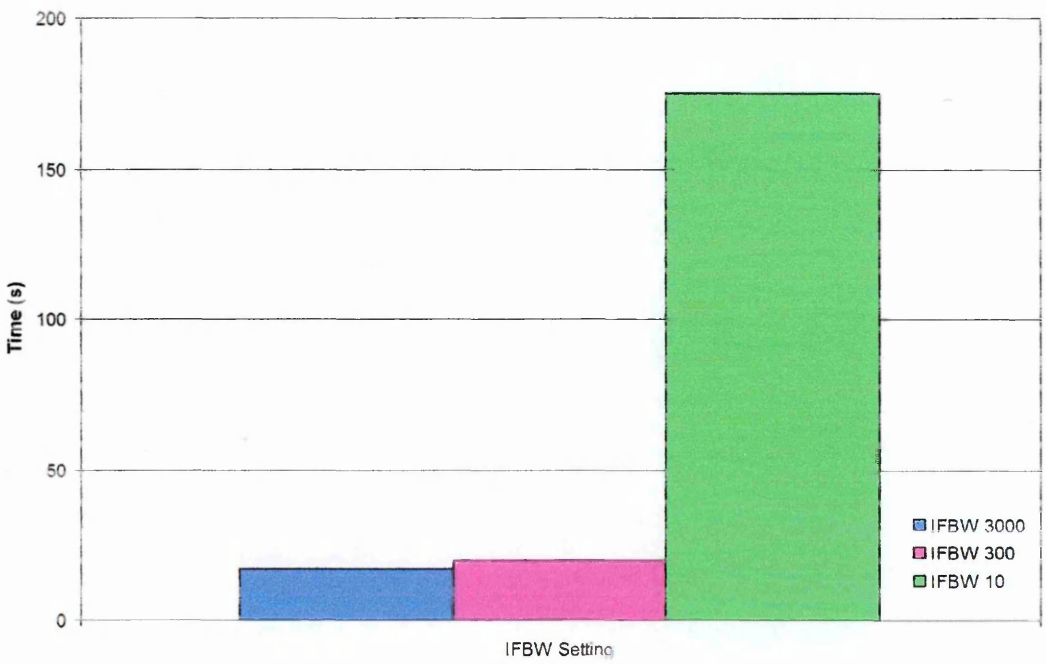

Figure 3.13 (B) Shows the total time taken to complete a single iteration at IFBW settings, 3000 Hz, 300 Hz and 10 Hz. (1601 points over 0-3 GHz measurement range)

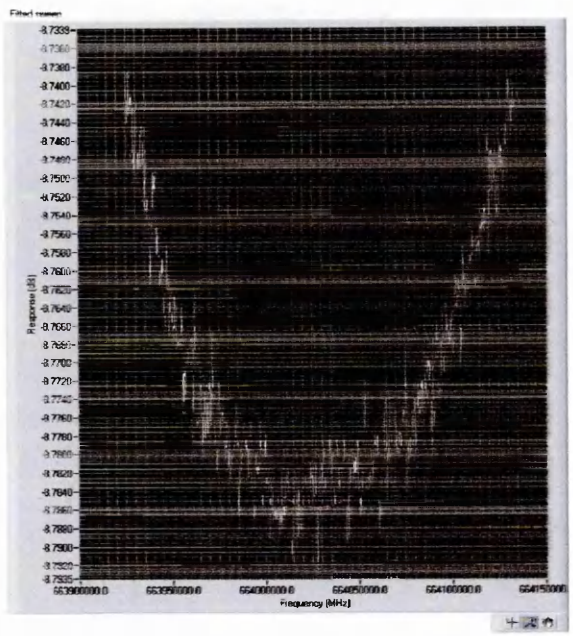

(A)

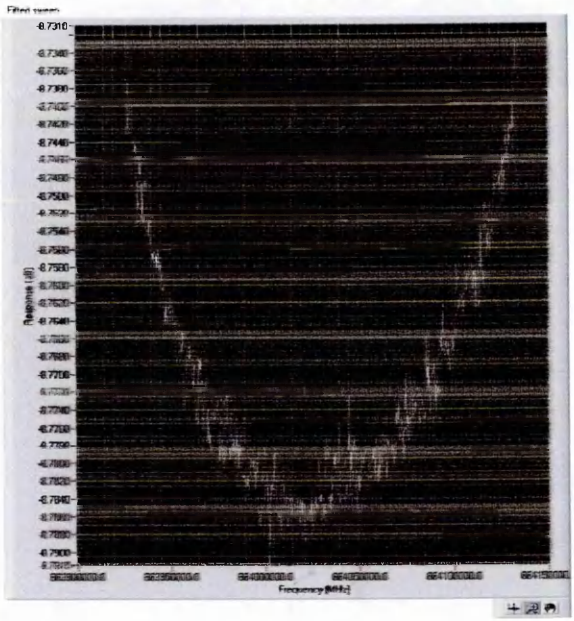

(B)

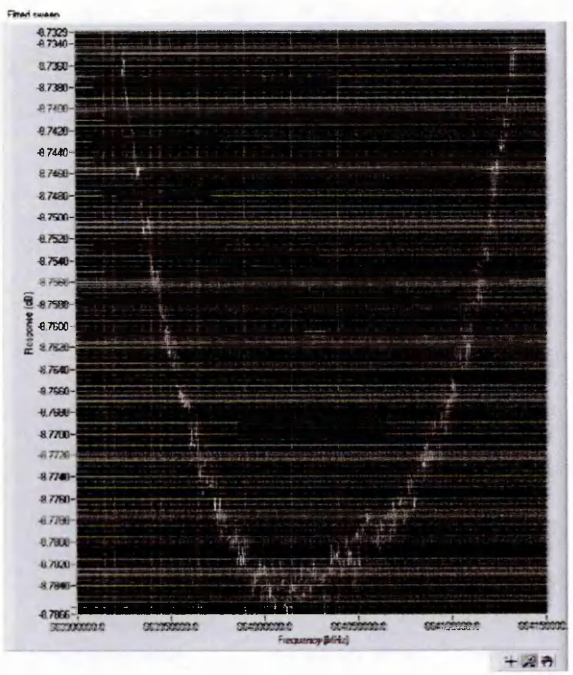

(C)

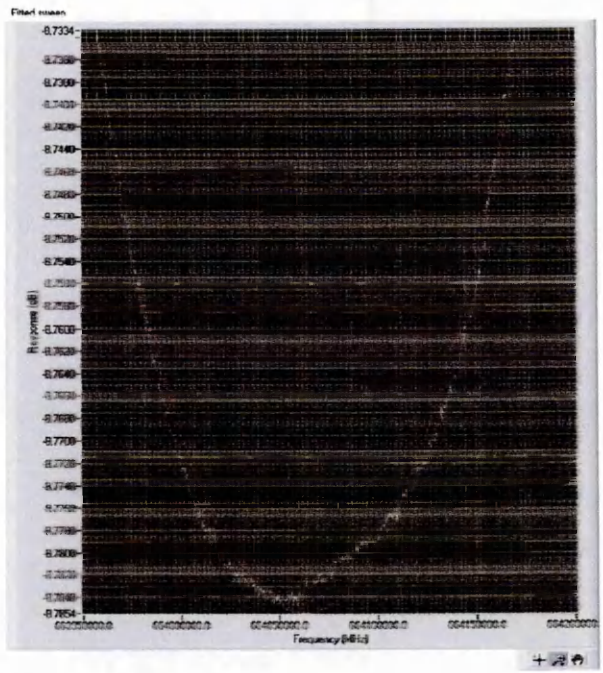

(D)

Figure 3.14 Actual real-time VI screenshots to show the effect of IFBW settings on random electronic noise from the NA. (A) IFBW 3000 Hz, (B) IFBW 1000 Hz, (C) IFBW 100 Hz, (D) IFBW 10 Hz

Erratum – Screen shot X axis reads MHz. this is actually Hz as recorded into the spread sheets.

3.4 Methodology for generating XY scatter graphs from the acquisition of many single resonance frequency values from the FBAR over time

The important definitions of the various measurement criterion are given in Appendix 3

3.4.1 Improving the recorded resolution of the FBAR iterative resonance frequencies (f_n) over time

It was desirable to develop FBAR output traces that were constructed from successive recorded iterations of f_n values since charts based upon these values could be used to easily follow changes in the S_{21} series resonance frequency of the FBAR in response to changes in measurand. These output traces should of course be as responsive as possible in accurately recording progressively smaller changes in FBAR S_{21} responses.

Higher resolution traces would allow for smaller changes in f_n to be successfully resolved and reported for subsequent analysis. this is in effect decreasing the quantisation or point to point (in Hz) spacing between the output data points. (*See Table* 2.1) It was also important to ensure that iterations and associated processing stages could be performed within acceptable time frames. ideally the responses should be in real-time. but there was always some unavoidable delay in the automated processing of the data between the VI and the NA

Increase in output trace resolution could be achieved by (i) increasing the number of raw data points collected over specified frequency bandwidth[58] or (ii) by constraining frequency bandwidth or by a combination of (i & ii). Practically. the limit for f_1 to f_2 bandwidth spacing distance on the FBAR S_{21} series resonance curve was 1 MHz[59] and the number of collected data points could be a set of integers from 3 to 1601[60]. Attempts to decrease the NA bandwidth span around centre frequency (f_c) to values below 1 MHz

[58] This is the specified measurement range in Hz

[59] This level of resolution was only possible on high quality FBAR devices

[60] Nearly all of the experiments used 1601 data points to calculate f_n over the bandwidth. but when an increase in time resolution was important (i.e. monitoring rapid changes), this number would be decreased from 1601 to 801 data points per measurement. This served to ~ halve the time taken to perform the iteration but point to point spacing would be doubled and therefore data resolution would be halved.

for a trace caused the R.01 software to fail to deliver a readable f_0 value. the bug suspected of causing this error was never successfully isolated

The results were available as a choice three possible output values:

(i) Frequency (f_0 in Hz on the X axis) at minimum S_{21} power transmission[61]

(ii) Minimum S_{21} transmitted power (dB on the Y axis)

(iii) Q-value[62] (Q bandwidth dB cut-off point setting specified by end-user).

The example calculation in Table 3.1 shows limit for point to point resolution over 1 MHz (f_1 to f_2) frequency bandwidth and the actual time determined from experiment to perform the specified iteration.

Table (3.1)
Theoretical minimum point to point spacing resolution (Hz) for measured frequency span of measurement range (f_1 to f_2 =1 MHz) from 26 to 1601 points per trace and the actual (from experiment) time taken to perform a single iteration with increasing number of measured data points over 1 MHz range.

NUMBER OF DATA POINTS	POINT TO POINT RESOLUTION (Hz) FOR *MEASURED* FBAR OUTPUT DATA OVER 1 MHz (f_1 TO f_2) SPAN	APPROXIMATE TIME (S) TO PERFORM SINGLE ITERATION with IFBW set at 300 Hz
26	38461	1.2
101	9901	2.0
201	4977	3.0
401	2494	5.0
801	1248	9.8
1601	624	18.0

3.4.1.1 Increasing the frequency resolution of the FBAR response output trace

The most sensitive arrangement. i.e.. the one with the highest resolution. would be the maximum allowable number of data points (1601) over the narrowest frequency range allowed (1 MHz). and with the IFBW set[63] to 300 Hz.

[61] Changes in this parameter were the major interrogation parameter throughout the thesis.
[62] In this case Q is defined as (f_2-f_1/f_0) where Q bandwidth (not frequency bandwidth) can be any value from 3 dB to 0.01 dB. *(See equation* 1.7)

These experiments were performed to additionally confirm that the VI↔NA interface was working properly at high data resolutions where there would be a greater memory load (in bytes) on the computer memory when processing and recording the results delivered to it by the network analyser. It was useful also to be able to actually visualise the effect of decreasing f_1 to f_2 span distance on the output responses by showing the effect of this on XY scatter charts and also to see the effect that reducing the network analyser electronic noise floor was having on the responses.

3.4.1.2 Constraining the frequency span around the centre frequency

3.4.1.2.1 Methods

For the FBAR to function appropriately as a sensor, the result was dependent on the development and maintenance of a stable and responsive output trace over time. This was generated from VI-controlled automated sweeps of the FBAR by the network analyser to give a XY scatter plot of many raw-measured and/or mathematically processed f_0 values over time. The delay at the network analyser in the numerical processing of the FBAR data was the limiting factor for real-time graphical representation of the f_0 values on the VI because it had to wait until the sweep was completed before it could request the data for display. The changes recorded on this iterative f_0 output were the basis of visualising and making analysis on the measurand measurement event on the FBAR.

To increase the absolute resolution of the output traces, it was desirable to make the minimum point to point spacing resolution for f_0 as narrow as possible. Here, it is shown how the resolution and hence dynamic range of the results are improved by increasing the data point density by constraining the f_1 to f_2 frequency span i.e., the measurement range using the highest possible number (1601) of data points allowed by the network analyser.

3.4.1.2.2 Results

The six graphs below Figure 3.15 (A-F) are the S_{21} frequency traces recorded from a FBAR device 9 on PCB 4 in the FHA when the temperature was held constant.

[63] IFBW settings below this value took too long to process, increasing the chances of a software failure.

(A) FBAR was interrogated over 0-3 GHz frequency bandwidth for a single iteration This gave an overview of the device over range. Primary and harmonic resonance overmodes are visible. a chart at this bandwidth could not be used for sensing since there would be multiple f_0 values and this impossible for the software to compute a realistic baseline response. *See Figure* 3.15 (A)

(B) This figure shows a constrained (10 MHz) band sweep of the primary mode it reveals a spurious mode of resonance within the main body of the resonance curve. A trace afflicted by such modes would not be used for sensing due to the increased potential for error in determining an f_0 data point.[64] *See Figure* 3.15 (B)

(C) This figure shows the effect of decreasing frequency range (i.e., the bandwidths) of the trace from f_1-f_2 = 10 MHz, 2 MHz, and finally 1 MHz on first harmonic overmode of the FBAR whilst keeping conditions stable, f_0 = ~664 MHz. Number of data points collected for each bandwidth trace is 1601. *See Figure* 3.15 (C)

(D) This figure shows a solitary 1 MHz bandwidth span trace of 1601 data points, and highlights the effect the auto-scaling function serving to increase the X and Y axis resolution on the graph. Close visual inspection of this trace reveals that it is beginning to show signs of noise at its resonance tip. This interference had been previously occluded from the previous less resolved traces although it was of course still present. The range indicated by "↔" denotes the level of indeterminacy of measured f_0 on the trace (estimated by eye) and a polynomial fitting was required to discover the most likely position of f_0 during any given iteration. It is noted that the visible asymmetry in the resonance curve, apparent when recorded over a wider frequency range is less apparent when the trace is constrained over a narrower frequency range. *See Figure* 3.15 (D)

[64] Although such a trace could probably be used for a sensing measurement as long as the change in resonance frequency during sensing was a lot greater (>>) than the error in f_0 determination that resulted from the presence of spurious modes, in reality the potential for error may also increase from cross-couplings of the spurious modes and it was considered unwise to use them at this stage.

(E) This figure shows a close-look over a narrow frequency range of a typical FBAR resonance tip as a screen shot from the GUI. Only the ~100 data points of the 1601 in the span are shown. These 100 points make up the apex/zenith of the curve. This magnification function was made available through Q factor bandwidth dB cut-off function (40 KHz visible frequency range (X axis)) ($8.8x10^{-3}$ dB visible noise range (Y axis)). Note this is a highly magnified and stylised screen shot chart taken directly from the GUI and it is used here only to show the effect of the polynomial smoothing function on the actual measured signal from the FBAR. A chart such as this would not be used analytically for sensing purposes. *See Figure* 3.15 (E)

(F) The span is seen to be centred around the second overmode for (i) 50 MHz and (ii) 2 MHz. with 50 iterations in the sequence, the measured frequency minimum (f_0) points are shown over time (s) along with their equivalent polynomial fits in identical format. A discrepancy of roughly 40 kHz between the means of the measured data and the fitted data is visible in the chart. *See Figure* 3.15 (F) The quantisation level (f_0 data point to data point minimum resolved frequency change per iteration) between the collected data points is shown to be:

50 MHz Span (measured data) = 31. 360 kHz
2 MHz Span (measured data) = 1. 152 kHz
(calculated data points are indicated in both cases)

The method of data presentation in Figure 3.15 (F) is important because it shows how a dynamic baseline response from successive or iterative f_0 data points is constructed with the Y scale indicating the actual resonance frequency (f_0 in Hz) and the X scale representing time (seconds (s)). This is the main type of graph used for analysis in the rest of the thesis. When an additional parameter is to be tracked, e.g., temperature, along with f_0 and time, an additional Y axis will be incorporated in to the chart to represent that parameter .

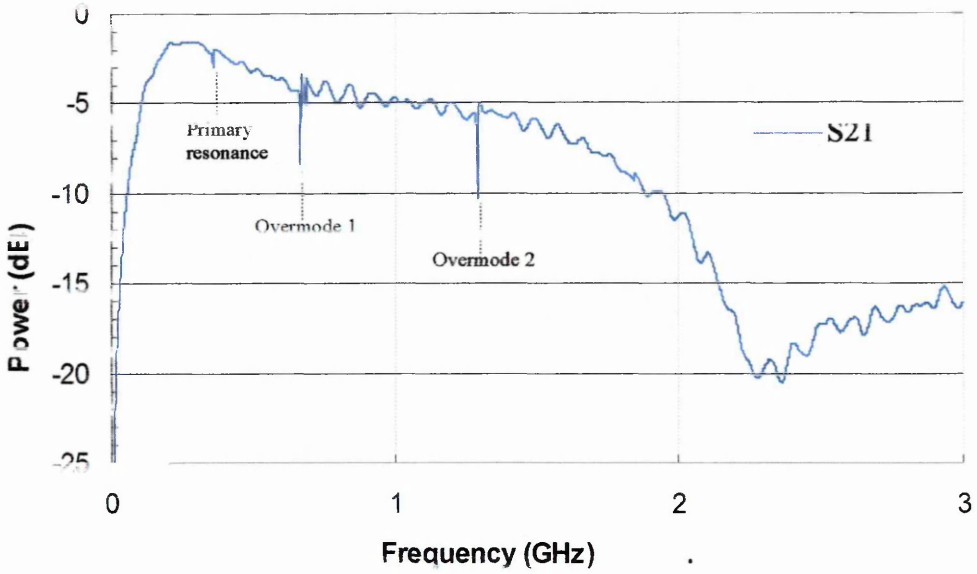

Figure 2.15 (A) Shows full band (0-3 GHz) frequency sweep of FBAR Device 9 on PCB 4. Primary (f_o). and overmode harmonic resonances (f_n.). of the device are indicated. Note the f_n. overmodes are of a better quality[65] for sensing purposes than f_0

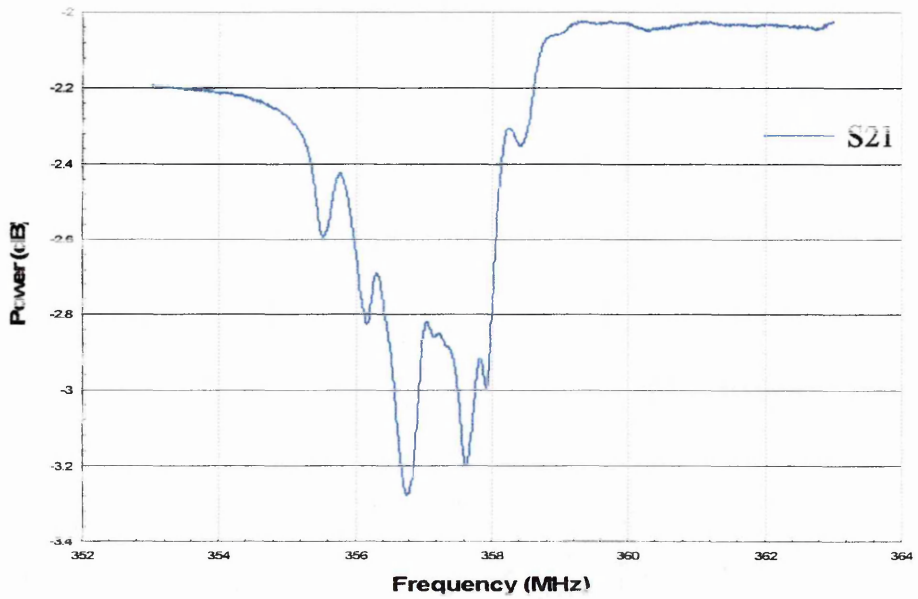

Figure 2.15 (B) 10 MHz span sweep centred on primary resonance (f_o). Spurious modes are clearly visible in the resonance curve. FBAR 9 on PCB 4.

[65] More negative power transmission. Less power transmission at resonance on a S_{21} sweep is desirable.

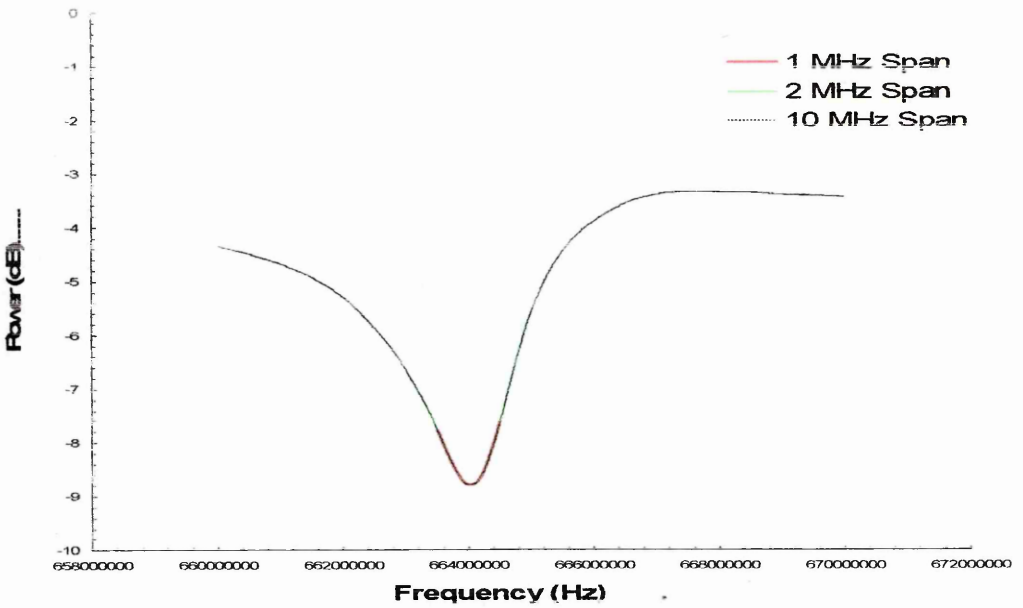

Figure 3.15 (C) Shows 3 traces for FBAR 9 on PCB 4. 1 MHz, 2 MHz, and 10 MHz spans are centred on the first overmode. (1601 points)

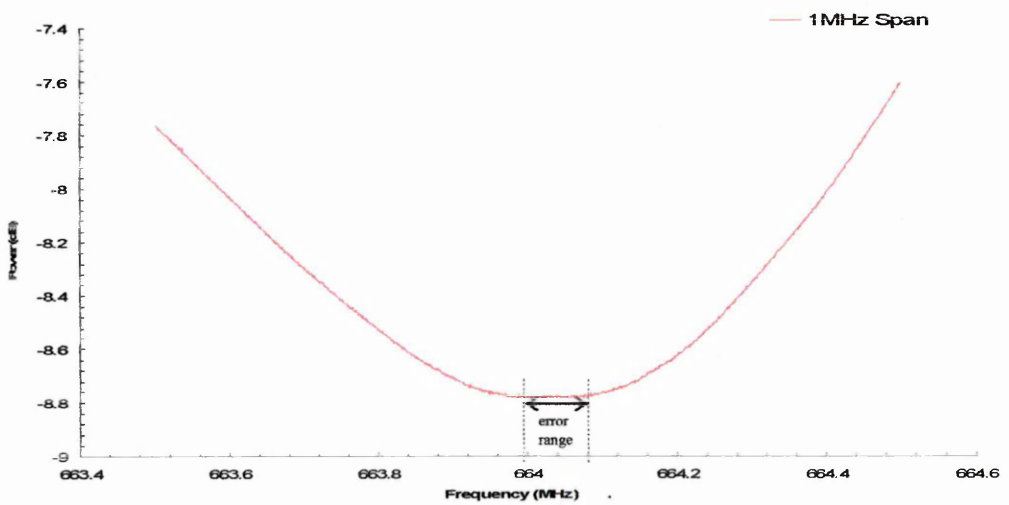

Figure 3.15 (D) Shows (1 MHz) bandwidth frequency span exclusively on the first overmode of FBAR 9 PCB on 4.(1601 points).

The dotted lines flanking the double headed black arrow give the estimated (by eye) range of measured f_0 indeterminacy (~ 80 KHz). This figure also highlights the effective increased *perceived* resolution of the chart due to auto scaling functions when the f_1 to f_2 bandwidths are reduced. Close inspection reveals some noise in the trace that, although present in Figure 3.15 C, is not visible on traces where the bandwidth is wider.

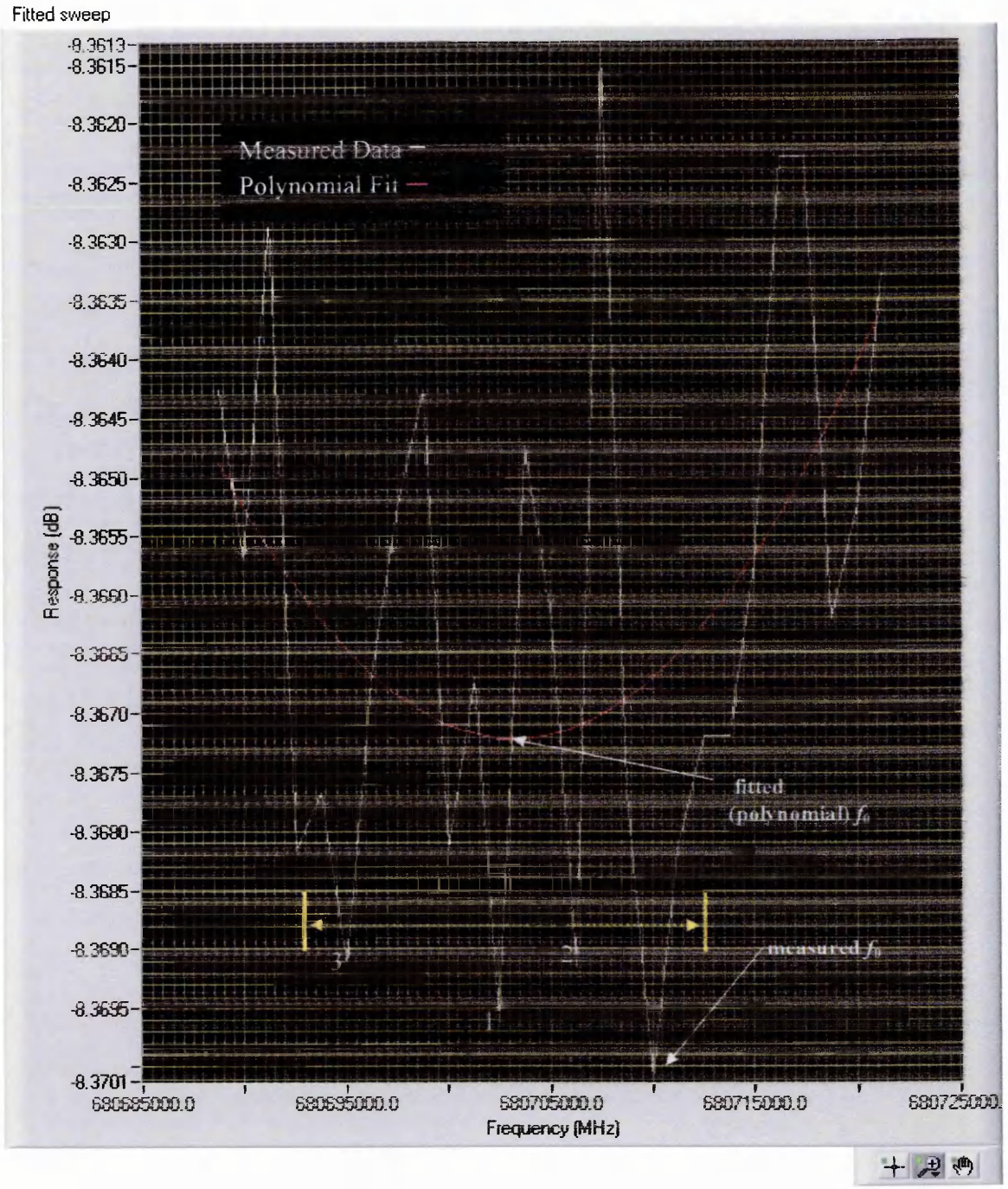

Figure 3.15 (E) Shows a highly focussed VI-GUI screen trace to highlight the actual polynomial trace running through a measured resonance tip (approximately 100 data points) of a typical sub GHz FBAR (X span = 40 kHz) (Y span = 0.0088 dB). The dynamic nature of the response meant that points marked "1" or "2" could readily become the f_0 data point on the *next* iteration. It was less likely, but possible that point marked "3" could become the f_0 recorded data point. In this way the measured f_0 indeterminacy error range was produced. The approximate range of indeterminacy for the *next* iteration in this case is marked by a double headed yellow dashed arrow on the chart.

Erratum – screen trace X axis should read Hz, not MHz as is stated on the graphic.

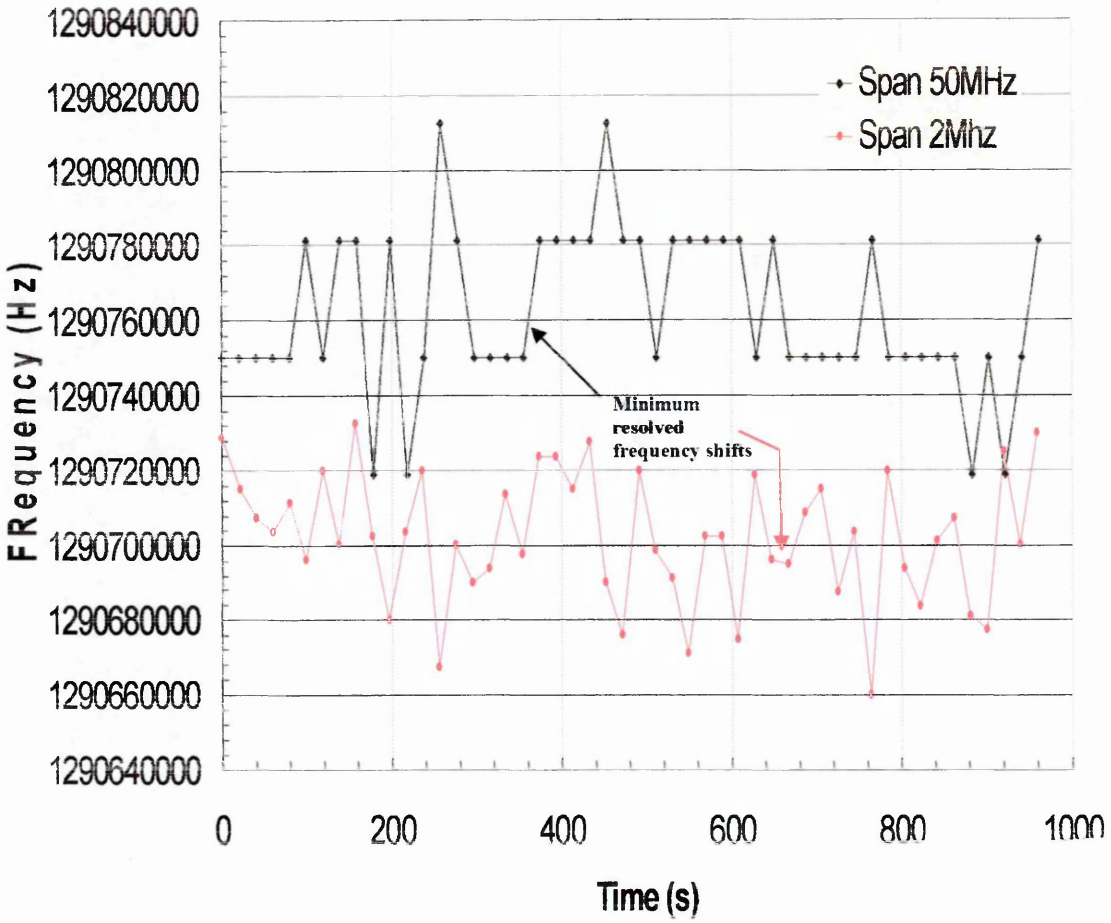

Figure 3.15 (F) Shows 50 iterations recorded over t = ~ 950 seconds, on the 1.29 GHz overmode of FBAR Device 9 on PCB 4 with temperature stabilised. ($\pm$ 0.1^{O}C)

The measured S_{21} resonance frequency is reported by the VI for each iteration in Hz. The resonance frequency centre set-point is ~1290 MHz. Measurement range is set at 50 MHz and 2 MHz. The minimum resolved frequency changes per iteration are indicated by black and red arrows for 50 MHz and 2 MHz ranges respectively.

Figure 3.15 (F) highlights the effective increase in dynamic range of the trace over time, and thus its useable sensitivity in analysis, which is obtained by decreasing the bandwidth frequency of the measurement range on the network analyser around the set-centre frequency (f_c) (1290 MHz) from 50 MHz to 2 MHz. The minimum quantisation or point to point spacing on the X axis, between the f_0 data points for both 50 MHz and 2 MHz measurement ranges is indicated on the chart with arrows, showing a minimum of ~31.4 kHz quantisation when (f_1 - f_2 = ~ 50 MHz), and ~1.2 kHz when (f_1 - f_2 = 2 MHz). The

time (in seconds) is given for the interval between iterations, it is presented on the X scale rather than the iteration number, since the iteration number can easily be obtained by counting the visible data points sequentially from left to right but it would be difficult to convert iteration number to a time value without consulting a table holding all of the pertinent settings used in any given test arrangement.

3.4.1.3 Increasing the number of collected data points over a fixed frequency span to increase effective resolution of the FBAR iterative output trace.

3.4.1.3.1 Methods

The f_0 value derived from S_{21} data from a typical wirebonded FBAR sample collected over a set of 50 iterations, under similar controlled environmental conditions is shown. The number of data points per iteration set was increased from a minimum of 26 data points to a maximum of 1601 data points per test whilst the measurement frequency bandwidth range (f_1-f_2) was kept constant at 5 MHz.

The Q bandwidth for these tests was set at 2 dB cut-off. Six XY scatter graphs are shown for the successive increases in data points collected per iteration set, 26, 101, 201, 401, 801 and 1601 data points are shown. At this stage the polynomial calculation on the measured data was also introduced into the iterative output response traces. This was done to ascertain the effectiveness of reducing noise in the measured FBAR response trace with polynomial fitting of the measured data and hence there are two f_0 values given per iteration, (i) raw-measured and (ii) polynomial-fitted, each clearly distinguished in the XY scatter graphs. (*See Figures* 3.16 (A-F))

3.4.1.3.2 Results

The results in figure 3.16 (A-F) show six responses for an unperturbed typical wirebonded FBAR held at a constant temperature.($\pm$0.1°C) The measured data point number per iteration is increased over same frequency span bandwidth (5 MHz). Both S_{21} measured and the 2nd order polynomial fitted data for FBAR frequency are shown giving two effective f_0 traces over time per chart. The measured data is appears to become progressively less quantised (i.e., point to point spacing is reduced between the collected data points) as the number of collected data points per iteration is increased from 26

points to 1601 points, this response trend is in agreement with the theoretical values given in Table 3.1. Note also the increase in time taken to perform the iterations, from 60s with 26 data points per iteration to 900s for 1601 points per iteration for the same number (50) of iterations.

Gaining an increase in the sensitivity of the FBAR response by increasing the number of data points collected per iteration is therefore tempered with a subsequent loss of temporal resolution in the response, since each iteration takes longer to process and record. This fact could become important when undertaking real sensing experiments especially if changes in a measurand event are rapid and reversible. It would also become problematic if the experiments involved assessment of affinity type binding kinetics, so the choice of time or frequency resolution needs to be considered against the type of experiment that is being investigated.

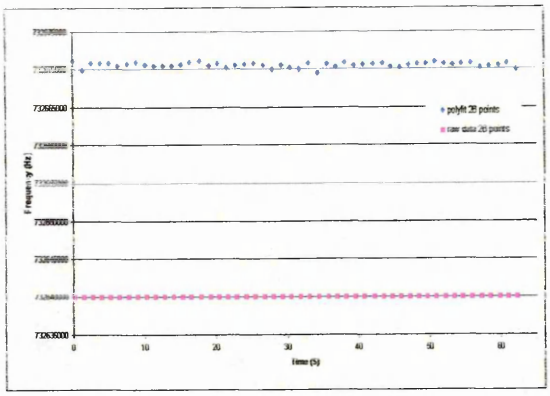

(A) 26 Data points

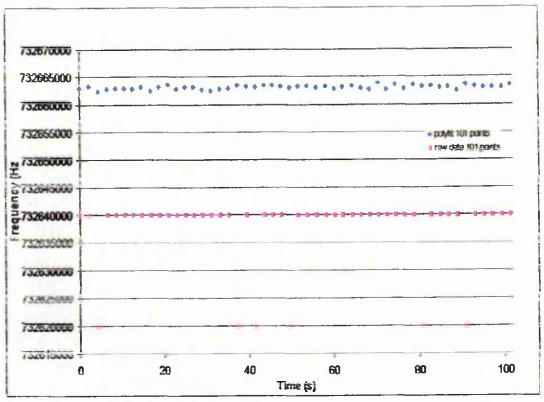

(B) 101 Data points

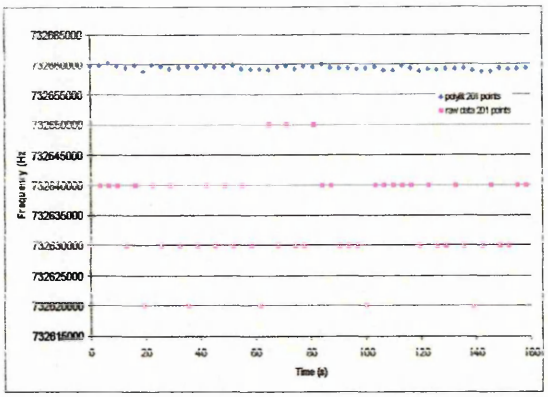

(C) 201 Data points

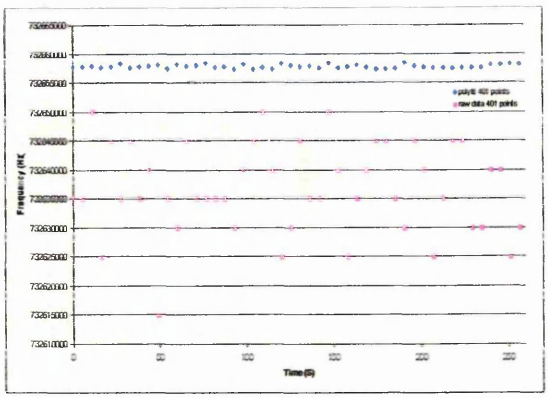

(D) 401 Data points

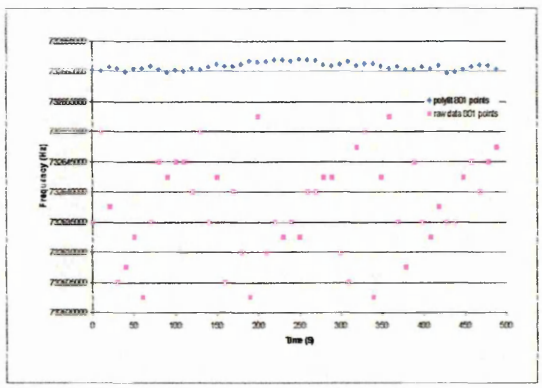

(E) 801 Data points

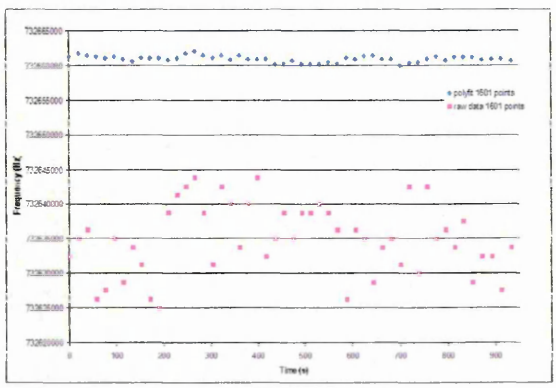

(F) 1601 Data points

Figure 3.16 FBAR S_{21} frequency output response to increases in data point density per iteration under similar environmental conditions over 50 iterations. f_1-f_0 = 5 MHz IFBW was set at 300 Hz. Measured and polynomial fitted data are shown. Each data point on the charts represents f_0 for each iteration. Note the increase in time taken to perform the 50 iterations as the collected data points per iteration is increased. 50 iterations for 26 data points is ~ 60 seconds, and for 1601 points, ~ 900 seconds.

3.4.1.4 Improving the correlation between measured data and polynomial fitted data.

3.4.1.4.1 Methods

It was noted that there was a frequency difference of ~ 30 kHz between the average reported f_0 values for the measured data and the fitted data on the iterative FBAR response output charts when the Q bandwidth was calculated from the 3 dB bandwidth. This is most easily visualised in chart where 26 data points are used to calculate the measured and polynomial f_0 values. (*See Figure* 3.16 (A)) A method was devised to reduce this discrepancy by bringing the polynomial fitted f_0 reported value closer to the measured average f_0 value since the discrepancy caused some minor concern about making f_0 determinations for the polynomial fit. The actual reason behind the discrepancy between the two values is shown in the GUI screen-shot Figure 3.15 (E).

There was a function specially written into the new software that allowed the Q factor bandwidth calculation to be made from any point on the resonance curve from the standard 3 dB Q bandwidth down to 0.01 dB. By decreasing the Q bandwidth, it was found that the correlation in Hz between the reported values of the fitted polynomial data and the measured data improved. This experiment also served to show that the Q factor calculator function of the beta tested R.01 software was working properly. The effect of manually choosing the Q bandwidth cut off value is represented pictorially below in figure 3.17

As previously stated in Chapter 1, (Equation 1.7), for the purposes of this thesis the Q factor is described by the following simplified term;

$$Q = \frac{f_2 - f_1}{f_0} \qquad \text{(Eq 1.7)}$$

The f_2-f_1 value is usually taken at 3 dB , the so called 3 dB bandwidth but was not always taken at this bandwidth in this thesis. (Q bandwidth is stated where appropriate)

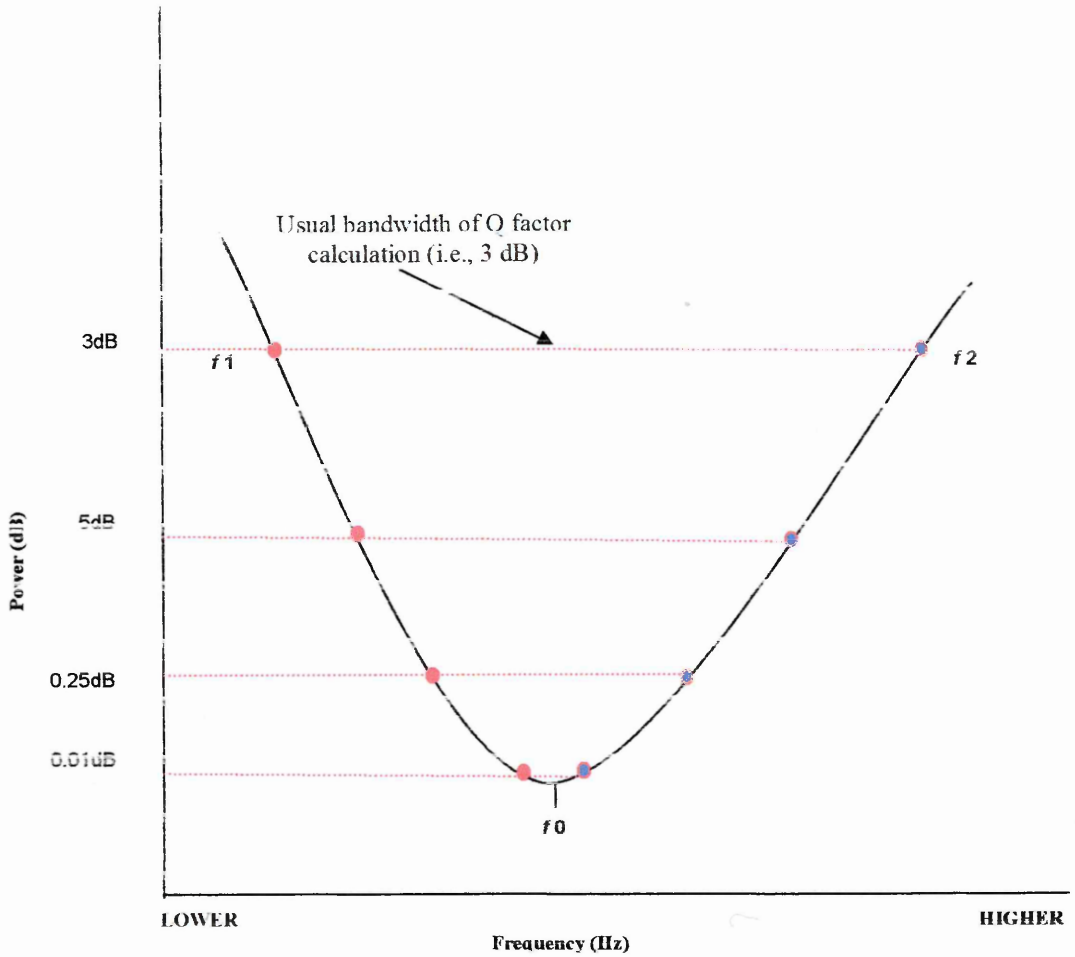

Figure 3.17 Shows the effect of manually setting the Q bandwidth. Careful observation shows that the slight asymmetry which is normally present in the S_{21} resonance curve at 3 dB and above is reduced as the bandwidth is decreased.(not to scale)

3.4.1.4.2 Results

The results in Figure 3.18 (A-F) show six graphs for Q factor bandwidth dB cut off points, (+3 dB, +2 dB, +1 dB, +0.5 dB, +0.25 dB +0.01 dB) on the Y axis aboove the measured f_0 transmission minimum at any given iteration. Where the bandwidth is set at +3 dB above the f_0 value, the discrepancy or mismatch between f_0 for raw (measured) and fitted (polynomial processed) data is shown to be ~ 150 kHz, and the discrepancy decreases markedly to ~25 kHz when the Q bandwidth is set to 2 dB, this improvement continues as the fitted data is seen to fall directly into the median of the measured data when the Q factor bandwidth dB cut off is 1 dB and below.

Some smoothing function appears to be lost at high resolutions (e.g., where the Q factor bandwidth is set to 0.01), This may be attributed to the higher resolution and hence the increased importance of the inflections at the tip of the resonance curve. Higher order polynomial functions are likely required to smooth this data, but were not implemented due to time constraints.

The reported "Q" factor is shown to increase and correlate almost perfectly with the power law: ($1/\sqrt{-2}$ = -0.7071.) when lowering the Q bandwidth target from +3 dB to +0.01 dB (i.e., bringing f_1 and f_2 measurement values closer to the resonance tip minima f_0 as shown in Figure 3.19.

This reported value is of course an artefact of the dB cut off function processing and in no way is it implied that there is a real improvement in the quality factor of the device.

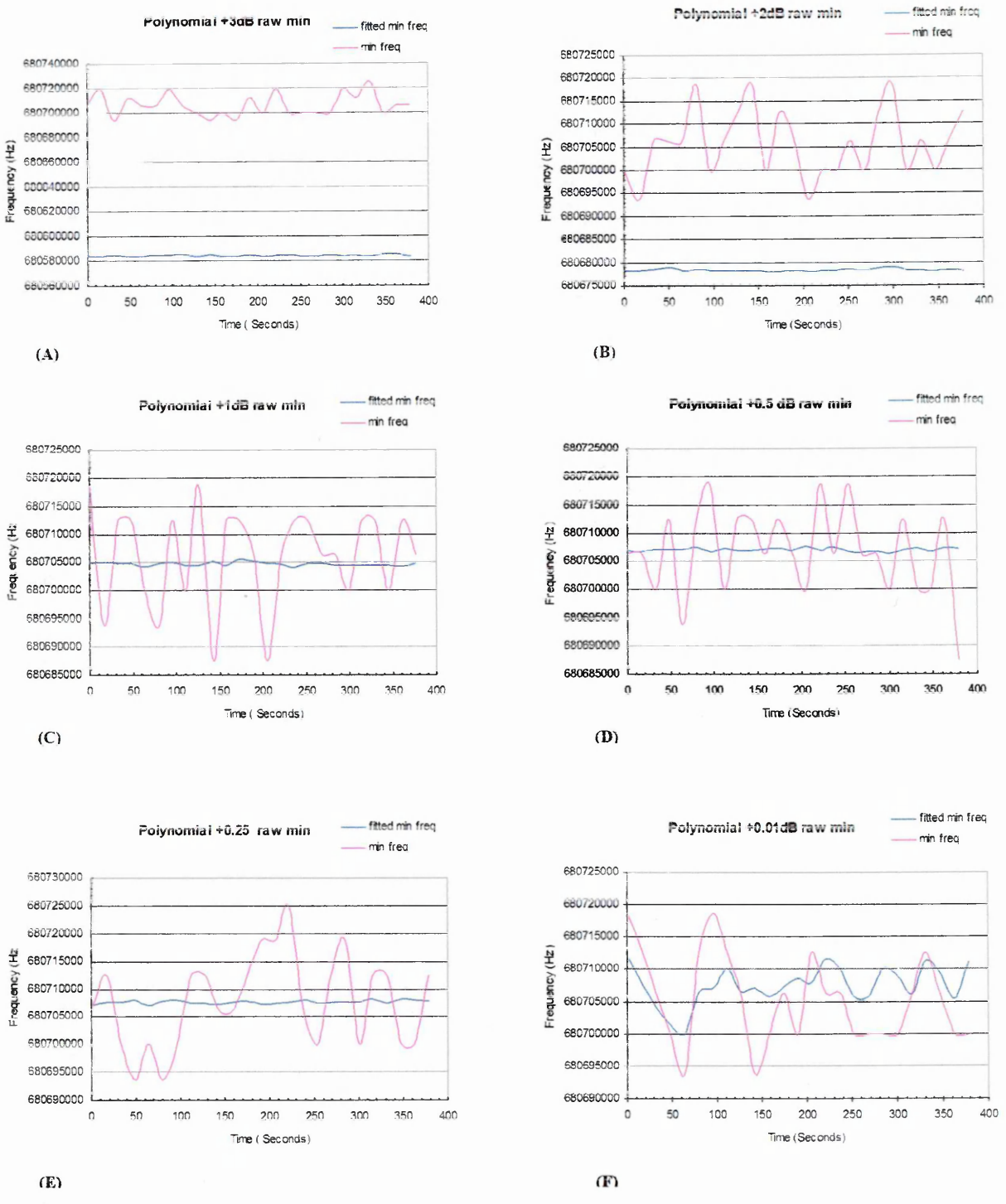

Figure 3.18 (A-F) Shows the decrease in discrepancy between measured f_0 and polynomial fitted f_0 iterative responses over time by decreasing the Q bandwidth dB cut off point. Range 3 dB to 0.01 dB.

3.4.1.5 Investigating relationship between changes in temperature and changes in FBAR output responses. (Temperature experiments 1A and 1B)

This section introduces the concept of following changes in f_0 over time as Δf induced by deliberate environmental changes in the immediate vicinity of the FBAR isolated within the FHA.

Pinkett *et al* (2002)[72] have shown empirically that the resonant frequency of an FBAR will change with temperature. Temperature change was considered to be an ideal initial variable to use for monitoring the baseline response of an FBAR as it is relatively simple to stabilise, alter and measure. Temperature also has the additional advantage of being free from any form of interferent. Stabilising the temperature would reveal the stability of the baseline, since the conditions in the FHA would be reasonably constant. Incrementally smaller shifts in temperature, may reveal the practical resolution limits of baseline response and assist in understanding the best method of approach to sensitise the baseline whilst to obtaining a set of responses as close to real-time as possible.

3.4.1.5.1 Methods

The FHA was placed on top of the digitally controlled Peltier heater and a good thermal connection to the base of the FHA and the Peltier heater was made with the addition of heat transfer paste between the two.

For temperature experiment 1A, the system was tested for ability to run over time periods (>14 hours overnight) to ensure that responses were stable and did not halt due to communication or memory errors, and further, to show if there was significant ageing of the FBAR[66] when under prolonged interrogation from the network analyser. Both thermocouples were periodically checked to ensure good correlation.. In this case, the FHA was not temperature controlled, as it was considered unwise to leave a heater apparatus powered up without human supervision overnight, so the device was left under

[66] Prolonged interrogation of the FBAR may have revealed significant S_{21} power changes or frequency jumps as the device aged and the piezoelectric became less efficient in converting electrical energy to mechanical energy.. However this was not the case in the time frames considered here.

the influence of ambient Laboratory room temperature for the tests where responses over extended time periods were under investigation. Experiment 1B shows the response of the FBAR to increase in Peltier heater temperature of ~ 0.5^{O}C over about 4000 seconds.

For clarity, the temperature data saved to the VI from the DAQ thermocouple in the same run is presented on a secondary Y axis. The temperature scale is *reversed* for easier interpretation of the data, to show the correlation between temperature fluctuations and FBAR Δf recorded as successive iterations.

The correlation between the manually read FHA "internal" thermocouple and the VI DAQ automated external thermocouple was periodically checked and always found to be in good agreement. (within < 0.1 ^{O}C difference)

For completeness and also to introduce the concept, alternative output charts in the form of S_{21} transmitted power and Q factor are shown along with the more commonly presented S_{21} series resonant frequency change.

Settings were;
Centre Frequency: 700 MHz Span Frequency: 50 MHz
Points in sweep: 1601
IF Bandwidth 300 Hz

3.4.1.5.2 Results

Figures 3.19 (A) and 3.19 (D) show a *good agreement* between FBAR fitted frequency response to temperature change for both the short temperature rising (1 hour) (↑0.5^{O}C) and extended time temperature fall (0.5 day) (↓1.1^{O}C)

FBAR fitted frequency response was calculated as ~6.5 kHz per 1.0 ^{O}C independent of whether the temperature was rising or falling and independent of rate of temperature change. Result in 3.19 (A) also serves to demonstrate the capability of the VI↔NI GBIP interface to run for extended time frames (>0.5 day)[67]. There is no significant

[67] This was one of the occasions that the software did not crash. A number of overnight tests were performed before one ran without a problem.

deterioration in FBAR performance due to ageing when continually probed in these extended time frames.

Other output formats for temperature experiment (1A) were graphed.
(i) Fitted Power (dB) (*See Figure* 3.19 (B))
(ii) Reported 0.5 dB bandwidth Q -value (*See Figure* 3.19 (C))

Results show (i) Fitted S_{21} minimum power transmission (dB) and (ii) reported 0.5 dB Q value response to temperature (^{O}C) was similar to the response shape for fitted frequency.

Experiment (1B) also examined the FBAR S_{21} transmitted power responses along with the reported Q factor, a similar shape response following temperature to fitted frequency was seen. Results not shown.

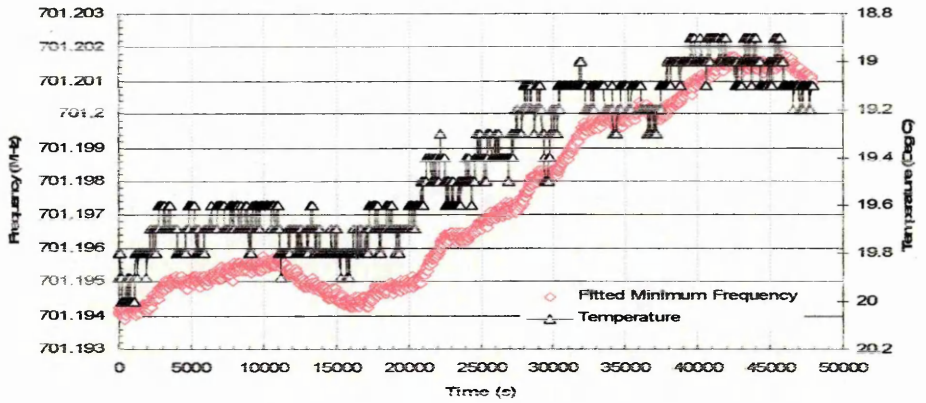

Figure 3.19 (A) Fitted S_{21} series resonance frequency and temperature over time

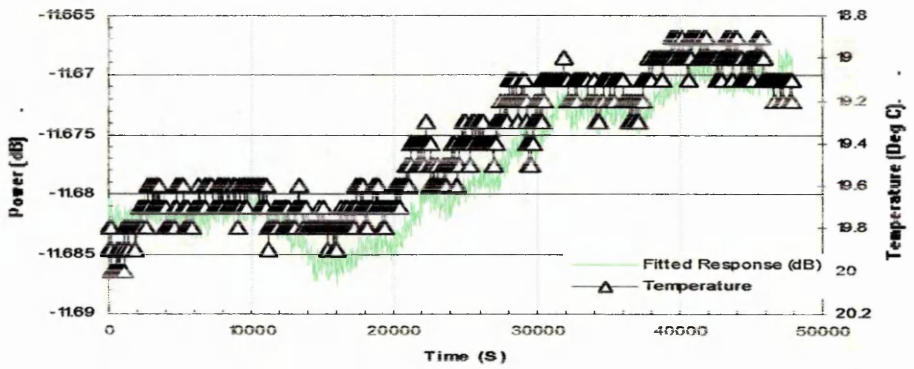

Figure 3.19 (B) S_{21} Fitted S_{21} transmitted power (dB) and temperature /time

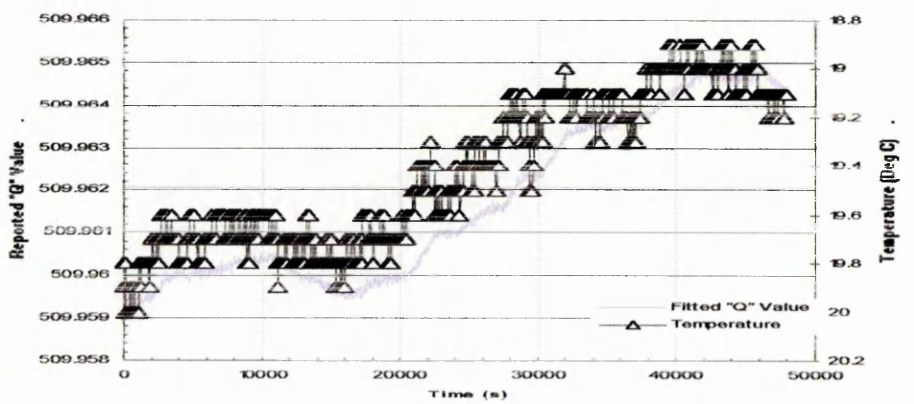

Figure 3.19 (C) Reported 0.5 dB Q value- and temperature/time

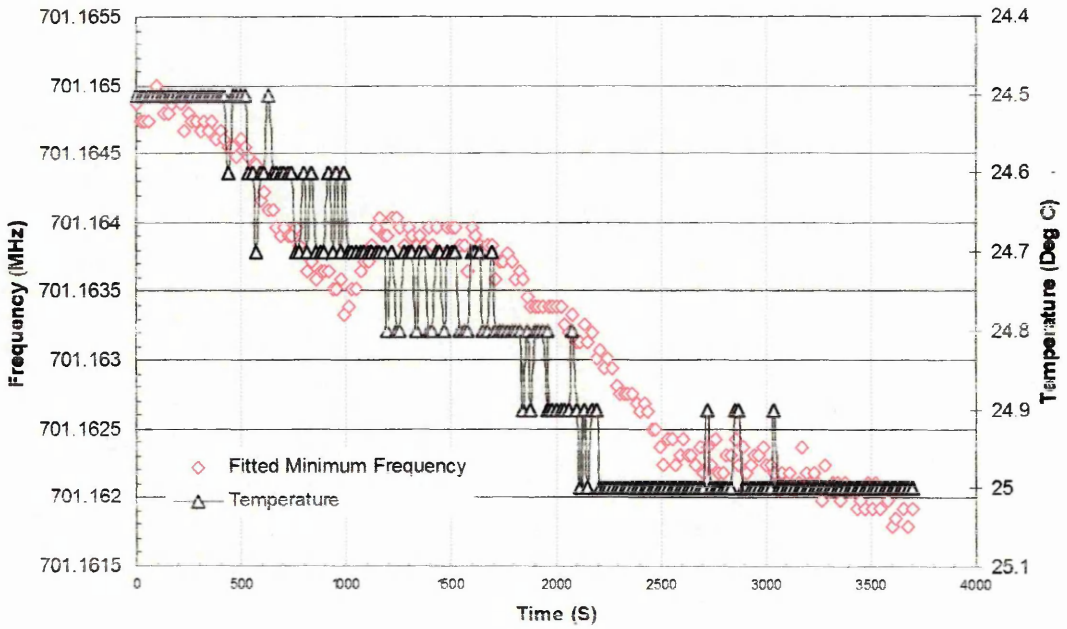

Figure 3.19 (D) Fitted S_{21} frequency and temperature/time.

3.4.1.6 Determination of the sensitivity of FBAR S_{21} output responses to temperature fluctuations. (Temperature experiments 2A to 2F)

3.4.1.6.1 Methods

The bandwidth was set to 10 MHz for Experiment 2D, 2E and to 2 MHz for Experiment 2A, 2B, 2C, 2F. This had the effect of increasing the measured data trace resolution. IFBW was set at 300 Hz to minimise Y axis error whilst completing the iteration loop within acceptable time frame (<1 minute).

Temperature was stabilised in experiments 2A and 2B to discover the baseline response of the FBAR in stable conditions and deliberately changed in experiments 2C, 2D, 2E, 2F to examine the magnitude of frequency change per unit measurand, which in this case was degrees centigrade. Fitted data is also shown, but the error range of this was not determined at this stage of the experiment.

Table (3.2) The settings used for temperature experiments 2A to 2F.

	2A	2B	2C	2D	2E	2F
Centre Frequency (MHz)	680	680	680	680	680	680
Span Frequency (MHz)	2	2	2	2	10	10
Points in Sweep	1601	1601	1601	1601	1601	1601
IFBW	1000	300	30	10	1000	1000
Iterations	100	100	100	100	50	50
Total Run Time (S)	370	460	1700	4500	800	800

3.4.1.6.2 Results

Figure 3.20 (A) Temperature stabilised 29^{O}C ($\Delta<\pm0.1$ ^{O}C). Measured frequency response is stable.

(Error range $\pm$12 KHz)

Run time = ~ 380s

Figure 3.20 (B) Temperature stabilised 29^{O}C ($\Delta<\pm0.1$ ^{O}C). Response as (A) but measured data is more tightly clustered. (Error range $\pm$10 KHz)

Run time = ~ 460s

Figure 3.20 (C) Temperature Range (~Δ 8.5 ^{O}C).

Measured frequency response (~0.1 MHz = 11.7 KHz per 1^{O}C)

Run time = ~ 1700s

The obvious temperature error seen in 3.20 (C) is due to a procedural error which was the accidental removal of the external thermocouple from the test arrangement before the termination of the experiment.

Figure 3.20 (D) Temperature Range (~Δ 0.3 ^{O}C)

Measured frequency response (~16 KHz = ~53.3 KHz per 1^{O}C)

Power response is also shown (*See Figure* 3.22 (A))

Q factor response is also shown (*See Figure* 3.22 (B))

Run time = ~ 4500s.

Figure 3.20 (E) Temperature Range (~Δ 5.5^{O}C)

Measured Baseline Shift (~80 KHz = 14.5 KHz per 1^{O}C)

Run Time = ~ 800s

Figure 3.20 (F) Temperature Range (~Δ 3.0 ^{O}C)

Measured Baseline Shift (~40 KHz = 13.3 KHz per 1^{O}C)

Run time = ~ 800s

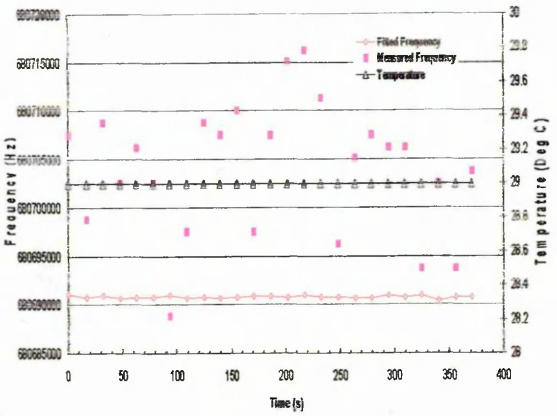

(A)

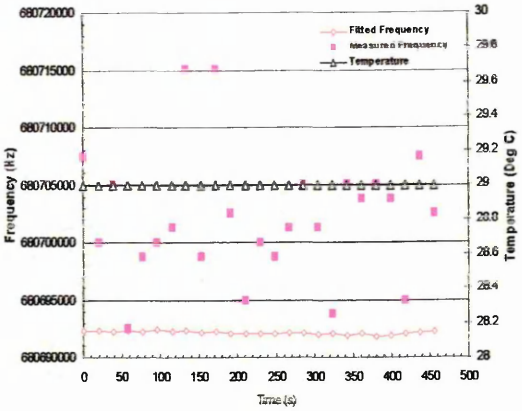

(B)

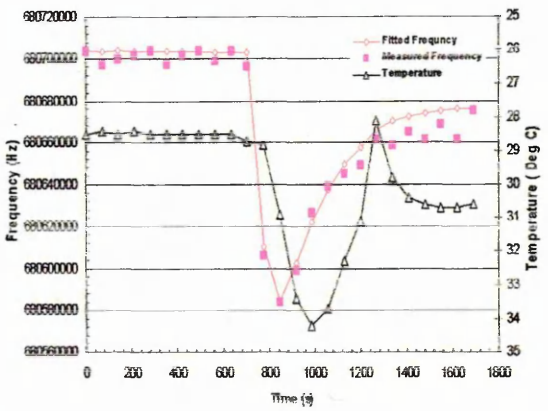

(C)

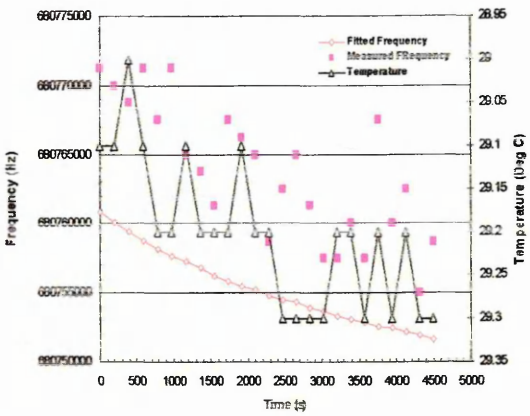

(D)

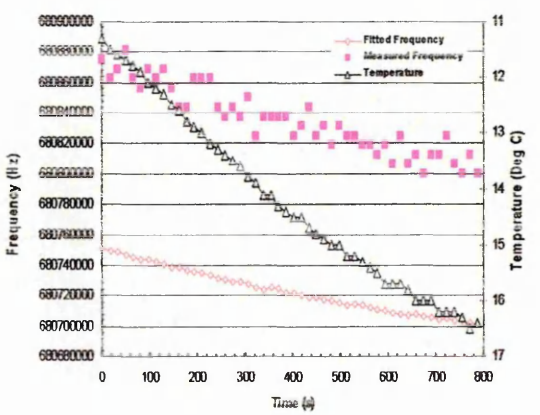

(E)

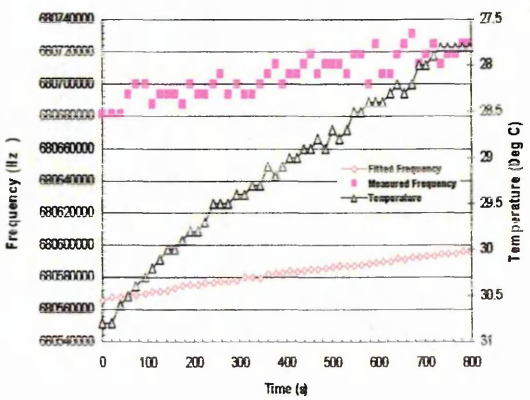

(F)

Figure 3.20 (A-F) FBAR S_{21} responses to controlled temperature changes over various time periods. The measured and polynomial values generated for the traces are shown.

3.4.1.7 Finding the Pearson moment correlation (r) for fitted and measured data (Temperature experiments 3A to 3H)

3.4.1.7.1 Method

The Pearson product moment correlation coefficient, (r), is a dimensionless index that ranges from -1.0 to 1.0 inclusive and reflects the extent of a linear relationship between two data sets, where one array is a set of independent values and the other array is a set of dependent values. In this case the measured data was chosen as the independent variable and the polynomial fitted data was chosen as the dependent variable.

The (r) value of the Pearson regression line is calculated as;

$$r = \frac{n(\Sigma XY) - (\Sigma X)(\Sigma Y)}{\sqrt{[n\Sigma X^2 - (\Sigma X)^2][n\Sigma Y^2 - (\Sigma Y)^2}} \qquad \text{(Eq 3.1)}$$

It is a function built into the Excel© software package.

This function was applied to fitted and measured data from an FBAR S_{21} output that was responding to changes in temperature. A value was obtained showing how well the responses correlated to each other and to temperature using the Pearson moment calculation. If the value was shown to approach 1 (or -1), then it would be possible to gain confidence that the fitted data was accurately reporting the values of measured data. If this was found to be the case, the measured data could be omitted from the graphs allowing them to auto-scale around the fitted mean, and in doing so give an increase in perceived output resolution, this increase being proportional to the difference (in Hz) between fitted data and measured data.

3.4.1.7.2 Results

Results in the three Figures 3.21 (A, B and C) show that the measured data becomes successively less quantised as recorded signal data density is increased by means of narrowing the frequency sweep bandwidth from 50 MHz to 10 MHz. Where the responses of fitted, measured and temperature data are roughly linear the Pearson value was calculated for fitted data vs. measured data with temperature.

Results 3.21 (D, E and F) show that disregarding measured data serves to increase the perceived resolution of result (due to graph auto-scaling function) The Pearson value for fitted data vs. temperature was calculated on responses where that response was roughly linear over range, r was not calculated where there is an obvious lag phase between the response of the thermocouple and the response of the FBAR.

Table (3.3) Pearson moment (r) correlation coefficient values for fitted and measured data.

	Fitted data vs. Measured data	Measured data vs. Temperature	Fitted data vs. Temperature
Graph A (n/a lag)	-	-	-
Graph B	r = 0.987198	r = -0.90575	r = -0.90575
Graph C	r = 0.996481	r = -0.99533	r = -0.99801
Graph D (n/a lag)	-	-	-
Graph E	-	-	r = -0.98823
Graph F	-	-	r = -0.76906

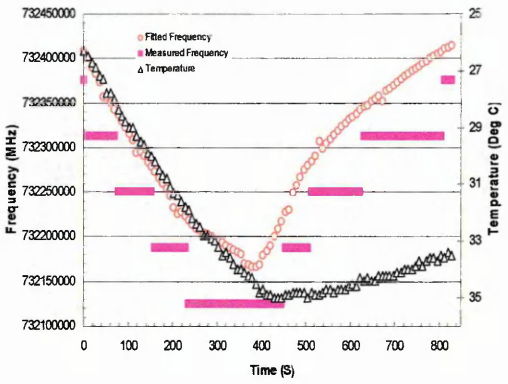

Fig (A)

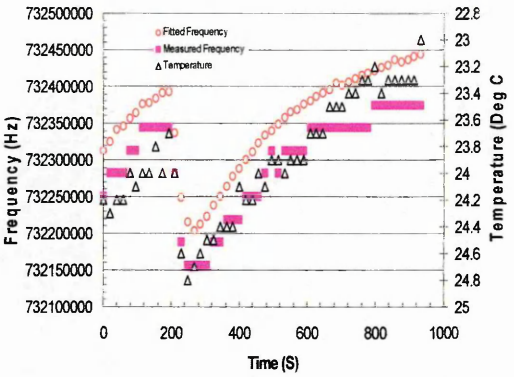

Fig (B)

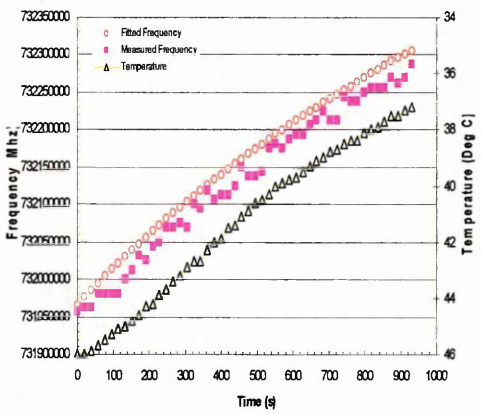

Fig (C)

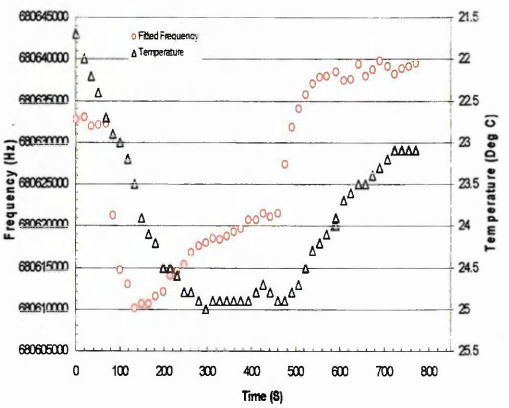

Fig (D)

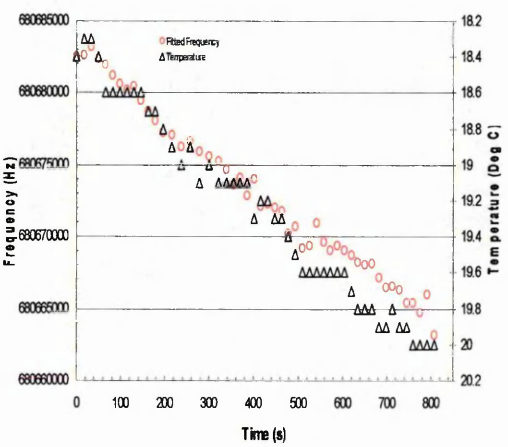

Fig (E)

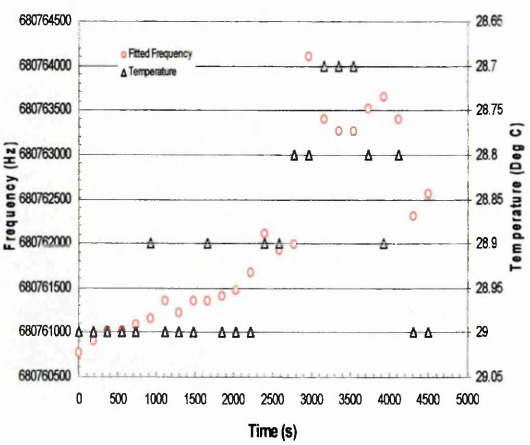

Fig (F)

Figure 3.21 (A-F) FBAR Measured and polynomial fitted S_{21} responses to temperature change over time. *Erratum – Fig A and C should read Hz, not MHz as is stated.*

3.4.1.8 Investigating the effect of temperature change on S_{21} transmitted power and Q factor responses of FBAR.

3.4.1.8.1 Methods.

The graphs shown in Figure 3.22 (A and B) were produced from the data that was obtained during experiment 2D (*See Figure* 3.20 (D)). The routines used to generate the graphs are obtained simply by choosing alternative labelled columns from the excel data chart recorded for the experiment and making XY scatter graphs with the temperature data superimposed onto them. As such it will be noted that the temperature data is identical for each of the charts.

3.4.1.8.2 Results

Figure 3.22 (A) show that the S_{21} transmitted power (dB) falls, i.e becomes more negative as the temperature of the FBAR is increased and that the power response recorded from the device rises as temperature falls. A clear trend for increases and decreases in transmitted power following rises and falls in frequency can be seen in response to rises and falls in temperature as recorded by the thermocouple. A pearson moment correlation was not performed because of the lag phase betwween the response of the thermocouple and the FBAR over the 300 to 500 second mark, however it is easy to see the trend from the graph. An estimate by eye reveals that the change is ~0.03dB over ~ 2^0C

Results in 3.22 (B) show calculated for 3 dB Q value against the temperature change and they reveal a remarkable similarity in terms of shape to the responses for power, this is indicative that the reported Q factor of the device and the S_{21} power transmissions are non mutually exclusive. The apparent Q factor however, rises with a concomittant rise in temperature and falls at approximately the same rate. An estimate by eye will reveal that there is an approximate change of 5 Q units over ~2^0C.

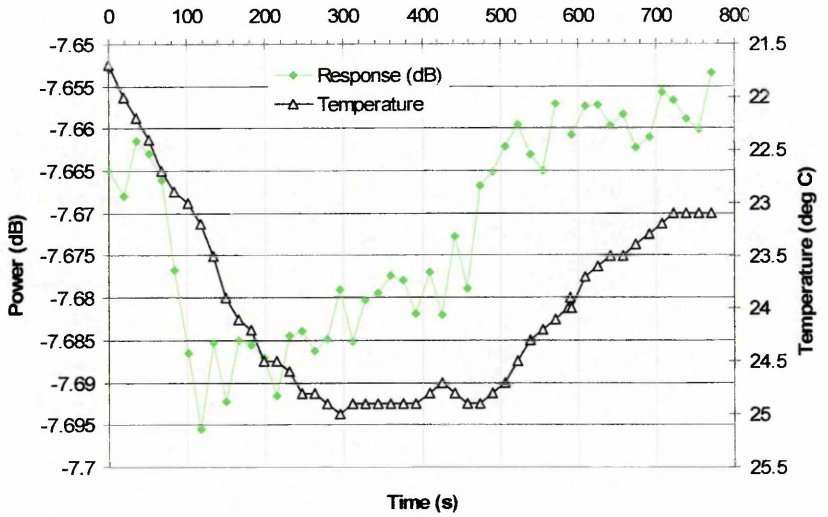

Figure 3.22 (A) Shows S_{21} transmitted power response for experiment (3D) (Axis reversed)

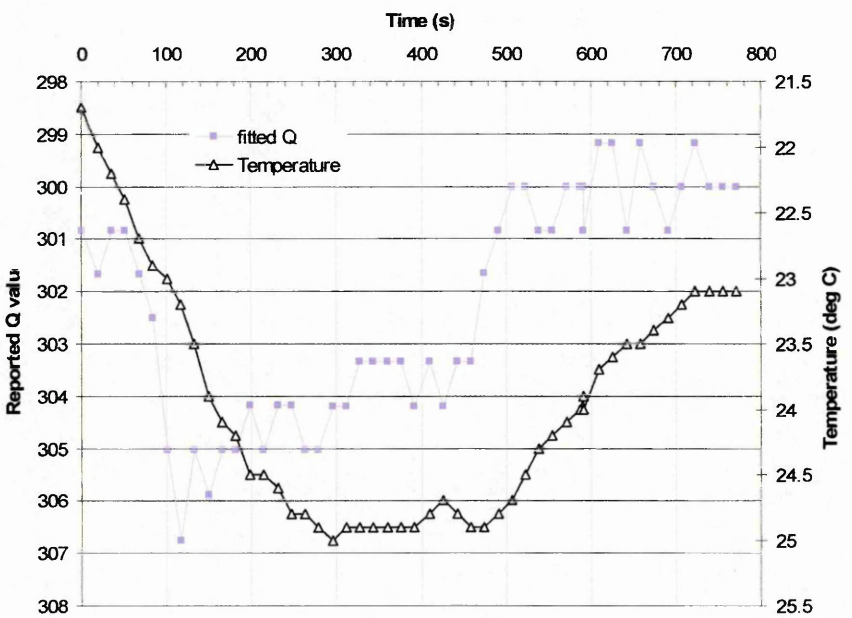

Figure 3.22 (B) Shows 3 dB Q value for experiment 3D. (Axis reversed)

3.4.1.9 Examining the use of FBAR overmode harmonics in response to temperature change.

It was useful to examine overmode harmonics of the FBAR since these higher frequency modes potentially offered more absolute frequency change per unit measurand, even if that increase was a simply a linear function and not a real increase in sensitivity *per se.*

3.4.1.9.1 Methods

A wire bonded FBAR with overmode harmonics[68] which were reasonably free from spurious resonances was subjected to a Peltier controlled temperature increase of roughly $3^{O}C$. When the responses were obtained, a linear segment of the graph representing a rise in temperature of $1^{O}C$ was taken for each of the overmodes at roughly the same temperature (within $\pm$ $0.25^{O}C$), the absolute negative shift in frequency ($-\Delta f$) was measured for each overmode and then represented as a separate XY scatter plot. See Figure 3.23 (A and B)

The absolute change in Hz was calculated for a $1^{O}C$ change, and this absolute value calculated against the centre frequency of the span for first and second overmode.

Settings
Centre frequency of first overmode ($f_{n=2}$) = 664.2 MHz
Centre frequency of second overmode ($f_{n=3}$) = 1291.0 MHz
Span frequency 2.0 MHz
Points in sweep 1601
IF bandwidth 300

[68] The primary mode was not useable in analysis due to poor characteristics.

3.4.1.9.2 Results

The two useable overmodes of the FBAR were utilised to correlate higher overmode frequency changes responses to the same absolute amount of temperature change.

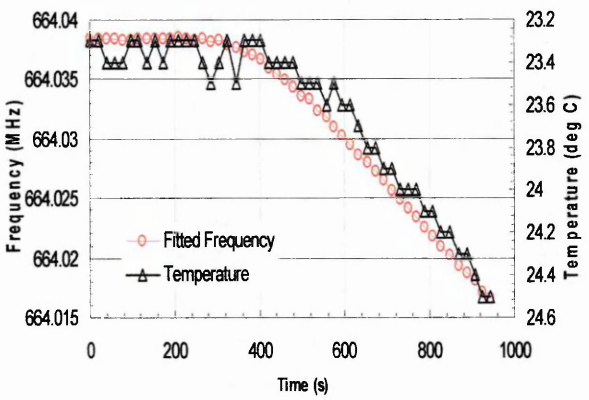

(A)

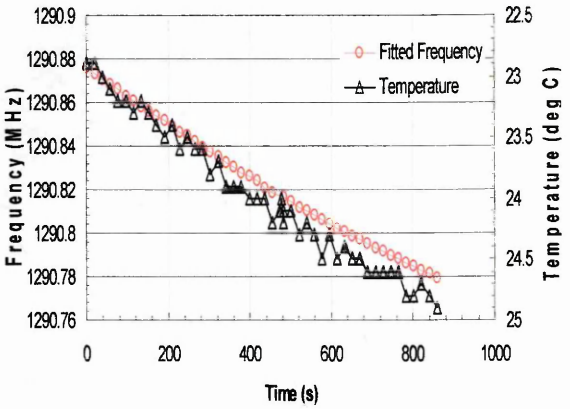

(B)

Figure 3.23 (A) Shows $\Delta f/\Delta^{O}C$ on first overmode. (Centre 664.2 MHz)
Figure 3.23 (B) Shows $\Delta f/\Delta^{O}C$ on second overmode. (Centre 1291.1 MHz)

The responses to a $1^{O}C$ rise in temperature are shown and calculated to give approximately;

$\Delta f / f_{n=2} = \sim -14$ KHz

$\Delta f / f_{n=3} = \sim -46$ KHz

3.4.1.10 Establishing the error range of fitted data with optimised settings under stable conditions.

3.4.1.10.1 Methods

The tests up to this point served to give a general overview of how the setting functions applied to experimental procedures and how they subsequently effected the FBAR output responses. It was necessary to discover the level of unavoidable noise in the system when environmental conditions had been stabilised and when the settings were set to the highest achievable resolutions. Signal drift on baseline response of sub-GHz FBARs was monitored over 700s and 4000s with temperatures stabilised. (25.5^{O} C $<\pm 0.1\ ^{O}$C) and ($29.2\ ^{O}$C $<\pm 0.2$) respectively. Different individual sub GHz devices were used to ensure

that the response was not limited to a particular characteristic response of any given single individual resonator unit. The measured data was not used and only the fitted data from the polynomial processing of that fitted data is shown. This is to allow for increased perceived resolution stemming from the graph auto-scaling function. The error is calculated as a fitted mean for all of the f_0 values generated from the iterations performed over the time frame of the experiments. The IFBW was set at 3000 to give 20 iterations over 700 seconds and the IFBW was set at 300 to give 22 iterations over 4000 seconds. 1601 points were collected for each iteration and the bandwidth was set at 1 MHz.

3.4.1.10.2 Results

An estimate was made of the error range of the FBAR fitted response over time when temperature was stabilised ($\pm$ 0.1 ^{O}C) and the instrumentation settings were optimised to deliver the maximum resolution. Graph (G) is shown from t=100 seconds as there was some minor fluctuation in temperature during the initial minute of the test.

The results show:

Figure 3.24 (A) Fitted f_0 signal drift over 700s (Mean SD = $\pm$ 0.5 KHz) 20 iterations shown

Figure 3.24 (B) Fitted f_0 signal drift over 4000s (Mean SD = $\pm$ 1.0 KHz) 22 iterations shown

For the graphs shown below in Figure 3.24 (A), the quantisation (minimum point to point spacing on the Y (frequency) axis) of the fitted data points is roughly 60 Hz, this value represents the highest currently achievable practical limit of S_{21} series resonance frequency resolution for the apparatus combined with the software when optimised for high resolution settings, 2nd order polynomial smoothing and stabilised temperature. There is signal drift apparent in 3.24 (B) and it is not possible to know if the FBAR in this case was responding to miniscule increases in temperature, well below the 0.1 OC resolution capability of the recording thermocouple or if the drift was due to other influencing factors.

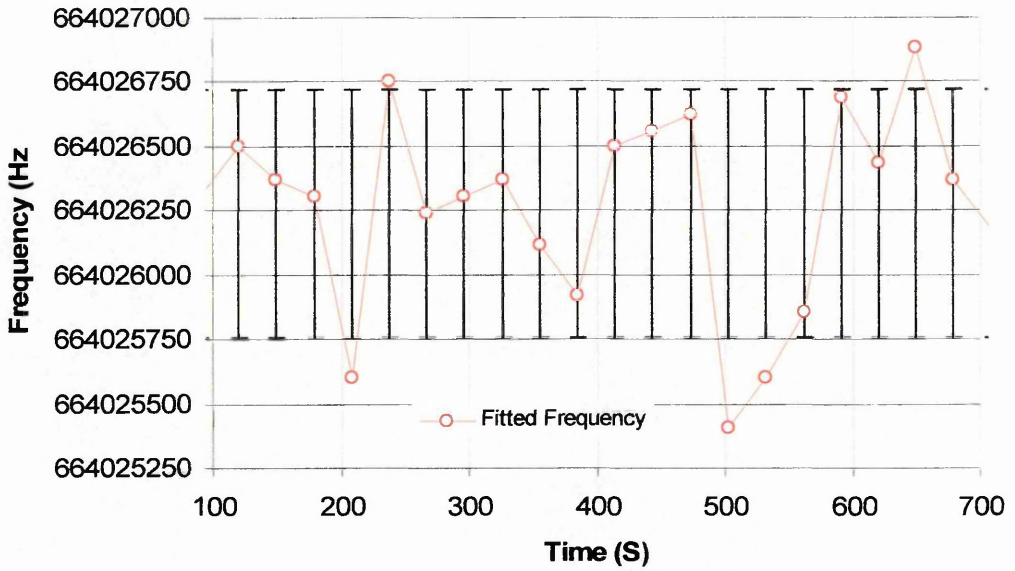

Figure 3.26 (A) Shows fitted f_0 signal drift over time. (700 Seconds) Temperature Stabilised (25.5 ^{O}C $<\pm 0.1$). IFBW set at 3000 (Error= fitted mean over range)

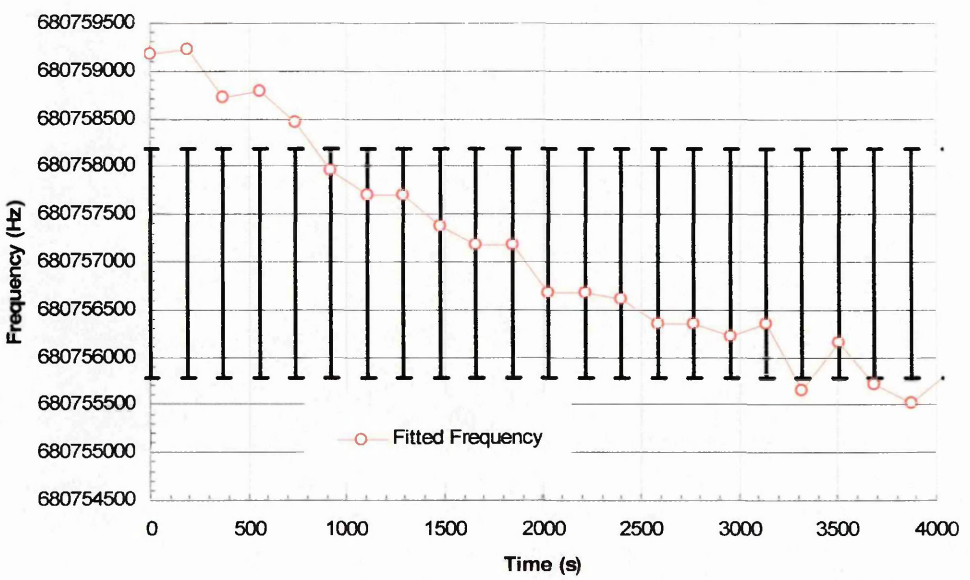

Figure 3.26 (B) Shows fitted f_0 signal drift over time. (4000 seconds) Temperature Stabilised (29.2 ^{O}C $<\pm 0.2$) IFBW set at 300 (Error= fitted mean over range)

3.4.1.10.3 Establishing practical sensitivity limits for the FBAR output responses

By paying careful attention to the FBAR output responses throughout all previous tests, a suspicion arose that the device was responding to lab fluorescent lighting albeit only slightly. Previous FBAR interrogation on the probe station had clearly demonstrated sensitivity to light (results not shown), but the probe station light was incandescent and powerful and became much warmer as it got brighter (this temperature change was not measured, but could be easily felt with the back of the hand), so the effect could not be divorced from temperature change which was now a clearly established influencing factor on FBAR baseline responses. Tests were performed to confirm or deny the validity of the suspicion that light could effect resonant frequency of the device whilst temperature remained stable. Since the effect was suspected to be small, this was seen as a good opportunity to test the responsiveness and resolution of the apparatus in practical terms.

3.4.1.11 Monitoring the effect of (i) white fluorescent light and (ii) blue light from LED on FBAR with temperature stabilised baseline

3.4.1.11.1 Methods

For illumination experiment 1A, the light sensor (photodiode) of the DAQ environmental monitoring board was placed in close proximity (i.e., on top of the housing chamber lid) but external to the wire bonded FBAR in the FHA. Lab lighting was turned off for a few minutes and on for a few minutes and then repeated. The responses of the FBAR were recorded over time and the responses of the light sensor were superimposed onto the baseline to look for correlations in FBAR in dark and light states.

For illumination experiment 1B, in a darkened room, a blue LED pen light was used to illuminate the FBAR and brought closer to the FBAR device in increments of 0.5 cm by means of a ruler and a retort stand.

Settings were
Centre Freq: 316 MHz
Span Freq: 2 MHz
Points in sweeps: 1601 IF Bandwidth: 1000

3.4.1.11.2. Results

Results for illumination experiment 1A shown in Figure 3.27 (A) track the effect of the fluorescent lighting vs. dark states on the FBAR S_{21} baseline. When the DAQ board photodiode was reporting ~40%, light saturation, the FBAR reported f_0 fell, on average, by approximately 2 kHz. This represented normal ambient room lighting from the two strip lights that were used to illuminate the windowless room.

Results for the S_{21} power transmission responses and also for the Q factor for this test were examined and no obvious correlations between the light and the dark test settings could be established from the graphs in response to either of the two parameters. These results are not shown.

Results for LED illumination experiment 1B do not reveal any obviously significant change in FBAR frequency response correlating to the increased brightness on the device brought about by closer proximity of the LED. This effect can be seen by the increase in % light saturation on the photodiode. Power and Q responses were not examined in this case.

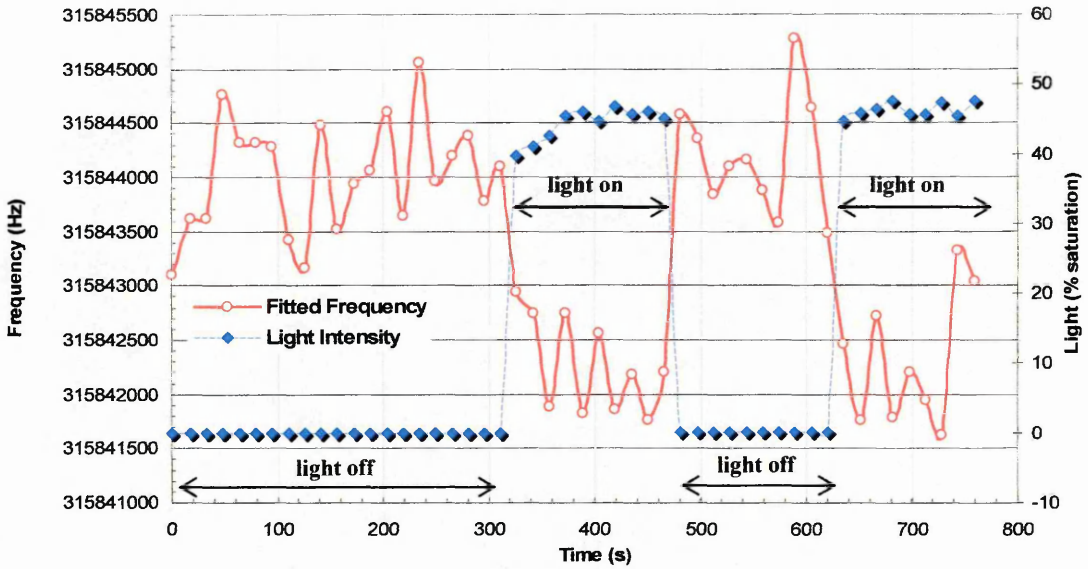

Figure 2.27 (A) The effect of fluorescent lighting on FBAR S_{21} response. Iterations (50) IFBW (1000) Number of points per iteration (1601)

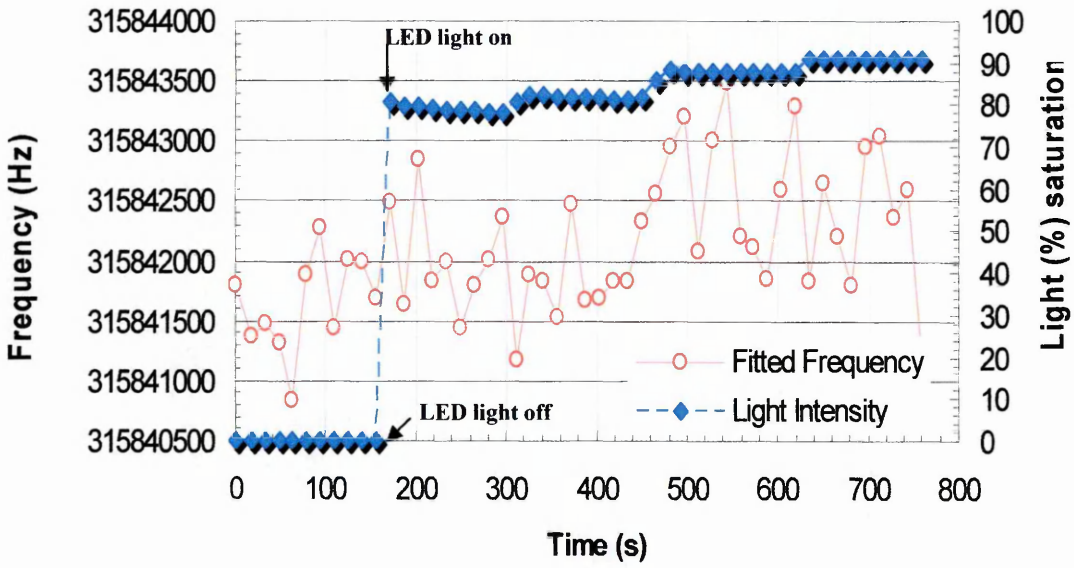

Figure 2.27 (B) The effect of blue LED off, then on and brought incrementally (1 cm) closer to the device with same settings as in 2.27 (A)

3.5 Discussion

The use of the four S parameters

There was not sufficient justification for pursuing the technicalities underpinning the problem where the resonance failed to manifest on the S_{22} parameter, it remains intriguing, but can not be explored or discussed any further in the thesis. S_{21} two port transmission signals were used exclusively in all tests from this point onward to measure FBAR responses. This test was useful in confirming functionality of the new software in terms of its ability to control the S parameter functions of the NA.

S_{21} Signal transmission, termination and cross-talk

The first experimental series was successful in confirming that the instrumentation was working as anticipated. S_{21} signals were delivered by the VI ↔ NA instrumentation (GUI interface) over the specified frequency span range. Results confirmed FHA and PCB 50Ω TL were delivering signal with minimal loss at relevant frequencies. Results were viewed with both NA and VI and indicated perfect correlation between the real hardware and the new VI which was also under beta testing at this stage. Signal termination gave result as anticipated, and it was now known that -100 dB indicated zero transmission.

In contrast, where the signal was not terminated but allowed to pass to Port 1 from Port 2 of the network analyser via the phenomenon of cross-talk, when there was 5 mm parallel spacing between the TL, a power transmission response of ~ -20 dB was seen @ 3 GHz.

Signal cross-talk was expected, but the magnitude of the signal transmitted by this route was higher than had been conjectured. In the test apparatus as it stands, cross-talk is not a major issue since the FBAR devices are run singly. It is helpful to know that the phenomenon exists in the present design only for the purpose a complete over view of the system. In future design where two or more FBARs are interrogated simultaneously and especially when the prototype is miniaturised, the issue of cross-talk will be more important and methods to accommodate its presence will be required.

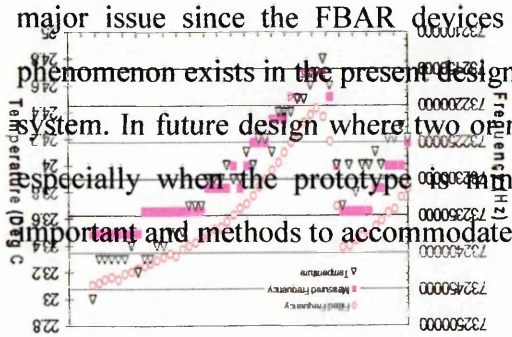

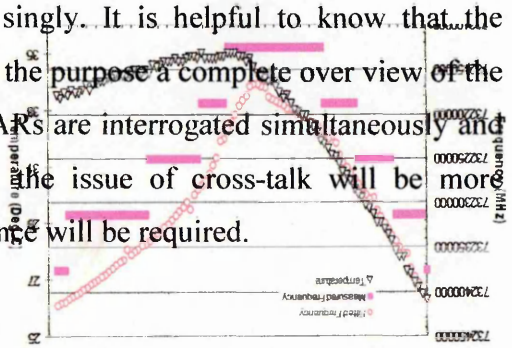

RF characterisation of the various components comprising the FBAR housing assembly

RF characterisation of the FR4 PCB with different thicknesses presented only slight variations in performance.(3.4 mm) thickness of board was preferentially used for all experimentation following this observation, but not especially significant. It was not known at this stage whether or not frequencies above 1.4 GHz would be used for sensing, it was considered the best approach to assume that higher frequencies would be employed later in the project. This assumption turned out to be correct since in the later stages of experiment, overmode secondary and higher harmonic resonances above 1.4 GHz

It was also useful to know that there would always be at least -2.4 dB attenuation in future S_{21} transmission experiments since all planned future interrogations would be two cable, two port S_{21} transmissions tests. Coaxial cables are sources of loss with increasing frequency, the longer the cable, the greater the loss. As with all RF design TL, wirebonds and all electrical cable carrying RF signal should be (i) fully characterised to mach input impedance (in this case 50Ω) & (ii) kept as short as possible to minimise losses.

Wire bonds were prone to failure[69] rendering the test device useless until repair. This failure could arise form accidental mechanical agitation or from thermal cycling. Adding Au wires in parallel with existing bonds not only improved signal transmission (-6 dB @3 GHz parallel compared with -10 dB@ 3 GHz single) but also served as a failsafe in case of single bond failure. It was not clear how important RF signals losses were at this stage to the accuracy of the test result and to the overall performance of the FBAR sensor.

Whilst laboratory bound and connected to a mains supply it may not be functionally deleterious. However, when the apparatus is developed further and designed for "in the field" operation with its own power supply, losses may be of detriment to the operational life span of the apparatus if battery powered. These findings indicated, as expected, that

[69] Meaning becoming physically dislodged from contact with either the electrodes of the FBAR or from contact with the transmission lines. .

the wire bond should be kept as short as possible in RF die mounting and circuit design. In total there was roughly a total 20 mm wire length on all four bond to FBAR structures and the losses shown are for the present unavoidable. These losses did not effect $f0$ from on die measurements to wire bonded measurements and this was of course was the parameter of most concern.

Memory normalisation tests

The use of the memory normalisation function seemed, at first, to be quite straightforward since the output results from the coaxial cabling and from the attenuator calibrations were very close to the expected values. However, running FBAR device 9 against memory from de-embedding circuit changed output characteristics in a way that was not wholly anticipated. The first problem was that the primary resonance occurred with a positive dB value, and the second unexpected component to the result was the non-linearity of the response beyond the 1.3 GHz resonance peak. The non-linearity of the signal indicated that the memory normalisation functions were not performing as expected[70] and highlighted perhaps some weaknesses in understanding of the fundamentals RF design or in the correct implementation of the function. No more time could be devoted to this avenue of research and, with reluctance, it was decided to perform all future experiments without the use of the memory function or the de embedding circuit.

IFBW control settings and their relationship with random electronic noise

The ability to control dB (Y axis) error range is important because in the final FBAR interrogation, where there is random noise (manifesting as Y axis error) scattered over the resonance curve, the likelihood increases that the determination of the all important f_0, parameter from which the iterative output responses are generated could also scatter in proportion to the noise level. In this way, it is shown that minimising Y axis error through the use of the IFBW control parameter, does by default, also increase accuracy (decreases error range) on the X axis and this directly influences the level of indeterminacy in the recorded frequency value.

[70] A simple linear trace close to the 0 dB mark except where the resonance condition occurred.

Decreasing the IFBW settings below 300 Hz was deemed counter productive since the time taken to perform single iteration was unacceptable (.> 2 minutes), the loss in temporal resolution outweighing the small increase in frequency stability gained. Also if the tests were unnecessarily protracted, then the chances of a system lock-up[71] were increased, and in general if such a lock-up occurred the experiment had to be repeated and this could waste precious time. The highly constrained IFBW procedure may prove fruitful where extreme accuracy is required on a single iteration. This test also served to ensure that the VI↔NA IFBW control settings were working as intended in the new software, and this was shown to be the case.

The aim here, it should be noted, was not to develop a thermometer, although this is of course a useful function. Instead, the experiments were performed to examine the robustness, accuracy and sensitivity of the system in response to change in a single physical parameter (i.e., a measurand) that could be easily controlled and measured and was free from potential sources of interferent. In a word, using temperature as the measurand was the simplest type of experiment that could be performed to put the newly developed system through a testing program to (i) gain understanding of its behaviours, noise levels, drifts etc and (ii) optimise sensitivity. However, obtaining this temperature data as an absolute value was also useful because it was now understood that FBAR response was not independent of temperature changes and values obtained for other parameters e.g. real biosensing applications, would require an accurate temperature measurement and any change in this value would require the appropriate compensation for Δf. This will likely be in the form of a relatively simple software calibration solution.

FBAR temperature dependency is a function of the intrinsic resonance frequency used to make the measurement. The work showed that FBAR is, unlike quartz, extremely temperature dependent. For future biosensing applications, the more sensitive the analysis (e.g., microweighing smaller and smaller quantities) will require a proportional increase

[71] A system lock-up means that the computer and the network analyser ceased useful communication with the particular iteration stuck in an infinite loop with no data transfer through the GPIB channel.

in the stabilisation of temperature or improved software compensations from extremely high quality thermocouples to ensure that the result is free from errors.

Output response sensitivity

The practical limit for setting sensitivities, data density and bandwidth was around 1 MHz f_1-f_2 bandwidth with 1601 data points collected over range and the IFBW settings programmed at 300 Hz. IFBW settings used at unnecessarily high resolution (10 MHz) caused unacceptable time delay in the iteration. The sensitivity limit was, in part, due to the quality of the resonance curve from individual FBAR samples, but was also a practical limit of the software curve tracking function.

On-wafer tests with the probe station on FBARs characterised their responses in terms of depth of resonance tip, and the narrowness of the tip (Q-value (f_2-f_1/f_0)) as well as any obvious lateral modes interfering with the smoothness of the resonance response. These modes could interfere with the with the polynomial fitting correlation to raw data (e.g. too many inflections for the low 2^{nu} order polynomial). It may have been necessary to increase the polynomial fitting order to accommodate for the number of inflections in the curve, but this route was not taken since it would require further coding and time delays in both development and the time taken to process the final data hence FBARs with seriously perturbed tips, even if deep and narrow would be rejected as part of the quality control procedure.

Reducing the f_0 mismatch between measured and fitted data

The Q factor bandwidth selection function was not native to the network analyser but it was an increased level of processing flexibility only made available through the dexterous Labview coding of newly developed analysis and control software. The usefulness of using this measured/fitted composite function analytically was not effectively determined at this stage. The primary or intended function of the Q bandwidth selection routine was to improve the measured and the fitted data average f_0 correlation and this was shown to be successful since the discrepancy in the traces was diminished when using a decreased Q bandwidth. A dB selection cut off point of +1 dB gave an

average polynomial value for the resonance frequency fo the FBAR over time within mean of the measured FBAR resonance frequency over the same time. The bandwidth could be decreased to 0.01 dB as this value represented the limit of numerical calculation for the network analyser. The reason for the improvement in the correlation between the respective f_0 of the measured and the fitted data was likely to be due to the fact that the natural asymmetry within the full 3 dB range of the FBAR resonance curve was diminished as the focus was brought closer down the Y axis toward the tip of the curve.

The apparent but artificial increase in "Q" factor was understood merely as being a side effect of using this function since Q is usually measured as $f2\text{-}f1/f_0$ +(3 dB) from the tip of the resonance curve. The fact that cutting the dB point gave "Q" values that almost perfectly matched the power law was an interesting observation, but not completely unexpected since the dB scale follows the power law also.

Temperature experiment 2 (Measured output responses)

The purpose of this experiment was to ensure that the measured baseline made up from successive f_0 determinations within the specified f_1-f_2 the bandwidth was responding to temperature change and that it could be effectively demonstrated by comparing f_0 as Δf to ^{O}C on a XY scatter graph over time. The measured baseline did respond to temperature change, but with differing degrees of sensitivity. The results for 2A and 2B were as expected, in that the baseline became more tightly clustered around the mean when the IFBW aperture was constrained. It was not possible to obtain an error range of the fitted baseline at this level of resolution. Experiment 2C, 2E and 2F gave similar Δf for temperature, but some minor concern was the somewhat large Δf value obtained for 2D. However, experiment 2D was run continuously for 4500s. Hence the result may not be entirely due to temperature change alone, and instead may also be due to prolonged interrogation of the device. Possible reasons for this may be, for example, the build up of some parasitic static charge inside the FHA or indeed this may be the product of prolonged interrogation of the piezoelectric substrate, i.e., it may be indicative of ageing in the device. The actual reason remains somewhat elusive at this stage. It may be necessary to obtain a high degree of temperature stabilisation with more sophisticated

apparatus and interrogate the devices for a long time e.g. over a few days, to develop a pattern for the response before attempting to confirm the reason for the downward frequency signal drift over time.

Practically speaking, with this potential signal drift effect in mind, for the rest of the experiments, it was decided to keep the run times as short as possible to avoid sources of drift caused by either temperature fluctuation or some other unknown parameter being given enough time to significantly influence the S_{21} series resonance frequency of the devices. Overall, the results provided persuasive evidence of the fact that the measured responses of FBAR were responding reproducibly to temperature changes.

Temperature experiment 3. Measured and fitted data correlations

Very good correlation (r) approaching +1 or -1 for measured, fitted and temperature data was shown with Pearson moment correlates. Using the Pearson moment calculation allowed for a definitive numerical value to be given to the relative rates of change for the measured and fitted data in relation to temperature. If this Pearson function had not been explored, then the term "good correlation" would have lacked precision and remained subjective.

It was now felt that the nuances of the baseline had been well explored, the setting parameters understood and the limit of resolution for practical sensing applications determined. Most importantly, the polynomial fitted data could be trusted to give a true representation of the measured data so that it could be confidently disregarded during runs. This in turn allowed the graph to auto-scale exclusively around the polynomial fitted data, and as such, it substantially increased the perceived resolution of the trace.

Use of the alternative output choices S_{21} power transmission and Q factor.

The Q bandwidth cut off function should not really be called Q factor *per se* once the dB cut off range was any value other than 3 dB, but no other name to call it is immediately obvious. However, the mutable f_2-f_1/f_0 function – which is a composite of the polynomial f_0 and the f_2-f_1 measured bandwidth may be viable as an alternative interrogation output

format if particular attention is paid to the intrinsic Q bandwidth value at any given cut off point.

It was interesting, but perplexing, to note the following Q value results. In experiment 1A the Q value parameter was seen to be following the rough trend shape of the temperature change recorded by the thermocouple, with the change in Q value auto scaled it was in the order of two decimal places. However in the later Q test for Experiment 2D, the Q value changed by a full 6 points over $3^{\circ}C$,. but to find the Q response shape or trend profile that was following the temperature change trend shape profile, the Y axis scale needed to be reversed. So, from this observation, it is not possible to draw any firm conclusions about the validity of the Q function usefulness in sensing at this stage. Q value changes when used in conjunction with frequency change potentially open up the possibility of making rheological assessments of material parameters of foreign layers on FBAR surface(s). Likewise, changes in the S_{21} transmitted power are indicative of a change in material rheology, where a material becomes more lossy, more power will be transmitted through the device because it becomes a less efficient resistor at resonance.

Determination of FBAR maximum output resolution and minimum indeterminacy of S_{21} frequency.

When the temperature was stabilised to within $\pm 0.1^{\circ}C$ and measured data values were disregarded, using only f_0 as determined by the mathematical processing of the polynomial fit on the charts, it allowed auto-scaling features of the graph focus the X and Y scales constraining them tightly around the pertinent data. This function served to present a much higher apparent resolution. Ultimately, a change in a mere **60 Hz** could be resolved point to point between the polynomial f_0 of successive iterations – but only in situations where the stetting parameters were optimised for maximum sensitivity and the environmental conditions of the high quality FBAR device within the FHA were stabilised. When the conditions were stable, the background noise in the signal gave rise to an uncertainty in frequency determination of $\pm$ 0.5 kHz over 700s interrogation, and $\pm$ 1 kHz over 4000s but in this case there was a definite downward frequency trend

Determination of the ultimate practical resolvable sensitivities of the polynomial fitted output responses

It seemed that the wirebonded FBAR was responding to light by changing S_{21} series resonant frequency between dark and bright states because the effect of frequency change was in this case, proven categorically not to be caused by changes in temperature. Interaction with ambient photons is likely to be the most subtle state change parameter that could be explored on FBAR with the existing apparatus.. The underlying physics causing Δf on FBAR S_{21} series resonance responses due to interaction with light (optoelectrics) are not fully understood by the author, but that ZnO is photoconductive is very well known. In this demonstration of sensitivity, the optoelectric physics underpinning this response do not require an in depth explanation. The point to be highlighted in this case is that by applying the polynomial fitting to the measured data and then disregarding the measured data on the output charts, the shift from fitted stabilised baselines produced by iterative f_0 values over time that can be clearly resolved out from light on to light off is in the region of just 500 Hz. This level of sensitivity was unexpected, and extremely encouraging, further providing an indication that the prototype device (i.e., FHA and software) was functioning with high fidelity and further vindicating the design strategy and providing confirmation that the interrogation software was fully operational, very accurate and exquisitely sensitive, meaning that it possessed a large degree of dynamic range within a constrained bandwidth.

The reason that the device did not appear to respond to blue light, may be linked to the frequency of the photons since the apparent brightness of the blue LED was greater than the white light due to its close proximity to the FBAR surface. However, it would of course be necessary to have a thorough understanding of the FBAR piezoelectric and its relationship with the optoelectric physics underpinning these responses to explain the effect, and this is not possible in this work. However it is also possible that if a much higher starting frequency had been used for these tests that a response to the presence of the blue light may have been resolved. The point of this test was to see what the minimum resolvable frequency shift was with the available apparatus.

3.5 Summary and conclusion

The results overall suggested that the design protocols for FHA were vindicated and that the software was functional in nearly all of the targets that had been stipulated during its development. It was considered that the output response baselines based on iterative f_0 data points collected over time were stable enough for mass sensing. A downward drift in FBAR S_{21} series resonant frequency over extended time frames was suspected, sensing durations were recommended to be kept to a minimum time period until software routines could be written to accommodate for the time/signal drift. The reason for this drift was not established, but it may have been due to some ageing of the FBAR or perhaps a build up of static charge within the FHA - but no more time would be spent investigating this any further.

The point to point spacing for fitted baselines at the highest resolution settings was shown to be a mere 60 Hz per iteration when using a high quality FBAR device, this was very encouraging. In real terms, what this means is that a measurand event causing less change than 60 Hz would not be able to be detected by the apparatus. At this stage of the experiment, it was not known what amount of mass would be required to change the resonance frequency of the FBAR by ~ 60 Hz, attempts to use the math model to make estimates for this were unsuccessful because the model did not possess this level of resolution.

Sub GHz-FBAR response to temperature on average was seen to be ~10 KHz per ^{o}C when settings were optimised but the absolute value of $\Delta f / \Delta_{temperature}$ was clearly shown to be entirely dependent upon the frequency of the particular harmonic chosen with which to track the temperature change with increased change per unit measurand for increased resonant frequencies. This increased change per unit measurand delivered by increasing the resonance frequency will be explored again in later sections of the thesis.

Further work exploring the potential of FBAR to perform as the transducer in chemical gas sensing and biosensing was now ready to begin because the software was clearly functioning well, the measured and polynomial traces were in agreement, and the

architecture of the FHA appeared to be robust with no significant problems identified during all of the previous tests. The only concern with the functionality of the acoustic interrogation system at this stage was that the computer would on occasion, stop communicating with the network analyser but this failure had a tendency to occur when the total time for the complete iteration sequence was over 30 minutes, so plans to keep the interrogation time periods short were made. No clear pattern other than protracted time frames were ever established for this fault, and it did not always happen on all protracted time frames. No further time could be spent isolating this intermittent GPIB communication fault.

The fact that photonic effects that are not related to changes in mass loads[72] on the resonating surface of the FBAR can cause frequency changes is considered to be non-trivial at this stage since it represents a possible source of error and is likely not to exist in QCM based systems. It would therefore be prudent to consider both the lighting conditions and temperature stability of the experimental arrangement when using FBAR to make chemical or biological measurements.

[72] The author does not consider that the apparent moving mass of a massless photon could have any effect on the FBAR as a mass response and the response is instead entirely electrical in nature.

REFERENCES
CHAPTER THREE

1. Wartenberg. A. (2003) Selected Topics in RF coplanar probing. *IEEE transactions on microwave theory and techniques.* Vol 51, 4.

2. Pinkett S., Hunt, W., Barber, B., Gammel, P. (2002) Determination of ZnO Temperature Coefficients Using Thin Film Bulk Acoustic Wave Resonators. *IEEE transactions on ultrasonics, and frequency control.* Vol 49, 11

3. Agilent HP5753D Network Analysers Users Manual (1999)

CHAPTER FOUR
4.0 EXAMINING THE EFFECT OF COATING THE TOP SURFACE ELECTRODE OF FBAR DEVICES WITH THE HYGROSCOPIC POLYMER (POLY-VINYL PYRROLIDONE .

4.1 Introduction

A suitable chemically selective sensitising layer was required to explore the potential uses of FBAR when acting as the transduction module central to a chemical sensor system. Certain polymers are good candidates for the detection of organic vapours because of their high sensitivity, fast vapour diffusion, reversible responses and good ability to work at room temperatures. The polymer coating must be chosen to interact with the analyte as selectively as possible, then, both the choice of the chemical film and the sensor design have a great influence in the frequency signal response. [1] A variety of partitioning polymeric materials were considered as candidates with which to sensitise the FBAR to measurand along with a number of potential analytes. There are a wide variety of polymeric sensor materials that can be used to sensitise BAW systems, for a Review of these *See* Harsanyi (1996) [7] The hygroscopic polymer poly-vinyl pyrrolidone (PVP) was eventually chosen for a number of reasons, these are outlined below.

It is known that when a hygroscopic material deposited on a BAW resonator makes the resonator sensitive to moisture [2] PVP is commonly known to be hygroscopic and so should in theory, sensitise the FBAR to the presence of moisture. If this were shown to be the case, then it would be in principal, a proof of concept for FBAR ability to behave as a chemical gas sensor. Demonstrating that FBARs can be used to detect water vapour adsorbed out of a gas stream into a polymer is attractive because water vapour is relatively easy to control and monitor, hence the delivery methods and the various experimental procedures required could be somewhat simplified. For example, there was no need to consider any safety issues when using water vapour as there may have been had the measurand been toxic and furthermore the amount of water vapour in a gas

stream could be independently monitored using simple hygrometers.[73] In essence, using PVP on FBAR surfaces to measure changes in the concentration of water vapour in a gas stream was considered a good "model system" on which to consider the development of a chemical sensor whilst examining and attempting to interpret the FBAR characteristic responses in the presence of measurand at various concentrations.

Neshkova *et al* (1996) [8] developed a QCM humidity sensor by coating the crystal with nitrated polystyrene as the water sorbing coating, they achieved a response time of less than 3 seconds and concluded that their system was of "high sensitivity" because the frequency shift recorded from a crystal with f_o = 9 MHZ gave a downward shift of 40 HZ per %RH. They go on to say that "it is still a challenge to develop such a water sorbing coating which will ensure a linear frequency vs water vapour concentration response of the sensor over wide measuring range and at the same time meet the requirements for high sensitivity, fast response and recovery time and long-term stability, selectivity being an additional bonus. Most often the developed humidity sensors has its specific range of application"

PVP is also known to be selective toward ammonia, and by coating a quartz crystal with this material, an ammonia sensor had been created.[3]. For the purposes of this argument, the important point to note from this paper was the fact that moisture was seen as an important interferent which could not be adequately separated from the PVP derived response to the ammonia concentrations and because of this, the workers needed to develop methods to carefully limit, measure and control the presence of moisture in the ammonia stream.

As the FBAR structures fabricated in this study consisted of a very thin, (micron range) unsupported membrane which was potentially fragile, it was critical to determine whether the membrane could support any polymeric sensing layer and survive the process of polymer deposition on the membrane and even if it did survive, it was not known if the

[73] One of these hygrometers was GPIB enabled and computer code was written to allow for fully automated humidity data collection from it

FBAR resonance signal would be so severely attenuated so as to preclude the accurate determination of the S_{21} series resonance frequency. The results of the procedures undertaken in this chapter are analysed, interpreted and considered within a wider framework with the perspective of FBAR acting as a central transducer module within a multi-analyte chemical sensor system. The emphasis in this case being on the high (~700 MHz -1.8 GHz) intrinsic operating frequency of FBAR and the potential advantage of "increased absolute frequency change per unit of measurand" over the established state-of-the-art BAW systems which *tend* to operate at much lower (10 MHz) frequencies although high frequency versions up to 2 GHz of the QCM device have been made.[74]

4.2 Methods

Experiments were performed to examine if the FBAR could (i) Support a polymeric sensing layer and (ii) Respond acoustically to changes in the sensing layer due to the presence of analyte[75] in the layer. Experiments to determine the increased sensitivity of the FBAR coated with polymer to an analyte are described in this chapter. Experiments also were done to see if the device could be reused after having the polymer coating applied to, and then removed from the top electrode working area of the FBAR.

The effects of loading the polymer on the characteristic shapes FBAR resonant frequency responses were observed in low and high humidity N_2 gas streams. Observations on the effect of polymer loading on FBAR characteristic S_{21} series resonance frequency in the presence of various concentrations of relative humidity were made for various film thicknesses and also for various concentrations of the deposited polymer film on the FBAR surface.

In all of the following experiments, temperature, time, iteration number,[76] and humidity concentration data were stored along with FBAR S_{21} series resonance frequencies

[74] A direct experimental comparison for frequency change per unit measurand between low frequency BAW oscillators (QCM) and FBAR is made with "model system" immunosensors in Chapter 5 of this thesis.

[75] In this case the analyte or measurand is various concentrations of water vapour or relative humidity (%RH) in a N_2 gas stream flowing over the FBAR which was isolated from the environment by being sealed within the specially designed FBAR housing assembly (FHA)

[76] Iteration number is the number in the specified VI ↔NA run repeat sequence

(measured and polynomial fitted on primary or overmode) (Hz)[77] the measured and fitted transmission minimum power responses (dB), and calculated (n dB)[78] bandwidth Q. These values could be presented in any combination for later graphical visualisation and data analysis.

4.2.1 Apparatus

Apparatus and experimental arrangements are shown in schematic Figure 4.1 and photographic Figure 4.2 and its the use in experiments is described in Section 4.3.

[77] f_0 in Hz is denoted by the S_{21} transmission minima in dB
[78] Where the Q factor bandwidth represents any number from 3 dB to 0.01 dB

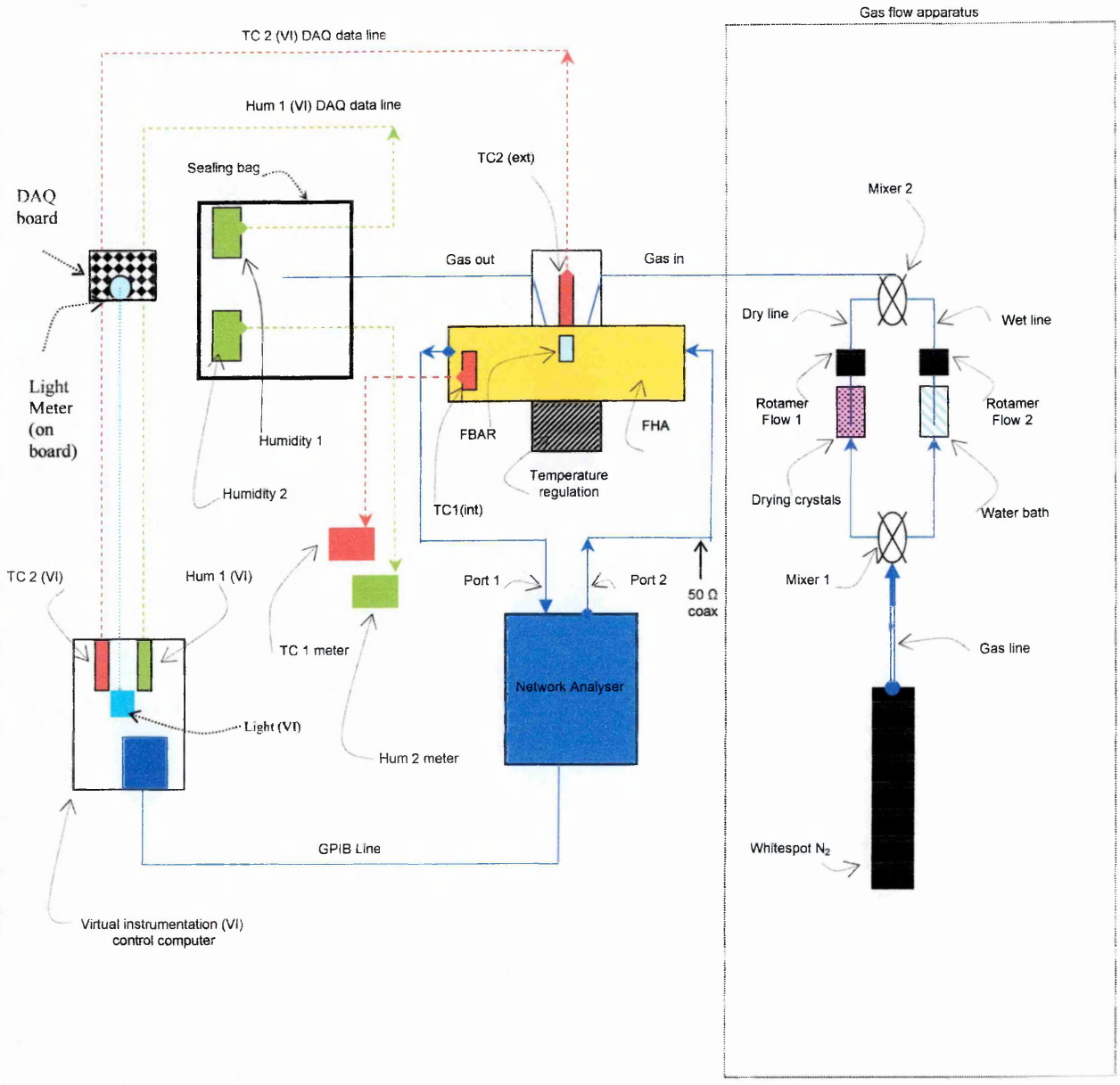

Figure 4.1 Complete Schematic of the apparatus used to deliver a gas flow of controlled relative humidity to the FBAR in FHA and the data acquisition from the environmental monitors and network analyser to the VI.

Abbreviations ("TC" means thermocouple "int" means internal, "DAQ" means data acquisition board, "FBAR" means thin film bulk acoustic wave resonator, "FHA" means FBAR Housing Assembly, "Rotamer" means the manual flow controls that regulated the gas flow rates into the FHA. "GPIB" means general purpose interface bus channel,[79] "HUM" means humidity and finally, "VI" means virtual instrument.)

[79] The light meter shown was not used in the PVP/humidity experiments. It was used in the illumination experiments described in Chapter Three of this thesis.

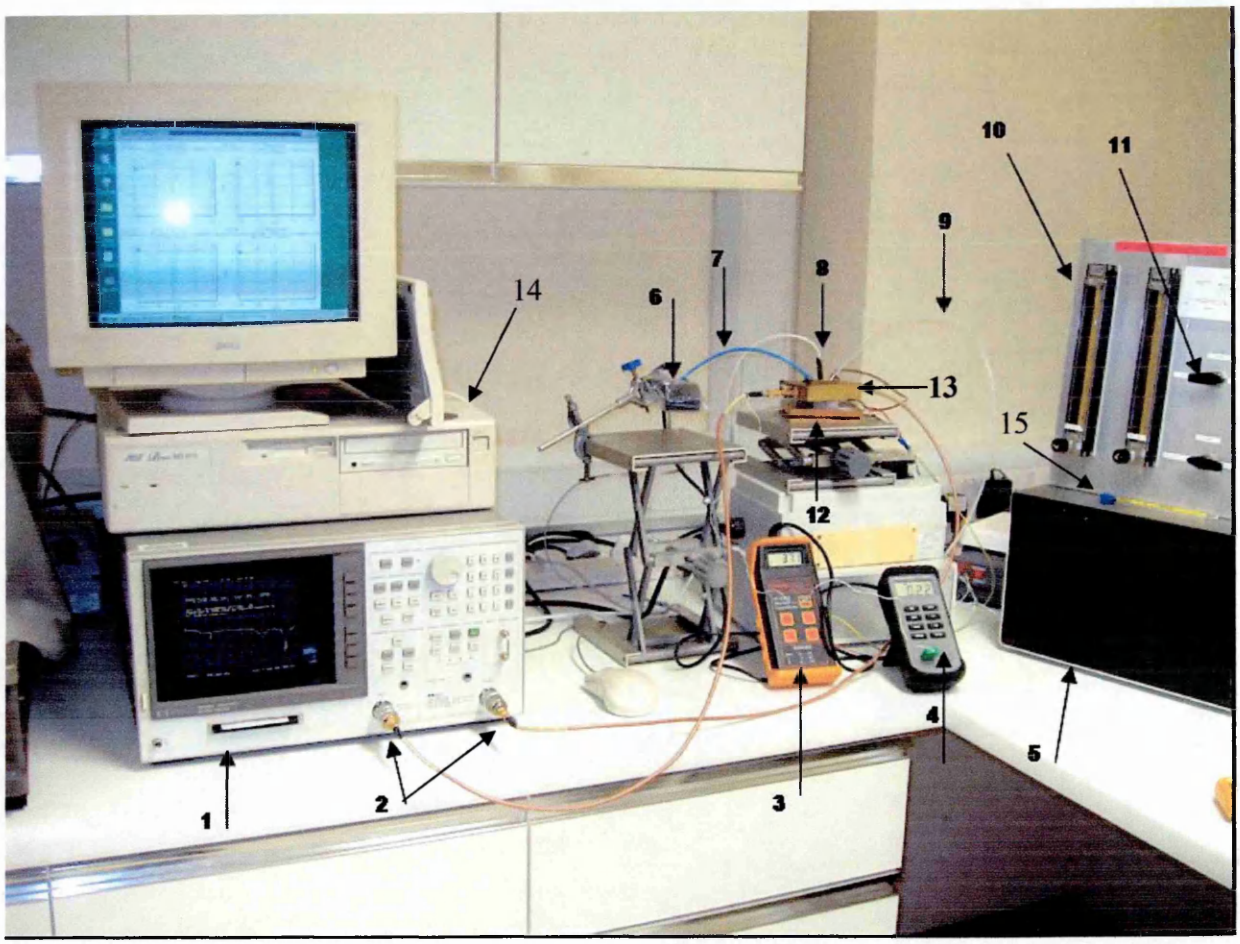

Figure 4.2 Photograph of principal testing apparatus.

1. HP8753D Network analyser (NA)
2. Coaxial cable link on N and SMA connectors from NA Port 1 and Port 2
3. Hannah instruments Humidity reading meter (manual)
4. Thermocouple reading meter (manual)
5. Water bath - usually left at room temperature
6. Humidity detectors (hygroscopes) 1 and 2 in a sealed bag fed by gas out-line.
7. Gas feed out-line (e.g. waste gas from the FHA)
8. External thermocouple. (Internal thermocouple not visible)
9. Gas feed in-line (delivered the humidity controlled gas into the FHA)
10. Rotamer gas flow controllers
11. Gas mixing taps (wet-line and dry-line)
12. Temperature controlled plate (Peltier heater)
13. FBAR housing assembly (FHA) (*See Figure* 3.1)
14. Lab Computer (The actual VI machine is not in the photograph)
15 Glass thermometer for measuring room temperature independently.

4.3 Control and measurement of relative humidity (%RH) in the N_2 stream.

The bench top experimental set-up developed in this study consisted of a gas delivery system that was specially designed and built for the project so that the %RH of the gas could be easily controlled and monitored. Gas flow rates were controlled with Rotamer flow controllers. Dry gas resulted from passing the N_2 stream through silica drying crystals sealed in an aluminium tube with a single gas inlet and a single gas outlet at opposite ends of the tube. The drying crystals were periodically recharged by heating. Gas wetting (i.e., increasing relative humidity (%RH)) was achieved by bubbling the N_2 stream through a water bath at room temperature. The gas stream was carried in tubing over 5m long letting the gas also equilibrate to room temperature.

The FHA was connected to the network analyser with the 50Ω coaxial cables that were fitted with N type connectors and SMA connectors. The FHA was temperature controlled by a Peltier heater which was stabilised ((~1^{O}C) (<±0.1^{O}C)) above room temperature to ensure that condensation from the additional humidity in the N_2. stream did not form on the inside of the FHA but particularly that it did not form droplets of liquid water on the resonating surface of the FBAR. Room temperature was checked periodically with a glass thermometer held in the air. The FHA internal thermocouple was read by means of manual meter whilst the external thermocouple was placed in contact with the quartz window (*See Figure* 3.1) of the FHA giving a close approximation of the internal temperature. The data from this thermocouple was collected via the DAQ board GPIB link directly into Labview running R.01 software on the computer

Uncoated FBARs and FBARs that were coated with PVP with a range of thicknesses and concentrations, were exposed to a N_2 gas stream with steady flow rate (~150 SCCM) which was controlled by manual adjustment of the Rotamer flow controllers. The N_2 stream was further manipulated to control the amount of water vapour in the stream. This control was achieved by manual adjustment of the wet/dry mixing taps. The gas could be directed in its entirety through the silica drying crystals or bubbled through the water bath, or a combination of wet and dry gas could be combined to establish a fairly stable

humidity level. The amount of water vapour in the N_2 stream was measured as relative humidity (%RH) by two separate humidity meters, which were exposed to the gas flow from the gas out line of the FHA. Both humidity meters were sealed in a polythene bag and a small pin hole was made allowing the gas to escape. The humidity meters themselves were bulky, and their excessive size did not allow for them to be set inside the FHA, although this would have been desirable. Readings from one of the humidity meters (Hannah instruments hygrometer) was taken manually and one (the DAQ hygrometer) was linked into the computer via the DAQ board GPIB link into Labview on the computer for fully automated humidity data acquisition. The DAQ humidity meter has response time of (>1s) (Range %RH = 20 to 90, Resolution 0.2% and accuracy $\pm$ 10%) .

The amount of water vapour in a body of gas is defined in this case as,

$$relative\_humidity = \frac{actual\_vapour\_density}{saturation\_vapour\_density} X100\% \qquad (\text{Eq } 4.1)$$

Where saturation vapour density is the dew point (100% relative humidity) that is, where moisture will condense out of the atmosphere, it is a temperature dependent function so relative humidity will therefore also rise as air cools without the water content necessarily being changed.

The responses of the internal and external thermocouples and both of the humidity meters were compared, the results are shown below in Table 4.1. The thermocouples gave identical readings whilst the hygrometers gave SD = 0.693 over the 10 readings.

In this case neither the temperature nor the humidity were strictly stabilised as the purpose of the demonstration was to observe how well the relative responses of the hygrometers compared with each other and how well the readings of the thermocouples compared with each other.

Table 4.1 Hygrometer comparison for humidity and thermocouple comparisons for temperature readings over 50 minutes for the manually observed and the GPIB data feed temperature and humidity monitoring instrumentation.

Comparison Between Relative Humidity and Temperature Reported Values From (i) RS Devices and (ii) VI DAQ Board				
Time (Minutes)	Hanna RS Instruments Hygrometer (%RH)	VI- DAQ Hygrometer (% RH)	RS Thermocouple (^{o}C)	VI -DAQ Thermocouple (^{o}C)
5	33.6	32.1	24.3	24.3
10	33.4	31.9	24.3	24.3
15	33.3	32	24.4	24.4
20	33.2	31.8	24.4	24.4
25	33.5	32	24.5	24.5
30	30.6	30.7	24.6	24.6
35	30.5	30.5	24.6	24.6
40	30.3	30.6	24.7	24.7
45	29.3	30.4	-	-
50	28.9	30	-	-

4.3.2 Coating FBAR with poly(vinyl pyrrolidone) (PVP)

Spin coating is probably likely to be the *ideal* method to deposit PVP films onto the FBAR surfaces because it would result in smooth films with controllable thicknesses (*See equation* (2.12)). However, because it was necessary to wirebond the samples ahead of the polymer deposition it was not possible to use spin coating as the attached wires would likely be removed during the spinning process and there could be a substantial delay of up to two weeks to get the wire bonds repaired and in the process there was increased likely hood of FBAR surface contamination. For this reason, spray coating of the polymer layer onto the FBAR device was investigated as a viable choice.. Spin coating would have provided a better method of approach and spray coating, in this case, should be considered a methodological necessity. Due to its inherent simplicity, spray coating of polymers in carrier solvents using air brushes onto BAW devices is a well established method of film deposition, and spin coating is rarely used. [5]

The PVP solution of 1.23% weight/volume (W/V) was produced in a fume cupboard by dissolving 0.5g of PVP with a molecular weight of (mr = 40,000), into a clean glass beaker containing 50 ml of methanol. A lid was placed onto the beaker and a magnetic bead was used to help dissolve the PVP which was a white-flaky powder in appearance. Typically, it took about 10 minutes of stirring before there were no longer any visible particles of PVP remaining in the methanol and it was considered sufficiently dissolved to be transferred to the delivery spray cartridge.

Batches of the 1.23% W/V PVP in methanol solution were transferred to a delivery spray cartridge (*See Figure* 4.3(B)) which had been previously rinsed in methanol. Under a fume hood, PVP in the methanol carrier was sprayed onto FBARs using an artist's airbrush capable of delivering variable spray atomisation droplet sizes. The spray nozzle was set to fine to give the smallest droplet size possible The airbrush nozzle was placed in retort stand and sprayed horizontally (to avoid gravity drops), it was switched on for 10 seconds before contact with the FBAR samples, this was to ensure that a regular rate spray was achieved by allowing the pressurised propellant to stabilise its output.

A PCB holding a wire bonded FBAR was then passed by hand through this spray for one second at a distance of 10 cm from the spray nozzle (measured with a ruler). The thickness profile of the PVP on FBAR was measured with Dektak and the spraying process was then repeated, the 2^{nd} pass being equal to 2 seconds coating, the 3^{rd} , 3 seconds an so on. The freshly coated device would be left for a few minutes to ensure the carrier solvent had evaporated before additional spray applied.

PVP was also drop cast onto the FBAR using a plastic pipette, the solvent was allowed ~5 minutes to evaporate off and the profile was then measured with a profilometer. A micrograph of the spray coated polymer film on the FBAR surface is shown below in Figure 4.3 (A) and the delivery apparatus in Figure 4.3 (B).

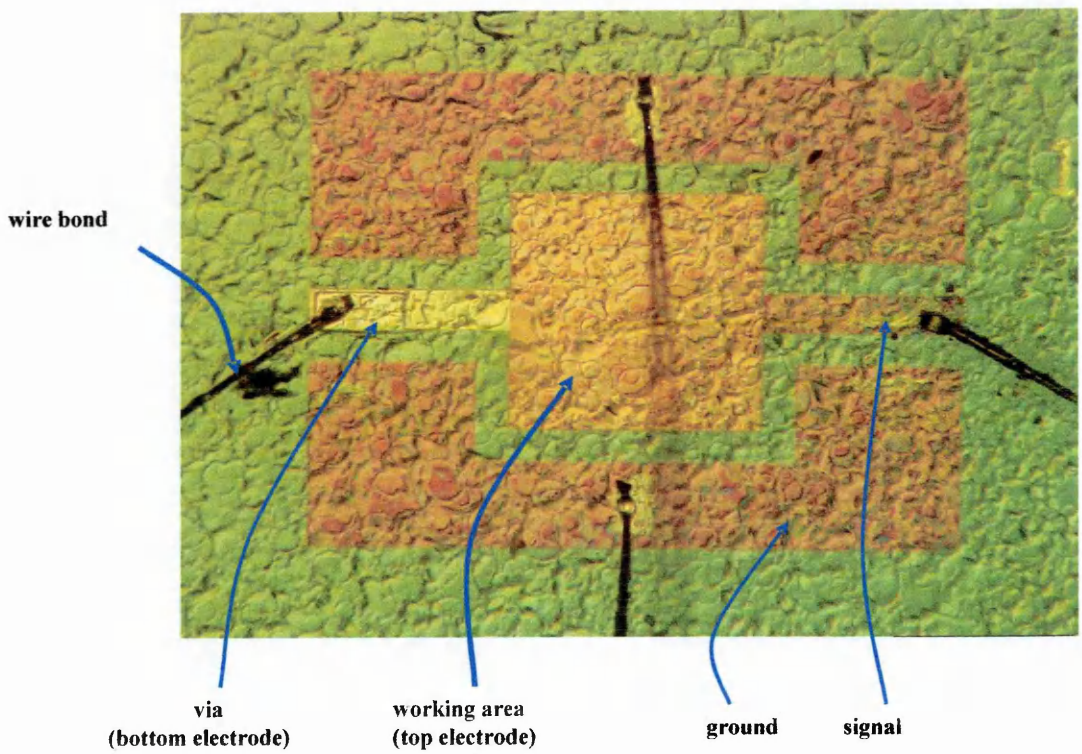

Figure 4.3 (A) PVP coating on FBAR Device 10A on PCB 6 after 5 spray passes.(~5 seconds delivery) Mag X 100 + 2X optical zoom. The mottling effect visible is the polymer coated over entire area of image.

The polymer has not coated the area immediately underneath the wirebond, droplets have formed on the wirebond instead. The chemical structure of the Poly-vinyl-pyrrolidone monomer is shown as an insert in the bottom right hand corner of the image.

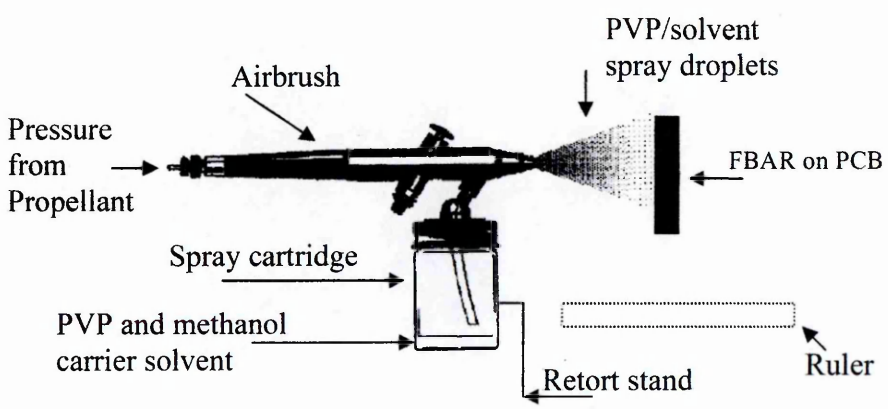

Figure 4.3 (B) Schematic shows air brush used for depositing PVP onto FBAR. Adapted from [5]

4.3.3 PVP thickness profiles

A profilometer (Dektak ®) was used to measure the thickness of the deposited PVP films by scanning over a section where the PVP had been scratched away. The profilometer scans were made over 600μm. Estimation of the thickness of the (1.23% WV) polymer is approximately (1 μm -1.5 μm) per single 1 second spray pass but estimation error increases with each subsequent pass. It appears not to be possible to develop a layer thicker than (~7 μm) using the spray coating method. This is likely due to the carrier solvent re-dissolving the previously deposited polymer and the pressure from the propellant of the air brush needs to be considered in that it may have put limits on the film thickness that could be achieved with this method. Difficulty in giving a precise definitive value for the thickness of the polymer was due to the rough surface profile of the polymer after deposition. Drop casting gave a much smoother coating profile, with nominal thickness of (~3.0μm -3.5μm). Adding subsequent drops did not increase the polymer thickness as this likely merely increased the total amount of polymer deposited over a larger area but did not increase the thickness., (result not shown) *See figure* 4.4 (A-D) for step-thickness surface profiles as measured with the surface profilometer.

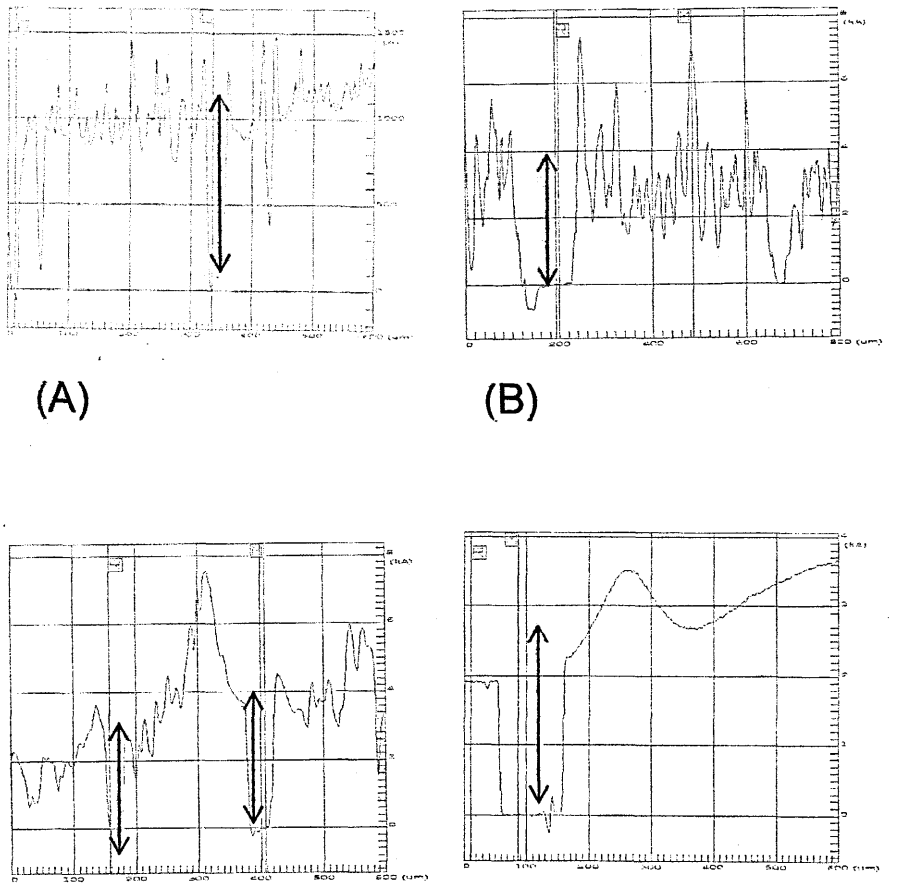

Figure 4.4(A-D). The thickness profiles for PVP (1.2%W/V) on FBAR. (A-C) are spray coated samples with 1, 2, 5, spray passes respectively, (D) is drop-cast. Arrows indicate steps made in the PVP layer.

The thicknesses are (A) = ~1μm, (B) = ~2 to 4 μm, (C) = 3 to 4 μm with increased error to 6μm and (D) = ~3.5μm.

4.4 Experimental section. (Experiments 1 to 7.)

4.4.1 Methods

All of the experiments described below were performed on wire bonded FBAR samples that were isolated from the ambient laboratory conditions by being sealed in the FHA.

Experiment 1 was split into three parts, 1A-C. Experiment 1A was devised to examine the S_{21} series resonance frequency response of FBAR to changes relative humidity when it was uncoated. Experiment 1B looked at the stability of the S_{21} series resonance frequency response of FBAR over time when it was coated with the PVP polymer film and exposed to a dry gas stream. This was done to ensure that there were no unexpected aberrations in the baseline due to the presence of PVP. Experiment 1C examined the S_{21} series resonance frequency response of the FBAR over time to changes in relative humidity (%RH) when it was coated with PVP. This was done to establish whether or not the applied polymer coating increased the sensitivity of the FBAR to changes in relative humidity.

Experiment 2 was split into two parts, the first, experiment 2A looked at the effect that the polymer loading was having on the shapes of the resonant peaks of the FBAR primary and harmonic overmodes whilst experiment 2B looked at the relative changes in S_{21} series resonant frequency responses for the primary modes and overmodes in response to changes in relative humidity.

Experiment 3 was designed to determine the reproducibility of the FBAR response to phases of successive wetting and drying, here along with changes in S_{21} series resonant frequency, the S_{21} power transmission and the Q factor are also examined.

Experiment 4 was done in two parts, 4A looked at the effect of increasing the thickness of the polymer film on FBAR resonance shapes in high humidity and in low humidity whilst experiment 4B was designed to ascertain the effect of variation in polymer thickness on FBAR S_{21} series resonant frequency in various concentrations of humidity.

This experiment was performed to determine if there was significant power loss from acoustic probe wave signal attenuation (i.e., damping), as well as frequency decrease due mass loading in the presence of the deposited polymer film. It was assumed that this would be the case since the polymer layer was known to be soft and therefore lossy.

Experiment 5 was also split into two parts, the first, experiment 5A, turned its attention additionally to the effect of the concentration of the polymer that made up layer as well as the layer thickness. A higher concentration of polymer was used for this experiment and FBAR characteristic resonance curves were examined in response to increasing thicknesses of high molecular weight polymer film in dry gas and in wet gas the resonant frequency along with the S_{21} power transmissions and Q factors are examined. The resonance frequencies of the FBAR under the various loading conditions over time are examined in the presence of variations in the relative humidity of the gas stream.. Experiment 5B looked at the S_{21} series resonance frequency response of the FBAR with a drop cast high molecular weight polymer layer on its surface with variation in the relative humidity in the gas flowing over the FBAR surface. The results were compared with the results of experiment 4 which used a lower concentration of polymer for the film deposition

Experiment 6 attempted to discover if the polymer layer could be completely removed from the FBAR surface so that the devices could be reused as they were in limited supply.

Experiment 7 was performed to confirm that the results of experiment 6 were not anomalous because they were unexpected.

4.4.1.1 Experiment 1A Observing the response of uncoated FBARs to changes in humidity in a nitrogen stream flowing over the FBAR surface of the FBAR top electrode

Experiment 1A was devised to reveal whether coating FBAR with polymeric PVP made it sensitive to humidity. This was demonstrated by comparing the response of an uncoated FBAR (Experiment 1A) with that of a coated FBAR (experiment 1B, 1C). In

effect, the response of the uncoated FBAR acts as a control experiment. For both experiments the sensitivity to humidity was monitored over the experimentally accessible humidity range.

After turning on the Peltier heater, the temperature of the FHA was allowed to stabilise for about 1 hour. After this time, the FHA was reasonably impervious to small fluctuations in room temperature. FBAR device 10A on PCB 5, without the addition of any polymer film, was placed into the housing chamber which was sealed and connected to the gas-inline and to the network analyser. Further time was given to allow the recently placed PCB and FBAR Si die to reach temperature also (~20 minutes). The network analyser was switched on for an hour or so before testing commenced.

The N_2 gas stream was humidified by bubbling through the water bath and mixing the wet line into the dry line and adjusting the flow rates allowing the system to stabilise in high humidity (~70 %RH). This allowed the generation of a baseline from FBAR S_{21} responses in high humidity. After 200 seconds, the gas stream was redirected through the drying crystals and the wet line was closed, this gave an N_2 gas flow with (< 20% RH). At ~700s the wet line was once again mixed into the stream to give (~65% RH)

The S_{21} series resonant frequency of FBAR was shown in relation to the computerised humidity data logger. Multiple scatter plots of FBAR S_{21} series resonant frequency (Δf_0) vs. relative humidity (Δ%RH) over time (s) were produced. Both measured frequency and polynomial fitted frequency data are shown to examine the effectiveness of the 2^{nd} order polynomial fitting at reducing system noise and thereby increasing useable sensitivity of the output response, this had previously been demonstrated for improving FBAR sensitivity to temperature, but not for humidity changes.

Settings for Experiments (1A), (1B), & (1C) were
FBAR used was Device 10A on PCB 5
Centre Frequency: = 701.0 MHz (second overmode)
Span Frequency: = 5.0 MHz
Points in sweeps: = 1601
IF Bandwidth: = 300
N_2 Gas flow rate: = > 150 SCCM

4.4.1.2 Experiment 1B Observing the baseline responses for PVP coated FBAR in a dry N_2 gas flow and making comparison with uncoated device

The FBAR coating used in this experiment resulted from one second spraying of the PVP solution, giving a final thickness of ~1.2μm ± 0.24μm. The carrier gas was directed through the dry line (i.e., passing through the silica crystals) for some time before starting S_{21} data acquisition, and the iterative f_0 baseline for this response was obtained for a 350 second time period to determine the stability of PVP coated FBAR responses in a dry gas with steady flow rate of (>150 SCCM). The humidity of the gas was controlled with the mixing taps to attempt to keep it as close as possible close to 20% RH which was the minimum limit of detection that could be recorded by the humidity meter that was sending data directly to the computer.

The frequency stability of the FBAR was checked to ensure that there were no anomalous readings generated due to either (i) the presence of the polymer on FBAR top surface electrode or (ii) the gas flow (iii) miscellaneous environmental fluctuations. Once a baseline value was obtained and evaluated for PVP coated FBAR in dry gas flow, (>150 SCCM) the stability and drift values were established for both the S_{21} resonance frequency of the device (Hz) and the S_{21} transmitted power (dB) over time (360 s). These results were compared with the original responses of the uncoated device in dry gas at the same flow rate from experiment (1A) under very similar experimental conditions. This was done to determine if there was increased sensitivity to the presence of measurand implied by more frequency change to the same amounts of measurand between the same FBAR unit in a polymer-coated and uncoated state.

4.4.1.3 Experiment 1C Observing the effect of changes in relative humidity from <20% to ~30% of the N_2 gas flow over PVP coated FBAR S_{21} series resonance response.

Before starting the experiment, the gas flow was directed through the dry line for some time (~20 minutes) to remove any residual moisture in the PVP layer (and inside of housing assembly) that resulted from adsorption from the ambient conditions in the laboratory during the coating procedures. If the humidity meter was out of range (<%RH20) the gas was taken to be dry. The data acquisition procedure commenced in a

dry gas flow and the baseline response for PVP coated FBAR was established during ~200 seconds in the dry gas, the wet in line was then mixed into to the flow for ~150 s to bring the humidity to (~ %RH 30.5) The wet mixing line was then closed, leaving the only dry line to feed the system, and the system was allowed to dry over the remainder of the experiment which was terminated at t=900 s. The controlled rate of gas wetting and gas drying are approximately equal, changing from 20% to 30% or vice versa over ~150 seconds this being achieved by careful manual adjustment of the mixing taps. The flow rate was steady (>150 SCCM).

4.4.2 Results

4.4.2.1 Humidity experiment (1A)

The effect of Δ%RH in the range %RH70 to <%RH20 in the N_2 gas flow over uncoated FBAR is shown in Figures 4.5 (A) and 4.5 (B). The actual measured data from the FBAR seen in Figure 4.5 (A) is, as expected, noisier (and more quantised) than the polynomial fitted data shown in figure 4.5 (B), but both measured and fitted traces are in good agreement, giving confidence enough to store, but not show, the measured data from the remaining experiments performed in this chapter. This is because it is more difficult to extract a clear response pattern for f_0 from the directly measured data due to the influence of the increased quantisation (point to point minimum spacing) and noise[80]

The fitted data shows that temperature stabilised ($< \pm 0.1^{\circ}C$) FBAR responds to the changes in the amount of water vapour (%RH range = ~70% - < 20%) in the delivery N_2 stream over ~16 minutes. A total (12 kHz) FBAR S_{21} series resonance frequency change was observed in relation to the recorded humidity change. The rates of change for the responses of humidity meters and the FBAR were in reasonable agreement.

The most rapid rate of change for the FBAR and the humidity meter occurred within the first 10 seconds of changing the gas stream from wet to dry or vice versa. It was assumed that the continued increase in frequency observed on FBAR whilst the humidity mete

[80] This noise interference could be from electronically generated random noise in the network analyser and also from FBAR lateral modes of resonance – these lateral modes were thought to contribute to the manifestation of spurious modes of resonance in the FBAR.

was out of range and the gas taken to be dry was due to the continued removal of residual physically adsorbed water films held the grain of the au surface of FBAR top electrode. It is likely that complete removal of monolayer H_2O over the FBAR surface will not be achieved using this method.

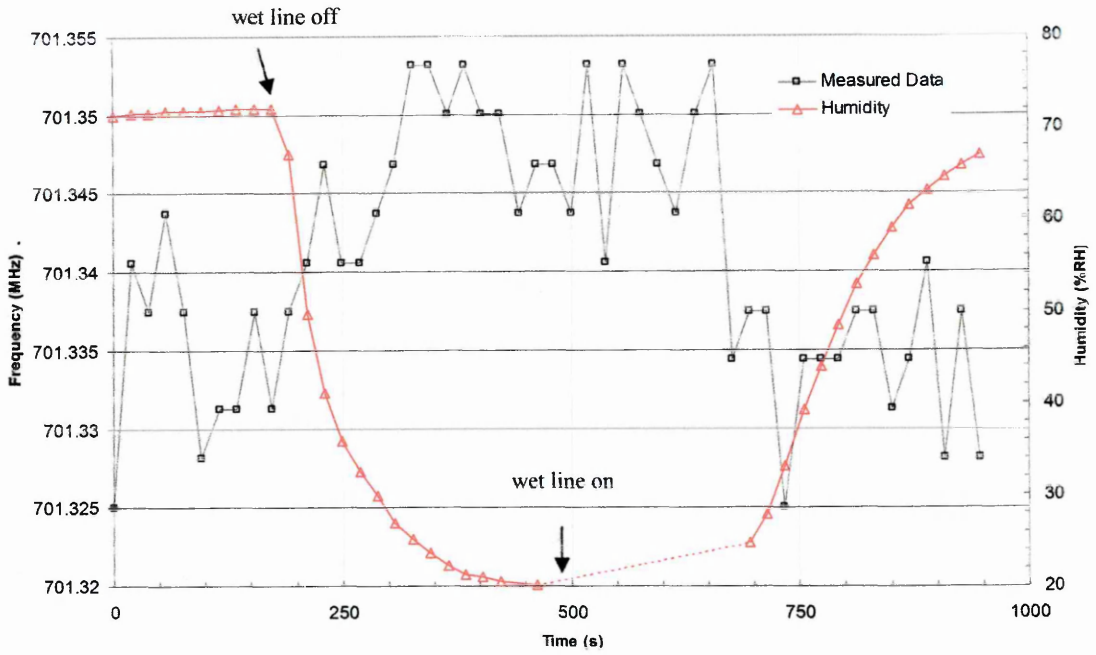

Figure 4.5(A) Measured S_{21} series resonance frequency response of *uncoated* FBAR layer in N_2 stream with flow rate <150 SCCM with humidity range over (%RH70 - ~ <%RH20)

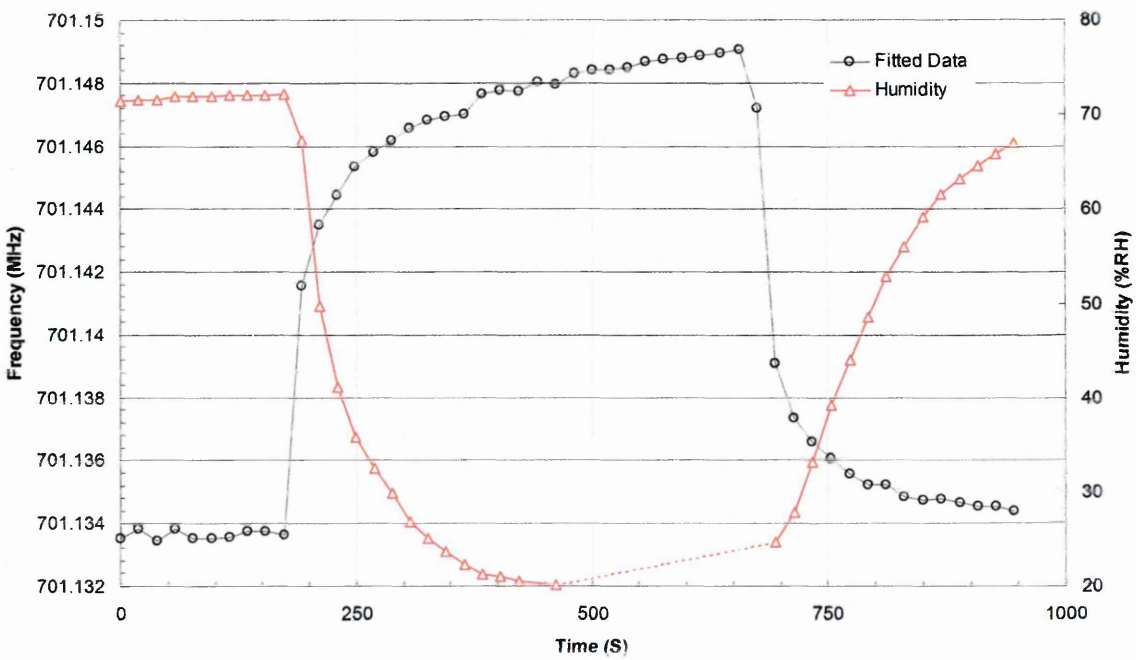

Figure 4.5 (B) Fitted S_{21} series resonance frequency response of *uncoated* FBAR in N_2 stream with humidity range over (%RH70 - ~ <%RH20)

4.4.2.2 Humidity experiment (1B)

Figure 4.6 (A) shows the baseline responses for PVP coated FBAR in a dry N_2 gas flow that were established over time as successive/iterative f_0 determinations. The polynomial fitted baseline responses for the uncoated FBAR were determined over 400 seconds for both S_{21} series resonance frequency f_0 (Hz) and S_{21} transmission power (dB) in a dry (~ %RH 20) N_2 gas stream with flow rate (>150 SCCM). The frequency drift is (~ + 200 Hz). and the transmitted power drift is (~ +0.0015 dB) over 400s. Temperature was stable (<+ 0.1^{O}C)

Figure 4.6 (B) Shows the FBAR S_{21} series resonance frequency and S_{21} power transmission responses after it was spray coated for 1s to give PVP layer of (~1.2 µm) thickness and interrogated to produce a baseline response in dry gas over the same time period with the same settings as in figure 4.6a It demonstrates that over 400 s, the frequency drift for the PVP coated device in dry gas flow is (~ + 3.5 kHz) Therefore the rate of drift is (+ 8.75 Hz s^{-1}) and the transmitted power drift is (~ + 0.1 dB) over the same time period.

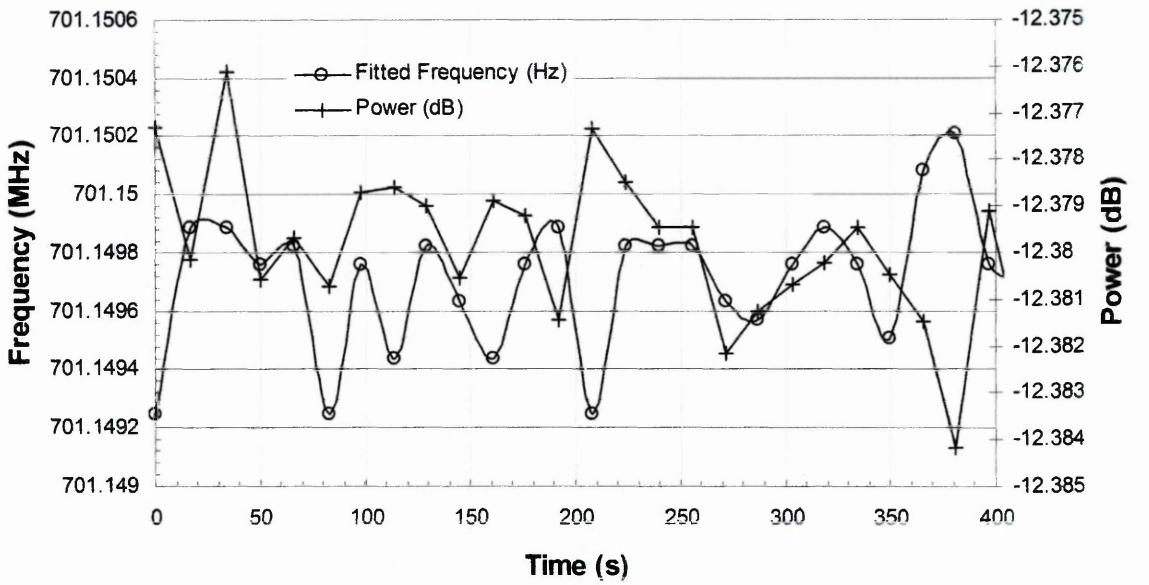

Figure 4.6(A) Baseline response (400s) of uncoated FBAR in dry gas flow (>150 SCCM) (20% RH). Fitted polynomials for both S_{21} series resonance frequency (Hz) and power response (dB) of the device are shown.

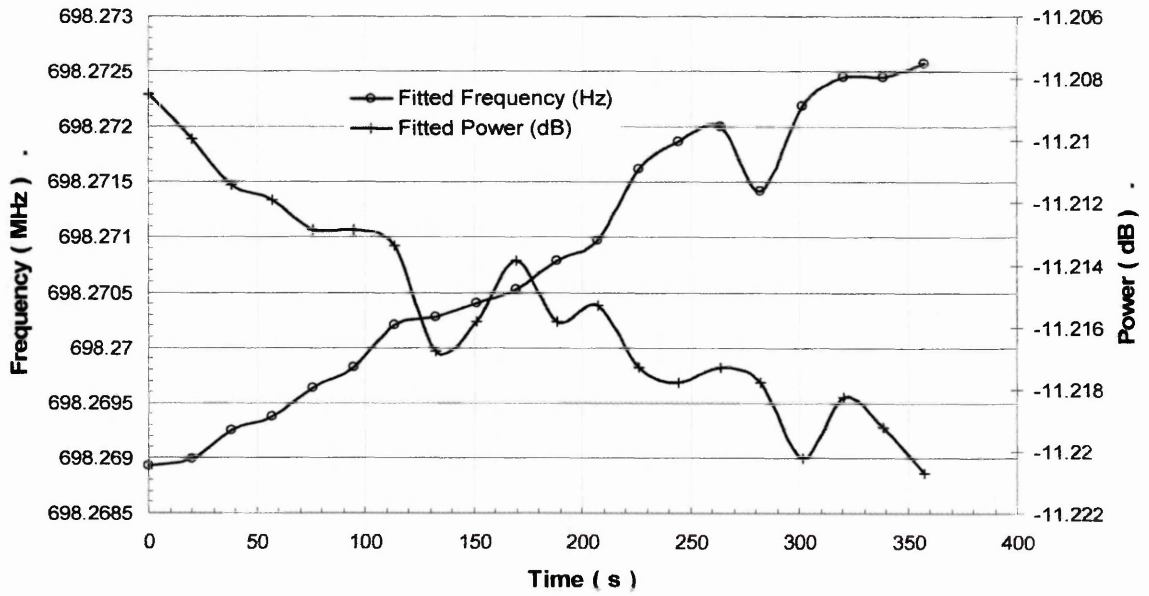

Figure 4.6 (B) Baseline responses (360s) of PVP coated FBAR (1 Spray pass (1 s) (~1.2 um + 20%)) in dry gas flow (>150 SCCM) (~ %RH 20). Fitted polynomials for both S_{21} series resonance frequency (Hz) and power response (dB) of the device are shown.

4.4.2.3 Humidity experiment (1C)

Figure 4.7 shows the effect of Δ%RH (<20% to ~30%) of the N_2 gas flow (>150 SCCM) over PVP (~1.2μm thickness (± 20%)) coated FBAR f_o (Hz) responses was determined The system was exposed to dry gas for some time before starting the data recording. The humidity values as given by both humidity meters were out of range, implying a dry gas flow from the beginning (t=0 s) of the experiment until 200 seconds mark, which accurately reflected the time point at which the wet line was mixed into the dry line. Both of the humidity meters and the PVP coated FBAR showed rapid response to the presence of the increased humidity in the flow. The FBAR response saturated faster than the humidity meter, most of the FBAR response ($-\Delta f$ = 670 kHz) occurring within 10 s of mixing humidity into the stream, a negligible continued decrease in resonant frequency (< - 50 kHz) is seen as the humidity meter continued to record an increase in relative humidity from 20% to 30% over 150 s. This may be due additional water retention in the PVP layer but occurring at a much reduced adsorption rate than that of the dried PVP layer.

The humidity of the gas was then decreased by switching off the wet line feed to the system, immediately this was done, the FBAR was seen to respond by increasing its resonant frequency by ($+\Delta f$ = ~ 560 kHz) within 10s. The humidity meter also responded quickly (within 2s) and continued to record a fall in relative humidity for another 150s until it went out of range at %RH 20. Over the same time period, the FBAR continued to show a relatively small resonant frequency increase (($+\Delta f$ ~ 50 kHz) until the end of the experiment at (t=900s) never quite reaching the original dry resonance frequency of (~ 698.27 MHz,) but asymptotically approaching it. The fact that the FBAR responded more quickly to the presence of humidity is because the PVP layer was so thin and could therefore saturate with humidity faster than the humidity meter.

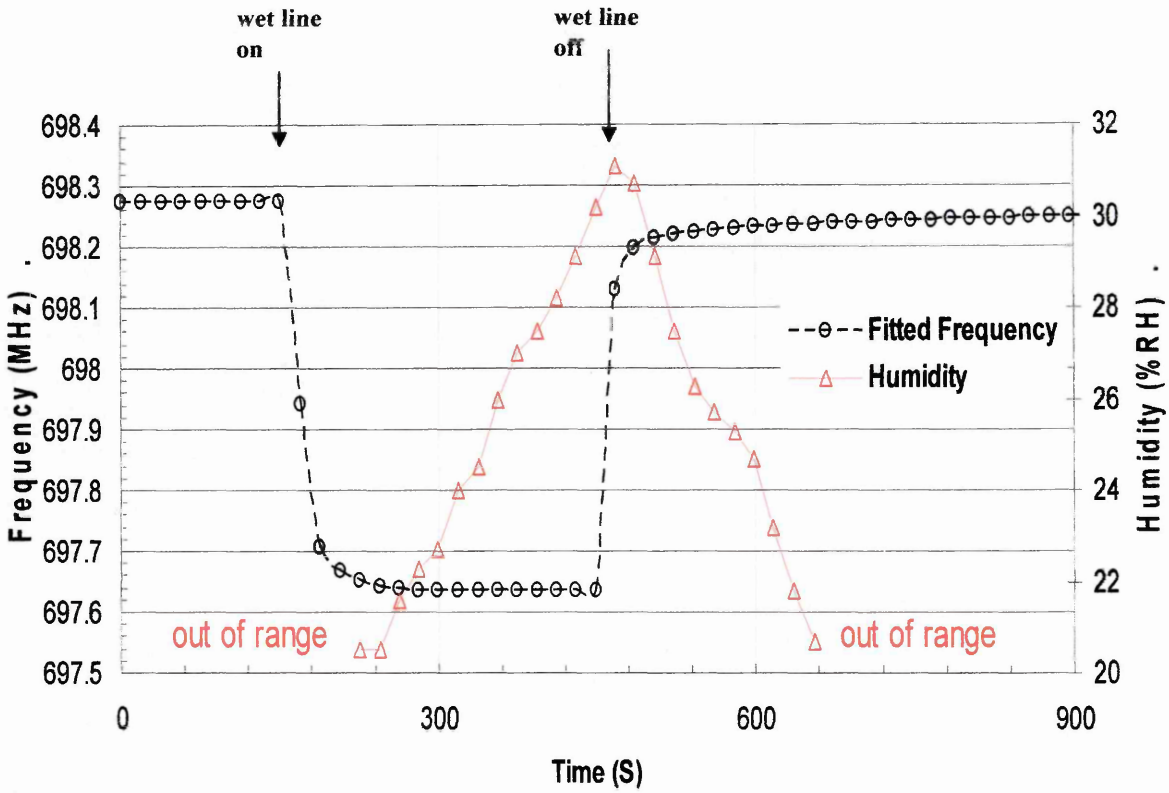

Figure 4.7 Shows the effect of changes in relative humidity on fitted S_{21} series resonant frequency of FBAR coated with PVP (~1.2 μm thickness) in stable (<+ 0.1^{O}C) temperature over time t = 900 seconds

4.4.3 Humidity Experiment (2A) Observing effect of polymer loading on FBAR primary and overmode S_{21} series resonant frequency characteristic response span shapes

4.4.3.1 Methods

The FBAR device 10A on PCB 13 was used for these tests because it had been previously shown from on die measurements to posses good response characteristics. The reason that the device is a different unit than the one used in the previous experiments is due to wire bond failure. The resonant frequency characteristic shapes recorded for the primary and overmodes recorded with no additional PVP load on its surface whilst it was isolated within the FHA. The primary mode was centred at (324.5 MHz), the first overmode centred at (701 MHz), and the second overmode centred at (956 MHz).

The effect of a 1s spray coating (~1.2 μm thickness) on the shapes of each of the resonant frequencies was observed in ambient room humidity and temperature to determine directly the effect that polymer load was having on the FBAR primary and overmode characteristic response shapes.

4.4.3.2 Results

The results shown in figures 4.8 (A), 4.8(B) and 4.8 (C) shows that the effects of loading the polymer are amplified as higher frequency overmodes are used to examine the effects on S_{21} series resonance frequency for *identical* PVP loading. At the highest frequency overmode, the Q factor was influenced along with resonant frequency and S_{21} transmitted power responses. Q factors did not appear to be influenced for the primary mode or the 1st overmode. The results are tabulated in Table 4.2, below

Table 4.2 Shows the responses of FBAR S_{21} primary and overmode characteristic resonant frequency curve shapes and f_0 (MHz) and power (dB) when device was coated with ~1.2 μm of PVP (W/V 1.23%) over top electrode.

	S_{21} resonant frequency Δf_0 (MHz)	**S_{21} transmitted power Δ_{power} (dB)**	**Notes on response shape or on Q factor**
Primary mode Centre = 325 MHz	-1	- < 0.5	Q factor no significant change
Overmode 1 Centre = 700 MHz	-2.5	+ < 0.5	Q factor no significant change
Overmode 2 Centre = 950 MHz	-3.5	+ < 1.5	Q factor diminished. and power responses attenuated

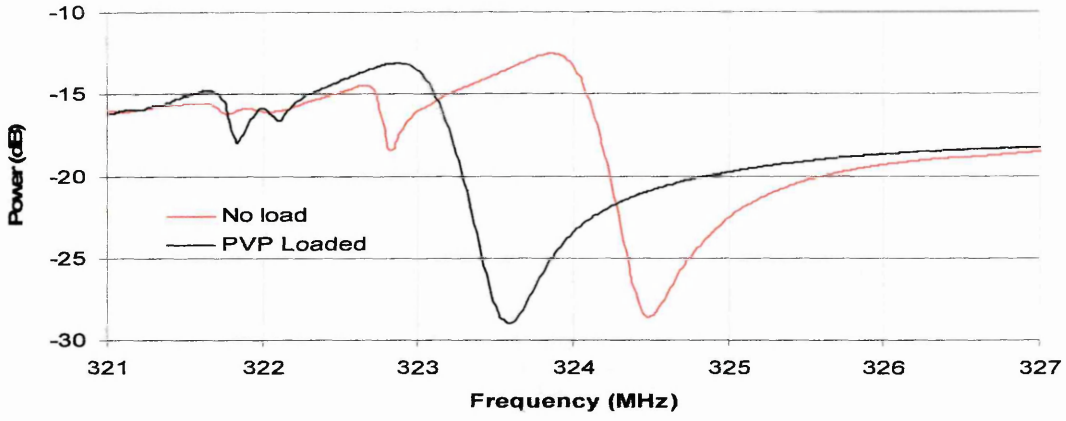

Figure 4.8 (A) Effect of PVP (1s) spray loading on FBAR primary resonance curve

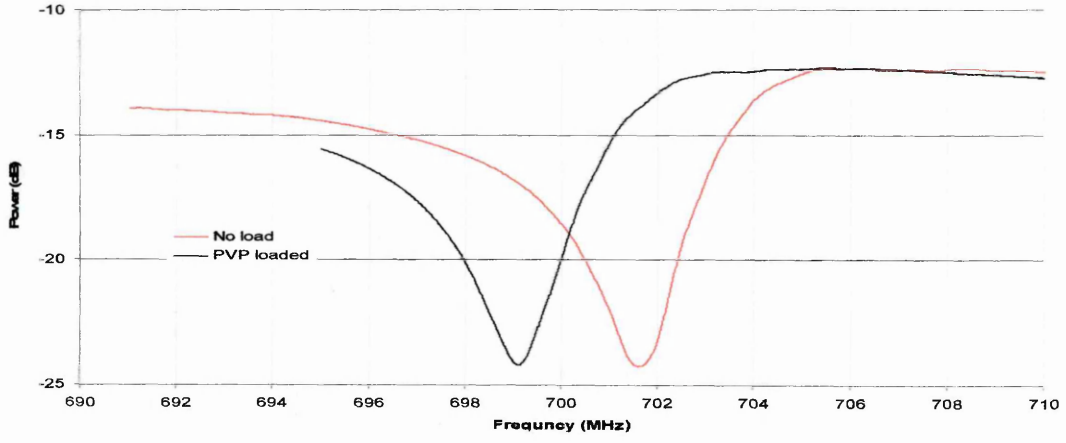

Figure 4.8 (B) Effect of PVP (1s) spray loading on FBAR overmode 2 resonance curve

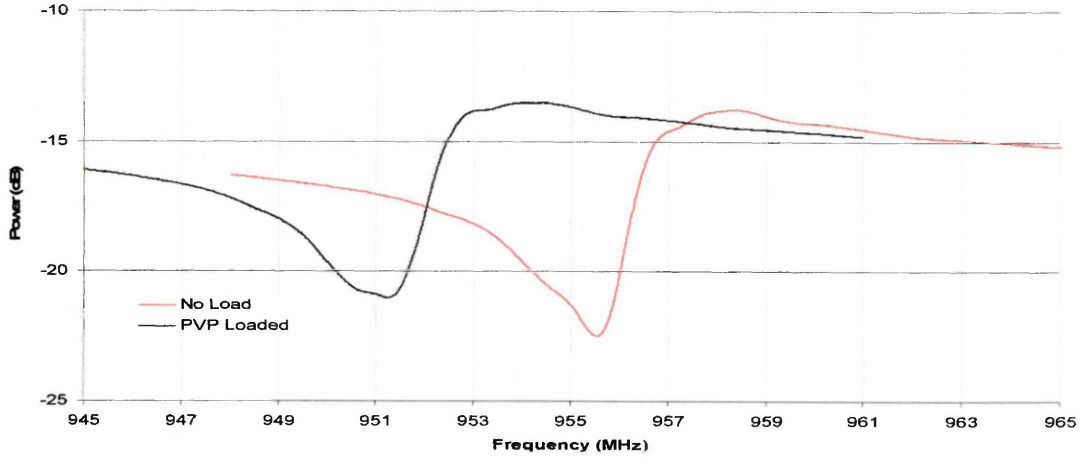

Figure 4.8 (C) Effect of PVP (1s) spray loading on FBAR overmode 3 resonance curve

4.4.4 Experiment 2B Observing the effect of changes in relative humidity on PVP coated FBAR for the primary resonant frequency and the 1st and 2nd harmonic resonant overmode frequencies.

4.4.4.1 Methods

The polymer coated FBAR device 10A on PCB 13 was tested for responses to Δ%RH the humidity range was %RH20 minimum to %RH65 maximum The N_2 gas stream was mixed through the dry line only for some time before starting the experiment to stabilise responses of PVP coated FBAR to dry gas. At t=0 seconds, the humidity meters were both out of range, and baselines were obtained for this value over approximately 60 seconds, at which point the wet line was mixed into the gas stream to increase the relative humidity of the gas stream entering the FHA where the FBAR was operating.

Humidity was allowed to rise for a further 90s, bringing the %RH as recorded by the humidity meters to (~% RH 65). At t=160 seconds, the wet line was closed off, the humidity meters both displayed rapid decreases in responses falling out of range within 20 seconds indicating that the gas was dried within this amount of time. The experiment was left to run in dry gas stream (<%RH20) and was terminated at t=200 seconds.

Direct comparisons on the effect of humidity change over the primary or fundamental resonance frequency and the harmonic resonance overmodes of the FBAR were made. So this process was performed initially with the NA span set to encompass the FBAR fundamental resonance mode (~ 323 MHz,), then repeated whilst centred around the 1st (700 MHz) and 2nd (953 MHz) harmonic overmodes. Responses were recorded as XY scatter graphs showing FBAR $f_{0(n)}$ vs. computerised humidity meter responses (%RH) over time (s) for each of the resonance modes.

The FBAR recorded data resolution[81] was decreased substantially from the settings used in experiment 1. The number of collected data points was decreased from 1601 to 801, this had the effect of decreasing the amount of time required for the network analyser and

[81] The resolution in this case means (i) point to point minimum spacing between successive iterations (*See Table* 3.1) and (ii) The noise floor compensation from the IFBW settings (*See Figures* 3.13 and 3.14)

the computer to complete an iteration. The span frequency was increased to 20 MHz and the IFBW sensitivity was reduced by increasing the setting from 300 Hz to 1000 Hz this further decreasing the time required to complete the iteration.. These settings were modified to attempt to bring data points for FBAR into the trace during the limited time window (~ 10-20s) in which rapid responses were observed from the FBAR and the humidity meter in response to changes in relative humidity. The FBAR actual data points could then be compared directly with data points from the humidity meter during the a linear segment of the trace.

A number of settings were attempted (results not shown).The setting parameters shown below represented the best balance, where a relatively high degree of sensitivity was still maintained whilst increasing the time resolution of the responses.

The settings for experiments (2A) & (2B) were:
Centre Frequency MHz: (i) 323 MHz, (ii) 700 MHz, and (ii) 953 MHz
Span Frequency: 20.0 MHz
Points in sweeps: 801
IF Bandwidth: 1000 Hz

4.4.4.2 Results

Figures 4.9 (A), 4.9 (B) and 4.9 (C) shows the effect of Δ%RH (range = 20%-65%) on the N_2 gas flow (>150SCCM) over PVP (~1.2μm thickness) coated FBAR for the primary or fundamental resonant frequency and the 1st and 2nd harmonic resonant overmode frequencies respectively.

The dry gas (< %RH20) flow was used to establish baseline responses for the primary and overmodes for 60 seconds before allowing the humidity of the gas to rise to(~ %RH 60) over a further 90 seconds. At ~ t= 150 s, the wet line was closed and both FBAR and humidity meters confirmed this change by responding within a few seconds to the decrease in the relative humidity of the N_2 gas stream whilst the FBAR was seen to respond by rapidly increasing its S_{21} series resonant frequency to a value close to the

original dry base line value within 10s, and the humidity meter falling out of range (<%RH20) within 20s. The results are tabulated in table 4.3 below.

Table 4.3 Change in FBAR S_{21} series resonance responses $f_{o(n)}$ (MHz) from dry gas (<%RH 20) to high humidity in N_2 gas (%RH65) flowing over FBAR sealed in the FHA.

	Frequency (MHz) @ Humidity (<%RH20)	Frequency (MHz) @ Humidity (%RH65)	$-\Delta f_0$ (MHz)	% change
Fundamental mode	**323.73**	**323.3**	**0.43**	**0.133**
Overmode 1	**699.4**	**698.23**	**1.17**	**0.167**
Overmode 2	**951.4**	**949.3**	**2.1**	**0.221**

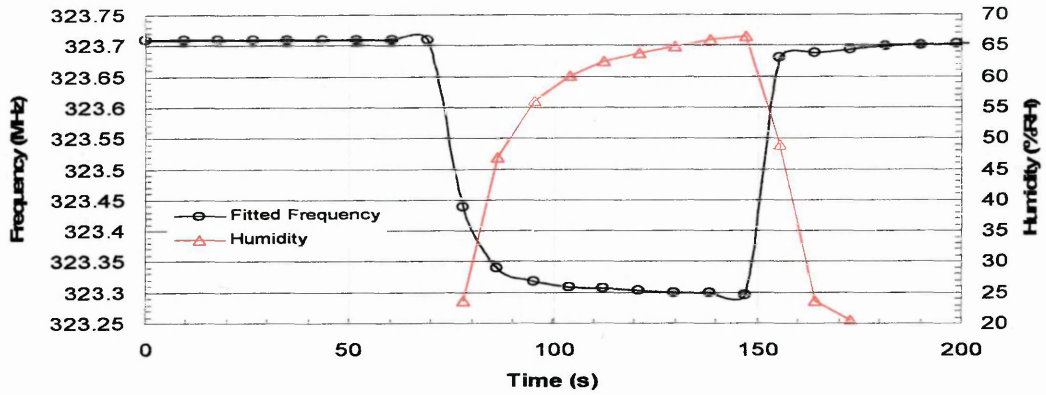

Figure 4.9 (A) Effect of humidity variation on PVP coated (1second) FBAR S_{21} primary resonance frequency over time

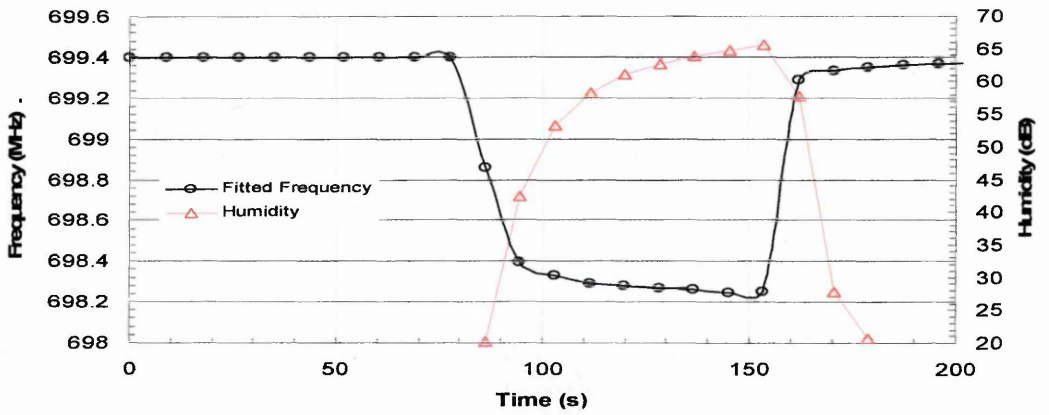

Figure 4.9(B) Effect of humidity variation on PVP (1 second) coated FBAR S_{21} on overmode 2 over time

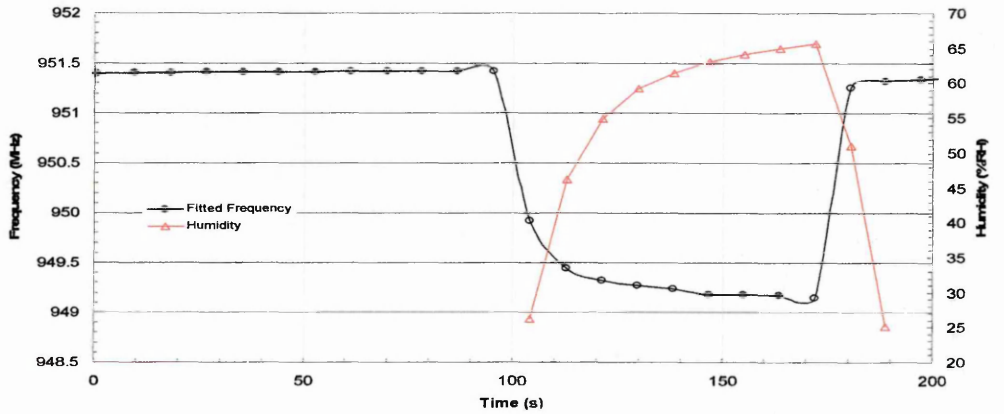

Figure 4.9(C) Effect of humidity variation on PVP (1second) coated FBAR S_{21} on overmode 3 over time

4.4.5 Experiment 3 Reproducibility tests

4.4.5.1 Methods

Once it was clearly established that the FBAR was sensitised to measurand (water) by the addition of the sensitising (PVP) layer, it was desirable to establish the reproducibility of the responses. This was achieved by cyclical exposure (23 cycles over 850 s) of the PVP coated FBAR to low levels (<%20) and high levels (~maximum %RH 56) of humidity in the gas stream. The device was allowed to stabilise in high humidity for some time, at t=0 the humidity was high (~%RH55). Every 30s, the humidity was varied by closing and then opening the wet line. On the 16th wet/dry cycle, the wet in line was left on for 1 minute, two more wet/dry cycles were performed before leaving the wet line switched on for approximately 2 minutes until the experiment was terminated at ~ t=850s.

The responses of FBAR to successive iterations of wet/dry cycling were recorded and presented as 3 graphs for (a) frequency (Hz) (b) power (dB) and (c) Q factor, these are overlaid with the humidity values as recorded by the humidity meter for comparisons as multiple scatter graphs over time. Graph of minimum responses to high and to low humidity exposure for FBAR frequency per iteration was constructed manually from the recorded data to show the decay of f_0 over time (~850s).

The settings for the reproducibility tests were,

FBAR Device 9 on PCB 7
Centre Freq MHz: 690.
Span Freq MHz: 25.
Points in sweeps: 801
IF Bandwidth: 1000

4.4.5.2 Results

Figure 4.10 (A) shows the polynomial fitting of the measured response of FBAR S_{21} series resonance frequency (Hz) over ~850 seconds to 23 cyclical variations of high (~%RH 55) and low(~%RH35 -25) humidity[82]. The FBAR f_0 value is seen to rise when the humidity is decreased to (%RH 36), ($-\Delta f$ = ~0.85 MHz) corresponding to (~Δ%RH 20.)

This pattern rising and falling f_0 was cyclically demonstrated as reproducible over the entirety of the test. However a clear decay in the FBAR frequency minima on each successive wet cycle is visible on the graph, this is shown as a manually generated graph,. (*See Figure* 4.10 (D)).

Figure 4.10 (B) is a graph of the polynomial fitting of the minimum S_{21} power transmission of FBAR under identical conditions as those of (Figure 4.10 (A)). A trend spanning roughly (0.5 dB) per wet/dry iterative cycle is visible and this compares well with both the humidity data and the FBAR frequency data, but note that the power transmission response is improved (i.e., more negative, less transmission) during the dry cycle corresponding to a frequency rise. The converse is true when the humidity is increased. A similar decay pattern in power response can be seen but this time it represents subsequent drying cycles rather than wetting or humidifying cycles

Figure 4.10 (C) shows theQ factor response calculated at the 3 dB bandwidth. The Q factor changes by approximately 100 Q units per wet/ dry cycle, indicating that there is significant damping of the characteristic FBAR resonant frequency curve during its exposure to high humidity gas flow. The response is seen to change rapidly and compares well with humidity rates of change and can be aligned almost perfectly to both Figure 4.10 (A) and (B). The decay seen in Figure 4.10 (A) and (B) is also apparent in the Q

[82] The requirement for manual adjustment of the wet/dry mixing taps meant inevitable error in humidity control when changing the sample and repeating the experiments.

response, but increased quantisation of the data make it much more difficult to observe on the graph.

Figures 4.10 (D) and 4.10 (E) are manually generated XY scatter graphs created by obtaining the minimum frequency values of FBAR in response to wet cycling at ~%RH50 and dry cycling at ((~%RH 30) with (error ~ $\pm$ %15)) They demonstrate the decay in response of FBAR highlighting the poor reproducibility of FBAR to successive wet/dry cycles.

The maximum total error over ~850s and 23 wet/dry cycles is roughly (200 kHz), this is a substantial error when considering the maximum change in FBAR resonant frequency over the maximum humidity ranges was only (850 kHz) at a nominal operating frequency of (~ 700 MHz). There was no immediately obvious frequency decay pattern observed for the FBAR on its return to low humidity from the graph (4.10(A)), but manual processing of the data did reveal a small (~47 kHz) rise in frequency over the 23 wet/dry cycles. The R^2 linear trends for both wet and dry FBAR frequency reproducibility decay rates are in good agreement. They are shown separately to highlight the response decay trends which are occluded if they were to be presented on the same sheet. (*See figures* 4.10 (D) and 4.10 (E))

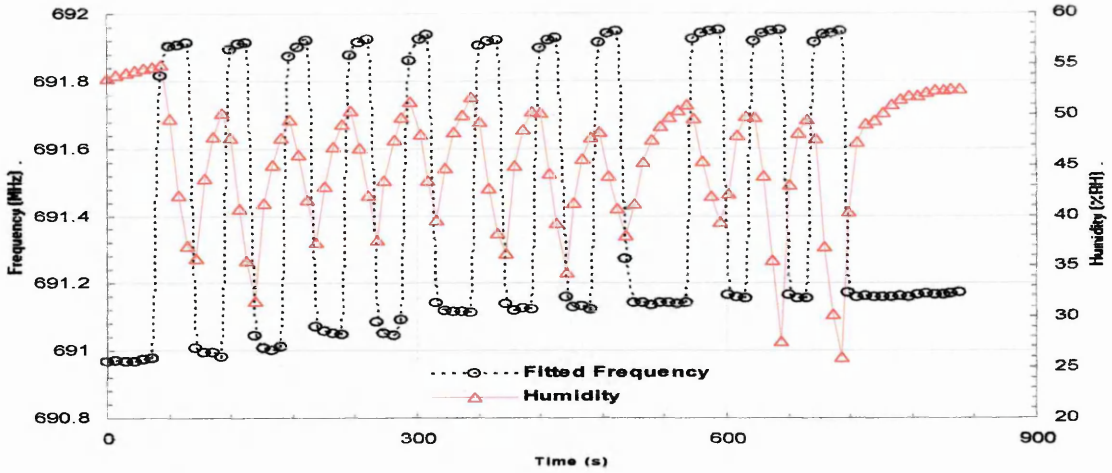

Figure 4.10 (A) FBAR S_{21} Series resonance frequency (MHz) vs. %RH over time. (*see also graphs* 4.10 (D) and (E))

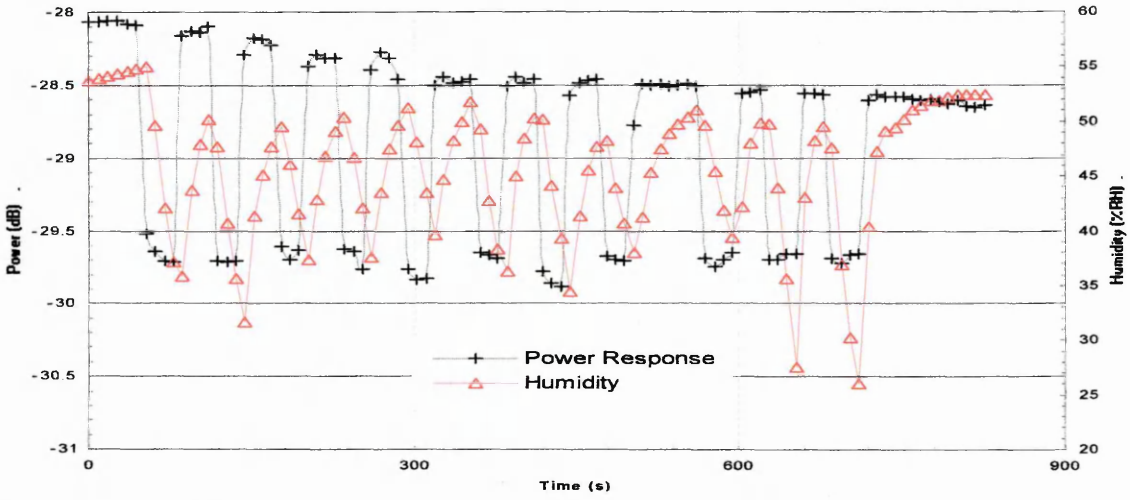

Figure 4.10 (B) FBAR S_{21} minimum transmitted power response (dB) vs. %RH over time

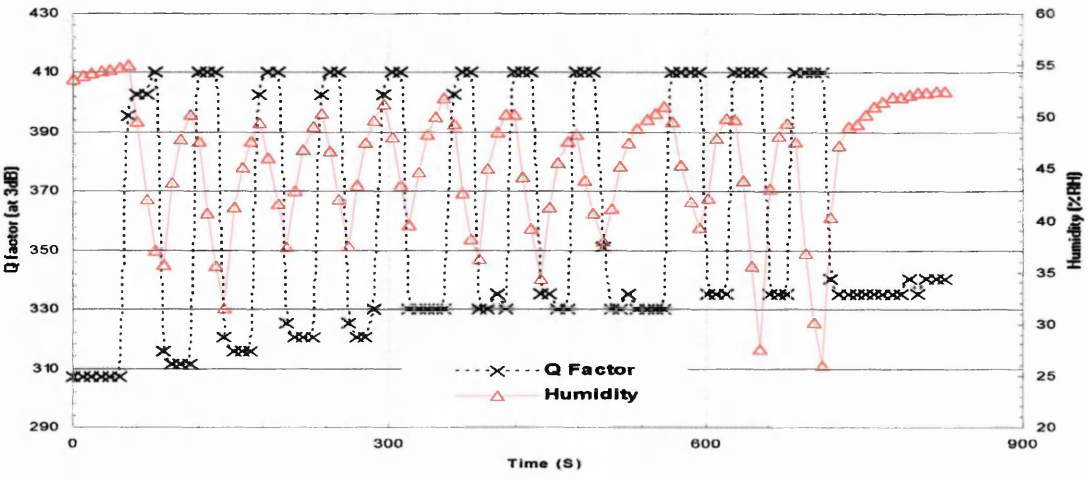

Figure 4.10 (C) FBAR reported 3 dB bandwidth Q factor vs. %RH over time.

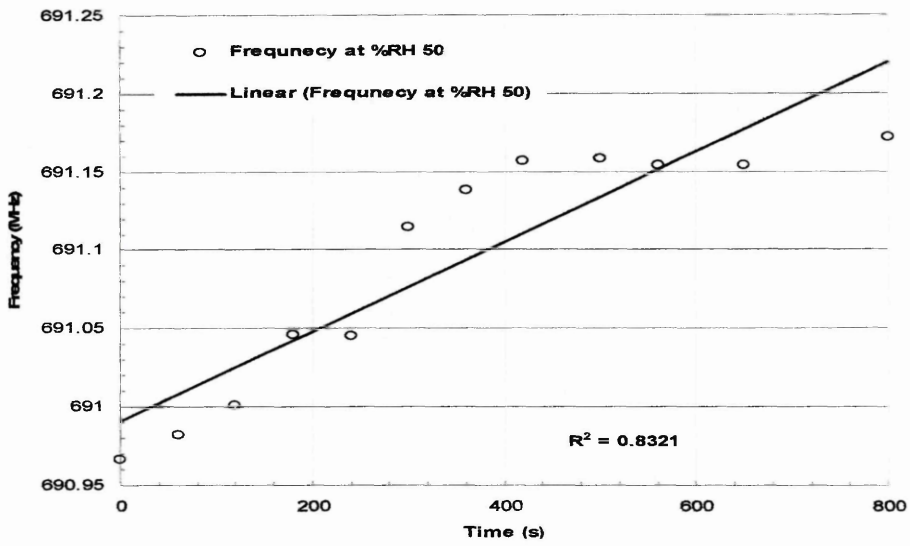

Figure 4.10 (D) FBAR S_{21} response (from Figure 4.10(A) at successive iterations of *humidifying* phase of the cycle. ($\Sigma\ \Delta f_o = \sim +\ 200$ kHz over 800s (final wetting phase))

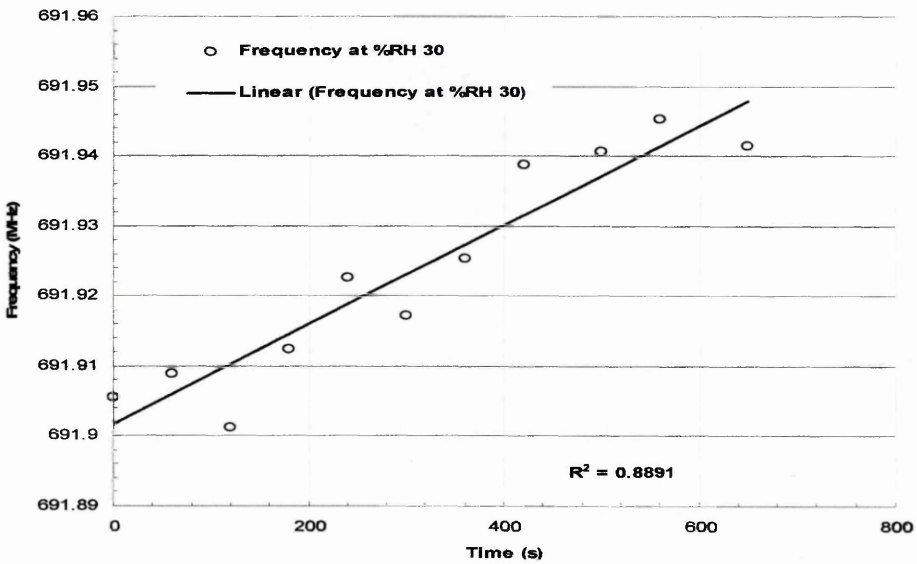

Figure 4.10e FBAR S_{21} response (from Figure 4.10 (A)) at successive iterations of *dehumidifying* phase of the cycle. ($\Sigma\ \Delta f_o = \sim +\ 47$ kHz over 650s (final drying phase))

4.4.6 Experiment (4A) Effect of increasing PVP film thickness on FBAR characteristic response

4.4.6.1 Methods

FBAR, device 11 on PCB 2 was characterised in the FHA without a lid or a gas flow, first without any PVP coating with 801 points over a 5 MHz bandwidth span for and then characterised for 2, 4, 30 and 100 PVP spray passes of roughly 1 second of time per pass with the same settings. The shapes of the S_{21} resonant curves were examined and XY scatter graphs plotted as S_{21} power transmissions over frequency for each spray pass.

4.4.6.2 Results

The results from the graph in Figure 4.11 show that there is both frequency drop ($-\Delta f_0$) as well as S_{21} signal power attenuation (Δ +dB) due to increased loading of polymer. There is slight improvement of power transmission[83] (~ -0.1 dB) on the first (2 seconds) pass, but a decrease in Q factor along with decrease in FBAR S_{21} resonant frequency. ($-\Delta f_0 = \sim$ 0.8 MHz). However, when the spray coat was deposited for 4 seconds (thickness not measured due to Dektak servicing) there was a significant decrease in Q factor along with significant attenuation of the S_{21} transmitted power signal (~ +1.6 dB). A change in power responses as large as this is very unlikely to have been a result of non identical PCB screw tightness from manual replacement of the board into the FHA.

When the PCB was passed through 30 passes of the polymer spray, the signal was, appreciably damped. (~ +5.5 dB) and the characteristic resonant frequency shape altered significantly enough to effectively make a 3 dB bandwidth Q determination impossible.[84] An approximation of the numerical value for f_0 for the 30 spray passes (i.e., 30 seconds of total load) is (~ 677.7 MHz), representing a frequency decrease of approximately (4.2 MHz) from the 4 second load.

---

[83] The small measured improvement in S21 power transmission (dB) is likely to be related to a better contact with the PCB to the earth plane and cables, since it will be remembered that manual adjustment of the screws was necessary each time the PCB was removed and replaced.

[84] In cases such as this i.e., where the S_{21} resonance curve is less than 3 dB it would be necessary to invoke the dB bandwidth cut-off function to obtain a calculated Q value for the response

The 100 s spray pass shows a response characteristic (shape, Q and frequency) very similar to the 30 s loading, suggesting that 30s loading, or less, represents the 7μm limit of PVP thickness deposition using the spray coating method, adding more spray passes likely merely increases the total amount of polymer over the planar area of the die but does not influence the important influential parameter of PVP layer thickness over the working area of the FBAR.

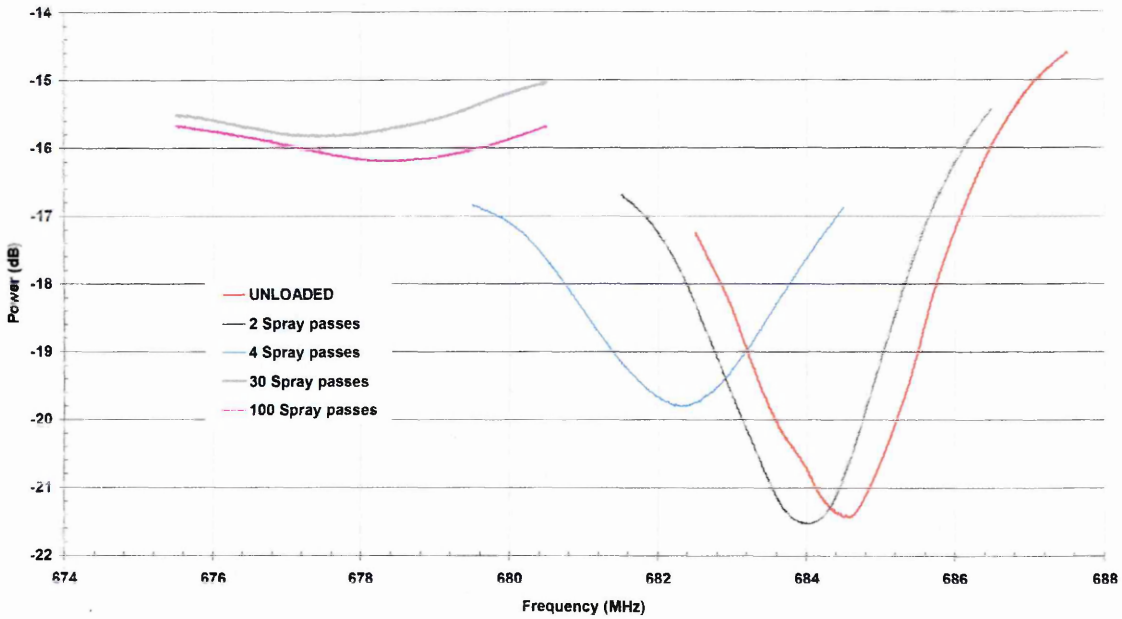

Figure 4.11. Effect of successive (0, 2, 4, 30 and 100) PVP loadings (1 second spray passes) on the characteristic resonant frequency span shapes of FBAR. S_{21} (801 points 5 MHz span) Ambient laboratory conditions.

4.4.7 Experiment 4B Observing the effect of change in relative humidity on FBAR Δf_0 (Hz) with increased PVP (W/V 1.23%) loading times.(2 -30 seconds)

4.4.7.1 Methods

The device was spray coated with PVP for 2s, 4s, and 30s. To allow the system to settle, the dry line only was used, drying the PVP coated FBAR and the insides of the housing chamber for some time (~20 minutes) before the start of the data recording.

At t=0 seconds the response on the humidity meter was (<%RH20) therefore out of range, and indicating a dry gas flow. At roughly 120 seconds, the wet line was mixed into the dry line to bring the humidly up to (~%RH55), over approximately 100 seconds. At t=250 seconds, the wet line was closed, and the humidity of the system was allowed to fall until the experiment was terminated at t= 400 seconds.

An XY scatter graph of FBAR f_0 vs. humidity (%RH) over time was produced for a 2, 4 and 30 second loadings of PVP. The thickness of the layer was not measured with the Dektak due to service issues.

4.4.7.2 Results

The results from experiment 4B shown in Figure 4.12 indicate that the thicker the PVP film thickness, the lower its S_{21} series resonance frequency was from that of the uncoated device under the same conditions, this of course, represents in increase in mass loading from the PVP sensing layer.

The S_{21} series resonance frequencies were, (684.55 MHz) for a 2 second load, (682.29 MHz) for a 4 second load and (678.31 MHz) for a 30 second load. The humidity change was from (<%RH20) to (~%RH55). The results are tabulated below in Table 4.4.

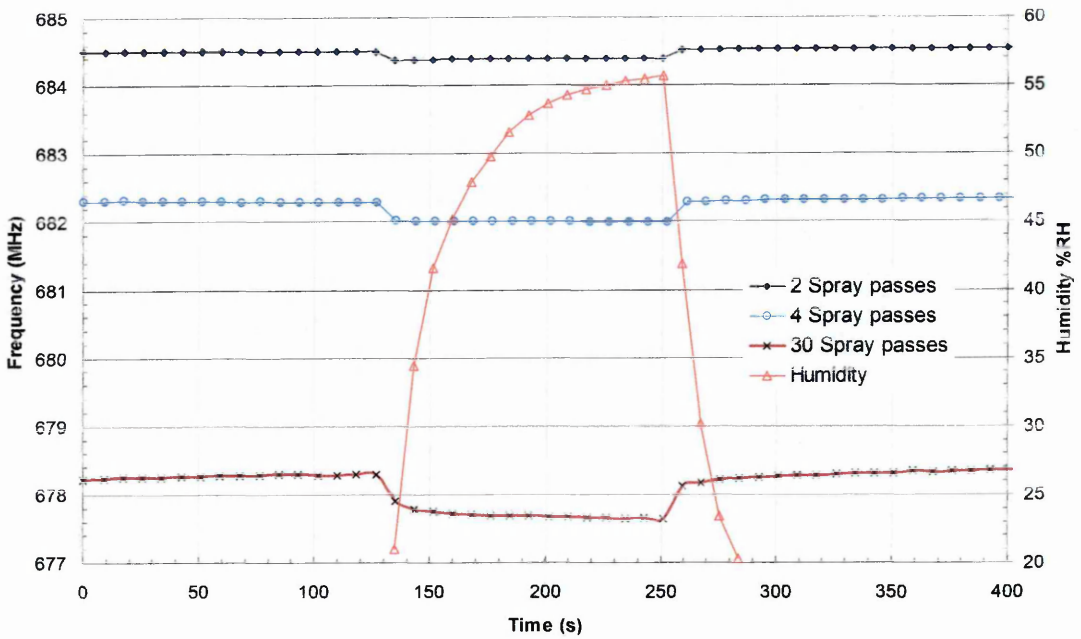

Figure 4.12 Effect on FBAR S_{21} series resonance frequency over time from increased thicknesses of PVP (WV 1.23%) in N_2 gas stream (>150SCCM) containing various amounts of water vapour. Minimum (<%RH 20) Maximum (%RH 55.2)

Table 4.4 FBAR S_{21} series response frequencies for different spray loadings of 1.23% W/V PVP measured in high and low humidity.

	f_0(MHz) in low humidity (%RH < 20)	**f_0(MHz) in high humidity (% RH ~55)**	-Δf (kHz) from low to high humidity
2s PVP Spray Pass	**684.507072**	**684.389824**	117.248
4s PVP Spray Pass	**682.286656**	**682.008448**	278.208
30s PVP Spray Pass	**678.30144**	**677.664576**	636.864

4.4.8 Experiment (5) Observing the effect of change in relative humidity on FBAR Δf_0 (Hz) when using high molecular weight ((130,000 Mr) (WV%11.07)) of PVP on FBAR for 0, 1, 2, and 5 seconds of spray pass time.

4.4.8.1 Methods

The molecular weight (mr) of the PVP stock used to make the spraying solution was increased from 40,000 to 360,000 i.e., a heavier batch representing an increase in the length of the polymer chain. Therefore, the W/V ratio in solution was increased from W/V =1.23% as used previously to W/V =11.07 % when 0.1g of the mr 360,000 stock powder was dissolved in 10 ml of pure methanol and transferred to the spraying gun according to the methods (4.3.2) The actual thickness of the high molecular weight layer could not be established.[85] The FBAR was characterised on its second overmode, since this particular resonance gave the best responses in terms of S_{21} power transmission. (i.e., the most negative). Since the polymer was now assumed to cause significant attenuation of the FBAR resonance curve due to damping, this overmode was chosen rather than a higher frequency overmode with less desirable characteristics response in the power domain. Graphs of frequency (MHz) vs. power (dB) are shown to highlight the effect of loading the polymer on FBAR in terms of the characteristic shape of the S_{21} resonant curve. This was important to show directly the effect of polymer as a (i) mass load i.e., decreasing the FBAR resonant frequency, and as (ii) a signal attenuator due to the lossy (non ideal mass loading) nature of the soft layer. The spans were taken over a (5 MHz) bandwidth, with (801) data points per trace. The number of data points per trace still precludes the use of symbols or dotted lines to distinguish between the data sets, and critical reliance is therefore still placed on the use of coloured lines to distinguish between the data traces.

Because the addition of moisture to the PVP layer was *assumed* to make it softer and hence, more lossy, a separate graph of polymer loading in dry (<%RH20) vs. highly humid conditions (~%RH60) was created for a resonant frequency curves to show the effect that humidity was having on the characteristic shape. The 2s and 5s loadings were

[85] Dektak surface profile apparatus and AFM were both offline due to servicing issues.

chosen arbitrarily to show the effect. The spans were taken over (5 MH)z bandwidth, with (801) data points per trace.

The device was exposed to a variation in humidity for each PVP loading. The dry gas was run for some time (20 minutes) before starting the data acquisition, so at t=0 seconds the humidity meter read (<%RH20), indicating the N_2 gas stream was dry. This was done to allow the PVP to dry-out any moisture that it had adsorbed from the ambient conditions in the laboratory during its initial loading onto the FBAR. At t =120 seconds, the wet line was opened and mixed into the dry line to allow the relative humidity of the gas stream to rise. Humidity rose to (%RH60) within 1 minute. At t=250 seconds, the wet line was closed and the experiment was allowed to run in drying phase until its termination at t=400s. Multiple scatter graphs of frequency vs. humidity over time are shown. Gas flow rate was steady (>150 SCCM) and temperature was set to $1^{O}C$ above room temperature and stabilised ($<\pm$ 0.1 ^{O}C) to ensure that the FBAR responses were not influenced by temperature change.

The settings were;

FBAR Device 8 on PCB 14.
Centre Frequency 756 MHz
Span Freq (MHz): 5.0
Points in sweeps: 801
IF Bandwidth: 1000
Scattering: S21

4.5.8.2 Results

The result in figure 4.13(A) shows that increasing loading times, i.e., more spray passes representing a thicker film of PVP on FBAR top surface electrode decreased the S_{21} series resonance frequency indicating the presence of increased mass load, but it also attenuated the S_{21} power transmission signal, and decreased the reported 0.5 dB Q factor indicating that the presence of a lossy material attenuates the high frequency acoustic wave as it probes the foreign layer.

Table 4.5 Effect of increased PVP (WV%11.07) spray times on FBAR S_{21} series resonant frequency (MHz) power transmission (dB) and 0.5 dB bandwidth[86] Q factor in a dry N_2 gas stream (>150 SCCM) with temperature stabilised <$\pm$ 0.1^{O}C.

	f_0 (MHz)	S_{21} power transmission (dB)	0.5 dB bandwidth Q factor	$-\Delta f_0$ (MHz)	$+\Delta S_{21}$ power transmission (dB)	$-\Delta$ 0.5 dB bandwidth Q factor
No PVP Load	**758.769**	**-8.475**	**1896.718**	-	-	-
1s PVP spray pass	**755.806**	**-8.103**	**1727.353**	2.963	0.372	169.365
2s PVP spray pass	**753.55**	**-7.4078**	**1452.416**	5.219	1.068	444.302
5s PVP spray pass	**748.649**	**-5.841**	**581.3574**	10.119	2.635	1315.361

The result in figure 4.13 (B) shows for the responses of FBAR initially in the presence of 2s and 5s PVP loads in dry (<%RH 20) gas flow. The FBAR with PVP 2s and PVP 5s loads was then exposed to high humidity (%RH 60) gas flow and the results are compared with the original low humidity values. The Gas flow rate was stable (>150SCCM) and temperature stabilised to within $\pm$ 0.1^{O}C.

The responses for S_{21} series resonance frequency (MHz), power transmission (dB) and 0.5 dB Q are shown in Table 4.6, as numerical values obtained directly from the spread sheet data used to construct Figure 4.13(B)

[86] NOTE – The Q factor (f_2-f_1 / f_0.) in this test was measured at 0.5 dB bandwidth. This exaggerates its real 3 dB bandwidth value It was necessary to perform this routine as some of the resonance curves that were utilised for analysis did not posses a peak with at least a 3 dB bandwidth signal. This useful function of mutable Q bandwidth was written into the R.01 analysis software and was not a function that could be performed by the network analyser alone.

Table 4.6 FBAR responses (S_{21} series resonance, S_{21} transmitted power and 0.5 dB bandwidth Q factor) to 2 and 5 seconds spray passes of PVP in low humidity (<%RH 20) and high humidity (%RH 55) N_2 gas streams (>150SCCM) Temperature stabilised <+ 0.1 ^{o}C

	f_0(MHz) low humidity (%RH < 20)	f_0(MHz) high humidity (% RH ~55)	S_{21} transmitted power (-dB) low humidity (%RH <20)	S_{21} transmitted power (-dB) high humidity (%RH~55)	Q factor in low humidity (%RH < 20)	Q factor in high humidity (% RH ~55)	- Δf_0 (MHz) from low to high humidity	+ΔS_{21} transmitted power (-dB) from low to high humidity	Δ 0.5 dB Q factor from low to high humidity
2s spray pass	**753.4452**	**751.5716**	**7.4782047**	**5.96013212**	**1452.424**	**626.3096**	1.8736	1.51807258	826.1144
5s spay pass	**748.5093**	**744.1057**	**5.8466076**	**4.7541961**	**587.0662**	**262.2399**	4.4036	1.0924115	324.8263

The shapes of the S_{21} curves in Figure 4.13(B) show not only the S_{21} series resonance frequency drop that would be expected from the addition of a mass loading, which in this case is from the addition of extra water in the PVP, but the responses also show significant S_{21} power transmission attenuation and Q factor attenuation. The hydration of the polymer makes it more lossy, the drying of the polymer makes it less lossy. In general, this is the response expected from the interaction of an acoustic probe wave with a lossy polymer due to acoustic attenuation. The addition of extra mass/thickness of polymer is evident in Figure 4.13(C) by virtue of the decrease in S_{21} series resonance frequency in low humidity gas stream for each of the passes. The response to increase in humidity of the N_2 stream is amplified with each spray pass. The results are shown below in Table 4.7

Table 4.7 Effect on FBAR S_{21} series resonance frequency from high and low humidity N_2 gas streams with 0s[87], 1s, 2s, and 5s PVP spray passes. Gas flow rate was >150SCCM) and temperature was stabilised <± 0.1 °C.

	f_0 (MHz) in low humidity (<%RH20)	f_0 (MHz) in high humidity (RH%60)	$-\Delta f_0$ (MHz) from low to high humidity
No PVP Load	**758.9900**	**758.5476**	**0.4424**
1s spray pass	**755.7168**	**754.6986**	**1.0182**
2s spray pass	**753.4471**	**751.5140**	**1.9332**
5s spray pass	**748.5176**	**744.1057** [88]	**4.4119**

[87] It will be noticed that Δf_0 for the unloaded (0s) sample was considerably higher (44.2 kHz) than expected (~12 kHz) as seen figures 4.5a and 4.5b. A probable explanation for this discrepancy is in the possibility that the device became contaminated with residue of PVP spray during the coating procedures on other devices.

[88] The reason for the slight increase in f_0 whilst the 5s load was exposed to (%RH60) is not clear but may be due to some swelling of the polymer layer as it expands over time in the presence of humidity and thus effectively decreases the density presented to the acoustic wave probing the material.

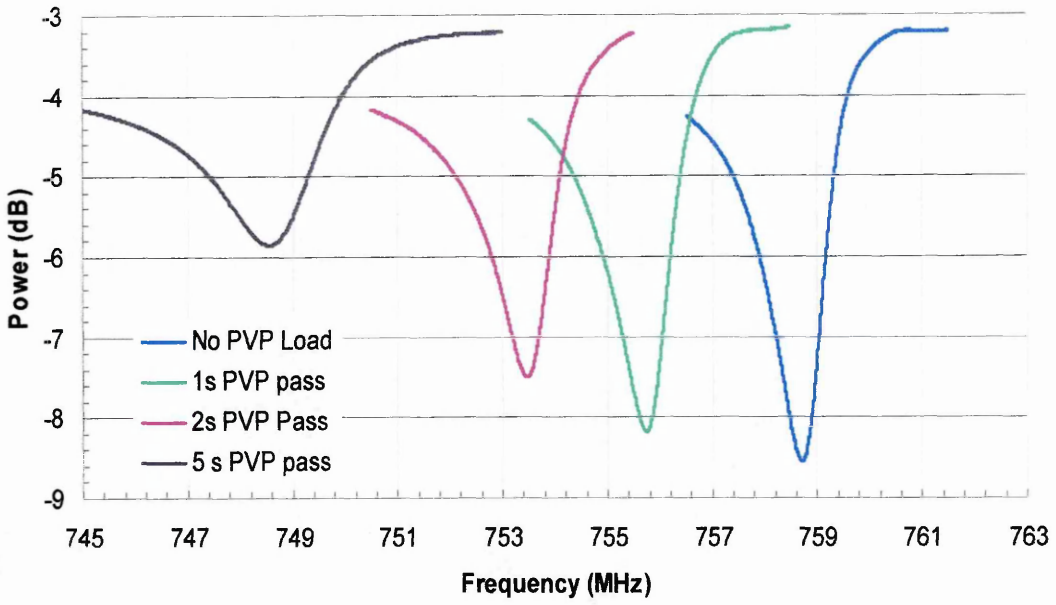

Figure 4.13 (A) Effect on FBAR S_{21} characteristic resonance frequency span shapes from spray coating FBAR with PVP (WV%11.07) for 0, 1, 2, and 5 seconds. ((5 MHz) bandwidth. (801) points per trace.) (N_2 Gas flow (>150SCCM) (Low < %RH20))

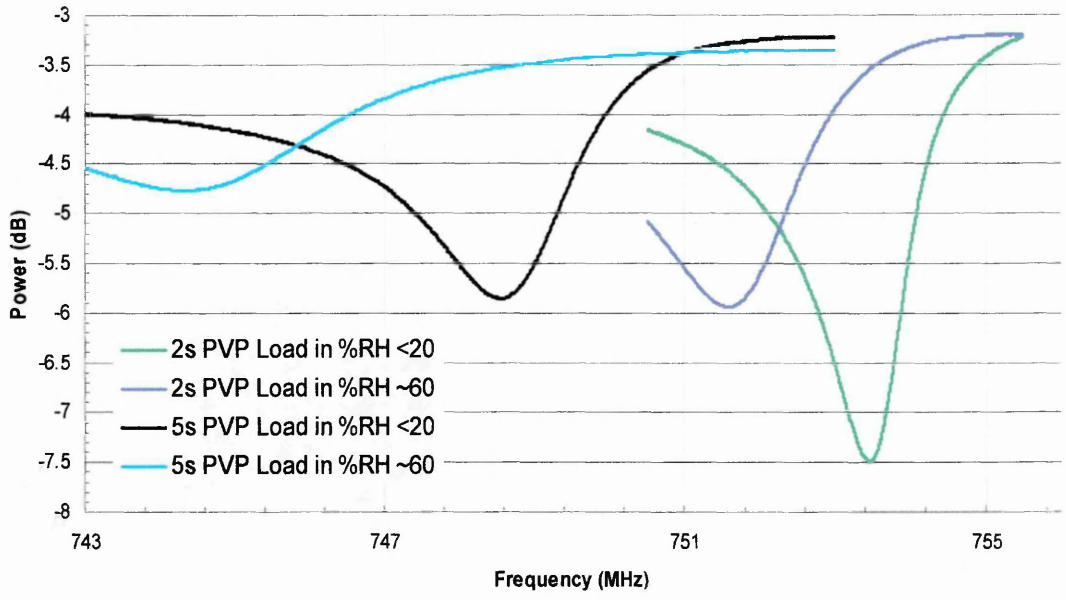

Figure 4.13 (B) Effect on FBAR S_{21} characteristic series resonance frequency span shapes from PVP (WV%11.07) spray coated (2s and 5s) FBAR in low (<%RH20) and high humidity (~%RH 60). ((5 MHz) bandwidth, (801) points per trace.) (N_2 Gas flow >150 SCCM)

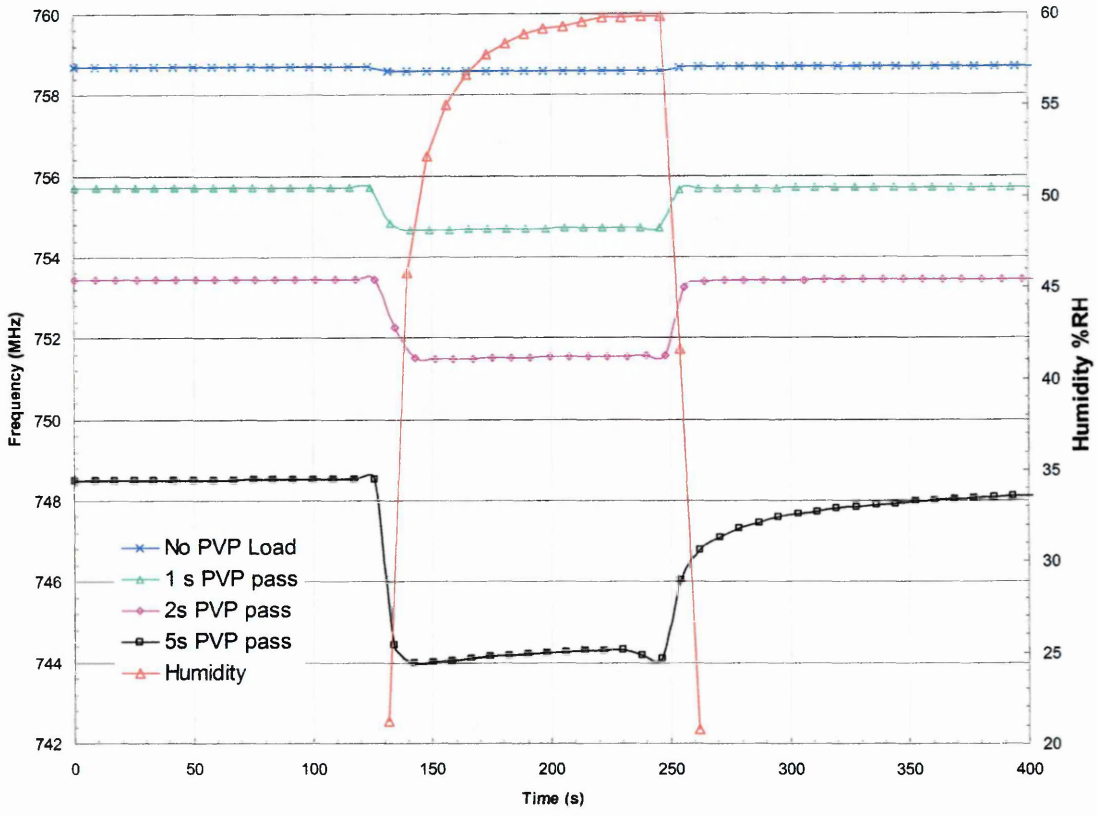

Fig 4.13 (C) Effect on FBAR S_{21} series resonance frequency (f_0) over time (t=400 seconds) from increased loading times of PVP (WV%11.07) in N_2 gas stream (>150SCCM) containing various amounts of water vapour. Minimum (<%RH20) Maximum (%RH60)

4.4.9 Experiment 5B Observing the effect of change in relative humidity on FBAR Δf_0 (Hz) when using high molecular weight ((130,000 Mr) (WV%11.07)) of PVP on FBAR when drop cast and with reduced gas flow rate.

4.4.9.1 Method

PVP was drop cast onto the FBAR instead of using the spraying method. This method gave a smoother coating profile than spray coating, the maximum thickness that could be obtained with this method was (~4 μm). A (100 μl) aliquot of PVP in methanol was deposited with a Gilson pipette directly on to the top gold electrode working area of the wire bonded FBAR and the solvent was allowed to evaporate off (~10 minutes) before the PCB was inserted into the FHA for RF testing with the network analyser.

The gas stream was directed through the dry line for some time (~10 minutes) before starting the recording phase of the experiment so at t=0 seconds, the humidity recorded was (< %RH20). At t=60 seconds the N_2 was manually redirected through the wet line and the humidity was allowed to increase until t=180 seconds, where it reached a maximum of (%RH 38%). At this time point the gas stream was redirected through the drying crystals, i.e., the dry line, until the experiment was terminated at t=400 seconds. The gas flow was (<< 70SCCM.) representing a much reduced gas flow rate as used in previous experimental methods.

The settings were
FBAR device 9 on PCB 8
Centre Frequency (MHz) 657.0 MHz
Span Freq (MHz): 20.0
Points in sweeps: 1601
IF Bandwidth: 1000
Scattering: S_{21}

4.5.9.2 Results

This result shown in figure 4.14 (A) ran contrary to all previous PVP coated FBAR humidity test results. The S_{21} series resonance frequency of the FBAR is seen to *rise* by ($+\Delta f_0$ = 2.75 MHz) when exposed to increasing humidity in the gas flow over the range (min <%RH20 max %RH38) but whilst still in the humidifying phase of the test the frequency of the FBAR is seen to begin to fall at ~t=100 seconds by 0.5 MHz over the following 50 seconds or so Upon drying of the gas stream (<%RH20), the frequency of the FBAR did fall, but did not return to its original dry state value remaining at (~659.8 MHz.) until the end of the experiment at t=400 seconds.

This may be due to either loss of polymer material from the surface, swelling of the polymer, effectively decreasing the mass load presented to the FBAR or a reduced adhesion of the polymer on the FBAR surface or a combination of all of these effects. See figure 4.14(B). The effect of the much decreased flow of gas can be seen to be influencing the time that taken to decrease the humidity, in previous tests where the gas flow rate was >150 SCCM, when the wet line was mixed out to give the dehumidifying phase of the experiment, the humidity would fall to <%RH20 in less than 20 seconds, but figure 4.14 shows that the time taken for the humidity of the gas to reach <%RH20 was ~90 seconds.

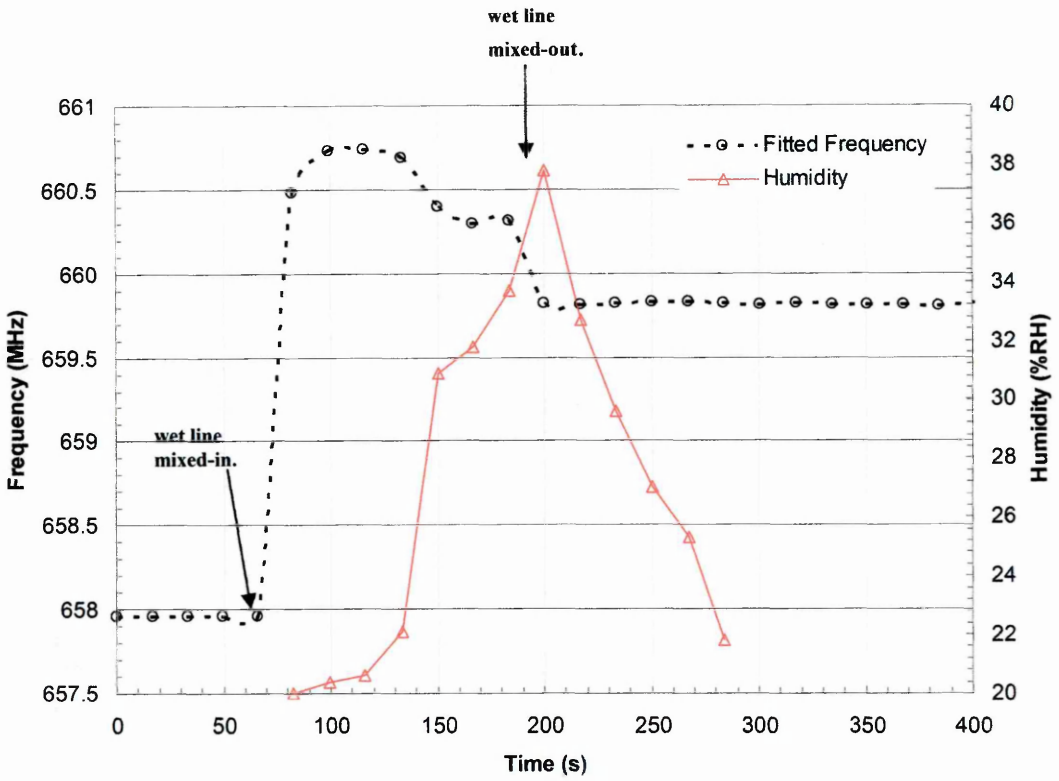

Fig 4.14 (A). Effect on FBAR S_{21} series resonance frequency (f_0) from drop cast PVP (WV%11.07) in gas stream (<70 SCCM) containing various amounts of water vapour. Minimum (<%RH20) Maximum (%RH38) over time (t=400 seconds)

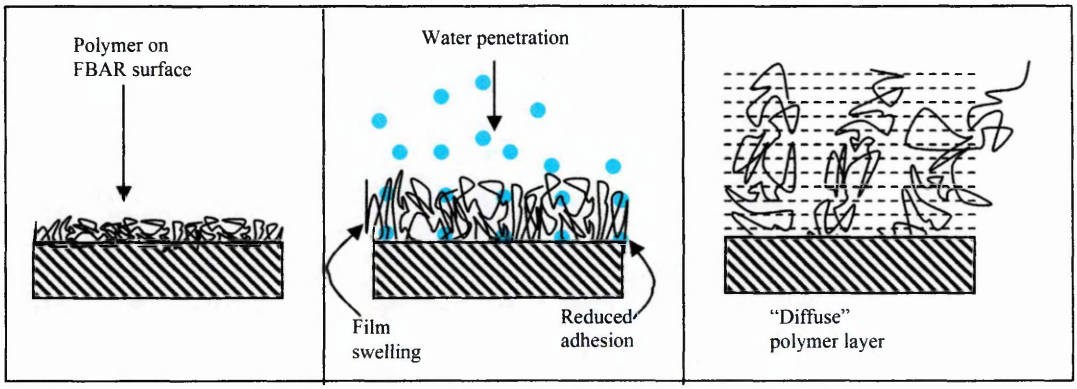

Figure 4.14 (B). Effect of hydration on polymer. Adapted from [5]

4.4.10 Experiment 6 Device reusability.

4.4.10.1 Methods

During the course of experimentation, regardless of the amount of care taken, damage to the devices was inevitable[89], as a result the number of FBAR wire bonded samples delivering high quality responses required became limited. For this reason, it was decided to conduct experiments to see if the devices could be reused after PVP layering by removing the polymer and returning the device responses (S_{21} f_0, transmitted power, and Q) to their original uncoated values. Since devices were becoming limited at this stage, an FBAR with a severe spurious mode was chosen as it was not considered particularly useful for actual calibration studies and could be sacrificed without interfering with overall humidity test progression if the regeneration study showed that it was not possible to reuse devices. This proved to be a fortuitous decision because the spurious mode of the FBAR in the uncoated state could be used as a kind of signature pattern in the shape of the response in addition to the frequency[90], power and Q for the uncoated state. This will become clearer as the argument presented in this section develops further.

An uncoated FBAR was characterised and its responses were recorded. The PCB was removed from the FHA and the device was then sprayed with PVP and responses for the PVP coated device were recorded after reinsertion into the FHA. Under the protection of a fume cupboard, the delivery heads of the spray coating system were then thoroughly washed in copious methanol, and a brand new, unused delivery cartridge was used to hold the solvent. The PVP coated wire bonded FBAR on PCB was removed from the FHA and under protection of a fume cupboard was then sprayed with copious methanol, and the methanol liquid was forced off the surface of the device before it had time to evaporate with a fast moving N_2 stream. This was done to ensure that the possibility of the methanol leaving a dry residue that would be detected on FBAR as a mass load was avoided. Care was also taken not to dislodge or alter the shapes of the delicate wire bonds as this would be likely to subtly influence the final result. Great care was also taken not to

[89] For example cyclical heating and cooling of devices could cause the bonds to fail, or repeated exposure to solvent could also cause the bonds to fail.
[90] Frequency of the response was difficult to determine with a high degree of precision due to the presence of the spurious mode of resonance.

pop the piezoelectric membrane as this would render the experiment void. The washing process was repeated 3 times and then results for cleaned FBAR were recorded. A scatter graph XY of S_{21} transmitted power over S_{21} series resonant frequency was produced to show the effect of loading the FBAR characteristic resonance curves with PVP over various thicknesses and cleaning the FBAR with methanol for removal of the polymer film. The original response of the FBAR when it was uncoated was used as the control value to which an ideally cleaned FBAR would return.

4.5.10.2 Results

The device that was chosen on which to perform the reusability test possessed a spurious mode, this mode is clearly visible in the trace of Figure 4.15 for both the unloaded sample and the same sample *after* it had been cleaned of the PVP layer with methanol This returned the cleaned device response with characteristic spurious modes returning to its original uncoated profile.

The results shown in Figure 4.15, therefore indicates that the device was successfully cleaned, the PVP being removed with methanol solvent leaving little or no residual traces behind and implies that the PVP coated FBARs are reusable with this cleaning regimen. The 0.5 second loading did not cause an overall frequency of the FBAR to fall, but it is difficult to precisely determine what the actual value of the resonance frequency of the FBAR is; this difficulty can be attributed to the presence of the spurious modes giving two equally valid f_0 data points, one of which appeared to be suppressed by the addition of the polymer film, in essence, polymer loading on the FBAR surface gave a single f_0 value over the lower frequency spurious mode. It appears that the presence of the polymer on the surface of the FBAR has interfered with the continued presence of the higher frequency spurious mode because the 0.5 s loading frequency can now be determined (1.793 GHz) since there is just one resonant peak. Loading the sample with 0.75s spray improved the S_{21} power responses by (~ 2.2 dB), caused the S_{21} series frequency to fall by ~ (-9.5 MHz) to give f_0 at (~1.783 GHz) and the spurious mode visible in the original trace is completely suppressed, indicating that all of the lateral

shear wave motions are cancelled in the FBAR in the presence of the PVP polymer with film- thickness ~1μm.

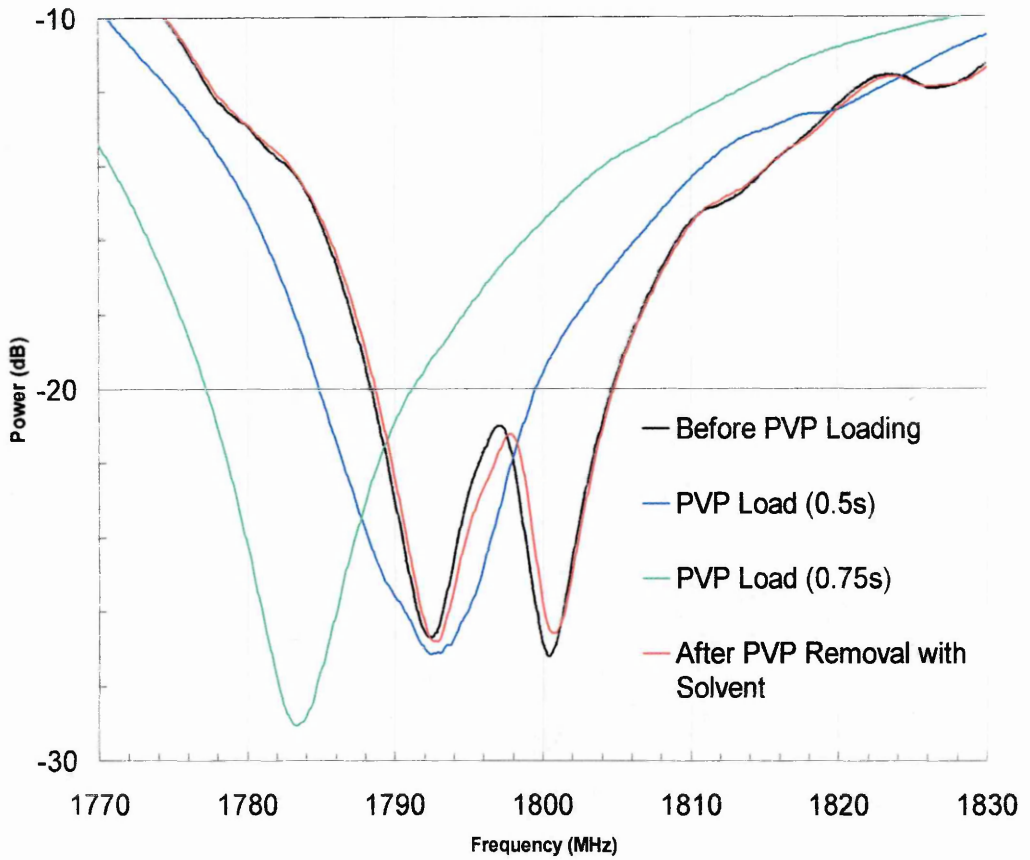

Figure 4.15 Effect on characteristic response shapes of FBAR before loading with PVP, during PVP loading , 0.5 seconds and 0.75 seconds exposure to spray and finally the removal of PVP with methanol. (No gas flow)

4.4.11 Experiment 7 Confirming the suppression of FBAR spurious modes of resonance resulting from the addition of a spray coated PVP film onto the FBAR top surface electrode.

4.5.11.1 Methods

The results from Experiment 6 shown in Figure 4.15 *unexpectedly* gave indication that the loading of PVP polymer on to the FBAR top electrode surface was interfering with and suppressing the unwanted spurious modes. These were thought to be generated from lateral/shear modes of excitation in FBAR.

Work has been active in our department to reduce the presence of these modes as they are detrimental to the quality of the final FBAR output responses, so this suppressive effect even though it was not strictly part of the humidity sensing experiments envisioned within the work plan of the FBAR sensor project was seen as non-trivial and worthy of further investigation from a purely experimental perspective, because potentially it could serve to improve the functionality of overall FBAR performance in general. Experiment 7 was done to check that the result in Experiment 6 was not anomalous and that the cancellation of the spurious modes could be repeated with the addition of PVP films on FBAR surfaces.

The FBAR, device 3 on PCB 16 was taken from storage. It was known from previous on die or wafer measurements to be afflicted by spurious modes, it had been wire bonded in error, and was certainly not envisioned to be used in the sensing tests. The wirebonded device clearly possessed a spurious mode when uncoated. This spurious mode was so severe as to make an estimation of f_0 for series resonance difficult, perhaps having to give two equally valid f_0 values if attempting to describe it.

The PCB was placed into the FHA and the uncoated device was characterised and responses were recorded. The device on its PCB was removed from the FHA and a very brief (< 0.25 seconds) PVP spray coating was applied in the fume cupboard. This time period represented the shortest interval that it was possible to coat the device for using the manual coating methods already established.

The responses were recorded after re-inserting the device into the FHA. It was removed once again, and PVP spray coating was re-applied for approximately the same time interval to give a total spraying time of 0.5 seconds, it was reinserted into the FHA and the responses were recorded. The characterisations were performed without a gas flow or temperature stabilisation, so ambient laboratory conditions can be assumed.

Traces of the characteristic responses of FBAR were produced as XY scatter graphs of S_{21} transmitted power over frequency to observe the effect of the polymer load on the spurious mode afflicting the device.

4.5.11.2 Results

Figure 4.16 shows that the uncoated FBAR device was clearly afflicted by the presence of a spurious mode, this effectively split the resonance frequency into two separate responses the lower more powerful response being placed at (f_0 1797.125 MHz with transmitted power at -28.654 dB) and the higher frequency less powerful response at (f_0 1805.750 MHz with transmitted power at -25.882 dB)

With the addition of a very brief (<0.25 s) spray exposure, the response showed some suppression of the spurious mode with an over all damping of the entire signal but it retained the characteristic signature of the unloaded response in that the original shape was still visible with spurious mode still manifest. At this stage, it was still impossible to make a clear value decision for f_0 since two are still visible. With the (0.5 s) exposure time, the spurious mode is completely suppressed hence f_0 is easy to estimate at (~1786.625 MHz and a power response of -27.989 dB).

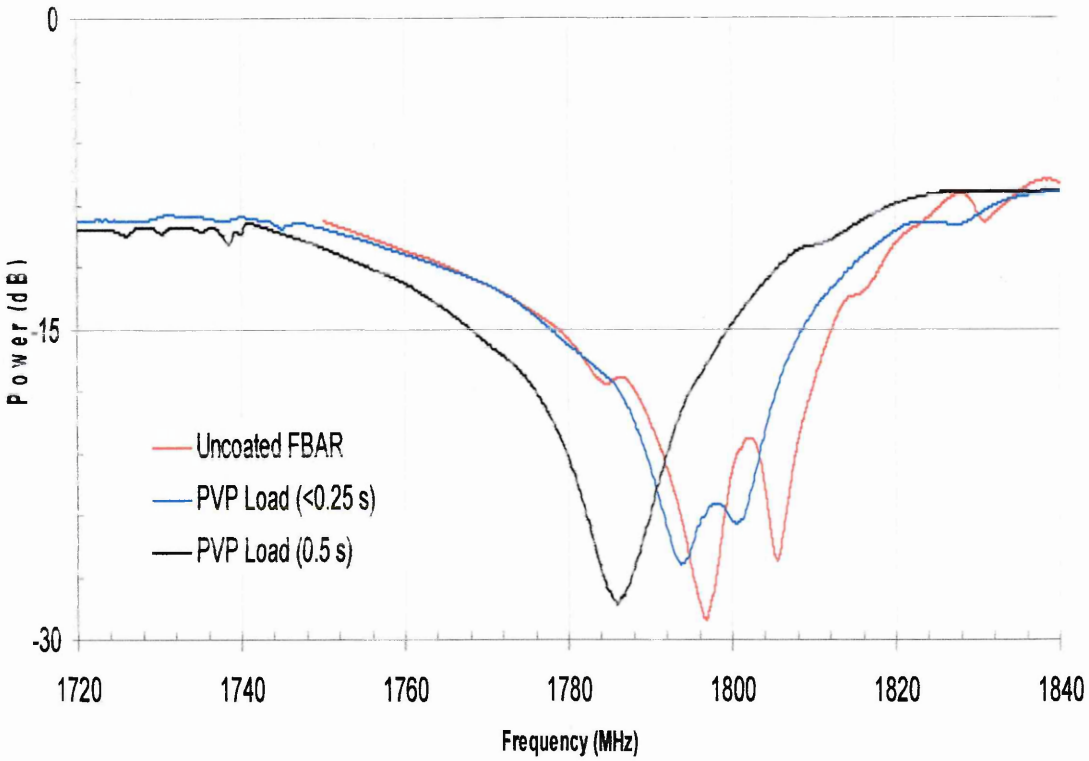

Figure 4.16. Effect of <0.25s and 05s PVP loading times on FBAR device 3 on PCB 16 top electrode surface and the subsequent suppression of spurious modes. (No gas flow)

4.5 Discussion.

The spray coating method was prone to errors (~20%) in estimation of the thickness of the film due to an extremely roughly presented polymer surface when dried. This spraying method was used to ensure the safety of the limited supply of wirebonded FBAR device modules. Spin coating would have given a more controllable thickness and likely a much smoother finishing profile. The spray coating method was acceptable for the range of tests that were performed.

The use of the 2^{nd} order polynomial fitting efficiently removed noise from the output responses and therefore increased the resolution of the final measurement when the actual measured data was omitted from the chart.

The responses of both thermocouples and both humidity meters were in good agreement. This gave confidence that the recorded humidity data was accurately reporting the true humidity levels in the gas stream. It also showed that the temperature stabilisation methods used were good enough to stabilise the FHA and therefore the FBAR to ($<0.1^{O}C$), ensuring that any responses from FBAR were not due to fluctuations in temperature, since previously it had been shown that the FBAR was responsive to changes in temperature as small as $0.1^{O}C$.

Experiment 1A demonstrated that FBAR was responsive to changes in the humidity of the gas stream even without the presence of a sensitising PVP coating on its top electrode. Experiment 1B showed that the baseline responses for FBAR S_{21} transmitted power and f_0 were more stable without the presence of the foreign film but this was likely to be the result of continued removal of moisture from the layer which remained from hygroscopic hydration during the initial coating stages which were performed in ambient laboratory conditions. The fall in frequency was of course related to the mass of the additional polymer, but since the bulk modulus of the film is not known, making an estimation of the actual mass deposited would be error prone since it is a far from ideal (perfectly elastic) mass load. Experiment 1C showed that the sensitivity of the device to

moisture was greatly enhanced with the addition of a film of ~1.2 μm of the hygroscopic polymer layer at a relatively low (1.23%W/V) concentration. The fact that the resonant frequency of the FBAR did not return to the original dry values indicates that there is response from persistent water retention in the layer.

Experiment 2A examined the effect of the polymer load on the characteristic response shapes of the FBAR S_{21} series resonance curves in primary and overmode harmonics. The increase in total frequency decrease from higher overmode harmonics was not unexpected. However, the effect of the loading on Q factor only becoming apparent at the 950 MHz overmode was not expected and this may be indicative that the effects of loading are amplified at higher frequencies. Experiment 2B examined the effect of humidity changes on PVP coated FBAR S_{21} (f_0) responses. The results clearly demonstrated that the higher overmode harmonics were more sensitive to changes in humidity on the same device under very similar conditions, that is total change in Hz per unit measurand.

Once it had been established that the FBAR was more sensitive to exposure to humidity when coated with PVP, Experiment 3 was designed to show how reproducible the results were. A clear decay in the iterative response of the FBAR is evident. Here two factors come into effect and must be considered separately. The first is the decrease in S_{21} series resonance frequency response per iterative wet cycle and the second is the increase in S_{21} series resonance frequency response per iterative dry cycle. These results can be explained if it is assumed that on each wetting phase, some of the polymer is dissolved away close to the surface of the layer. On the successive dry cycles, the small increases in frequency are most likely due to decrease in mass loading as a result of the polymer dissolving away from the main body of the deposited film on the FBAR working area. However, on the successive wet loading cycles, the much larger decay is due to the fact that the missing polymer is no longer available to hold the additional moisture, so the response is due not only to the loss of a small amount of surface polymer, but also to the loss of the mass contribution that would be made by the water if the polymer were still present to adsorb it. Transmitted power follows the same trend as the S_{21} series

resonance, but in the opposite direction and Q appears to follow the same trend as the S_{21} series resonance in the same direction, but increased quantisation of this data make firm conclusions about this somewhat difficult. The responses of Q and power decay are not fully understood at present, they are likely due to changes in the bulk modulus of the PVP film when hydrated/dehydrated, in its hydrated state the polymer film likely becomes softer, hence more lossy and this serves to attenuate the acoustic wave as it probes the film which is turn reflected in the decrease the performance of the S21 power transmission characteristics (i.e., increasing and moving toward 0 dB) All that can be said at present is that the Q factor falls when the polymer is hydrated, indicating a more lossy material and damping of the resonance curve due to this. In the future it may be possible to calibrate this phenomenon and exploit it in more strictly controlled rheological studies. The responses of Q and power are shown additionally to f_0 to highlight the different ways in which FBAR can deliver information about the changes in the propagation of its probing wave into the sensing layer. At this stage a deep exploration of the G and G' states of the polymer is not possible since the PVP bulk modulus and viscosity remains unknown and the calculations involved linking the BVD resistor (loss) values to the model are likely to be impossible without these values. A precise analytical model probably does not yet exist as a complete derivation in the literature since nearly all the research work on polymer modulus state changes has been preformed at lower frequencies on devices operating in thickness shear mode. The effects of high frequency longitudinal acoustic probe waves on the rheologies of materials is still largely unexplored at present and likely offers a fruitful research path.

Experiment 4A was designed to show the effect of increasing the mass loading influence on the FBAR characteristic resonant frequency curves by increasing the spray pass number and therefore increasing the total loading time and hence the thickness of polymer film attached to surface of the FBAR. Once these responses were, the effect of humidity change on the FBAR characteristic resonance response shapes with various thicknesses of PVP was demonstrated. As expected, there is both frequency decrease and power transmission increase with increased polymer load. At above a 30s loading time, the response of the FBAR was attenuated so severely to make a 3 dB bandwidth Q

determination impossible. Increasing the spray loading times beyond this point did not further influence the responses of the FBAR indicating that the maximum thickness load of polymer which was estimated from the profilometer results at a maximum of 7μm, was achieved in under 30 spray passes. Further tests need to be done to find the actual number of spray passes required to obtain this maximum thickness, but a more fruitful approach to this may be gained by spin coating the polymer on to the FBAR if the technicalities of wire bond fragility can be solved. Experiment 4B examined the relative responses of FBAR to incrementally increasing PVP layer thickness. As the layer became thicker, the response of the device to the same humidity variations increased - with a 4s spray pass being roughly twice as sensitive (i.e., doubling the absolute frequency change) to humidity as a 2s spray pass under very similar conditions.

Experiment 5A was devised because it was useful to ascertain whether or not the concentration of the PVP polymer film, as opposed merely to the thickness of the polymer film was an important parameter in PVP FBAR coated response to changes in humidity. It was suspected that it would increase sensitivity to humidity since the increase in molecular weight of the polymer was due to increases in the polymer chemical chain length, so this would provide more hygroscopicity per unit volume of PVP film on the surface of the FBAR. There was some concern that the increased density of the polymer would damp the FBAR resonance signal, but this was shown directly by experiment not to be the case. It was unfortunate that at this stage of the tests, access to thickness profilers (Dektak or AFM) was not available. Although this was a highly undesirable situation, it was considered more productive to continue with the tests and make assumptions about the thicknesses of the layer from previous spray time profilometer calibrations than to halt the tests for lack of the required instrumentation. The data density on the graphs is rather high, precluding the use of symbols because each trace on the graph could contain up to 1601 data points. The results show a trend of decreased S_{21} series resonance frequency and increasing S_{21} transmitted power with additional loading times of polymer. The characteristic response shape of the resonance curve was examined in low and high humidity and the presence of additional water load in the attached high molecular weight PVP layer decreased S_{21} series resonance

frequency whilst simultaneously increasing the power transmissions, indicating losses. The increased water load in the polymer from increased humidity in the gas stream has two distinct effects. The first is the obvious additional mass load represented by the decrease in f_0, in FBAR but the second effect is the change in the physical state of PVP in the presence of moisture. The significant decrease in Q factor suggest that the layer is becoming more lossy, most likely indicating that the bulk modulus of the PVP is moving further away from the ideal elastic state when water adsorbs into the layer. Increasing the amount of polymer over the working area top surface electrode of the FBAR increased the sensitivity of the device to humidity. There may have been some slight contamination of the uncoated FBAR sample with PVP since the response was greater ($-\Delta f_0$ 44 kHz) than the original ($-\Delta f_0$ 12 kHz) uncoated sample. The total (%) of frequency change in response of FBAR was seen to increase from (0.13%) with a 1s load to (0.59%) with a 5s load.

Experiment 5B gave results that were contrary to all previous tests. The frequency of the device increased with increase in humidity. This frequency rise (Δf =+2.5 MHz) was substantial. The main difference in the experimental parameters was the flow rate of the gas <<70SCCM. and the method of polymer film deposition, where drop casting instead of spray coating was used. A possible explanation for this rising frequency effect is that the slow gas flow delivered the increasing humidity to the polymer more slowly giving it time to swell. *The key features of the acoustic wave devices* (in this case FBAR) *for the purposes of gas-phase sensing is that the measurable acoustic wave characteristics are altered upon sorption of the analyte onto (i) The surface of the device or (ii) The surface of the sensing layer (adsorption) or (iii) into the bulk of the sensing layer (absorption)* [6]. If the water molecules did absorb into the bulk of the PVP its hygroscopic nature suggests that it may swell. Upon swelling the effective density of the polymer would decrease, serving to effectively present the FBAR with, a decreased mass load.

The possible penetration of the vapour may also have interfered with the weak physical forces involved in binding the PVP layer to the resonating gold surface fo the FBAR. The fact that the frequency did not return to the value of the original dry state even when the

humidity meter clearly showed that the gas stream was dry could indicate that there had been some decrease in the binding of the polymer to the gold electrode surface, another but somewhat less likely cause for this effect is in that the polymer had dissolved away and the FBAR was reporting a decreased mass load. The answer to this could likely be found merely by measuring the thickness of the polymer before and after a set number of wet/dry cycling phases – a profilometer or an AFM would serve this function well.

It would be prudent to repeat all of the PVP/ Humidity tests outlined above taking gas flow rate as an additional important calibration parameter along with relative humidity, polymer layer film thickness and polymer concentration. and of course the method of polymer deposition onto the FBAR surface. Only in retrospect is the importance of a definitive value of the gas flow rate obvious. During assembly of the dedicated gas delivery system, the Rotamer type manual flow controllers were seen as a cost effective and relatively simple method of controlling the gas flow, but they had some serious limitations that were not obvious until the apparatus was actually under test. The main one being that to get a steady flow of gas from the gas out line of the FHA, the flow rate of the Rotamer controllers needed to be set to a value that was beyond the maximum value that the Rotamer flow rate indicators could show but not beyond the range of their ability to deliver that rate, hence >150 SCCM is all that can be said for the gas flow rate under these conditions. It was necessary to obtain heaver gas flow rate indicator balls to actually calibrate the gas flow rate, but they were not available in the time frames open to the project.. If these experiments are to be repeated, it would be probably be best to use dedicated mass flow controllers since the flow rate of the gas now appears to be an important measurement parameter since the rate of delivery of the additional moisture to the hygroscopic polymer seems to serve to markedly influence the response.

Experiment 6 was designed to discover if the dwindling supply of wire bonded FBARs could be reused after using them for the humidity tests by complete removal of the polymer coating by re-dissolving it in its carrier solvent and physically removing the solution with fast moving N_2 stream. By chance, a device that was not intended to be used for actual measuring purposes was used for the cleaning tests.. This choice proved to

be serendipitous for two reasons in that the spurious modes of resonance that it was afflicted by served to clearly indicate the characteristic response signature shape of the FBAR when it was uncoated, this greatly assisted in making a comparison between the uncoated, the coated and he recycled device states relatively unambiguous due to the presence of the spurious mode. It was shown that the PVP layer could be removed and the device would return to a state very closely approximating its original uncoated response. However, what was not expected was the suppression of the spurious modes when the device was loaded with the polymer later.

Experiment 7 was done to ensure that this suppression was not anomalous and that the suppression could be repeated. The suppression of the spurious modes was successfully implemented. The most likely explanation for this is that if the spurious modes are produced by lateral motions on the FBAR working area, then these shear modes readily couple into the viscoelastic polymer layer where they are subsequently damped, leaving only the bulk longitudinal modes to predominate in the FBAR response which probably do not couple with the layer so efficiently.

All of the experiments outlined in this Chapter, except experiment 7, were primarily a demonstration of the FBAR being able to perform two useful functions (i) Support a partially selective sensitising layer, and (ii) Respond to changes in that layer brought about by the presence of analyte specific to that sensitising layer. Clearly then, the FBAR even when uncoated was shown to be responsive to the presence of increased humidity in the gas stream, but with the addition of PVP to the top electrode surface the hygroscopic properties of PVP served to sensitise the FBAR to the presence of the water analyte.

It follows therefore that since PVP is also selective toward ammonia[3] that if water vapour was completely removed from the gas stream, and ammonia was used as the analyte instead, then it is extremely likely that FBAR would respond strongly to the presence of ammonia and the concentration of ammonia in a delivery gas stream could be monitored with the apparatus already in place. It may therefore be possible to detect microbial activity where ammonia is evolved during normal metabolic functions, as is the

case for the human pathogenic bacteria *Hylobacter Pylorii* which is known to cause stomach ulcers and contribute toward certain kinds of stomach cancers. (Personal communication, Professor H. Barr, Dean of Cranfield Postgraduate Medical School)

The fact that the FBAR will support partitioning polymer of one type, most likely indicates that it will support many other partitioning polymers and this opens the door for development of FBAR arrays serving as the oscillator timing units in an ultra sensitive electronic nose. This type of device would be based in the known selectivity of the mature partitioning polymer libraries that are presently in existence [17] and that are already used routinely in QCM acoustic transduction methodologies.

REFERENCES
CHAPTER FOUR

1. Fontecha. J., Fernandez. M. J., Sayago. I,. Santos. J. P., Gutierrz. J., Horrillo. M. C., Gracia. I., Cane. C., Figueras. J. (2004) Fine-Tuning of the resonant frequency using a hybrid coupler and fixed components in SAW oscillators for gas detection. *Sensors and Actuators* B **103** pp 39-144
2. Mecca. V. M. (1994) Loaded vibrating quartz sensors. Review paper. *Sensors and Actuators* A. **40**. pp 1-27
3. Mirmohensi, A., Oladegaragoze, A. (2003). Construction of a sensor for determination of ammonia and aliphatic amines using polyvinylpyrollidone coated quartz crystal microbalances. *Sensors and Actuators* B **89**. pp 164-172.
4. Iwata. H. (2004) Measured resonance characteristics of a 2-GHz fundamental quartz resonator. IEEE transactions on ultrasonics, ferroelectrics, and frequency control.l **51**, No 8. pp 1026-1029.
5. *Chemical Sensors and Biosensors for Medical and Biological applications.* Spichiger-Keller. U. Wiley-VCH Publishing. (1998)
6. Grate. J. (2000) Acoustic wave microsensor arrays for vapour sensing. *Chem Rev.* **100**. pp 2676-2648.
7. Harsanyi. G. (1996) Polymeric sensing films: new horizons in sensorics? *Materials chemistry and physics*. **43**. pp 199-203.
8. Neshkova. M., Petrova. R., Petrov. V. (1996) Piezoelectric quartz crystal humidity sensor using chemically modified nitrated polystyring as water sorbing coating. *Analytica Chimica Acta* **67**. pp 93-103

CHAPTER FIVE
5.0 INVESTIGATING THE POTENTIAL OF FBAR AS AN IMMUNOSENSOR.

5.1 Introduction

A major application of biosensors is in environmental monitoring, and research aimed at this sector has been active for over a decade. [1] A biosensor is a special type of chemical sensor where the selective coating existing between the transducer surface and the environment is derived from a biological source. An immunosensor is a special class of biosensor where the high binding specificity of naturally occurring antibodies is technologically exploited to detect targets[91] at the molecular level. The QCM has been in laboratory use as an acoustic immunosensor for a number of decades, and the initial development of this technology can likely be traced to the pioneering work of Shons *et al* (1972).[2]

5.1.1 Bulk acoustic wave immunosensors

Bulk acoustic immunosensors are a well developed and mature biosensor technology, still usually based on the original QCM technology, [3] but more recently (1997) also on MEMS cantilevers. [4, 5] MEMS cantilevers are promising mass sensitive devices with recently developed systems demonstrating the ability to resolve mass change at 10^{-19}g.[22] This sensitivity however needs to be tempered with other desirable characteristics such as ease of signal interpretation for the end-user, sensor portability, and in the field applicability. Surface acoustic wave (SAW) devices have also seen some recent success as immunosensors. Stubbs *et al* [23] used 250 MHz SAW devices in the gas phase, coated with thin films of monoclonal antibodies to detect picogram quantities of one specific analyte whilst rejecting binding from similar chemical classes of measurand to which they were exposed

[91] Immunology uses the term "epitope" or "antigen to define the molecular target that is specifically recognised by the "antigenic determinant" of an antibody. The targets are also generically known as analytes, or measurands.

It was decided to adopt the established immunosensor principles from QCM technology, and use them to coat FBAR devices with target protein layers and to perform the affinity type reactions with biological antibodies to examine FBAR characteristic responses at various resonant frequencies[92]. The perceived detection event is made by the decrease in resonance frequency ($-\Delta f$) of the resonator caused by the increased mass load, which should, in theory, correlate directly with the amount of immuno-accumulation from the antibody binding to target epitopes previously physically adsorbed onto the resonator's top gold surface electrode.[6]

This development was in essence, a "model" FBAR immunosensor system but it was not a particularly ambitious one, since QCM devices, which are known to function well in the aqueous phase[93],[7] and have become sophisticated instruments capable of dynamically monitoring antibody binding kinetics in solution in real time [8] whilst this FBAR immunosensor prototype was designed only to operate[94] the gas phase and was capable only of making static single use analysis. However, the FBAR experimental results were compared directly against a QCM system, also in the gas phase, with an identical antibody protein loading protocol so as to evaluate the *relative mass-loading sensitivities* of the high frequency (>700 MHz) FBAR against the lower frequency (~10 MHz) QCM.

Surface plasmon resonance (SPR) optical methods were used additionally to compliment the acoustic tests since SPR was a convenient and well established method which is routinely used to determine the thickness and the density of a coating on a surface. The development of SPR as a biosensor for the investigation of specific biological interactions including adsorption and desorption kinetics, antigen-antibody binding and epitope mapping has become the fastest growing application for SPR [9].

---

[92] Fundamental and overmode harmonic resonances.

[93] The results from the responses of FBAR in aqueous phase are shown in Section 6.2.2 but interpretation of them is non-trivial.

[94] The antibody binding reactions were performed in the aqueous phase, but the FBAR interrogation step was done after the reaction scheme was dried down. Obviously no kinetic studies could be made using this method of approach.

5.1.1 Antibody – form and function

In nature, the antibody glycoprotein which is synthesised by specialised immune system lymphocytes called B-cells. Antibodies circulate in the blood, lymphatic fluids and on mucous membranes, they are a first line of defence in protecting the host organism against perpetually invading pathogens such as viruses, bacteria and fungi. Antibodies also protect health by assisting in the neutralisation of certain toxins and also in identifying tumours during routine immunological surveillance activities.

The most important functional feature of an antibody is in its ability to modify its two identical hypervariable binding sites with over 30 $x10^6$ separate geometric arrangements, serving to specifically identify a vast number of molecular targets, with some antibodies having the ability to bind to more than one target, i.e., redundancy or cross-reactivity. A new geometric version of the antibody hypervariable binding region, the so-called "idiotype" will be produced[95] in response to new types of immunological challenge, this is brought about by (i) Rapid "VDJ"[96] gene rearrangement in the host, this is known as the somatic recombination hypothesis and (ii) Through an extraordinarily high level of immunoglobulin gene mutation during B-cell differentiation, this is known as the somatic mutation hypothesis. Once an antibody idiotype has been identified by the host as viable against a particular epitope on a target, the B-cell producing it undergoes clonal expansion, making millions of identical idiotypic antibody producing clone cells called B-memory cells. These cells can persist for many years, usually in the lymph nodes, and this is part the basis of immunity to diseases and the basis of medical immunisation/vaccination because the pathogen is identified and destroyed very rapidly the next time it attempts to invade the host with no lag phase involved in identification and synthesis of the effective antibody.

The basis of **all** immune responses is in the ability of the immune system to differentiate between "self", and "non-self". It is critical that antibodies do not identify host self specific targets otherwise the powerful machinery of the immune system is turned against

[95] Seemingly in a "trial and error" fashion until the correct binding geometry is found
[96] This is the nomenclature used to describe the region on the host genome that is responsible for programming antibody specificity to new targets..

the self. This desirable state is known as self tolerance but unfortunately, some cross reactivity can occasionally occur in antibodies, this is most often caused by invading pathogens attempting to evade the immune system by presenting forged epitopes designed to appear as "self" to the immunological surveillance mechanisms. When antibodies are made inappropriately against the self, the conditions that follow are always deleterious and often fatal. These so called auto-immune illnesses include multiple sclerosis, myasthenia gravis, systemic lupus erythematosis, and more commonly. rheumatoid arthritis and insulin-dependent diabetes mellitus.[10] In terms of immunosensors, the possibility of antibody cross-reactivity is a source of potential error through false positive results.

Immunoglobulin type G so called IgG antibodies[97] are large biological molecules (relative molecular mass (mr) = ~150 kDa) composed of two heavy polypeptide[98] chains (50 kDa) and two light polypeptide chains (25 kDa). Binding of antibodies to epitopes is a highly specific non-covalent event occurring due to physical forces such as electrostatic charges, hydrogen bonding, Van der Waals forces and hydrophobic forces. The reaction is a reversible one although with slow dissociation rates. [11]

In the current chapter, a physically adsorbed layer - rabbit immunoglobulin type G isotype (rIgG) - was acting as the antigen, or analyte (i.e., the protein possessing the target epitopes) and the polyclonal[99] goat immunoglobulin type G isotype (gIgG) was acting as the antibody (i.e., the protein possessing the antigenic determinant regions with high specificity for various epitope targets on the rIgG.) It should be remembered however, that both rIgG and gIgG are antibodies in their own right.

Recently, work has been in progress to recreate the binding specificity of antibodies artificially through biomimicry using the so molecular imprinted polymers (MIP).

[97] Immunoglobulin isotypes IgM, IgD, IgE and IgA also exist they are functionally distinct due to differences in the carboxyl terminal of the 50 kDa heavy chain. IgG is the simplest form of the immunoglobulin isotypes. Variants of the isotype are termed idiotypes

[98] A polypeptide is a segment of many individual amino acids linked together by peptide bonds. Functional proteins, such as enzymes or muscle tissue are made from many polypeptide chains bound together by physical forces.

[99] Meaning that the antibody could bind to various epitopes on the target protein.

Success has been achieved in detecting low levels (5 X 10^{-9} M) of phenacetin on 10 MHz QCM devices using MIP in place of the naturally derived antibody.[12] Unfortunately even though MIPs were being actively developed in our laboratory, time did not allow for the exploration of MIPs onto FBAR surfaces, but this will make for an extremely interesting future study.

5.2 Methods.

The simplest method for immobilising protein on surfaces is physical adsorption where mutual attraction between the solid surface and the protein results in coverage of the surface. Protein adsorption results from attractive forces such as ionic, hydrophobic, and van der Waals forces, [13] and it is also entropically driven [14] This was the method of choice for all protein to gold surface[100] depositions used in the experiments comprising this chapter of the Thesis.

5.2.1 Deposition of the protein solutions onto gold surfaces of quartz crystals, FBARs and optical prisms.

Phosphate buffer solution (PBS) containing 0.01M phosphate buffer, 0.0027M potassium chloride and 0.137M sodium chloride was made at pH 7.4. Immunoglobulin G type antibody from Rabbit (rIgG) and polyclonal anti rabbit IgG from goat (gIgG) were obtained from Sigma Aldrich (Poole, UK). These were both diluted to a final concentration of 100 µl/ml in PBS

Using a Gilson pipette, a 50 µl aliquot of rIgG was loaded onto the gold surfaces of (i) the SPR prism samples, (ii), the QCM samples and (iii) the FBAR samples. (Each of the samples (i, ii and iii) had been previously characterised in their respective apparatus to obtain values for the uncoated devices). All of the experiments in this chapter were conducted in air. They were each left for 12 hours to incubate in a high humidity environment to ensure that the PBS did not evaporate off to leave a salt residue on the

[100] Prisms, quartz plates and FBARs all had clean gold surfaces on which to layer the target proteins. Of some **concern** was the statement of Pan *et al* (2004) [28] who stated that to date, no piezoelectric sensor has ever been made to detect IgG , and that because anti-human igG is water soluble, it is not possible to coat a piezoelectric gold surface with the protein. The author does not know if the morphological differences between IgG from a goat and a rabbit are sufficiently different to human IgG so as to allow them to bind on a gold surface. Rabbit IgG physical adsorption to an gold surfaces was empirically determined in this study

gold surface. The humid environment was simply a sealed container with tissue soaked in reverse osmosis (RO) water. This period of 12h was considered sufficient time to allow the protein (rIgG) to physically adsorb onto the gold surface. After 12h, using a Gilson pipette, the surface was then cleaned with copious quantities of clean RO water. The samples were dried in a fast moving argon stream or nitrogen stream to avoid adulteration of the gold surface by the RO water and then each of the samples were re-tested using the appropriate instrumentation to look for the presence of a physically adsorbed protein layer on the gold surfaces. After the results had been recorded in the presence of the rIgG adlayer, 50 μl of gIgG was pipetted onto the surface of the samples. These were left to incubate in a high humidity environment overnight or for 12 hours. To remove any unbound gIgG protein, the respective devices were then cleaned with copious amounts of RO water, dried in fast moving gas stream and re-tested for responses.

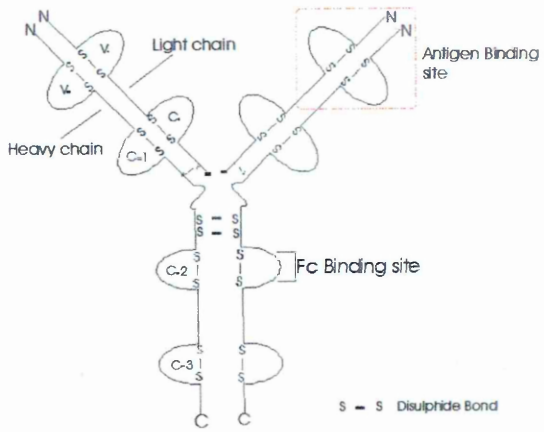

Schematic of general form of IgG antibody. Taken from lecture notes " Cellular Immunology" (1995) Liverpool University

Rabbit Immunoglobulin Type G (rIgG)

Polyclonal Goat anti Rabbit Immunoglobulin Type G (gIgG)

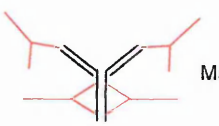

Multiple epitopes on the rIgG are bound by the gIgG

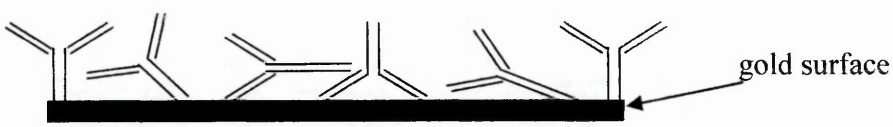

Stage 1: Physical adsorption of rIgG onto gold surface

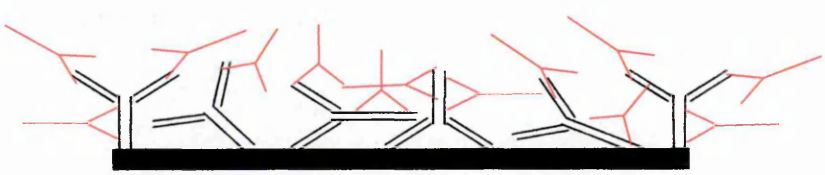

Stage 2: Multiple binding of gIgG to rIgG on gold surface

Figure 5.1 Schematic to show the structure of a typical IgG antibody and (i) Physical adsorption of rIgG to a gold surface and (ii) Binding of polyclonal gIgG to rIgG.

5.2.2 Observing the effect of antibody antigen interactions on the angle of surface plasmon resonance excitation on gold coated prisms

The phenomenon of Surface Plasmon Resonance (SPR) is an optical sensing technology that is routinely exploited for determining thicknesses and densities of thin-film coatings on surfaces and for characterisation and quantification of biomolecular interactions.[15] SPR was used in this project to compliment the acoustic probing methods of FBAR and to a lesser degree the quartz crystal microbalance (QCM). This optical analysis was performed because values with regard to the average mass of an attached layer as a product of its thickness and of its density can be established with SPR. The SPR analysis data could therefore be used to make frequency to mass calibrations for FBAR undergoing (i) physical adsorption of protein and (ii) immunological accumulation of protein.

SPR is used to determine the average mass (thickness and density) of a deposited material as a function of refractive index change, and thin metal films, typically 50 nm, of gold or silver deposited onto transparent substrates (e.g., optical prisms) are predominantly used to exploit this phenomenon. When employed as a biosensor, the variation in refractive index can be caused by the immobilisation and binding of proteins.

5.2.2.1 SPR basic principles of operation.

SPR systems measure the variance in the angle of reflectance of incident light at which surface excitation occurs.[16] This excitation creates surface plasmon resonance waves[101] which are in effect, an oscillation of the resonating electrons at the boundary of a thin metal films [17]. The phenomenon only occurs with transverse magnetic (TM) polarised light. TM polarised light reflected from the internal prism surface typically increases with increasing angle of incidence until a critical angle (θ_C) is reached and total internal lection (TIR) occurs. When there is a thin metal film on the surface of the prism, weak attenuation of the incident photons occurs due to partial absorption but there is also a second angle greater than θ_C where the incident light is absorbed strongly by the metal

[101] These are also known as evanescent waves

film due to energy transfer from the light into the surface electrons of the metal film at resonance, this angle is denoted as (θ_{SPR}) The diminishing intensity of the reflected light can be detected with a photo-detector.

When foreign films are placed onto the surface of the thin metallic layer coating on the prism, the θ_{SPR} angle will change due to changes in interfacial refractive index and this allows for changes in refractive index to be monitored between native and modified prism/metallic surfaces. If the refractive index of the interface component is known, it is possible to calculate the thickness of the layer attached to the surface. [18]

5.2.2.2 Metal coating of the optical prisms.

Prior to metal coating, SF15, 60^{O} equilateral 10 mm x 10 mm optical glass prisms (obtained from Global Optics, Bournemouth, UK) were cleaned thoroughly by ultrasonication in deionised (DI) water for 10 minutes, followed by ultrasonication in HCl for 10 minutes followed by a further 10 minutes of ultrasonication in DI water. Finally the prisms were ultrasonicated in isopropanol for 10 minutes before being blow dried in fast moving argon stream.

Two methods of gold coating the prisms were used, the first method used an Edwards 306A vacuum evaporator, equipped with a high vacuum diffusion pump and resistively heated evaporation boats. The cleaned prisms were placed into a holder to allow one face of the prism to face the gold target. The evaporator was filled with liquid nitrogen and evacuated for 3 hours to a pressure of 2.5 x 10^{-6} mbar. An 0.5 nm adhesion layer of chromium (from chrome plated tungsten rods, code NR1, Megatech, Cannock , Staffordshire UK) was deposited on to the prism surface with a deposition rate of 0.05 nm s^{-1}. The gold target was heated and deposited onto the chromium adhesion layer at a rate of 0.1 to 0.15 nm s^{-1}. The optimal thickness for SPR is ~50 nm so when this thickness was reached, the coating process was terminated, the prisms were allowed to cool for an hour under vacuum and then stored in sealed containers. (desiccators holding silica drying crystals under partial vacuum) until required for use.

The second method used to coat the prisms with the same thickness of chromium (0.5 nm) and gold (50 nm) were physically vapour deposited (PVD) onto the surfaces using the Nordiko apparatus.(*See Section* 2.2.2.2). The reason that this second method was used was because there are morphological differences between vacuum evaporated gold and PVD.[102] The FBAR was gold coated using the PVD method during the microfabrication procedures, so it was thought appropriate to use a gold layer as similar as possible to the FBAR for a more accurate comparison study of protein layering in optical systems (SPR). However, the chrome gold deposited by this PVD method was so poorly adhered to the prisms that it was not possible to use them for SPR analysis. (results not shown) so there were minor morphological differences between the gold surfaces of the FBAR and the prisms and the QCMs, the extent to which this factor influenced the results was not established.

5.2.2.3 The surface plasmon resonance apparatus.

The SPR apparatus was already in place and operational in the laboratory. (*See Figure* 5.2) The parts were attached to a matt black 600 X 300 mm optical table with M8 mounting points at a separation of 25 mm centre to centre. The polarised light from a helium-neon laser (λ670 nm) was first passed through a neutral density filter to reduce the light intensity, preventing saturation of the light detectors. The beam was then passed through a polariser and the rotation of the plane-polarised beam adjusted to either TM or TE polarisation by means a half wave plate. The TE or TM light was then fed through a beam chopper which modulated the light beam to a frequency of 200 Hz, this was the phase detection frequency of the light detectors. An in-house produced Labview code was used to implement a "lock-in" amplified type signal extraction in conjunction with an analogue to digital converter (ADC) interface card to measure the voltage output of the light detectors.

The TE/TM separated - 200 Hz modulated beam was then passed through a beam splitter, half of the beam was passed to a reference detector which could be used to compensate for any fluctuations in light intensity from source. The other half of the bean interacted

[102] The PVD technique generally delivers a smoother surface profile than vacuum sputtered coatings.

directly with the metal coated prism which had been previously aligned on the rotational stage where it was now rotated through the θ_{SPR}. The lection from this passed directly into a light detector mounted on a lower rotation stage. The detector was rotated twice as far to match the angle of the prism.

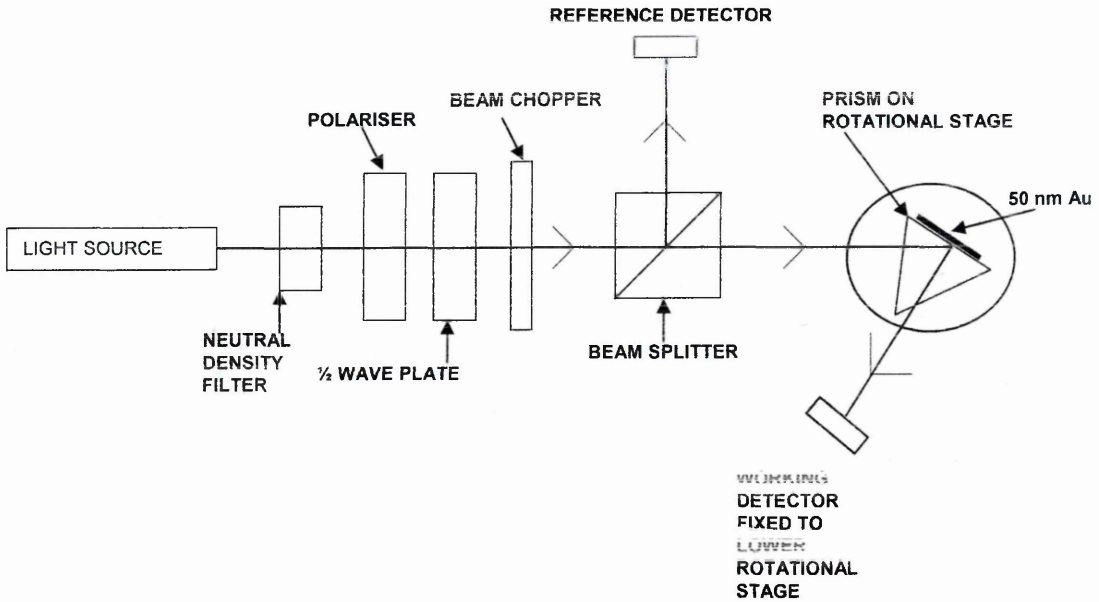

Figure 5.2 Arrangement of the principal components of the SPR apparatus. (*See appendix* 2 for apparatus list)

5.2.2.4 SPR scanning, data acquisition and analysis.

The SPR angles for gold coated prisms lacking any additional protein layer was established. This was done by placing the prism into the rotational stage prism holder and aligning the laser beam with the prism and the light detector. The prism was rotated with TM light through 9^{O} in 0.1^{O} increments The maximum dip in intensity of the reflected light as a function of θ was the θ_{SPR}. The process was repeated for the non-protein coated prism in the presence of TE light. The TM and TE ratio was calculated using Fresnels equations[103] for reflection losses and gave the SPR response independently of the light intensity, the external angles of the prism were then converted to internal angles using Snells law[104]. The process was repeated for rIgG protein coated prisms and again for prisms having undergone antibody/antigen (rIgG + gIgG) reactions on their gold coated

[103] The Fesnel equations were already programmed into the in-house SPR data analysis spread sheets
[104] The equations to calculate Snells law were also already pre-programmed into the SPR spread sheets.

surface. Data was acquired though an ADC which was GBIP interfaced with Labview running in Windows 98 on an x86 IBM compatible computer, the numerical data was saved into spread sheets which were used in the generation of XY scatter plot graphs.

5.3 Experimental section

5.3.1 Experiment 5.1 SPR based analysis of protein loading.

5.3.1.1 Method

4 gold coated SPR prisms were cleaned and characterised to obtain SPR angle for (i) the bare gold, (ii) ii) rIgG incubated and (iii) rIgG + gIgG. It was necessary to create a control to ensure that any accumulation of protein after the first physical adsorption was due to immunological accumulation. An SPR prism was incubated with rIgG, the second protein load was also rIgG (as opposed to gIgG) which was allowed to incubate in high humidity overnight, then washed in RO and blow dried in argon before undergoing SPR analysis. Thickness calculations for the layers were performed with a pre-existing spread sheet formula table. The calculation converted the difference between the SPR angle on bare Prism surface (i.e., gold surface) and the SPR angle recorded in the presence of a film on the Prism into a value for film thickness in nanometres (m^{-9}).

5.3.1.2 Results

Although 5 SPR repeats were performed, only 3 delivered any useable data. The aberrant results (not shown) were most likely attributable to damage with minimal abrasion from the Gilson pipette tip to the gold layer on the Prism samples that were PVD coated in the Nordiko apparatus.

Figure 5.3 (A) shows the result from Prism 1. The thickness of the physically adsorbed rIgG layer is 2.6 nm and the immunological accumulation of gIgG onto the rIgG layer increased the thickness to 6.8 nm.

Figure 5.3 (B) shows the result from prism 5. The thickness of the physically adsorbed rIgG layer is 3.5 nm and the immunological accumulation of gIgG onto the rIgG layer increased the thickness to 7.0 nm.

Figure 5.3 (C) shows the result from the control sample prism. The thickness of the physically adsorbed rIgG layer is 3.5 nm the second incubation of rIgG (i.e., the same protein) increased the thickness of that layer to 4.9 nm.

The relative standard deviation for the three separate initial rIgG loadings on the Prisms was RSD 29.25%

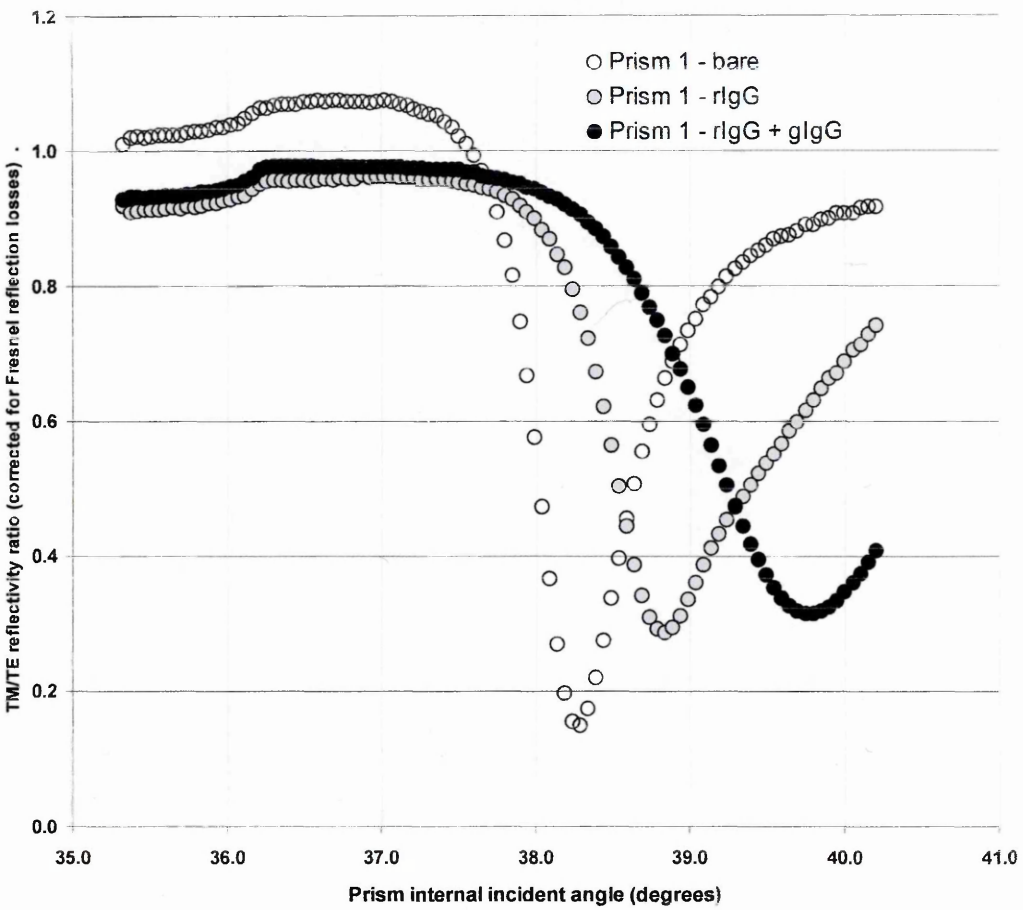

Figure 5.3 (A) Shows the TM/TE corrected reflectivity SPR for prism 1 in unloaded state, with physically adsorbed rabbit protein layer (rIgG) and subsequent immunological accumulation of polyclonal goat anti rabbit immunoglobulin (gIgG).

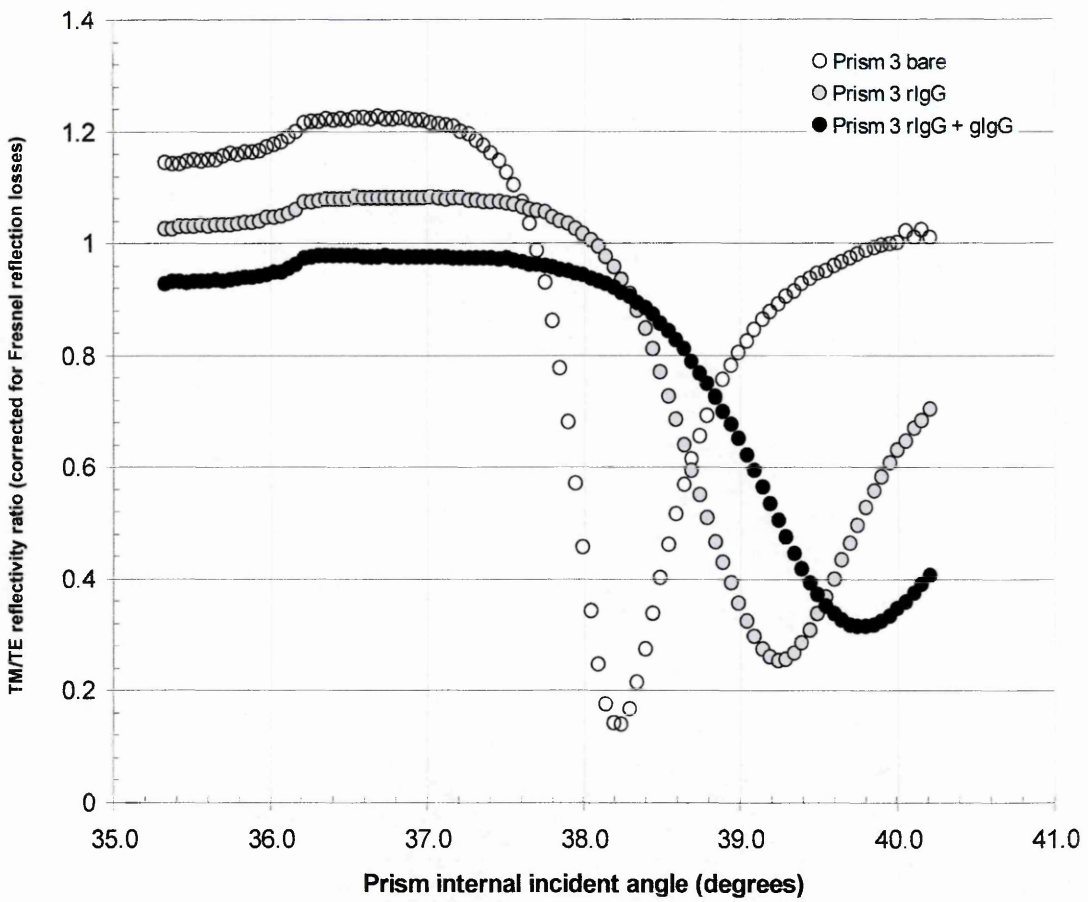

Figure 5.3 (B) Shows the TM/TE corrected reflectivity SPR for prism 3 in unloaded state, with physically adsorbed rabbit rIgG and subsequent immunological accumulation of gIgG.

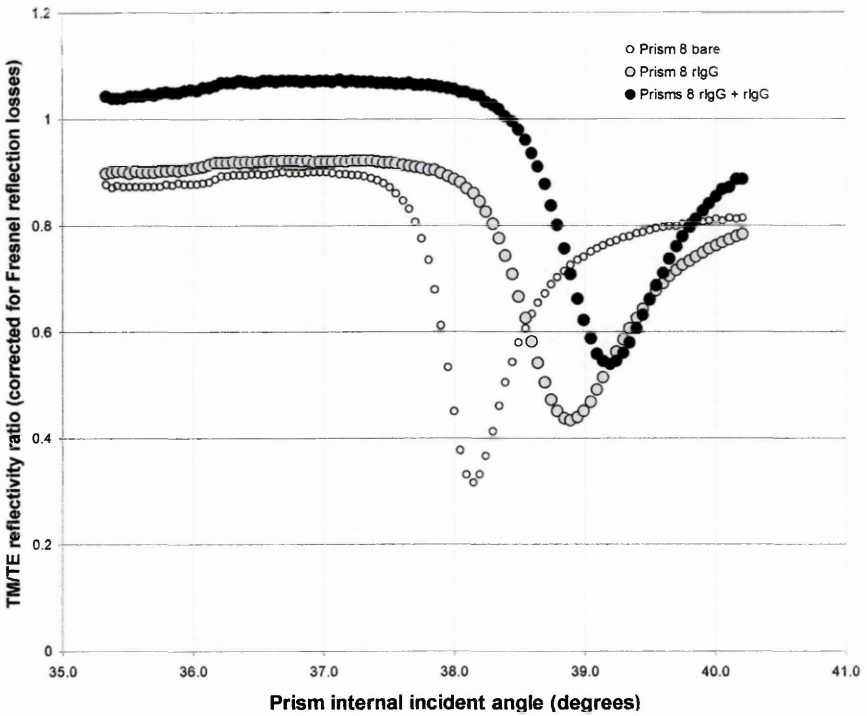

Figure 5.3 (C) Shows the TM/TE corrected reflectivity SPR for Prism 8 (Control) in unloaded state, with physically adsorbed rIgG and then with rIgG + rIgG.

Table 5.1 Summary of SPR internal angles and thicknesses of protein adlayer on gold coated prisms

Internal angle at minimum TM reflectivity	Prism 1	Prism 3	PRISM 8 (control)
θ air	38.2948	38.2454	38.1465
θ rIgG	38.8426	39.2448	38.8927
Thickness rIgG	**2.6 nm**	**4.7 nm**	**3.5 nm**
θ rIgG + gIgG	39.7519	39.7519	
Thickness rIgG + gIgG	**6.8 nm**	**7.0 nm**	
CONTROL θ rIgG + rIgG			39.1943
Thickness of the control rIgG + rIgG			**4.9 nm**

5.3.1.3 SPR Result Summary

Much of the body of literature relating to SPR analysis reviews experiments that were performed in aqueous environments. For the purposes of this thesis, there was no need to employ liquids during the analysis since the comparison to be made was with FBARs loaded with identical protein protocols whilst operating in air.

The change in SPR angle is due to the change in the refractive index at the surface of the prism caused by the addition of proteins to the gold surface and the decrease in SPR depth is due to the absorption of the light on the surface of the Prism due to interaction with the proteins. The SPR data showed that there was additional thickness increase when incubating rIgG onto the physically adsorbed rIgG layer. This was most likely attributable to either further physical adsorption on to the gold surface, if assuming the initial 12 hour incubation had not completely covered the surface, or to further non-specific protein-protein binding. The additional thickness was not due to immunological accumulation[105] since the rIgG did not posses self epitopes. On average, the physically adsorbed rIgG layer thickness on the three Prism samples was 3.6 nm. and the total estimated average thickness of the combination of rIgG + gIgG protein adlayers on the gold surfaces was 6.9 nm.

5.3.2 Experiment 5.2 QCM based analysis of protein loading

5.3.2 1 Method

The protein samples used for the QCM experiments were from the same stock solution and in the same concentration (100 µl/ml) as for the SPR experiments. The gold surfaces of the QCM (top and bottom electrode) were cleaned with an acetone/IPA solvent rinse and then blow dried with N_2 stream. This was done since it was not possible to clean FBAR samples rigorously due to PCB mounting. So this cleaning procedure was identical to the FBAR cleaning procedure to maintain experimental standardisation.

[105] Immunological accumulation strictly implies binding of targets to epitopes.

Three standard off-the-shelf AT-cut QCM disks (QCM 1, 2 and 3) with nominal operating resonance frequencies of ~10 MHz were obtained from in-house storage. (*See Figure* 1.3). The crystals were interrogated with the Libra® quartz piezoelectric measuring system manufactured by Technobiochip Ltd which sent the frequency data to a standard x86 computer. After allowing the Libra ® to warm-up for 30 minutes, baseline responses were obtained for each of the three uncoated QCM samples, these were generated over 50 iterations. The QCM unit was then physically removed from the measuring system and replaced. This was done on four separate occasions to ensure that the baseline response was recording similar f_0 values each time the QCM plate was inserted into the frequency counter as there was some concern with regard to wear and electrical contact continuity in the electrode insertion plug. Likewise for protein sample testing, the QCM was replaced into the measuring system four times, but the frequency response of the QCM was generated over 100 iterations rather than 50.

When handling QCM 3 with tweezers (prior to the 2nd protein loading but after the initial base line determination and 1st protein loading), a small section (< 1^2 mm) of the edge of the brittle crystal shattered. The crystals are known to show greater mass sensitivity on the centre of the electrodes: the sensitivity decreases monotonically with the radius of the electrode in a Gaussian manner becoming, in the gas phase, negligible beyond the electrode boundary.[19] But this of course does not bear strict relevance to the *stability* of the device if it is damaged at the edge. Since the QCM units were expensive and in extremely limited supply and because the damage was distant to the electrodes, the decision to continue using the device was made, but to pay special attention to the stability of the responses generated from that sample.

After characterisation of the uncoated QCM devices, they were then tested in the presence of rIgG protein layer and the frequency responses of the QCM were recorded. The devices were then re-tested in the presence of rIgG and gIgG. The aliquot amounts and concentrations were identical to those used for the SPR experiments as were the incubation times and washing procedures. A control sample was used to determine the effect of water (50 µl) in PBS in place of rIgG in PBS on QCM 1.

The samples were interrogated continuously for 100 iterations (~30 minutes) on four separate occasions to obtain four baseline responses. The average of this response was taken and a standard deviation for all the data was calculated. The average unloaded nominal operating frequency (f_0) was normalised and set at zero Hz to measure $-\Delta f$ for the two protein loading conditions (i) rIgG and (ii) rIgG + gIgG on the QCM.

5.3.2.2 Results

Figure 5.4 gives the average change (over 4 consecutive 100 iteration tests) of the QCM resonant frequency ($-\Delta f$) away from the frequency of the normalised unloaded sample. (i.e., (uncoated QCM baseline average $f_0 = 0$ Hz) and the standard deviation for (i) rIgG and (ii) rIgG +gIgG for each of the QCM samples is given. QCM 1 showed $-\Delta f$ -6.41 Hz for the water/PBS control, $-\Delta f$ 130.66 Hz for the initial rIgG incubation and $-\Delta f$ 631.78 Hz for the rIgG + gIgG loading, response was stable. QCM 2 showed a response of $-\Delta f$ 220.58 Hz for the initial rIgG incubation, and $-\Delta f$ 705.79 Hz for the rIgG + gIgG and the response was stable. Finally, QCM 3 showed $-\Delta f$ 163.39 Hz for the initial rIgG incubation and $-\Delta f$ 391.92 Hz for the rIgG + gIgG. Response stability was good for the initial loading, but faltered to over 30% error on average for the second protein load.[106] The relative standard deviation (RSD) between the three separate initial physically adsorbed rIgG loadings on QCM was RSD = 26.5%.

[106] This was also the first measurement on made with the device since it was damaged at is edge with tweezers during handling.

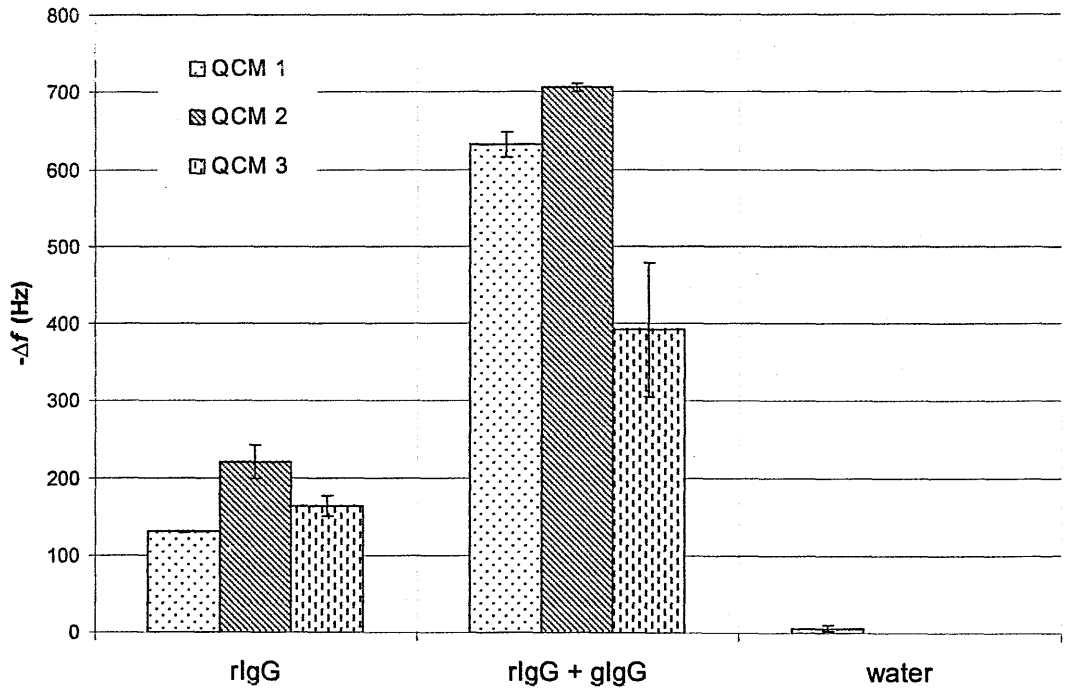

Figure 5.4 Shows the average change in resonant frequency from four repeats each of 100 iterations of three QCM units (with nominal operating frequencies of 10 MHz) caused by the mass loading effects from the addition of 50 µl (100 µl /ml) rabbit IgG and 50 µl of (100 µl /ml) polyclonal goat anti rabbit IgG. QCM 1 also shows blank PBS/ water control. (Error = RSD).

5.3.2.3 Discussion

The control on QCM 1 sample which lacked any protein (replaced by the same aliquot volume of RO water) gave minimal response, this was as expected. QCM 3 appeared to suffer from unacceptable response error after damage to the crystal edge caused by tweezers handling. It is therefore suggested that damaged QCM devices should have special attention paid to their stability, or should not be used at all. The data from the second protein loading (rIgG + gIgG) on this device (QCM3) will not be input into any further calculations due to the potential of the error to skew the overall results.

The general guidelines from the instruction manual accompanying the Technobiochip Libra ®_QCM measuring system suggests that for a 10 MHz AT cut crystal such as the ones used in this set of tests, when $-\Delta f$ =1 Hz then mass loading should be assumed to be ~ +1 ng. This is figure is calculated using the original Sauerbrey equation. Although this is only an approximation, and does not take into account any dissipation factors[107] due to acoustic attenuation from lossy or non ideal layers, this approximate value, ($-\Delta f$ =1 Hz +1 ng mass load) shall therefore be adopted as an estimate of the mass of the protein loading on QCM in this thesis. The value of +1.07 ng per -1 Hz for a 9 MHz QCM system is given in the literature by Kuosawa (1990) [25]

It was considered by Tessier *et al* (1997) [24] that it was important not only to consider the mass effects, but also the boundary viscoelastic properties, with respect to changes of the shear acoustic impedance when antibody binding reactions take place at the surface of a thickness shear mode acoustic sensor, but they concluded that the effect was very small and that mass loading from immuno-accumulations dominated the response, even when the experiments were carried out in a liquid. Martin *et al* (2000) [26] state that the Sauerbrey model works well for acoustically thin films ($\varphi<\pi/4$) even if the film is not rigid (as is often stated in the literature), a viscoelastic layer can be treated as an ideal mass layer, with response dependent only upon its area mass density. Also since, the SPR data revealed that the protein adlayers combined were no more than a maximum of 7 nm thick, they are

[107] The dissipation factor is the reciprocal of the Q factor

likely to be thin enough not to cause any significant phase shift during the interaction of the transverse acoustic probe wave with the protein layer and hence the approximate guideline given in the user manual may be quite accurate after all. To be certain that the FBAR was not losing mass response to the viscoelastic effect of the protein layer, a brief study was done where the characteristic shape of the resonance curve of the FBAR was examined directly to look for changes in the power response or in the Q factor of the device

However, with this manufacturers recommended value in mind, the mass estimated for the protein loads on the QCM samples then are simply the values in Hz converted into ng. For example, the mass load of QCM 1 for initial physical adsorption of rIgG onto the gold electrode is ~131 ng because $-\Delta f$ was 130.66 Hz, the additional mass of gIgG was ~501 ng because $-\Delta f$ was 631.78 Hz in total. Likewise for QCM 2 the mass of the initial physically adsorbed rIgG load was 220 ng and subsequent immunological accumulation of gIgG onto the rIgG adlayer was 485 ng.

If the molecular weight of both rIgG and gIgG are assumed to be the same (~150 kDa), then, on average, for QCM 1 and QCM 2 samples combined, there were 3.8 units of polyclonal gIgG binding to 1 unit of the physically adsorbed rIgG protein layer. It was interesting to note the close agreement for the relative standard deviations for the initial rIgG loading onto *both* 3x QCM crystals (RSD = 26.50%) samples and 3x SPR Prism samples (RSD = 29.25%)

Where the comparison of the results obtained between the two methods appears to begin to deviate is in the second protein loading involving immunological accumulation. The SPR results indicated an rIgG + gIgG adlayer that was just over double the thickness (6.9 nm) of the initial physically adsorbed rIgG layer. (3.6 nm). However, the mass loads that are inferred by $-\Delta f$ for the QCM tests indicated that the rIgG +gIgG mass load was ~3.8 times that of the initial load. Of course, it may not necessarily be the case that the increased mass load increased the thickness of the layer by the same proportion, the additional mass could possibly be attributed to increased density in the layer where

exposed epitopes are nested within the rIgG layer, that is, the rIgG epitopes were not all neatly lined up on the rIgG surface. This possible protein adlayer density increase may be shown in the decrease in the SPR reflectivity minima value, quite independent of the SPR angle. It is also possible that the 3D conformation of the rIgG layer is changed during its binding to the gold surface making it thinner than the antibody would have been had it been allowed to bind to its epitope. This finding perhaps shows that the two methods SPR and QCM, are complimentary, as is indicated by Koblinger and Uttenthaler (1995) [20] who compared the QCM and the SPR method for surface studies in immunological applications as did Laschitsch *et al* (2000)[27] but in this case surface plasmon spectroscopy was used where the actual QCM was modified with a surface corrugation grating to allow for simultaneous determination of acoustic and optical foreign film thickness.

From the SPR data, it is estimated that the for the initial rIgG loading, the thickness of the protein layer (whether conformationally altered or not) was on average 3.5 nm, and that the 10 MHz QCM frequency response to this SPR derived thickness was on average $-\Delta f$ 171.5 Hz.

The purpose of the two preceding experiments was not to consider the relative pro's and con's of QCM/SPR, the purpose was, of course, to use the combination of the two well established complimentary optical/acoustic analytical systems to make an estimate about (i) the actual mass load and (ii) the thickness of physically adsorbed protein films onto a gold surface and then the subsequent immunological accumulation of further protein loads onto the surface as a calibration step for making calculations regarding the observed S_{21} series resonant frequency on FBARs with the same protein loading protocols.

At this stage of the tests, it was considered that there was sufficient data obtained from QCM/SPR to embark on immunosensor experiments using FBAR as the transducer module and relate its performance against the AT-cut shear mode QCM devices operating at 10 MHz.

5.3.3 Experiment 5.3 FBAR based analysis of protein loading

5.3.3.1 Method

5.3.3.1.1 General operating procedures

Various FBAR samples with wirebonds connecting them to 50Ω transmission lines on a PCB were loaded into the FBAR housing assembly (FHA). The FHA was connected to the Network Analyser with coaxial cables and SMA and N type connectors. (*See Figure* 4.2) The S_{21} characteristic responses of the devices were recorded. The nominal (uncoated) FBAR response f_0 was recorded, then normalised and set at zero. The change in FBAR S_{21} frequency responses due to protein loadings were observed, and presented for graphical analysis.

5.3.3.1.2 Care and cleaning of the FBAR top surface electrode

Some undetermined level of organic contamination of the FBAR gold surfaces was inevitable from general (gloved) handling of the devices during the wire bonding and PCB mounting procedures and also from general exposure to ambient laboratory conditions whilst in storage, and during testing, especially when the PCB sample in the FHA was changed. Organic contamination of the gold surface was assumed to interfere with protein physical binding to the gold surface, so immediately before loading the FBARs with the rIgG protein, the gold surface was cleaned with an acetone/IPA solvent rinse and then blow dried with N_2 stream, this solvent clean was, on balance, considered the best method of approach. Other more harsh treatments involving a sonication step were considered too harsh, since sonication would have probably dislodged the delicate wire bonds – although this was not tested. Also, the extremely effective method of plasma barrel etching which had previously been used to remove any organic residues on the gold surface of FBAR during microfabrication stages was not possible at this stage since the PCB on which it was now mounted contained organic plastics and was therefore was not amenable to the plasma treatment for a variety of reasons, but mainly because there was some concern about excessive organic contamination to the Biorad® barrel etcher vacuum chamber. A piranha cleaning treatment (H_2O_2-H_2SO_4)(1:3)) was also considered too harsh since the gold top electrode was only 100 nm thick and quite delicate.

5.3.3.1.3 Loading the FBAR top surface electrode with rabbit immunoglobulin type G antibody and polyclonal goat anti rabbit immunoglobulin type G antibody protein solutions in phosphate buffer and subsequent FBAR characterisations.

Using a Gilson pipette[108], a 50 µl aliquot of rabbit antibody (rIgG) in PBS was deposited on to the FBAR top electrode which had been very recently cleaned with an acetone/IPA solvent mixture. The protein/PBS solution was allowed to incubate on the FBAR top surface electrode for 12h in high humidity at room temperature. After this time, the antibody/PBS solution remaining on the FBAR surface was washed off with copious amounts of RO water and dried in rapid N_2 stream and the device was then characterised in the FHA on the network analyser to obtain traces showing the effect of physical adsorption of the initial rIgG protein adlayer onto the FBAR top electrode gold surface.

The adlayer was now estimated as 3.6 nm (± 1 nm) thick the assumption being made on the basis of the SPR analysis for an identical protein loading condition on a gold surface[109] and the mass of the protein film was estimated as 171 ng (± 45.5 ng) deposited per 50 ul aliquot from the QCM tests involving identical loads.

A 50 µl aliquot of polyclonal goat, anti-rabbit antibody (gIgG) in PBS was then deposited onto the FBAR surface with physically adsorbed rIgG adlayer The FBAR was then incubated for a further 12 hours in a high humidity environment at room temperature and then washed in copious RO water to remove any unbound material from the surface, dried in rapid N_2 stream and finally characterised in FHA on the network analyser, this time to show the mass loading effect of an antibody/antigen epitope binding affinity reaction as a function of change in the S_{21} series resonant frequency of the FBAR.

5.3.3.1.4 S_{21} characterisation of protein loaded FBARs

[108] A number of high quality FBAR units were lost from damage to the delicate piezoelectric membrane by accidental piercing from the Gilson tip. Great care was also required to avoid brushing against the wirebonds with the tip because they were easily dislodged. If a single earth connecting wire became dislodged, experimentation on the device could continue, but if a single signal wire was dislodged, the device was rendered useless until repair.

[109] The chrome/gold surface deposition methods were different (PVD (FBAR) vs vacuum sputtering (Prism) and likely had different surface smoothness profiles.

In its unloaded state an FBAR which was wire bonded to 50Ω transmission lines on a PCB and fixed securely to the FHA was interrogated with the network analyser over 0-3 GHz frequency range. The response traces were generated and the useable harmonic overmodes of the FBAR were additionally identified by narrowing the bandwidth focus over the tips of each of the overmodes. FBAR S_{21} responses of lower and higher harmonic resonant frequencies that were suitable for analysis[110] were recorded.
FBARs were then loaded with the initial 50 µl aliquots of rIgG and characterised to show the mass loading effect of the physical adsorption of the protein to the gold surface of the FBAR. The FBARs were then loaded with the gIgG antibody and characterised for a final time. The average frequency from the specified number of iterations for each of the tests was calculated against the normalised unloaded ($f = 0$ HZ) FBAR resonant frequency at the particular overmode in focus and the results were displayed as bar charts.

It should be noted that each time the FBAR was loaded with an aliquot of protein, the PCB on which the FBAR was mounted and wire bonded was, by necessity, removed from the FHA for incubation in highly humid environment and it was then replaced. This procedure was considered to be a potential source of error due to the possibility of non-identical electrical connections. To minimise the possibility of response instability due to this, care was taken to ensure the PCB's were fitted to the base of the FHA with snug fit and the same number of screw turns were used each time.

5.3.3.2 Experiment 5.3 (A, B, C and D) Observing the effect of loading target rIgG and subsequent loading of polyclonal anti rabbit gIgG on FBAR S_{21} series resonant frequencies

This experiment, 5.3, considered the S_{21} series resonance frequency responses of four individual FBAR devices due to the additional mass from physical protein loading and from subsequent immunological accumulation of antibody to the epitopes on the target protein layer. The repeats were used to observe reproducibility, the protein loading procedures were identical for each device.

[110] Some of the overmode resonance curves of FBARs were afflicted with spurious resonant modes at their tips, and this prevented them from being analytically valid since the spurious modes could cause the recorded f_0 to flip between two or more values over a relatively wide frequency bandwidth substantially increasing the error range.[22]

The devices used in experiment 5.3 (A, B and C) used FBARs with a ZnO piezoelectric membrane backed by an SiO_2 layer, this incorporated mass layer had the effect of lowering the fundamental resonance frequency of the device, so that the overmodes could be brought into the measurement range of the network analyser. The usable harmonic overmodes were used to examine the effects of mass loading from protein deposition at progressively higher harmonic frequencies on the same device. The FBAR device used in experiment 5.3 (D) was AlN based piezoelectric device with only a single resonant mode manifesting within the measurement range of the network analyser, this was because it lacked an buried SiO_2 backing layer in the wafer on which it was microfabricated[111].

5.3.3.2.1 Experiment 5.3 (A)

5.3.3.2.1.1 Method

FBAR Device 20 on PCB 10 was used for experiment 5.3(A). The device was S_{21} characterised on the network analyser with 1601 data points over a full frequency range (0-3 GHz) to show the fundamental and harmonic resonant overmodes. The usability of each of the resonant harmonics was evaluated taking the magnitude of the response and the presence of any spurious modes into consideration.. The lowest usable resonance frequency ~321 MHz and the highest useable resonance frequency ~943 MHz were both interrogated over 50 iterations with 1601 data points collected per iteration, and the average resonance frequency was calculated for both curves under the following conditions. (i) Nominal (uncoated device which was normalised and set at (f = 0 HZ) (ii) Device with rIgG adlayer after 12 hour incubation and washing step. (iii) Device with rIgG + gIgG bilayer after further 12 hour incubation and washing step.

Data showing the effect of protein loading was presented as a bar chart with average frequency change ($-\Delta f$) against the normalised nominal operating frequency.(f = 0 Hz). Standard deviations for the average of 50 iterations were (< 0.00015[112]) and at this level of accuracy, it would not be possible to visualise error bars on the bar charts, so the

[111] The author personally microfabricated the ZnO based FBARs and wirebonded them to PCB, but was not involved in the manufacture or wire bonding procedures for the AIN based device.
[112] This high level of FBAR signal stability is most likely attributed to the automated polynomial fitting of the measured data.

standard deviations were not included with the graphical output in the final analysis, but they were calculated and stored.

5.3.3.2.1.2 Results

Figure 5.5 (A) shows characteristic response of FBAR over S_{21} full band frequency sweep (0 -3 GHz) with 1601 data points collected over the range. Two high quality harmonic resonant peaks at f =321.390 MHz and f = 943.162 MHz were found to be available for analysis, and various non-useable resonances are also apparent. The resonance peaks that were used for the analysis clearly marked with arrows. The full band trace is also shown in truncated form to assist in data visualisation. (*See Figure* 5.5 (B)). A representative sample of a resonance curve that is unusable for the analysis due to the presence of spurious modes of resonance is shown in Figure 5.5 (C) For sensor applications, a clean resonance spectrum clear from spurious modes is obligatory. This is because the resonance utilised for the sensor function shifts within a certain frequency range depending upon the measurand. If there are spurious modes, or any other modes with different dependencies upon the measurand, resonance-frequency crossings and mode couplings may occur within the measurement frequency range. Such mode couplings not only produce significant deviations from linearity, but sometimes even produce frequency jumps and activity dips.[21] So FBAR characteristic responses with spurious modes such as the example one shown in Figure 5.5 (C) would not be used for protein analysis due to increased potential error

Figure 5.5 (D) Shows a bar chart of -Δf from the nominal (unloaded condition) S_{21} series resonance frequency of the FBAR at the particular useable harmonic overmodes when rIgG was incubated for 12 hours on the gold surface and the subsequent effect of additionally incubating gIgG to give an adlayer of rIgG + gIgG.

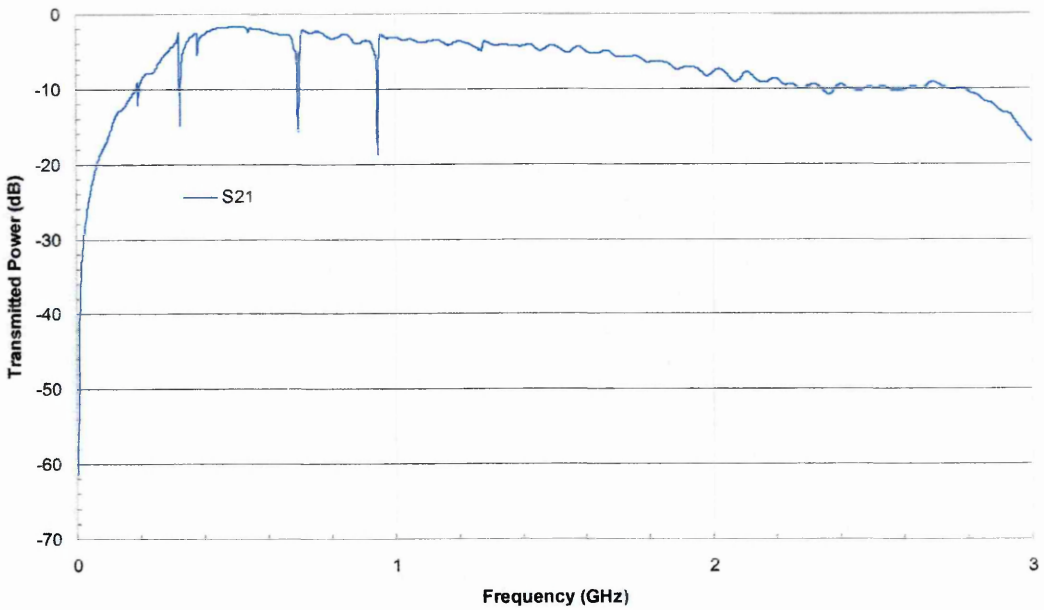

Figure 5.5(A) Shows a full band (0-3 GHz) S_{21} sweep with 1601 data points of FBAR device 20 on PCB 10.

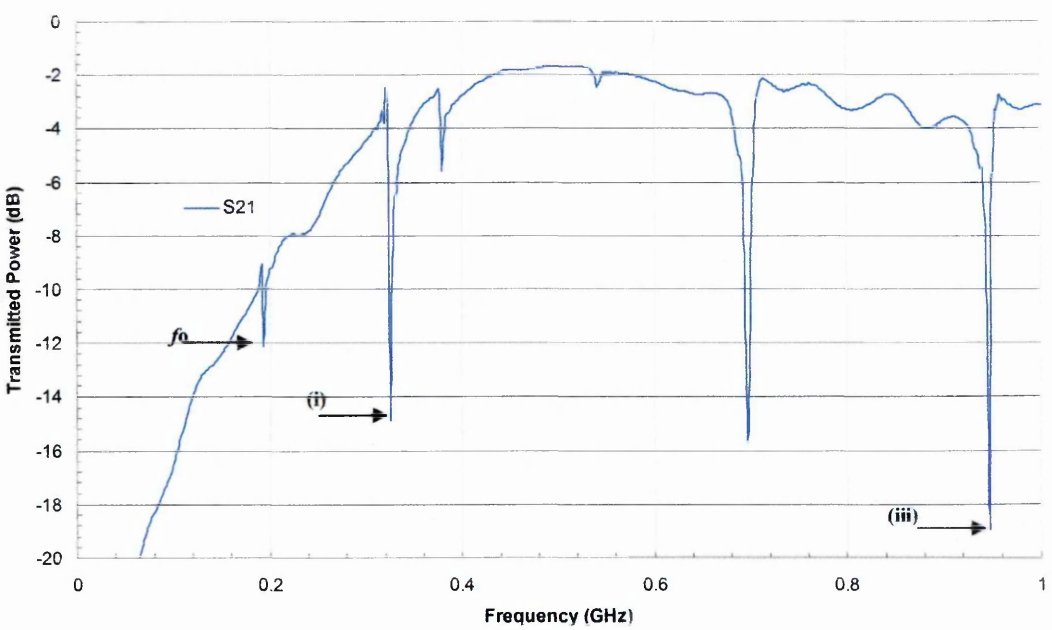

Figure 5.5 (B) As above, but X and Y scales are truncated down to 1 GHz and 20 dB respectively to assist in data visualisation. The resonant peaks at (i) 321.386 MHz and (iii) 943.162 MHz that were used in the protein analysis are indicated with arrows.

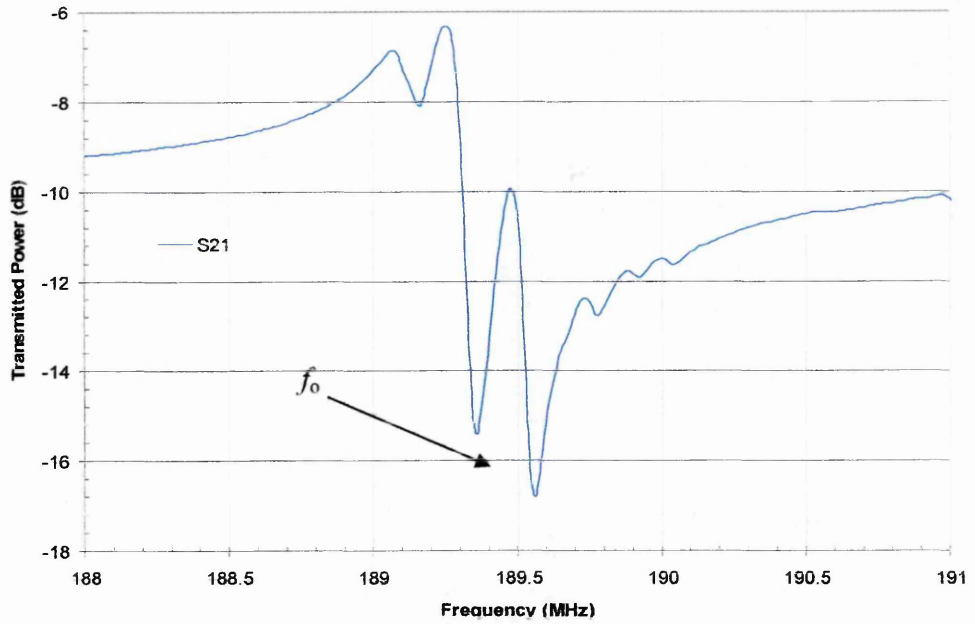

Figure 5.5 (C) Shows an example of a spurious mode of resonance. S_{21} 3 MHz (188-191 MHz) span sweep over the FBAR device 20 on PCB 10 *fundamental* series resonance curve. 1601 points.

It is not possible to state f_0 with precision of > ~150 kHz for this response since there are two distinct peaks in the main body of the f_0 resonance curve. The analysis software would choose the curve with the least power transmission as f_0. So in this case 189.6 MHz. But it is possible that these states could flip causing apparent frequency jumps.

Spurious modes were not limited to primary modes and could occur on any of the overmode harmonic resonance curves as well. It was not possible to predict their presence, and only narrow band (< 5 MHz) focus over each of the tips would reveal the presence or absence of them. This was quite time consuming and an automated process would have been beneficial in this case. The spurious modes of resonance not only increased the potential error range of the response, but also, transverse wave mode (which was thought to produce the spurious modes in the first place) coupling into a foreign film had previously been shown in this work to damp the spurious mode to give clear f_0 but that mass sensitivity as a function of $-\Delta f$ was likely to have been diminished during this process. (*See Figures* 4.15 and 4.16) It was considered unnecessarily complicated to use curves with spurious modes at this stage of the project.

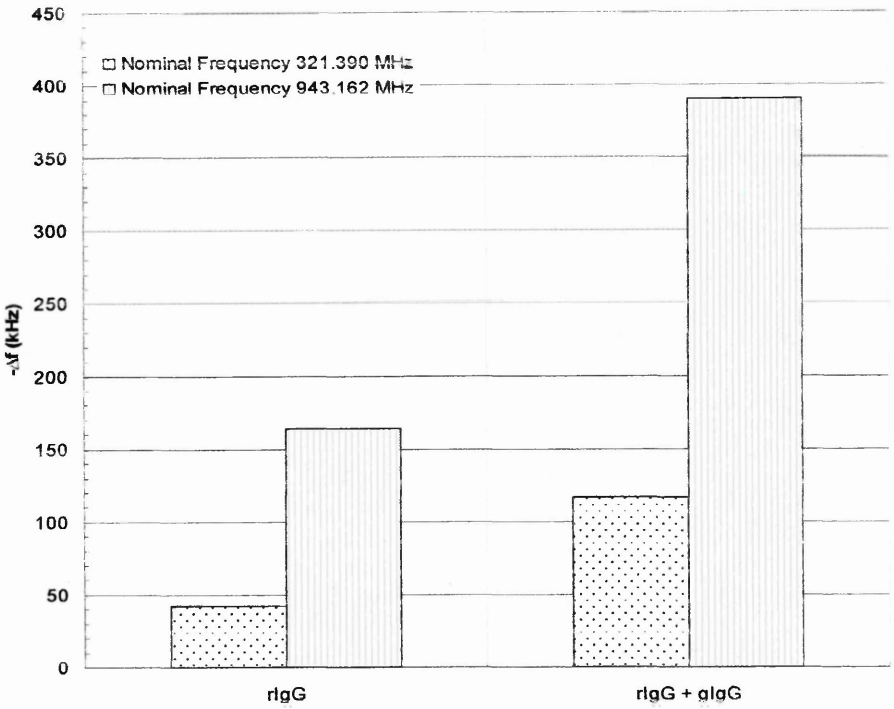

Figure 5.5 (D) Shows the relationship between changes in FBAR (device 20 on PCB 10) S_{21} series resonance frequencies ($-\Delta f$) caused by the mass loading effects from the physical adsorption of an adlayer of rIgG onto the gold surface of the FBAR after 12h incubation on the gold top electrode surface and then the subsequent antigenic binding causing immunological accumulation of polyclonal gIgG to multiple epitopes expressed on the rIgG protein layer.

Table 5.2 Result summary FBAR device 20 on PCB 10 S_{21} series resonance frequency change due to mass loading from proteins.

Nominal Frequency (f) (MHz)	$-\Delta f$ (kHz) due to rIgG loading	% change of f due to rIgG loading	$-\Delta f$ (kHz) due to rIgG + gIgG loading	% change of f due to rIgG + gIgG loading
321.390	41	0.013	115	0.036
943.162	162	0.017	490	0.052

5.3.3.2.2 Experiment 5.3 (B)

5.3.3.2.2 1 Method

FBAR device 9 on PCB 11 was used. The protein loading procedures and FBAR interrogation methods employed were identical to those described for Experiment 5.3 (A). In this case, the Q factor of the FBAR response is also considered as an additional output parameter to ascertain how much, if any, signal damping was being experienced by the acoustic probe wave during interaction with the protein adlayer.

5.3.3.2.2 2 Results

Figure 5.6 (A) Shows characteristic response of FBAR over S_{21} full band frequency sweep with 1601 data points collected over the range but the figure is truncated to 1 GHz showing only the relevant parts of that trace. The resonant harmonics used for the protein analysis are indicated. The useable FBAR S_{21} series resonance frequencies were found at 316.858 MHz[113], 679.818 MHz and 922.361 MHz.

Figure 5.6 (B) Shows that the physically adsorbed rIgG layer decreased FBAR S_{21} series resonance frequency and the subsequent affinity binding of the polyclonal gIgG decreased the resonant frequency further due to the additional mass loading. The values for this change are tabulated below in Table 5.2

Table (5.2) Summary of FBAR device 9 on PCB 11 S_{21} series resonance frequency change due to mass loading from proteins.

Nominal Frequency (MHz)	-Δf(kHz) due to rIgG loading	% change due to rIgG loading	-Δf(kHz) due to rIgG + gIgG loading	% change due to rIgG + gIgG loading
316.858	26	0.082	162	0.511
679.818	88	0.129	438	0.64.4
922.361	115	0.124	664	0.719

[113] This mode was also analysed for its characteristic responses to protein independent of Δf

The results shown in Figure 5.6 (B) show only the frequency change (Δf) of the device, and although mass loading was expected to dominate the response because the protein adlayers were thin (maximum ~7 nm), it was decided to look closely at the characteristic resonance shape of the first overmode (316.858 MHz) to check if there were any significant changes in the S_{21} power transmission or in the Q factor upon the two protein loading events. Changes in these parameters can be indicative of some form of signal attenuation due to loss experienced by the probe wave entering the protein. If carefully calibrated, these values can give the amount of deviation from "ideal" gravimetric loading, to non ideal or the so called non gravimetric responses, and ultimately they can be used to make rheological determinations about changes in the physical material state of intimately attached foreign films on BAW devices.

Figure 5.6 (D) shows that although mass load dominates the response, there are two additional factors to consider. The first is the apparent improvement of the power transmission, by~ -0.2 dB upon protein loading, but also a significant improvement from the original trace where the minimum S_{21} power transmission was ~ -27 dB (See figure 5.6 (A)). However, this discrepancy can almost certainly be attributed to non identical electrical connections from the PCB to the FHA when the PCB was replaced by hand each time the test was performed. More importantly, there is also a change in the Q factor of the responses and this can be inferred by the increase in the width of the curve it is highly unlikely that Q factor response of the device could be altered due to the physical replacement of the PCB into the FHA. In this case the 1 dB Q factor was taken, so the real value is exaggerated, the Q factors from the spread sheet for this overmode are as follows.

(i) Unloaded Q value = 1949.892

(ii) After protein physical adsorption Q value = 1689.768

(iii) After immuno accumulation of the gIgG Q value = 1689.041

The significance of this change in the characteristic response of the FBAR is not known at this time, other than to indicate that there is some minor perturbation of the acoustic signal indicative of a non perfectly ideal mass load response from the protein layers

However, the frequency decrease from the mass loading of the proteins dominates the response and the frequency response can ostensibly be treated as ideal. These results are in general agreement with those of Tessier *et al* (1997) [24] who concluded that the viscoelastic effects of antibody thin-films on QCM devices could, on the main, be ignored and that they could be treated as ideal mass loading layers. It also finds agreement with Martin *et al* (2000)[26] who consider sufficiently thin viscoelastic layers to behave for all intents and purposes as ideal mass loads.

However, if this the biological layer were to become thick i.e., into the micron range, for example if attempting to monitor whole cell populations, then the small ΔQ factor responses that are seen in Figure 5.6 D and which are so over shadowed by the mass loading responses, would probably become very significant.

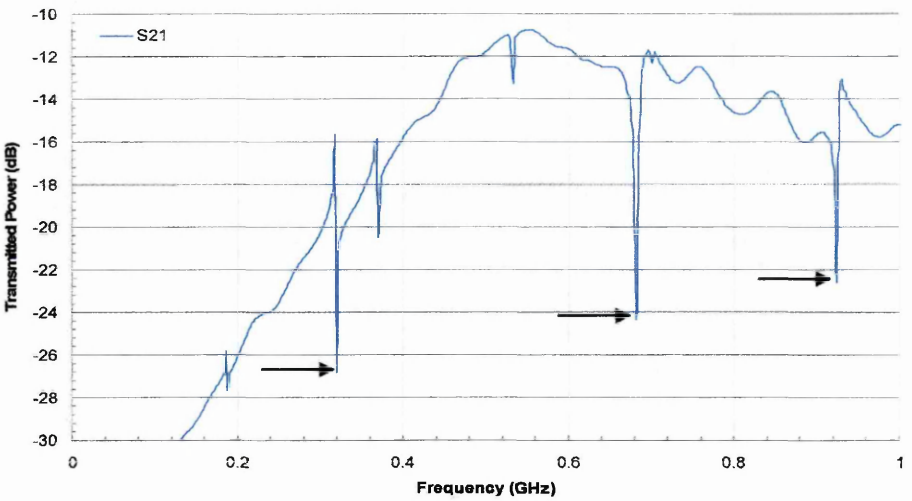

Figure 5.6 (A) Shows the truncated response (1 GHz) of a full band (0-3 GHz) S_{21} sweep of FBAR device 9 on PCB 11. About 520 data points are visible from the 1601 points obtained in the original sweep. The harmonics used to generate Figure 5.6 (B) below are indicted.

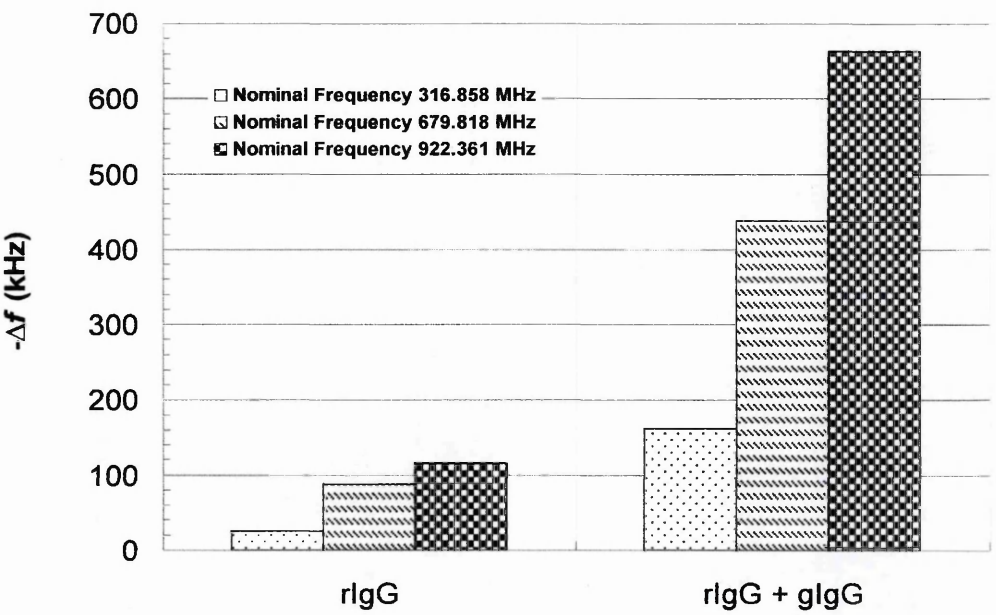

Figure 5.6 (B) Shows the relationship between changes in FBAR device 9 on PCB 11. S_{21} series harmonic overmode resonance frequencies ($-\Delta f$) caused by the mass loading effects from the physical adsorption of adlayer of rIgG onto the gold surface of the FBAR and the subsequent antigenic binding of polyclonal gIgG to multiple epitopes expressed on the rIgG protein layer.

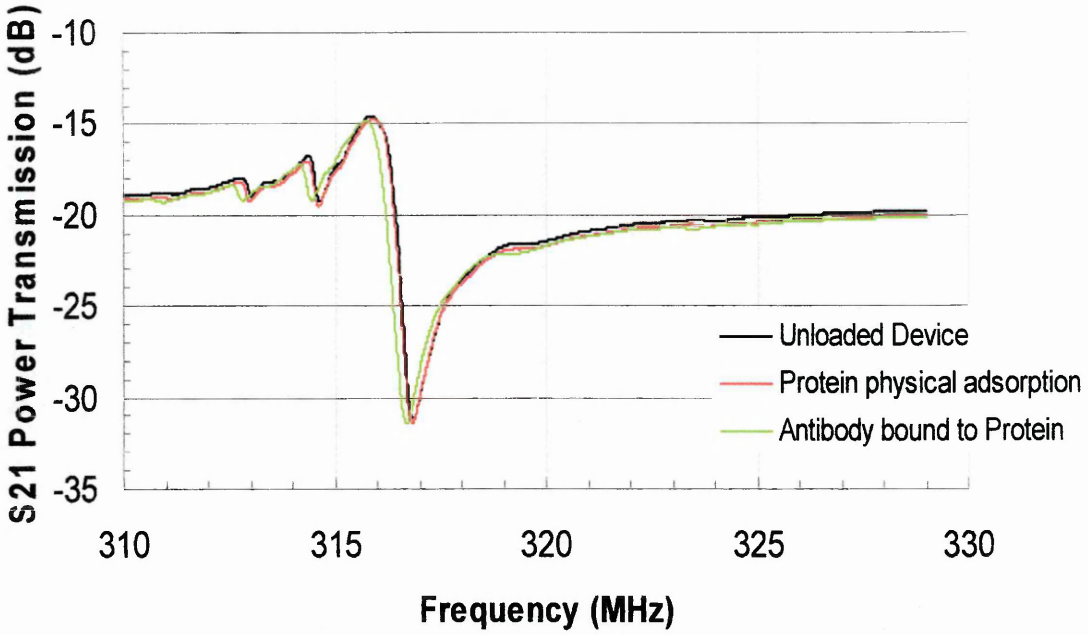

Figure 5.6 (C) The characteristic responses of the first overmode (316.858 MHz) of FBAR Device 9 on PCB11 in its unloaded condition and with the physical adsorption of rIgG and then immuno accumulation of rIgG + gIgG. (1601 data points, Measurement range 20 MHz.)

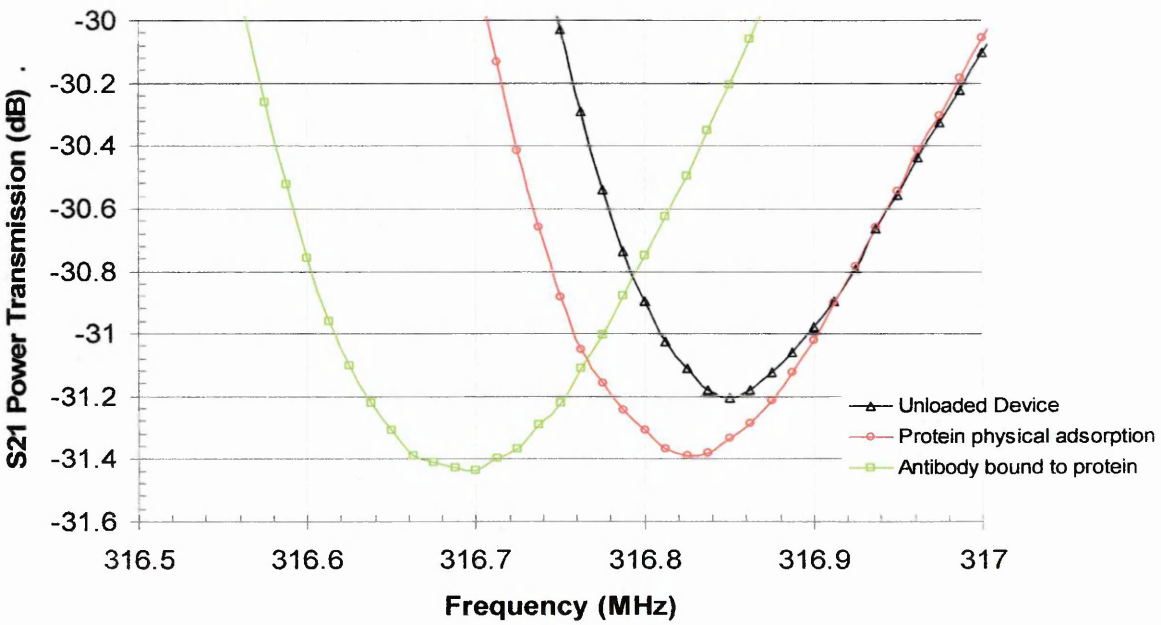

Figure 5.6 (D) As above, but data is truncated to X = 1.5 MHz, Y = 1.6 dB to assist in visualisation of the characteristic response. About 23 data points of the original 1601 are shown.

5.3.3.2.3 Experiment 5.3 (C)

5.3.3.2.3 1 Method

FBAR device 10 on PCB 11 was used. The methods used were identical to those of Experiments 5.2 (A) and 5.2 (B). However, one of the wire bonds connecting the device to the earth plane became dislodged at the second protein loading phase, the decision to continue with the tests was made, increased focus on the stability of the device S_{21} responses was maintained.

5.3.3.2.3 2 Results

The loss of one of the two earth wire bond connections from the FBAR to the earth plane of the PCB did not appear to significantly detrimentally influence the FBAR output responses. A future study should examine the effect of the loss of both earth wire bonds.

Figure 5.7 (A) Shows characteristic response of FBAR over S_{21} full band frequency sweep (0-3 GHz) with 1601 data points collected over the range but the figure is truncated to 1 GHz showing only the relevant parts of that trace. The resonant harmonics used for the protein analysis are indicated. The useable FBAR S_{21} series resonance frequencies were found at 684.476 MHz and 929.167 MHz.

Figure 5.7 (B) Shows that the physically adsorbed rIgG layer decreased FBAR S_{21} series resonance frequency and the subsequent affinity binding of the polyclonal gIgG decreased the resonant frequency further due to the additional mass loading. The values for this change are tabulated below in Table 5.3.

Table (5.3) FBAR device 10 on PCB 11 S_{21} series resonance frequency change due to mass loading from proteins.

Nominal Frequency (MHz)	**$-\Delta f$ (kHz) due to rIgG loading**	**% change due to rIgG loading**	**$-\Delta f$ (kHz) due to rIgG + gIgG loading**	**% change due to rIgG + gIgG loading**
684.476	104	0.1519	331	0.4835
929.167	156	0.1678	503	0.5413

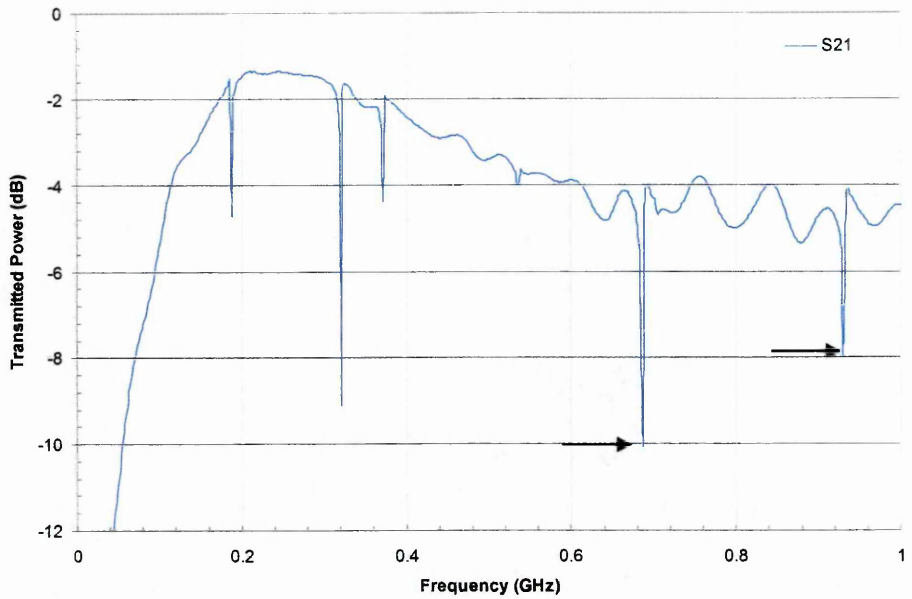

Figure 5.7(A) Shows the truncated (1 GHz) response of a full band (0-3 GHz) S_{21} sweep of FBAR device 10 on PCB 11. About 530 data points are visible from the 1601 points obtained in the original sweep. The harmonics used to generate Figure 5.7 B are indicated.

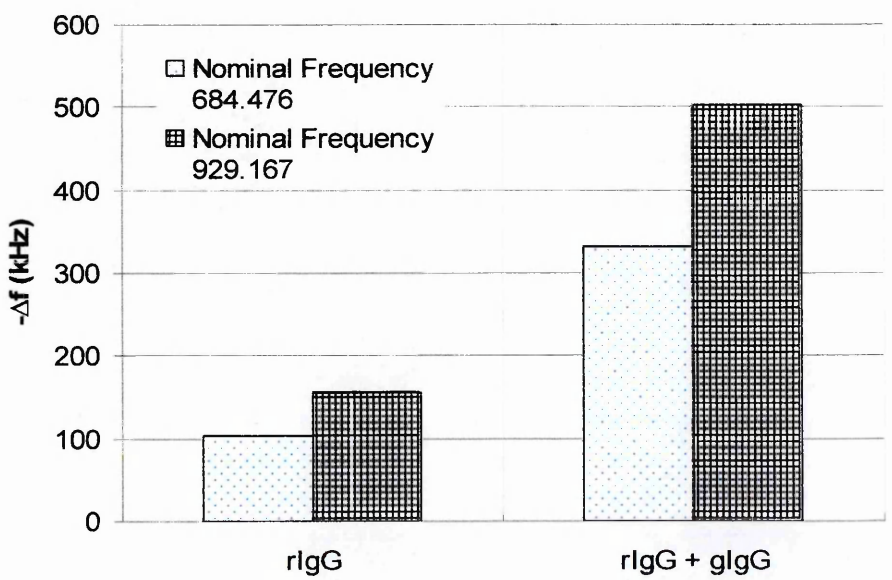

Figure 5.7 (B) Shows the relationship between changes in FBAR device 10 on PCB 11 S_{21} series resonance frequencies ($-\Delta f$) caused by the mass loading effects from the physical adsorption of an adlayer of rIgG onto the gold surface of the FBAR and the subsequent antigenic binding of polyclonal gIgG to multiple epitopes expressed on the rIgG protein layer.

5.3.3.2.4 Experiment 5.3 (D)

The FBAR used in this test utilised a piezoelectric membrane constructed from PVD sputtered AlN (aluminium nitride) as opposed to PVD sputtered ZnO (zinc oxide). This FBAR unit also lacked the buried SiO_2 layer which was embedded into the Si wafer to generate the harmonic overmodes within the measurement range of the network analyser (0-3 GHz) shown in the previous set of tests. AlN FBARs typically generate high quality responses with good electromechanical coupling coefficients even at high frequencies where there is a pre requisite for a relatively thin piezoelectric membrane. (< 1 μm). The AlN FBARs were transported offsite for a specialist wire bonding procedure using an epoxy rather than a ball and wedge procedure The level of contamination on the surfaces of the AIN FBARs was not established, and solvent cleaning of the AIN FBARs was not possible because the solvent caused the epoxy[114] (as opposed to ball wedge) wire bond to fail and a number of AlN devices were lost to this type of failure before this fact came to light. The AlN FBARs used a molybdenum electrode in place of gold and thermosonic ball wedge bonding is not generally successful on molybdenum.

5.3.3.2.4.1 Methods.

FBAR device 7 on PCB 17 was used. The methods used were identical to those of experiment 5.2 (A) and 5.2 (B) and 5.2 (C) Of five devices, this was the last remaining AlN FBAR due to significant losses of the epoxy wire bonded devices during the initial solvent cleaning stages.

5.3.3.2.4.2 Results.

Figure 5.8 (A) Shows a full band S_{21} sweep of the device. It gives a high quality single resonance curve with unloaded f_0 = 1.788654 GHz. The inability to solvent clean the gold surface of the device before loading the rIgG protein almost certainly interfered with the binding efficiency and this may be reflected in the low initial frequency change of ~-Δf 112 kHz. -Δf for the addition of gIgG to the rIgG layer was 735 kHz (*See Figure* 5.8 (B))

[114] Ball wedge bonds could not be made directly to the molybdenum electrodes used for the AIN based FBAR, that is why epoxy resins were used and so drastically failed during solvent cleaning..

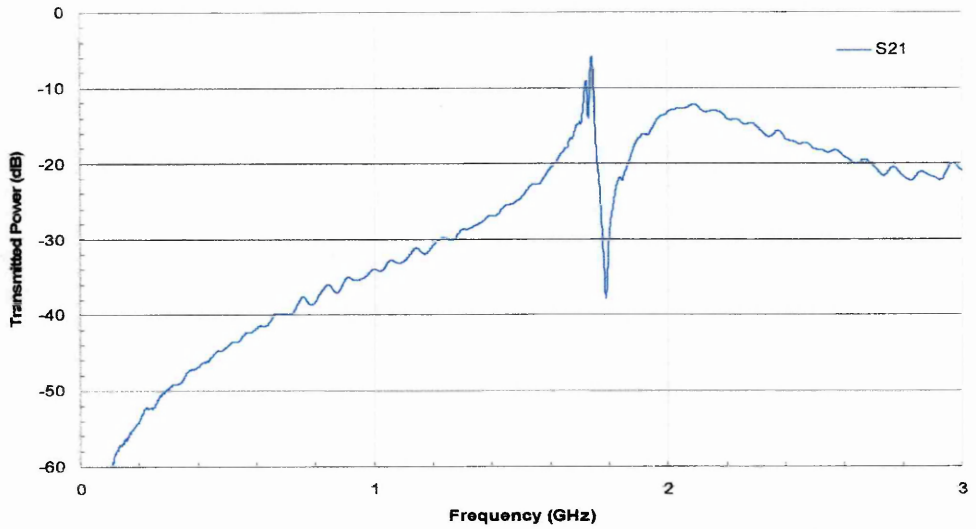

Fig 5.8 (A) Shows a full band (0-3 GHz) S_{21} sweep with 1601 data points of AlN based FBAR device 7 on PCB 17. S_{21} Fundamental series resonance is at 1.788654 GHz

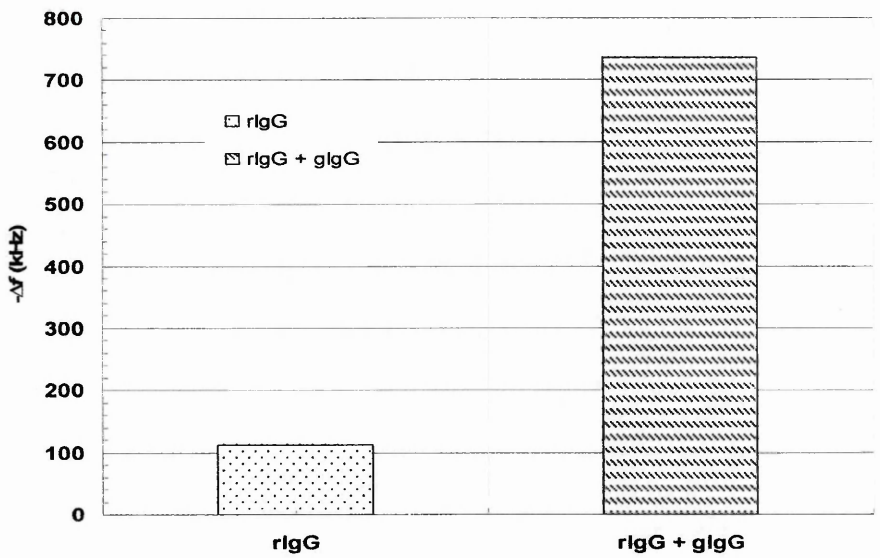

Figure 5.8 (B) Shows the mass loading effect from the physical adsorption of rIgG to the FBAR gold surface and the subsequent binding of gIgG to rIgG on FBAR S_{21} series resonance frequency.

5.3.4 Summary of FBAR results

The responses from both the rIgG loading and the rIgG + gIgG loading for all the repeats were graphed into an XY scatter plot to highlight the increased response of the FBAR S_{21} series resonance frequency to the identical protein mass loading and immuno accumulation but at higher harmonic frequencies[115]. A trend is clear showing that the FBAR gives more absolute change (Hz) per unit measurand as the frequency of the device increases and that the mass sensitivity overmode harmonics is linearly related to the fundamental operating frequency.

Initial physical adsorption of the protein layer to the AlN FBAR was low, but increased sensitivity to the mass load from the subsequent immuno accumulation is seen. The presence of the AlN device on this graph probably skews the response trend downward

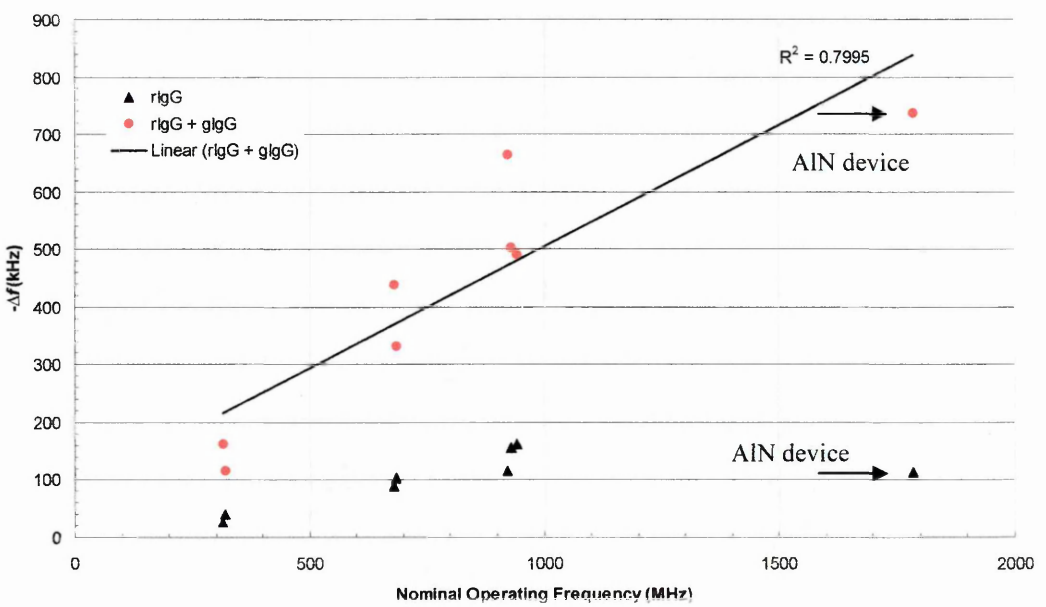

Figure 5.9 Shows summary of FBAR S_{21} series resonance harmonic frequency change in relation to unloaded frequency for protein load and immuno accumulations described in experiment 5.3. AlN resonance frequency is fundamental.

[115] This does not follow for the AlN FBAR with its higher *fundamental* mode, since the response has been undermined by the low level of initial physical adsorption of the target protein to the dirty gold surface which could not be solvent cleaned due to failure issues with the epoxy bonds used to link them to the molybdenum bottom electrode. Theoretically the response should be related to f_0^2

5.3.5 Discussion

The sensitivity as frequency change per unit measurand of the FBAR devices increased as higher frequencies in the form of overmode harmonics were used for the analysis. The linear fit for Δf vs. nominal operating frequency showed that the response did *not* follow the expected Sauerbrey term, because this extremely well vindicated term requires that the sensitivity per unit of measurand response of resonating piezoelectric devices to increase as a function of the square of the nominal *primary* or *fundamental* operating frequency. (f_0) The modes examined in this case were of focused on higher overmode harmonics, not higher primary modes so the linear increase in sensitivity that was observed was expected.

The objective of this exercise was to examine the relative sensitivities of the two acoustic analysis methods, FBAR and QCM in relation to a given protein load. The QCM measurement apparatus was a simple frequency counter and as such not equipped to deliver power or Q characteristics unlike the sophisticated network analyser that was used to probe the FBARs. But in any case, the changes in Q were negligible and are summed to zero in this case to give a blanket approximation of the protein load as an ideal mass load. But it is to be noted that thicker layers will inevitably move toward the more non gravimetric regimes and a more sophisticated analytical approach will be required in these cases.

What is unambiguously demonstrated in the results is that the FBAR is more frequency sensitive to mass loading from protein deposition on its surface than QCM is to the same load. Consider that in experiment 5.2, the average change in resonant frequency for QCM in response to the physical adsorption of the rIgG layer for the 3 samples was ($-\Delta f$ ~170 Hz) and the nominal operating frequency was 10 MHz. This represents a change of 17 parts in 1 million. When looking at FBAR in experiment 5.3 however, with nominal operating frequencies typically hundreds of megahertz the responses were measured in kilohertz. E.g., an FBAR operating at ~900 MHz showed ($-\Delta f \sim$ 170 KHz) to the same amount of physically adsorbed rIgG protein load. This is a change of 189 parts in 1

million and represents a relative increase in sensitivity of 11.1 times for FBAR compared to quartz with the same load. But of course in terms of absolute frequency change for given loads, 900 MHz FBAR is approximately 3 orders of magnitude greater than 10 MHz QCM.

It will be recalled from Chapter One that the relationship between frequency change and the mass accumulated on the resonator in the gas phase is given by equations[116] (1.4) and (1.5), and the mass sensitivity (M_s) of a quartz system in the gas phase is the quadratic function of the fundamental frequency f_0 as shown in equation 1.6.[22]

For the sake of argument simplicity, if the density and shear modulus are ignored then equation (1.6) indicates that a 10 MHz crystal would give M_s = 200, and a 900 MHz FBAR[117] would give $M_s = 1.62 \times 10^6$, this is theoretically 8100 times more sensitive than the 10 MHz QCM, and clearly from experiment, FBAR sensitivity increase does not reach this value. The reason that the exaggerated sensitivity function is calculated from the equation 1.6 is very likely due to the fact that the frequency was obtained from an overmode harmonic not the all important fundamental resonance frequency and that the term does not take into account the different Q factors (Q = hundreds for FBARs and Q = thousands for quartz crystals) of the devices since the term was derived solely for quartz in the first place. A more realistic Ms equation would include the Q factor of the device to act as a kind of weighting factor.

In Chapter three of this work, it was shown that when combined with a software polynomial fitting routine, the measured S_{21} series resonance frequency tracking function was able to clearly resolve out frequency changes of ~ 2 KHz from background noise (when f_0 = ~360 MHz) (*See Figure* 3.27 (A)), and if this level of resolution can be obtained from an FBAR say, with f_0 = 2 GHz and there is no reason to think that it could not, then it would represent a 1 part in 1 million resolution and although not yet at the resolution of QCM systems (1 part in 10 million) it is favourably comparable because

[116] Various other forms of this are given in the appendix 1 supplemental chapter.
[117] This was of an overmode not a fundamental mode.

the sensitivity increase subsequently obtained may outweigh the reduction in resolution generated from lower Q factors.

It was also shown (*See Figure* 3.26 (A)) that the resolution (minimum point to point spacing) of the polynomial fitted FBAR S_{21} series resonant frequency response was a mere 60 Hz when the software measurement parameter settings were optimised. In any case, work is also underway at our department to improve the Q factors of FBARs and if the Q factors of FBAR can be improved by for example decreasing series resistance and ohmic losses, then the sensitivity of the devices will only increase further.

5.3.5.1 Comparing the experimental results with mathematical models.

The SPR data indicated that the thickness of the initial rIgG layer was 3.5 nm ($\pm$ 1 nm) and the complimentary mass data obtained from the QCM[118] indicated that the average mass of this was 171.5 ng ($\pm$ 45.5 ng). If this is the case then the $-\Delta f$ of a 900 MHz overmoded FBAR was approximately 1 kHz per 1 ng per unit area of physically adsorbed rIgG protein or ~49 kHz for a 1 nm thick protein film per unit area on the top electrode.

The value above was considered against the Mason based mathematical FBAR simulation model that was modified for this Ph.D. project.

Using mathematical modelling software (MathCAD), a virtual FBAR was set up with a piezoelectric thickness of 2.739 μm and 100 nm thick gold electrodes of 100 μm^2 to give a fundamental S_{21} primary series resonant frequency of f_0 899.7 MHz, approximating the resonant frequency of the higher harmonic overmodes used in this experiment[119]. To the virtual FBAR, a 3.5 nm thick *mass*[120] loading layer with a density of 1 Kg/m^3 (the estimated density of a protein) was added to the top surface electrode, the resonant frequency shift as given by the software was $-\Delta f$ 150 KHz, this compares favourably

[118] If the assumption was made that 1 Hz was equivalent to 1 ng of mass on the gold electrode surface of the crystal as instructed by the users manual.
[119] Of course the modelled value was a fundamental frequency, attempting to calculate an overmode at the required frequency by modelling additional back plate thicknesses on the FBAR never gave the desired frequency at the desired harmonic.
[120] The acoustic properties (density, velocity and attenuation) are approximated as the values of ZnO.

with the values (171 kHz) that were obtained directly from experiment for the protein film.

5.4 Conclusion

Wire bonded FBARs mounted on PCBs and housed in the FHA were shown to be responsive to the presence of proteins when interrogated for S_{21} series resonance frequency with the network analyser which was under the control of the software that was developed as part of the Ph.D. project.

The FBAR was shown to be more sensitive to the presence of protein films on its surface than a quartz crystal was for the same given load this was both in relative (%) and in absolute (Δf per unit of measurand) terms. This was to be expected since the fundamental resonance frequencies of the FBAR are much higher than quartz in the first instance. The lower Q factors of FBAR in relation to quartz do serve to somewhat undermine the ideal theoretical frequency to sensitivity relationship of the Sauerbrey equation

The work in this chapter has shown that the optical SPR methods when combined with acoustic methods such as FBAR or QCM are more powerful than when each is performed individually. For example if the thickness of a layer can be elucidated by SPR, and the frequency shift experimentally determined acoustically then the density of the layer can be calculated quite easily. However, consider that if there were to be a function programmed into the existing math model where the resonance frequency change could be directly input, if the density of the layer was known and input, then the software could generate a thickness value relating to the specified resonant frequency change in the same If this were found to be accurate, the requirement for an SPR would then become superfluous. It may be necessary to take dissipation factors into account if the layer deviates substantially from an ideal layer, this value can be obtained from ΔQ.

Finding alternative wire bonding procedures that do not use an epoxy bond to connect the AIN piezoelectric based FBAR devices to the transmission lines of the PCB is important if the devices are to be used in biosensing arrangements where connection of sensing

layers to *clean* gold surfaces is critical. This is because the devices, once mounted onto PCB can not be cleaned with a plasma treatment, and there seems to be an absolute requirement for some solvent to be involved during the cleaning of the gold surfaces. Four extremely high quality, high frequency (~1.8 GHz) FBARs of this type were lost from the project due the epoxy dissolving the epoxy bond. This interfered with the capacity of the work to examine the effect of utilising higher fundamental modes to observe Ms in protein loading.

FBAR devices are much cheaper to produce than QCM plates but the much higher cost of the interrogation equipment for FBARs, e.g., the network analysers, as opposed to frequency counters for QCM may be prohibitive for wide-scale commercial deployment of the technology and it may be important to develop scaled down oscillator circuitry to excite and record the FBAR responses to give the technology widespread appeal. However, a simple oscillator circuit that followed Δf alone would not be able to provide the end user with any rheological information.

REFERENCES
CHAPTER FIVE

1. Marco. M., Barcelo. D (1996) Environmental applications of analytical biosensors – Review Article *Meas. Sci. Technol.* 7 1547-1562
2. Shons, A., Dorman, F., Nagarian, J. (1972). An immunospecific microbalance. *J Biomed. Matter. Res.*, **6**
3. Bunde. R., Jarvi. J., Rosentreter. J. (1998) Piezoelectric quartz crystal biosensors. *Tantala* **46**. pp 1223-1236.
4. Baselt D, Lee. G., Hansen. K., Chrisey. L., Colton. R. (1997) A High-sensitivity micromachined biosensor. *Proc. IEEE* **85**(4), pp 672-680
5. Lee. H., Yoon. H., Hwang. S., Park. J., Ahn. S., Kim. S. (2004) Label free novel electrical detection using micromachined PZT monolithic thin film cantilever for the detection of C-reactive protein. *Biosensors and Bioelectronics.* **20** (2) pp 269-275.
6. Griffiths D., Hall. G. (1993) Biosensors – what real progress is being made? *TIBTECH.* **11** pp 122-130.
7. Bruckenstein. S., Shay. M. (1985) Experimental aspects of the use of the quartz crystal microbalance in solution. *Anal. Chem* **69**. pp 1439-1443
8. Liu. Y.,Yu. X., Zhao.R., Shangguan D., Bo. Z., Liu. G. (2003) Real time kinetic analysis of the interaction between immunoglobulin G and histidine using quartz crystal microbalance biosensor in solution. *Biosensors and Bioelectronics.* **18.** pp 1419-1427.,
9. Green. R. J., Frazier. A. R., Shakesheff. M. K., Davies. C. M., Roberts. J. C., Tendler J.B. S. Surface plasmon resonance analysis of dynamic biological interactions with biomaterials. *Biomaterials.* **21** (200) pp1823-1835
10. G and J Voet. (1995) *Biochemistry* Chapter 34. Wiley, New York
11. Janeway. C., Travers. P. *Immunobiology.*(1997) Garland publishing. New York Tan. Y., Peng. H., Liang. C., Yao. S. (2001) A new assay for phenacetin using

biomimic bulk acoustic wave sensor with a molecularly imprinted polymer coating. *Sensors and Actuators B.* **73** pp 179-184.

12. Lin JN, Andrade JD, Chang I-N. (1989) The influence of adsorption of native and modified antibodies on their activity. *J Imm Methods* 125:67-77.
13. Norde W, Lykleman J. (1991) Why proteins prefer interfaces. *J Biomater Sci Polym* Ed; 2(3): pp183-202.
14. Homola, J., Yee. S., Gauglitz. G. (1999) Surface plasmon resonance sensors: review. *Sensors and Actuators. B.* **54.** pp 3-15.
15. Liedberg. B., Lundstrom. I. (1993) Principles of biosensing with an extended coupling matrix and surface plasmon resonance. *Sensors and Actuators B*, **11**, pp 63-72
16. Davies, J.(1994) SPR- the technique and its applications to biomaterial processes. *Nanobiology*, **5**, pp5-16
17. Weston. D.G. Molecular engineering of the biosensor interface.(1999) *Ph.D. Thesis.*
18. Gomes. T. M., Duarte. C.A., Olivira. (1995) P. J. Comparison of two methods for coating piezoelectric crystals. *Analytica Chimica Acta* 300 pp329-334
19. Koblinger. C., Uttenthaler. E., Drost. S., Aberl. F., Wolf. H., Brink. G., Stanglmaier. A., Sackmann. E. (1995) Comparison of the QCM and the SPR method for surface studies and immunological applications. *Sensors and Actuators B.* 24-25 pp107-112.
20. Benes. E., Groschl. M., Burger. W., Schmid. M. (1995) Sensors based on Piezoelectric resonators. *Sensors and Actuators A* 48 pp 1-21.
21. Campabadal. F., Esteve. J., Figueras. E., Boisen. A., Barniol. (2000). *N. Proc. 14^{in} Eur. Conf. on Solid-state Transducers, Eurosensors XIV* (Copenhagen) Pp 487-490.
22. D. Stubbs, W. Hunt , S. Lee , D. Doyle (2002). Gas phase activity of anti-FITC antibodies immobilized on a surface acoustic wave resonator device. *Biosensors and Bioelectronics* **17** pp 471_ 477

23. Tessier. L., Schmitt. N., Watier. H., Brumas. V., Patat. F. (1997) Potential of the thickness shear mode acoustic immunosensors for biological analysis. Analytica Chimica Acta **374.** pp 207-217.

24. Kurosawa. S., Tawara. N., Kobatake. (1990) Oscillating frequency of piezoelectric quartz crystal in solutions. *Anal Chimica Acta.* **230** pp 41-49

25. REF = Martin. S. J., Bandey H., Cernosek. R.W. (2000) Equivalent Circuit Model for the thickness-shear mode resonator with a viscoelastic film near resonance. Anal. Chem **72,** 141-149.]

26. Laschitsch. A, Menges. B, Johannsmann. D (2000) Simultaneous determination of optical and acoustic thicknesses of protein layers using surface plasmon resonance spectroscopy and quartz crystal microweighing. *Appl Phys Lett.* **77.** 14. pp 2252-2254.

27. Pan. N., Shih. J. (2004) Piezoelectric crystal immunosensors based on immobilized fullerene C60-antibodies. *Sensors and Actuators* B. **98.** pp 180-187.

CHAPTER SIX
6.0 FUTURE WORK

6.1 INVESTIGATIONS INTO FBAR RESPONSES TO VARIOUS LOADING CONDITIONS AND TO THE MODELLING OF FBAR ARRAYS.

This chapter is presented for a number of reasons, but mainly because the results from experiments described in it are difficult to explain but their implications may have far reaching consequences in further pursuit of the FBAR sensor. It is hoped that the results will shown in this chapter may help to stimulate future research in directions that may not have otherwise been considered.

The first experiment in this chapter examines at the effect of irradiating a physically attached surface population of extracted cellular DNA on the FBAR with ultra-violet (UV) radiation. The experiment was not performed with sufficient repeats to justify a place in the main body of the experimental work, and to compound this, a minor procedural error went unnoticed during the testing stages and only came to light when the results were being analysed. The decision to include the results was made on the basis of the nature of the response trends that were observed. These trends may highlight a potential source of error in the subjective interpretation of sensing responses from biological samples on FBAR. Since the experiments were performed without sufficient repeat samples and due to the procedural error, the results can only be viewed qualitatively but they are considered by the author to be of some importance.

The second FBAR experiment included in this chapter was one where the FBAR was submerged in a semi-infinite liquid layer. It was anticipated that the device would simply cease to oscillate completely and the results would not be presented in the thesis because they would be so obvious. However, the results that were obtained were not at all as anticipated. The FBAR still behaved as a resonator when it was totally submerged in a liquid, but as it will be shown, the underwater responses are by no means simple to interpret. The decision to include these perplexing results in this chapter lays in the

critical requirement of many biological sensing procedures to be undertaken in the aqueous phase and hence the potential importance of this in consideration of the FBAR as a useful and sophisticated complete biosensor system.

The third and final experiment described in this chapter was modelled not physically performed. For the FBAR to be exploited to its maximum potential, the prototype development should progress from testing of single resonator units, to arrays of devices operating simultaneously. This type of simultaneous interrogation gives rise to sophisticated pattern recognition chemical sensors often referred to in the literature as electronic noses. FBAR concept arrays were designed and mathematically modelled. The results from some the investigations are not easy to interpret, but they show a proof of principle. The decision to include these results in the thesis was made on the basis of the perceived importance of array formats for the continuing research and development of FBARs as chemical and biological sensors.

6.2 Experimental section

6.2.1 Using FBAR to study the *massless* accumulation of photoproducts induced from UV irradiation to physically adsorbed DNA surface populations

6.2.1.1 Introduction

Deoxyribose nucleic acid (DNA) is the medium on which biological hereditary information is stored and transmitted. In eukaryotic cells, it usually exists in a hydrogen bonded, double stranded 5', 3' anti-parallel helix. One strand (the sense strand) contains clusters of information (genes) that are directly accessible to the organism for biological instructions and the other strand (the non –sense strand) holds ostensibly a mirror image of the sense information and this is used for error repair and proof reading of the sense strand during replication and transcription. The DNA molecule itself is physically constructed of identical repeating units (i.e., it is a polymer) of covalently linked ribose-sugar-phosphate residues, and the hereditary information is stored in the specific sequence i.e., the order, of four bases linked to the ribose sugar residues. The bases are either purines (adenine (A) and guanine (G)) or pyrimidines (cytosine (C) and thiamine

(T)) Nearly all of biology on the Planet[121] is coded for from the sequential reading of the ACTG bases, which basically instructs the cellular machinery to connect one of twenty possible amino acid types adjacent to the previous amino acid on a chain known as a polypeptide. From this procedure, functional proteins which are the fabric of life are created.

For the purposes of this demonstration just one of the properties of DNA is to be explored further, that is the massless accumulation of the so called photoproducts of DNA. These chemical entities form deleterious mutations on a single strands of DNA in the form of covalent linkages of adjacent pyrimidine residues when the DNA molecule exposed to UV light. It is very likely that the physical state of DNA, and hence its acoustic properties will change in response to these mutations, and if enough of them are formed on the FBAR surface DNA sample, it was interesting to perform experiments to see if the FBAR could respond in some way to their presence.

Ozone depletion caused from pollution entering the Earth's stratosphere results in enhancement of UV-B (280–315 nm) radiation at the Earth's surface. This is known to have pronounced deleterious biological effects The main class of UV-B-induced DNA lesions consists of dimeric pyrimidine photoproducts. The two most frequent types of DNA lesions induced by UV-B radiation are the cyclobutane pyrimidine dimers (CPDs) and pyrimidine (6-4) pyrimidone adducts, commonly referred to as (6-4) photoproducts (6-4 PPs) [1] Both of these lesions can be repaired by light-dependent enzymes called photolyases (a process called photo-repair or photo-reactivation). In photo-repair, a single enzyme, photolyase, uses light energy in the range from 300 to 500 nm to reverse the dimerization of pyrimidines.[2] Dimerisation is deleterious to the organism because it draws the adjacent thymine residues together, distorting the DNA helix in such a way that replicative polymerization past the dimerised site is blocked.

[121] Exluding the retro viruses such as influenza and HIV which use RNA instead of DNA to store their information – but not express it since they ultimately hijack the DNA machinery of the host cell.

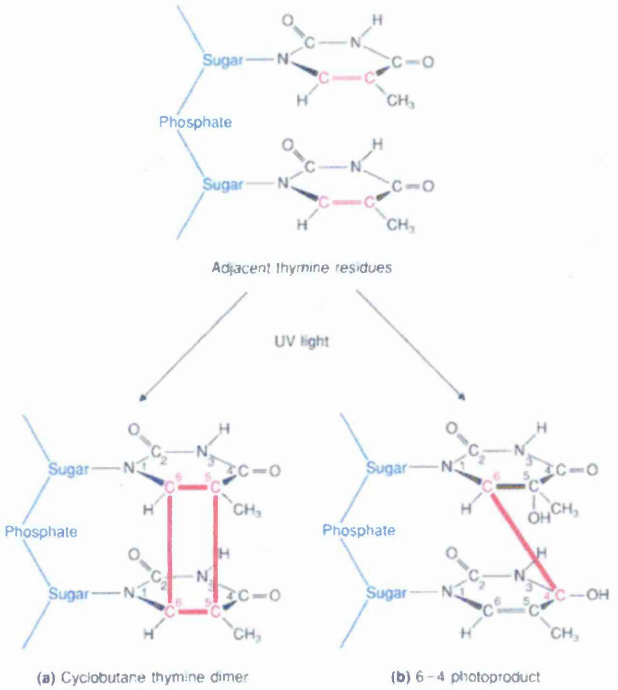

Figure 6.1 shows the formation of the most common forms of UV induced lesions in DNA. Taken from internet site (http://www.aw-bc.com/mathews/ch25/fi25p9.htm)

6.2.1.2 Methods

Whole cell DNA was extracted and purified from a cultured human cancer cell line with the QIAGEN QIAamp ® DNA mini extraction kit (Boundary Court, Gatwick Road, Crawley. West Sussex RH10 2AX) The DNA concentration of the purified DNA sample in buffer was shown, by optical density testing to be ~40 µg/ml.

A wirebonded FBAR (Device 23 on PCB 9) in the FBAR housing assembly (FHA) was S_{21} characterised on the network analyser, and a wide bandwidth (0-3 GHz) frequency scan of the FBAR was made. A number of potential resonance curves were identified as analytically useful. The useable overmode with the highest operating frequency was chosen because it was considered to be the most sensitive due to its higher intrinsic operating frequency it also lacked spurious modes and was quite a powerful resistor at resonance.

Using a Gilson pipette, a 200 µl aliquot of the DNA solution was deposited onto the top electrode surface of the FBAR and this was allowed to dry in the dark under a fume hood for 24 hours. It is likely that buffer residues remained on the surface of the FBAR along with the DNA surface population.

The FBAR, with the dried DNA layer, was S_{21} characterised in the FHA by the network analyser with appropriate measurement rage focussed around the highest frequency overmode. The FBAR was then taken into the clean room where the MA56 mask aligner was already powered up and its UV light source was well warmed but hidden under the UV shade of the mask aligner.

The DNA coated FBAR was exposed to the UV for 5 seconds using the method one would normally use to expose photo resists through masks. Great care was taken not to damage the mask aligner with this non-standard loading procedure. The UV exposed sample was then covered into darkness by replacing the lid of the FHA and it was then taken back into the Measurement room, and once again S_{21} characterised on the network analyser from within the FHA. The sample was taken back to the UV source in the clean room and a further 10 second exposure was performed this process was repeated to give totals of 45s and 90s UV exposure times. Obtaining a thickness profile of the DNA was not possible due to servicing issues with the Dektak surface profilometer.

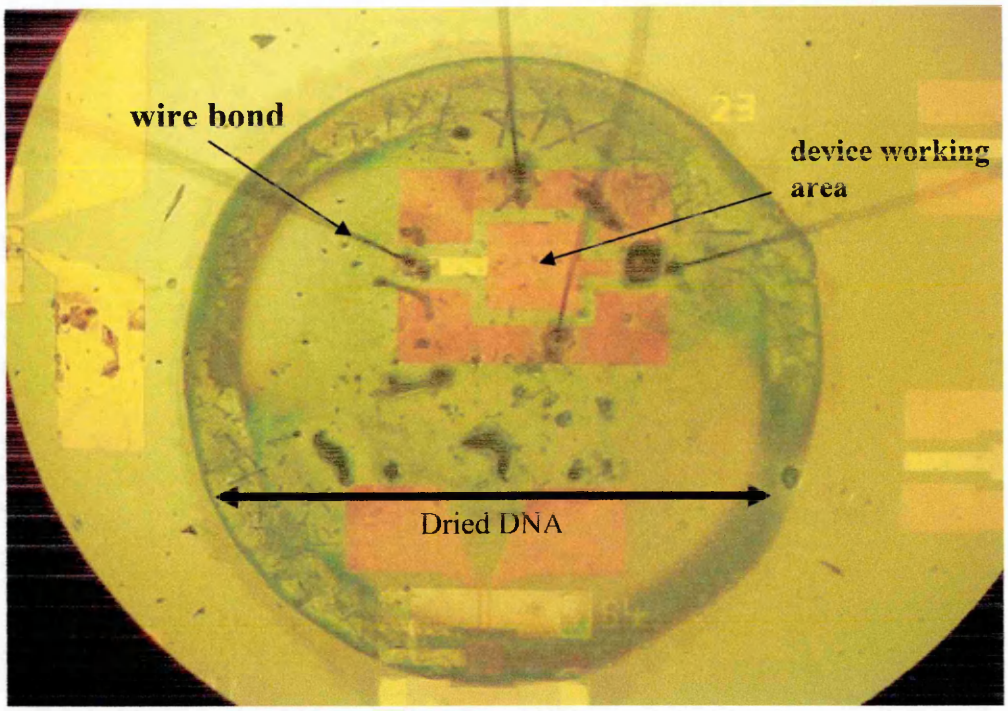

Figure 6.2 Photograph (100X magnification + 2X optical zoom) of whole cellular DNA fraction (40 µl/ml) deposited onto FBAR device 23 on PCB 9 after being left to dry down for 24 hours.

The bulk of the nucleic material appears to have formed a ring of increased thickness at the outer edge of the droplet profile. Various crystalline entities, possibly residues from the buffer are visible.

6.2.1.3 Results

The nominal (unloaded) operating frequency of the chosen *harmonic overmode* was 993.4 MHz. When the DNA was loaded onto the gold top electrode of the FBAR, the frequency as recorded by the network analyser fell by ~3.3 MHz to 990.1 MHz. Lacking a direct determination of the thickness due to profilometer servicing issues an approximate theoretical thickness of (0.05 µm) for the dried down DNA layer was calculated by manually configuring the Mathcad FBAR model set at (990 MHz

fundamental[122] resonance frequency) to decrease the frequency by the recorded decrease of 3.3 MHz and monitoring the thickness required to cause this shift in the math model. A density of 1.0 Kg per m^3 was assumed for the dry DNA.

Figure 6.3 (A) shows the results from 10 iterations over ~150s for DNA loaded FBAR with UV exposure times ranging from zero to 90s. The non-exposed operating frequency of 990.183 decreased by 80 kHz to 990.103 during the first 5 seconds of exposure, and at 15 seconds fell a further 18 kHz to 990.085 MHz, at 45 seconds the decrease in resonance frequency was 12 kHz with the average reasoned frequency at 990.072, and finally at 90 seconds exposure the resonance frequency had fallen a further a further 11 kHz to give an average operating frequency of 990.061 MHz.

Figure 6.3 (B) shows the 1 dB bandwidth[123] reported Q factor for the device under the same experimental conditions. The figure shows that the 1 dB bandwidth falls by ~20 points, during the period 5s to 15 s, but beyond this it is not possible to clearly resolve out changes in Q factor any further at this level of resolution. However, the figure suggests that the sample is becoming more "lossy" as it is exposed to the DNA.

[122] This is a potential error, since the 900 MHz FBAR overmode will not have been as sensitive as the 900 MHz fundamental mode that was modelled. It was too complicated to set up the math model to generate harmonic overmodes at specified resonant frequencies

[123] An error was made in the settings for the zero seconds exposed DNA sample, this error being that the Q bandwidth was set at 3 dB whilst the settings for 5 seconds exposure to 90 seconds exposure were set at 1 dB bandwidth. This will have had a downward effect on the recorded resonance frequency and without a repeat set of tests, the result from 0 seconds – to 5 seconds exposure can only be viewed qualitatively.

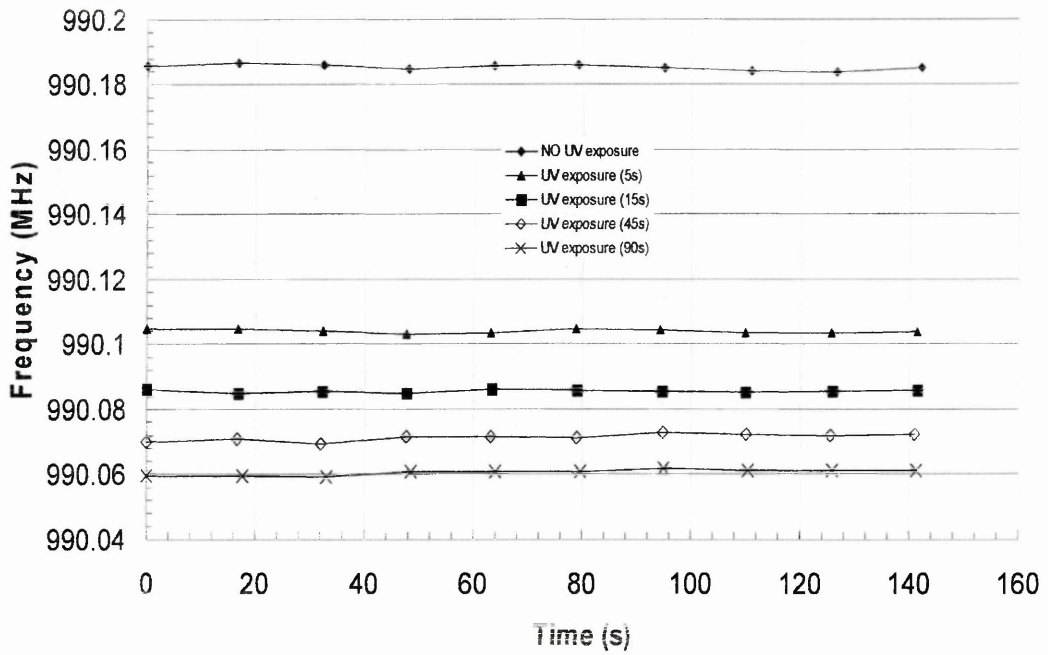

Figure 6.3 (A) Shows the effect on S_{21} series resonance frequency of FBAR response from increasing exposure times of UV light on a surface population of DNA physically adsorbed onto the FBAR gold top electrode and dried down for 24 hours. The mass of the DNA is *assumed* to have remained constant throughout the test. 10 iterations, each iteration was over 1601 data points and 2 MHz frequency bandwidth span over the ~ 990 MHz overmode.

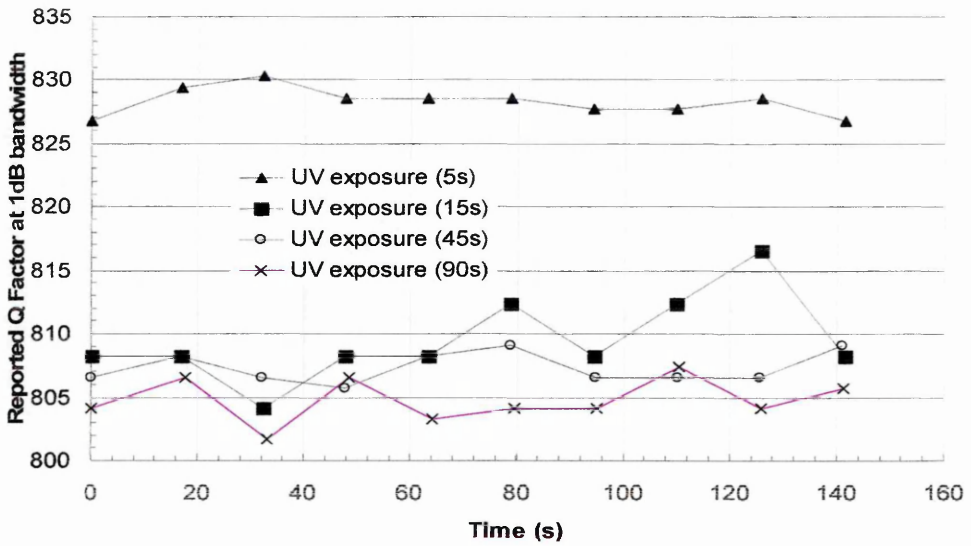

Figure 6.3 (B) As above, but shows the effect on reported Q factor of sample. The IFBW was set at 1000. The Q bandwidth was set at 1 dB. The Q factor for the initial unexposed sample was recorded at 3 dB in error. (not on graph)

6.2.1.4 Discussion

At first sight, due to the decrease in resonance frequency of the FBAR, the results would indicate that there had been an additional mass load on the surface of the resonator, but this almost certainly is not the case. The clean room is free from dust, and the FHA was sealed when transporting between the clean room and the measurement room, so accumulation of mass from flocculent is highly unlikely. If the mass of the DNA layer on the FBAR is assumed to remain constant, then according to the rules of operation of FBAR as they are understood in this thesis, then a decrease in resonant frequency could be brought about by either an increase in the density or an increase in its thickness. Both of these scenario's are unlikely, an increase in the thickness of the layer caused by swelling would likely decrease the density of the layer and the converse is true that if the layer density were to increase then the volume and hence the thickness should decrease. It is possible that the UV induced photoproducts changed the stiffness of the DNA layer.

The results demonstrated here are in general agreement with previous work done on DNA UV-C damage BAW sensors based on quartz by Zhang et al (1998).[3] These researchers found that when DNA, bound to the surface of a 9 MHz quartz crystal, was irradiated with UV-C (254 nm) the frequency of the DNA/BAW device decreased over time (30 minutes) by up to Δf = -60 Hz and they attribute this to the formation of UV induced lesions/accumulated photoproducts in the DNA layer linked to the surface of the resonating device, and suggest that increased mass loading is not the contributory factor in the response. In their work, Zhang *et al* find it necessary to use impedance analysis on the BVD circuit in the form of separate L,C, and R responses to comprehend their results with significant detail.

Consider that the FBAR device operating at ~990 MHz in this work responded with a negative frequency change of roughly Δf = -100, 000 Hz during the 90 seconds DNA UV irradiation time, suggesting that FBAR is responsive to the same UV induced changes in DNA that quartz is able to acoustically transduce, but at with increased sensitivity. However, since the DNA loading methods and concentrations and the UV frequencies

used in this test are than in different Zhang's study, the increase in sensitivity is implied, but it is not confirmed.

From the photograph of the DNA loading state it is obvious that there is a bulk of DNA all over the die, and it is possible that the layer contracted on the X plane whilst increasing thickness on the Y plane and in doing so, has increased the total amount DNA presented to any given unit of the working area. It is also possible, that there has been a change in the stiffness of the material (this being independent of thickness and density) due to the accumulation of photoproducts and as such the propagation velocity of the acoustic probe wave has increased, thereby decreasing the resonant frequency. The observed change in the Q factor runs contrary to the authors expectations since it was considered that the accumulation of covalent bonds in the sample would increase its stiffness, and hence increase the elasticity and cause the Q factor to rise – but obviously this is an oversimplification and is not the case. The interesting point to be note here is the fact that a rheological interrogation has been made which is potentially distinct from any changes in mass loading whatsoever.

This brief "look-see" type test shows the flexibility in the responses of the FBAR to changes in the physical state of the surface loading layer. It also brings with it a valid and possibly very important caution, in that there is scope for interpretive error in making mass determinations on resonators if the physical properties for, example stiffness or viscosity of the mass layer are to change for some reason and go unnoticed. Much more work obviously needs to be done with experiments involving calibrated stiffness changes and material rheology on loading layers before serious conclusions can be drawn from the results shown in this section.

However, what is almost certain is that exclusively monitoring the frequency change of a BAW device can not deliver enough information alone to draw comprehensive scientific conclusions about acoustically probed sensing responses unless the experimental conditions are rigorously controlled. Loss or dissipation factors may need to be integrated by means of software embedded calibration and compensation, into the final output

responses of BAW sensors to obtain a clear picture of any sensing event more complicated than the "ideal cases" of additional thin metal film mass loads on to the surface. This topic has been explored by Voinova *et al* (2002),[4] where the "missing mass" as an experimentally observed deviation from a linear dependence of QCM resonant frequency on viscoelastic mass deposition has been calculated against the "true mass" calculated from other means. Rigorous formulae has been developed to compensate for the difference between the two culminating in a more accurate form of the original Sauerbrey equation. Denaturation in Herring DNA on the basis of the viscosity-density effect on quartz has been explored by (Wu et al 2000).

The potential for interpretive error related to the estimation of mass loads for materials with unknown, but most especially with *mutable rheologies* increases exponentially as the fundamental operating frequency of the device increases and the subsequent increases in sensitivity are gained as a consequence of this fact.

6.2.2 The effect on FBAR responses when submerged in semi-infinite water load.

6.2.2.1 Introduction

Because water vapour as an increase in the relative humidity of a gas stream was being used to test FBAR responses, it was interesting from a purely experimental perspective to examine the effect of complete submersion of the uncoated device loaded under a semi-infinite water layer. If resonances were still seen, it would prove to be both theoretically interesting and of some practical sensing significance in considering the FBAR as a biosensor because many biological sensing procedures have absolute requirement for the aqueous phase.

Since Sauerbrey up until ~ 1980, it was assumed that the QCM would not operate in liquid because excessive energy loss would cause the crystal to cease oscillation. Nomura and Minemura proved this assumption be incorrect by actually putting it to the test in real experiment.[5] and this has opened a whole new avenue of fruitful acoustic sensing

possibilities, including the development of the electrochemical variant of the QCM, the so called ECQM. Much work has been done to explore the effect of loading TSM QCM with semi-infinite liquid layers, both Newtonian and Maxwellian in nature.

Theory has been constructed to explain the effects of liquid loading on QCM operating in TSM.

The surface mechanical impedance contributed by a semi-infinite Newtonian fluid on a shear mode QCM is given as (Bandey 1999)[6]

$$Z_s = \left(\frac{\omega\rho_l\eta_l}{2}\right)^{1/2}(1+j) \qquad \text{(Eq 6.1)}$$

Where $\omega = 2\pi f$, and ρ and η are the density and viscosity of the contacting medium respectively.

Liess (1997) *et al* [7], use a modified the BVD circuit model to represent a semi-infinite liquid load.

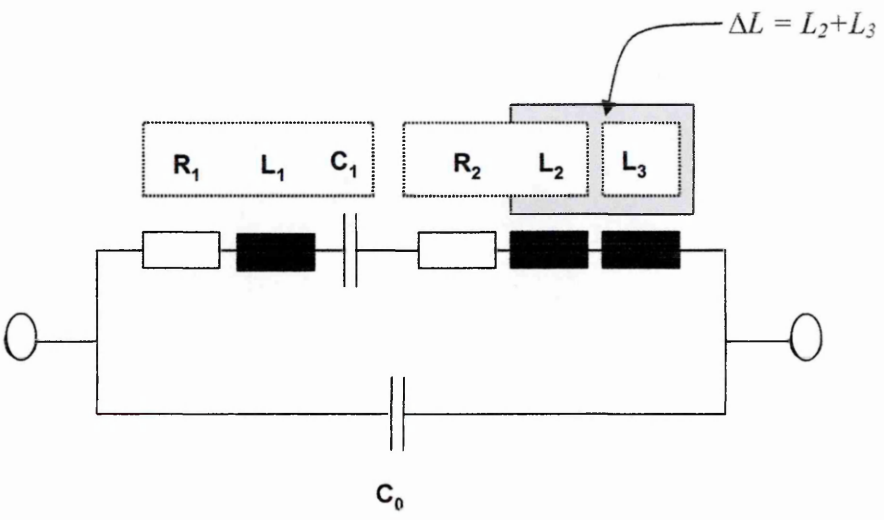

Figure 6.4 Equivalent BVD circuit of a liquid loaded quartz resonator, R_2 and L_2 represent the viscous coupling, L_3 represents the mass loading.

The change in series resonance frequency due to liquid induced mass change is calculated as; (Liess 1997)[7]

$$\Delta f = f_{liquid} - f_{air} = \frac{1}{2\pi\sqrt{[(L_1 + L_2 + L_3)C_1]}} - \frac{1}{2\pi\sqrt{(L_1 C_1)}} \qquad \text{(Eq 6.2)}$$

At this stage it is not known how relevant (*if at all*) these terms are to the present work with FBAR in contact with liquid. The theory was developed for QCM operating in TSM, and it now becomes important to distinguish between the shear modes of AT quartz and longitudinal (i.e., compressional modes) of FBAR acoustic probe wave propagation. Refer back to Figure 1.4 A and B which shows compressional waves are produced in FBAR and transverse shear motion is generated from the common AT cut of quartz plates. Shear modes of wave propagation are not supported by a liquid so the energy of the wave remains trapped in the shear mode crystal and only couples evanescently with the liquid but this is enough to make accurate interrogations about changes in the liquid.

In their paper on Acoustic wave – liquid interactions, McHale et al (2000), discuss the theory of SAW and QCM interactions with liquids to the level of solving the Navier-Stokes equations but do point out that the terms (not shown) do not take into consideration the compressional element of the Rayleigh SAW. [8] Hence the theory described in McHale's work would most likely would *not* serve to explain the behaviour of the FBAR and the interaction of the high frequency compressional waves through liquids. As a rule of thumb, low frequency compressional waves, e.g., audible sound and sonar are supported well by liquids, but at higher frequencies they are not supported. A literature search has revealed no reports of studies involving microwave frequency mechanical transmissions through aqueous media.

6.2.2.2 Methods and apparatus

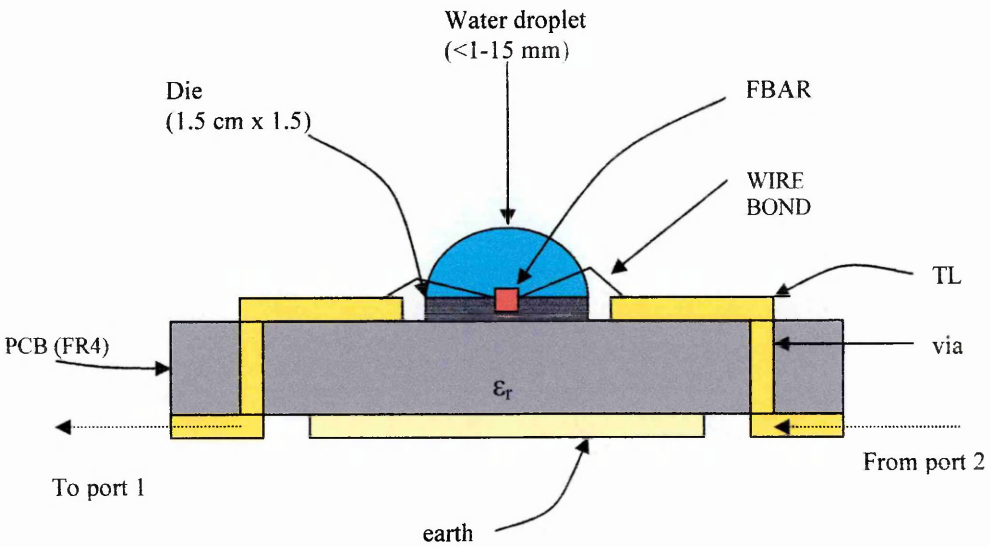

Figure 6.5 Schematic of the submersion in liquid water of FBAR on die, mounted on PCB and wire bonded to 50Ω TL in the FHA. (not to scale)

6.2.2.3 Water loading experiment 1

6.2.2.3 1 Methods

FBAR (Device 7 on PCB 3) was placed into the FHA but the lid was not attached. It was characterised (S_{21} 1601 points over 0-3 GHz span range) in air to obtain characteristic responses for the dry sample. As much water as possible (~1 ml) was then pipetted onto the device with a Gilson dispenser until a droplet with meniscus about 15 mm above the FBAR formed. The droplet was held on the die (1.5 cm X 1.5 cm) by surface tension.

The device was tested for responses whilst submerged. The vast bulk of the water was then removed from the sample by removing it from the device with the Gilson, leaving the thinnest possible water layer, likely not to have been a monolayer, but certainly no thicker than few microns. The device was then re-submerged for a second time by depositing a 1 ml droplet of water over the FBAR, it was and retested in the submerged state. A 0-3 GHz range XY scatter graph of S_{21} transmitted power over S_{21} series resonant frequency showing the comparisons for the unloaded and submerged (x2) loading conditions was created.

Notes on graphical data presentation

The 1601 data points (per trace) on the graph make it counter productive to use symbols represent the data, since they greatly increase the thickness of the line and are not individually separated in any case. The use of dotted or dashed lines does not improve the visual output style of the graph because the density of the data renders the perceived graphic as a continuous line. As such, only lines represented by different colours can be used in this case, and will make it impossible to read the information if this thesis is black and white photocopied. Wide span (0-3 GHz) graphs are shown with truncation of the X and Y axis to focus on the overmode in question, this is done to assist in data visualisation because the wide band graphs hold so much data and are not easy to decipher.

6.2.2.3.2 Results

The result (Figure 6.6 (A to F,)) shows S_{21}, 1601 point, 0-3 GHz span for device 7 on PCB 3 in air and when it was submerged in a droplet of water with the top most part of the meniscus being ~15 mm from the FBAR. E.g., totally submerged. A repeat submersion followed and the data for this is shown also..

In the gas phase, the FBAR shows five distinct S_{21} series resonance curves (primary resonant frequency and overmode harmonics). Analysis of the results for both of the submersion events reveals that there is no immediately obvious pattern to the response. Overall, the first and second submersion events did yield results that gave very similar patterns both in FBAR frequency and FBAR power characteristics . When considering the change in FBAR response between the dry and the submerged states it is shown that the primary mode frequency (~186 MHz) was not discernibly effected by submersion at this level of resolution, but there was some change in the transmitted power response of the FBAR observed. This is shown by the 0.8 dB increase in insertion loss and attenuation of the resonance curve "magnitude" by about 0.5 dB in the submerged state.

(*Magnitude in this case is almost certainly a misnomer, but implied is the difference in power (dB) between the value of the frequency of the parallel mode of resonance and the power at* $f_{0(n)}$ *of the series mode of resonance. Usually, this is given as the difference between the parallel and series frequencies (Hz) when calculating the electromechanical coupling coefficient* (K^2) *of the FBAR but the power transmissions are not usually taken into consideration. In this case, this description is necessary because merely stating a transmitted power value for the curve could be misleading since the resonance curve could begin its descent into pure resistance starting at different power levels.(For an example of this see resonant overmode 4 in* Figure 6.6(B). *In effect, the term "magnitude" is attempting to denote the total size of the resonance curve completely independent of its insertion loss.*)

The first overmode was strongly effected by the submersion. Although the resonance frequency (~322 MHz) remained very similar for the dry and submerged states, the

change in power transmission characteristics was profound. In its dry state, the FBAR first overmode power transmission at $f_{0(n=1)}$ was ~ -13.5 db, but when submerged the transmitted value was recorded at ~ - 6.3 dB indicating that this mode losing energy when it was submerged since the magnitude of the dry resonance curve was ~11.5 dB and the submerged magnitude was ~ 2.8 dB. The second overmode at 360.4 MHz was not analysed. The third harmonic at ~680 MHz showed an *increase* in resonance frequency of about 4 MHz when the submerged value was calculated. The return to capacitance from the pure resistance at $f_{o\,(n=2)}$ is severely truncated at -12 dB as opposed to -2 dB for the dry state, in effect the left had side of the resonance curve at this overmode is for the most part vanished.

The final overmode of the FBAR at ~ 920 MHz shows a *decrease* in resonance frequency of about 3 MHz, but here $f_{0(n=4)}$ is at ~ -35 dB as opposed to ~ -12 dB in the dry condition. The magnitude of the submerged resonance response is increased to about 20 dB in total, from about 8 dB in total in the dry state. The second submersion returns FBAR values very close to those seen during the initial submersion. The trace beyond 1.1 GHz up to the 3 GHz point on the submerged sample, shows an unusual periodic function, that is not present in the non-submerged state .

The results described above, lacking any pattern that is immediately obvious, are shown as for the readers convenience as a set of tabulated values (*See Table* ())and also as a set of graphs (*See Figures* 6.6 A-F) over range 0-3 GHz, and truncated to show the responses over each of the overmodes.

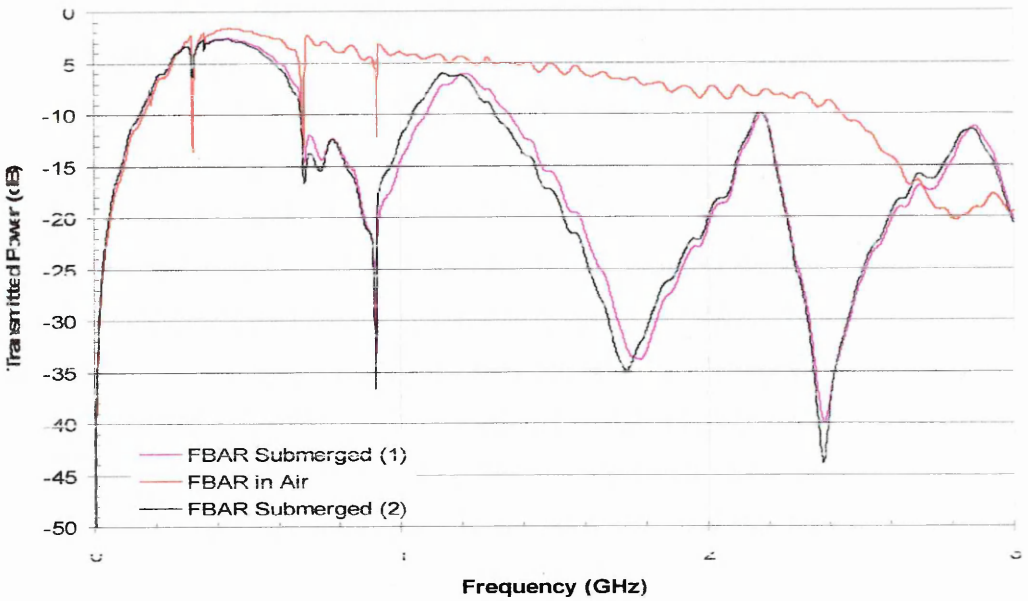

Figure 6.6 (A) Shows the S_{21} response of device 7 on PCB 3 in air and also when submerged in semi infinite (15 mm) water load. The loading was repeated. 1601 points over 0-3 GHz 1601 data points.

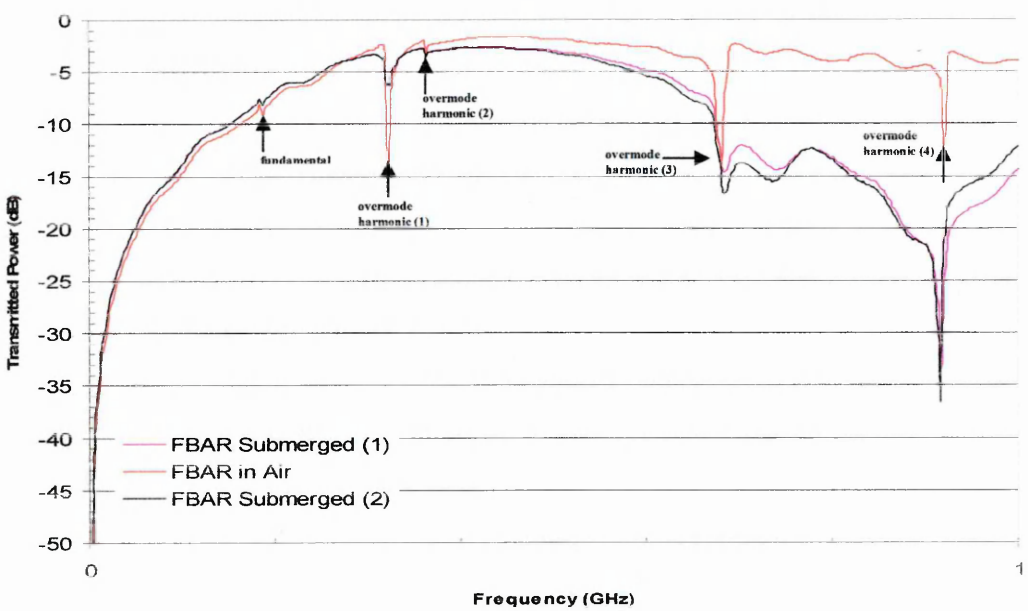

Figure 6.6 (B) As above but the fundamental and overmodes harmonic resonance peaks of the dry trace are clearly marked with arrows. This graph X scale is truncated (range = 1 GHz) to assist in data visualisation, about 550 of the original 1601 data points are visible.

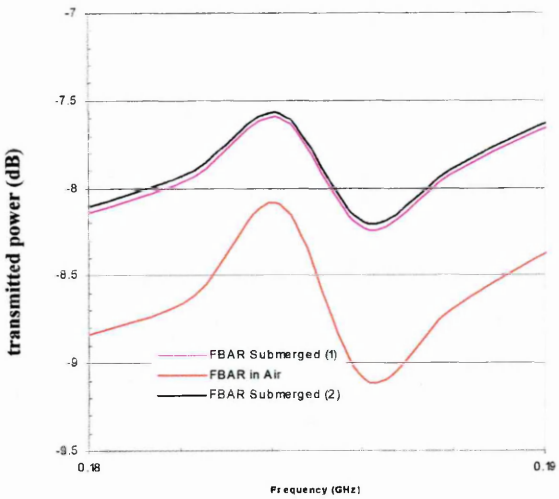

(C) Fundamental Mode (range = 10 MHz)

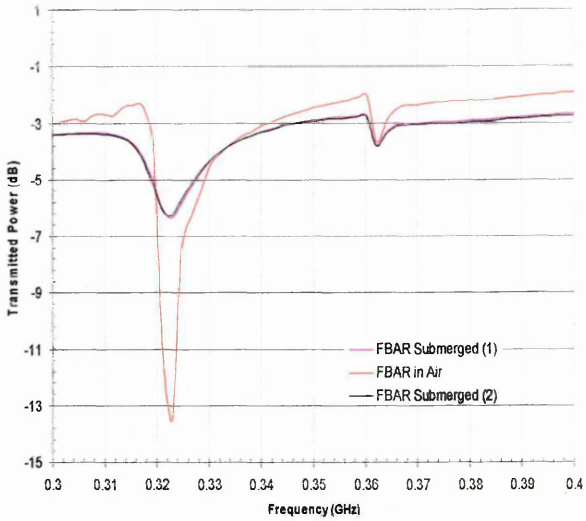

(D) Overmode 1 and 2 (range = 100 MHz)

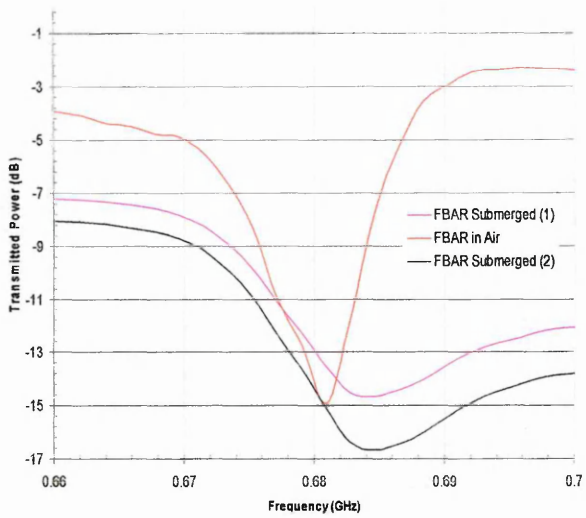

(E) Overmode 3 (range = 40 MHz)

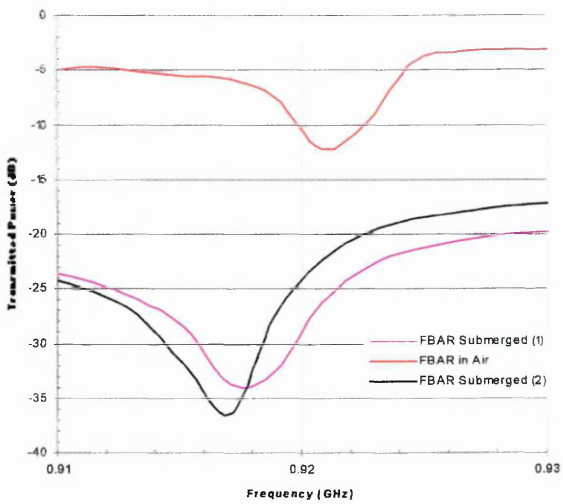

(F) Overmode 4 (range = 20 MHz)

Figure 6.6 (C, D, E and F) truncated forms of figure 6.6 (A) shows each of the S_{21} resonance curves from device 7 on PCB 3 in air and in response to submersion. Submersion was repeated after drying the device. The Y scale (dB) is also truncated to enhance visualisation of the data.

Note the S_{21} frequency *increase* in (E) and S_{21} frequency *decrease* in (F) in response to the *exact same* submersion events relative to the frequency recorded for the device in the dry state or gas phase. **Note** also the increase in S_{21} transmitted power in (C) but especially overmode 1 in (D), indicating damping, but the converse is true for (E) and, especially (F).

Table 6.1 Shows processed data from water experiment 1 X (frequency (Hz)) and Y (transmitted power (dB)) coordinates for the FBAR trace in the dry and submerged states. (overmode 2 was ignored due to small response) Red text indicates increases in resonance frequency or decreases (i.e. improvement) in power transmission.

	S_{21} series resonance frequency in air (MHz)	S_{21} transmitted power in air (dB)	S_{21} series resonance frequency when submerged		S_{21} transmitted power when submerged (dB)	
			1st load	2nd load	1st load	2nd load
Primary Mode	**186.063**	**-9.095**	**186.063** (Δf= 0 Hz)	**186.063** ""	**-8.192** (Δ dB =+0.903)	**-8.228** (Δ dB = +0.867)
Overmode 1	**322.892**	**-13.498**	**322.892** (Δf= 0 Hz)	**322.892** ""	**-6.352** (Δ dB =+7.146)	**-6.272** (Δ dB =+7.226)
Overmode 2	**360.428**	-	-	-	-	
Overmode 3	**680.089**	**-14.915**	**684.646** (Δf= +4.557 Hz)	**684.646** ""	**-14.648** (Δ dB =+0.267)	**-16.683** (Δ dB = -1.768)
Overmode 4	**920.818**	**-12.229**	**917.069** Δf= - 3.749 Hz)	**917.069** ""	**-33.802** (Δ dB = -21.573)	**-36.521** (Δ dB = -24.292)

6.2.2.4 Water loading experiment 2 (A) and 2 (B)

6.2.2.4.1 Methods

The experiment was repeated on to see if effects observed shown for the initial submersion tests in experiment 1 were similar when using a different, but equivalent FBAR device. In this case, the device used was Device 7 on PCB 7.

Water experiment (2A)

S_{21} series resonance frequency responses of the device was recorded in air, the device was then completely submerged in 15 mm droplet and responses compared. The XY scatter

graph is shown (range = 0-3 GHz) and also truncated to show in detail the areas of the chart that have responded.

Water Experiment (2B)

A calibration of the FBAR S_{21} series resonance response to water loading was then attempted. The depth[124] of the water droplet then increased by individual incremental additions of fluid with the Gilson pipette.(~100-200 µl) to look for any obvious patterns/trends in the response. The graph is shown over the whole 0-3 GHz range and also truncated with narrow bandwidth focus to highlight and explore the responses with increased clarity.

6.2.2.4.2 Results

Water Experiment 2 (A)

The response of the dry unloaded FBAR sample shows a fundamental mode (denoted as f_0) followed by 6 ($f_{0(n = 1 \text{ to } 6)}$) overmodes[125]. These are marked clearly on the graph (*See Figure* 6.7 (A). The resonant frequency of the fundamental mode and the first 5 overmodes does not appear to change at any discernable amount at this level of resolution (1601 points over 0-3 GHz) for the submerged sample. Indeed of the 6 resonant modes shown in the dry sample there are at least 5, possibly 6 resonant modes still visible in the submerged sample.

At f_0 (194 MHz) the response of the dry and the submerged sample are roughly equivalent in terms of frequency and transmitted power. At overmode 1 $f_{0(n=1)}$ (326 MHz), there is significant damping of the resonance curve in the submerged sample. The responses of the second overmode $f_{0(n=2)}$ (384 MHz) are roughly equivalent for the unloaded and the submerged samples. The attenuation seen in the first overmode is *not* apparent here. The extremely small resonant mode marked as position 3 on the graph for

[124] This means the height of the meniscus from the surface of the FBAR. This was measured by inserting a pin into the droplet until it reached the die, and then removing it and measuring the amount of wet area on the pin with a ruler. This method was not of high accuracy, but it was considered adequate for the purposes of the experiment.

[125] Overmodes marked at point s 3 and 6 are partial overmodes and would likely not be of significant value in sensing analysis since the resonance peak in its entirety is << 3 dB.

the unloaded sample is discernable with careful observation of the submerged trace at the same resonant frequency (554 MHz) but with significant insertion loss. At overmode 4 $f_{0(n=4)}$ (707 MHz) and 5 $f_{0(n=5)}$ (967 MHz) an unusual form of spurious mode has manifest in the resonance curve, and although the resonant frequency[126] for the dry and submerged specimens are equivalent, the response characteristics for both of these curves is dominated by the spurious mode and this pattern is repeated for both overmodes. There is some question as whether or not to the point marked (*) on the graph bears a relationship to overmode 6 (1.275 GHz). No further comment can be made on this point or apparent similarities between the shape of the dry and submerged traces at frequencies beyond 1.275 GHz.

Figure 6.7 (B) shows the same trace but in a truncated from to highlight the damping of overmode 1 in relation to the fundamental frequency and the overmode two where there was no significant alteration of the S_{21} transmitted power of the FBAR as measured by the network analyser.

Experiment 2(B)

The traces successive immersion of the FBAR in incrementally increasing water depth is shown against the unloaded sample. Again, as for 2 (A) the major characteristic response frequencies are still clearly visible within the trace and the responses of the FBAR are not dominated by frequency change, but instead the responses appear to represent changes in the S_{21} power responses of the FBAR.

Figures 6.8 (A and B) show that the responses of FBAR in submersion at 1 mm and 2 mm depth deviate from a general emerging calibration pattern that is generated as the water load increases in depth.

As the traces for 1 mm and 2 mm loads proceed beyond overmode 4 (707 MHz) both the 1 mm and 2 mm submersion power responses (dB) decrease (i.e. improve) markedly. The traces representing the 4 mm, 7 mm, 10 mm and 15 mm water depths all show power

[126] The automated $f0_{(n)}$ detection of the software would have reported the value with the most negative power transmission (dB), this would appear to be at the tip of the spurious mode of resonance for both overmode 4 and overmode 5 and would most likely have been an error.

transmissions becoming more positive (i.e degrade) as they traverse the intervening frequency range of 260 MHz to reach over mode 5 (967 MHz). This trend is exaggerated at the water depth increases, ultimately clearly separating out overmode 4 and overmode 5 The resonance frequencies $f_{0(n=4)}$ and $f_{0(n=5)}$ for these loads appears to have fallen by approximately 3 MHz ($\pm$0.5 MHz) from the unloaded dry FBAR in the gas phase.

Careful inspection of the trace reveals the partial overmode 3 (the first mode visible in Figure 6.8 (B)) is still quite visible when submerged and that frequency and power responses have not been significantly effected at levels that can be discerned at this resolution. There are indications that resonances have also occurred for all water loading sample depths at overmode 6, this overmode is of extremely small magnitude but can be discerned by careful inspection of the trace.

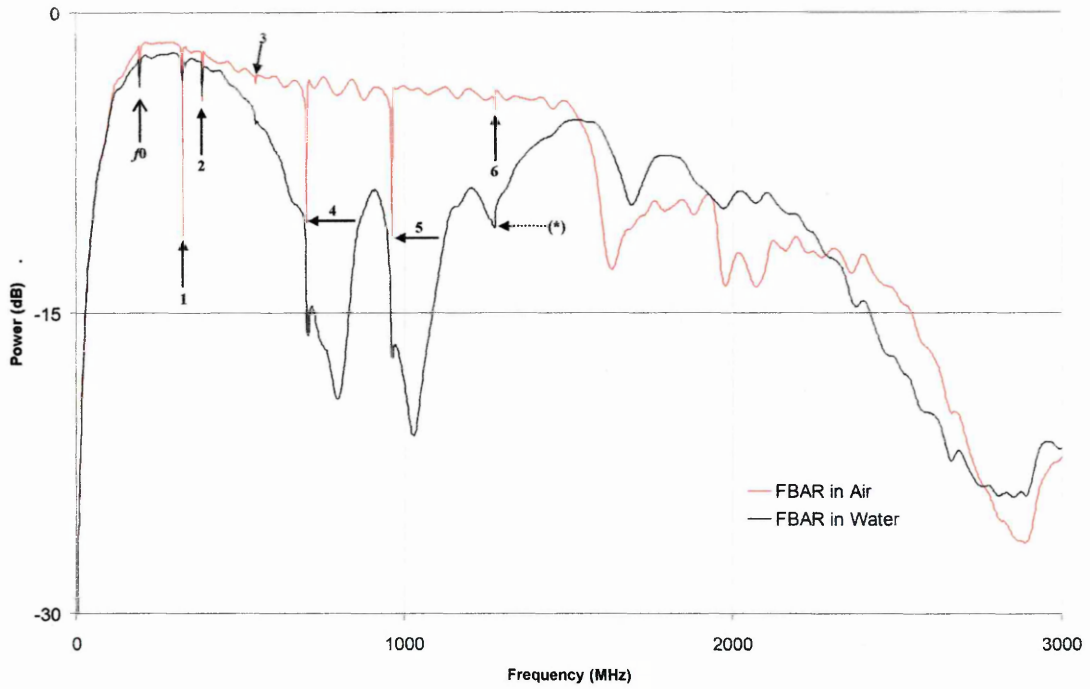

Figure 6.7 (A) Shows response of FBAR (Device 7 on PCB 7). in air and submerged in semi infinite liquid water loading layer. (15 mm). (S_{21}, 1601 points over 3 GHz)

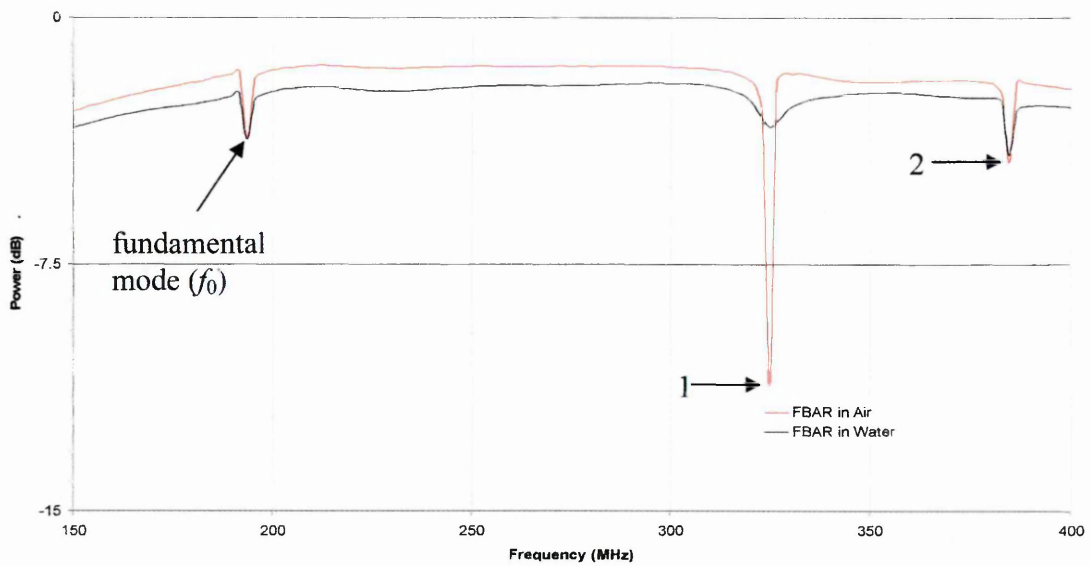

Figure 6.7(B) As above but X scale truncated (150 MHz to 400 MHz) and Y scale truncated (0 to -15 dB). Highlights significant damping of the 1st overmode at 326 MHz.

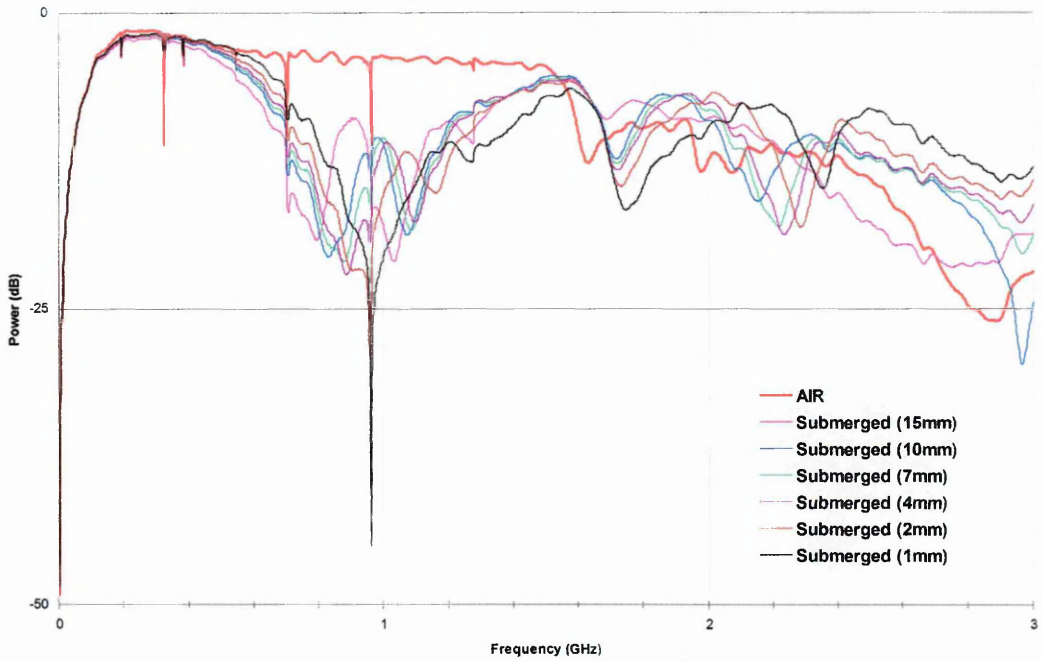

Figure 6.8 (A) Shows S_{21} calibrated responses of FBAR (Device 7 on PCB 7). under various water aliquot depths. Overmodes are indicated in Figure 6.7 (A)

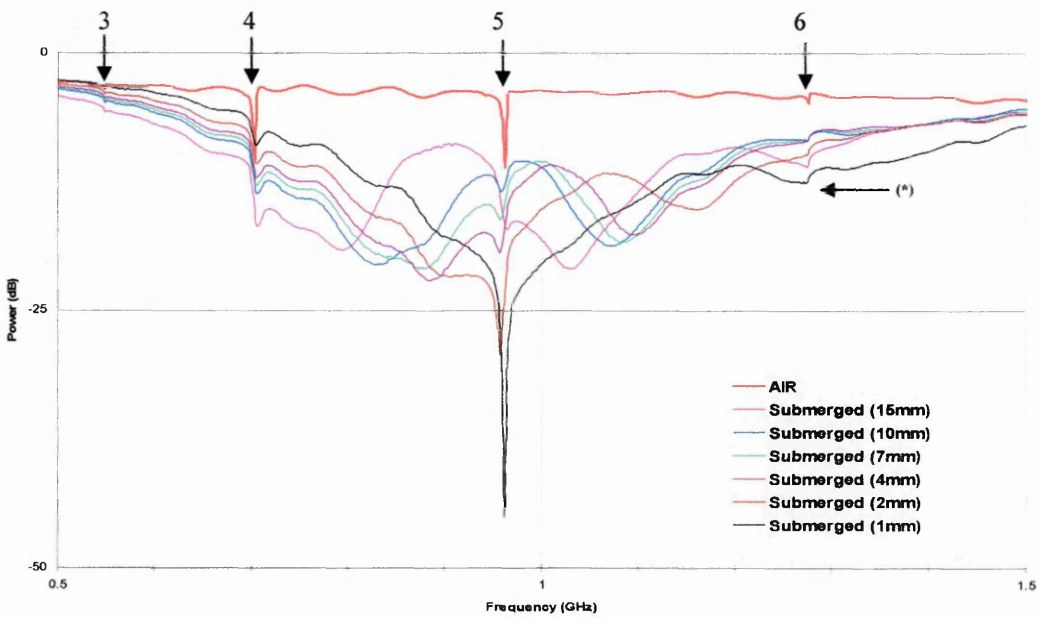

Figure 6.8 (A) As above but with truncated (0.5-1.5 GHz) X scale to assist in data visualisation. Overmodes 3, 4, 5 and 6 are visible.

6.2.2.5 Discussion and suggested further work.

A compressional probe wave entering a liquid should experience a geometrical spreading loss with amplitude reduction proportional with distance. In addition there should be significant amplitude reduction due to absorption in the water. (This absorption coefficient in dB/m) increases with the frequency squared. The value at 1 MHz is ~ 0.3 dB/m and 1^6 higher than this for a 1 GHz signal.[9] If these rules were in operation for the experiments shown above, then clearly there should be little or no response at all from the FBAR and its signals should have been damped almost to 0 dB as the device ceased to oscillate due to excessive energy loss, but the results clearly show that this was not the case and some resonance of the FBAR continued during its submersion.

The wirebonded FBAR samples that were mounted on PCB and probed from within the FHA gave results that at first sight suggested that S_{21} series resonance still occurred when they were submerged. There was a difference in the response of FBAR between 10 mm and 15 mm thickness, this suggests that in this case the concept of a semi-infinite layer is not valid at 10 mm, which was unexpected because although the wavelength penetration depth was not calculated, it was assumed to be in the order of nm, certainly not mm.

Using thinner water layers, ~1 mm droplets, may enhance or amplify the FBAR signal, it was interesting to note that the main enhancement of signal for both experiments was at roughly 950 MHz. The reason that the periodic functions observed beyond 1.1 GHz in experiment 1 are not present in experiment 2 is likely due to the fact that different FBARs were used, but as to why this happened, or did not happen remains elusive at this time. Whether these periodicities are resonances is not known. It is possible that some shear component of the FBAR response played a part in the responses, but again this can not be clarified at this time.

The difference between the distance of the meniscus from the working area of the device strongly influenced the results but this response did not display any clear linearity, and further, there was not the expected frequency shift due to additional mass loading from

the additional water aliquot. The frequency rose and fell on particular overmodes and no pattern could be discerned for this. Only a decrease in mass either by decreased layer thickness or decreased layer density could cause a frequency to rise in the rules of operation described for resonators in this thesis and the fact that the resonant frequency has not fallen significantly in response to the mass load of the water is of some continuing concern

Clearly then, some FBAR mechanism of operation that has not been explored in this thesis is at work in these responses, and before any conclusions can be drawn, it will be necessary to look at alternative models e.g., the transmission line model and its response to variables in dielectric properties of composite resonators. This demonstration is likely to have created more questions than it has answered, and it would be prudent at this stage to suggest that the assistance of a vibro-acoustical physicist and a microwave engineering specialist be sought. However, the most important point to be considered at this stage is the simple fact that the FBAR continued to resonate during submersion.

It is not difficult to imagine a simple arrangement like that set out in figure, where the opposite face of the FBAR is used, since the etched substrate forms a natural liquid holding vessel. It may make sense to exploit this facet, design the wirebond as in flip-chip form thus keeping the electronics away from any liquid layers. Perhaps, even micro pumps could be integrated into the substrate to deliver and remove aliquots at a set rate. Additionally, measured glycerol aliquots could be added to the water samples to increase its viscosity to look for damping or dissipation of resonance curve if this were found to be the case then the operation of the FBAR in liquid loading conditions could begin to be calibrated.

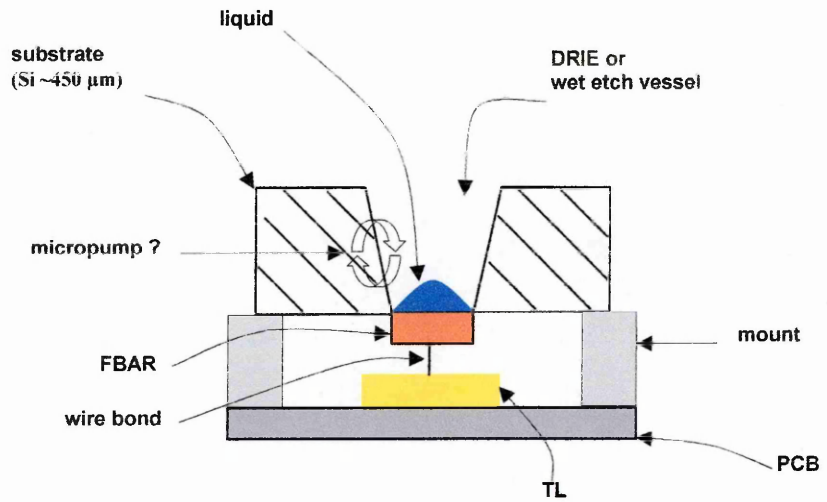

Figure 6.9 Schematic of proposed apparatus to be used for testing aqueous samples with FBAR sensors. Liquid samples would be interrogated directly in the natural holding vessel created by the etch-through the Si substrate transferred in and out with a micro-pump.

6.2.3 Modelling of Fbar array responses with the MathCAD Mason equivalent model

The powerful MathCAD mathematical FBAR simulation model that based on the equivalent Distributed Mason Model and which was already in place at our department was originally written by Dr. Qin-Xing Su and further adapted for this project by Dr. Mark Potter. The technical details underpinning the programming of the model are beyond the scope of this text. Dr. Potter kindly assisted in adapting the existing departmental FBAR simulation to encompass the perceived requirements of the FBAR sensors project; namely in the addition of an extra top layer with acoustic velocity, acoustic attenuation, layer thickness and layer density as variable parameters and also in the matrix wiring for array format of virtual devices with the additional resonators capable of being connected in both series and in parallel chain arrays.

6.2.3.1 Theoretical array design.

In all cases of array concept, individual units, and chain linked, the transducers' operating frequencies are frequency fine-tuned by the addition of simulated extra gold thicknesses of the top electrode, which is typically in the order of 50 nm – 100 nm per unit. An additional set of terms has been written into the model to accommodate the presence of an additional surface layer over the gold layer. Constrained by cost and time limitations, the individual FBAR unit array scenarios presented are indeed ideal and perhaps not feasible at this time. A more likely approach to the successful implementation of an array format may be in the design an array mask which allows a single electrical input to drive multiple resonators simultaneously, either in series or parallel.

6.2.3.2.1 Arrays of individual independently operating FBARs

In an ideal world, the schematic (*See Figure* 6.10 (A)) would offer the ideal solution to the functionality of any array and the results obtained would be quite simple to interpret. However, the arrangement is not plausible since its cost and large size is prohibitive. It is therefore logical to start from the ideal arrangement and work backwards to what is realistically achievable but offers a best fit approach to the problem of designing an array of FBARs for multiple analytes. So, in Figure 6.10 (B) an array made of independently resonating units is shown, but the devices are switched on an off sequentially with a switching mechanism that is capable of handling RF signals, but would not have to switch devices on and off at this frequency, each component in the array could, for example, be interrogated for a few seconds, and then switched off and the next device would then be probed. Such a switch has been sourced from Agilent.

It has been possible to cut single FBAR resonators out from the silicon grid by means of a high powered laser. (See Figure 6.10 (A)) Since the resultant devices are ~ 400μm, this allows for much scope in the design of a miniature array perhaps approaching the more ideal situation involving individual devices operating independently. An example conceptual schematic of such an array is shown in Figure 6.10 (A) also. The advantages of such a system would be that the losses caused by the excessive wire bond length in the

current scheme could be obviated and an array of individual devices and could be incorporated onto a relatively small PCB. Finally since the device is envisioned to work "in the field." It would be impractical to be reliant upon a NA for powering an interrogating the devices. NA are extremely sophisticated apparatus and posses much hardware that is superfluous to the requirements of the sensor under development. Various forms of oscillator circuits are available and it may be possible in the future to employ or adapt such a circuit possessing only the components essential to power and interrogate the FBAR.

6.2.3.2.2 Results

The results shown in Figures 6.11 A and B are quite simple to interpret. The individual ~ 1.2 GHz modelled resonators with a zero additional mass load of course showed no change in resonant frequency and the individual traces seem to show only a single trace because all five traces are identical and as such overlaid on top of each other. With sequential 50 nm gold top electrode thickness increases, the frequency is fine-tuned and falls linearly with roughly Δf = -25 MHz per 50 nm additional gold top electrode thickness load.

The S_{21} power transmission for all of the resonators remains very similar at ~ -11 dB as does the overall shape of the resonance curve and hence the Q factor. Individual traces can be clearly seen, but it would be important to identify which resonators these traces were coming from in a physical apparatus as this would not be immediately apparent.

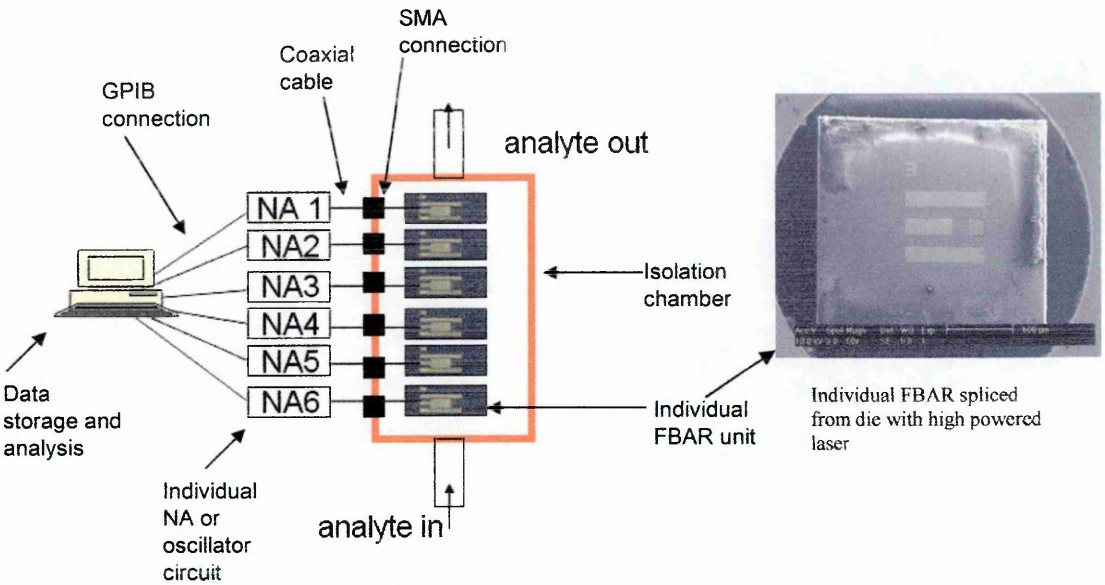

Figure 6.10 (A) Shows "ideal" hypothetical arrangement of six FBAR sensors where each individual module is excited and interrogated by its own NA or individual oscillator circuit and the array is housed within a single FHA.

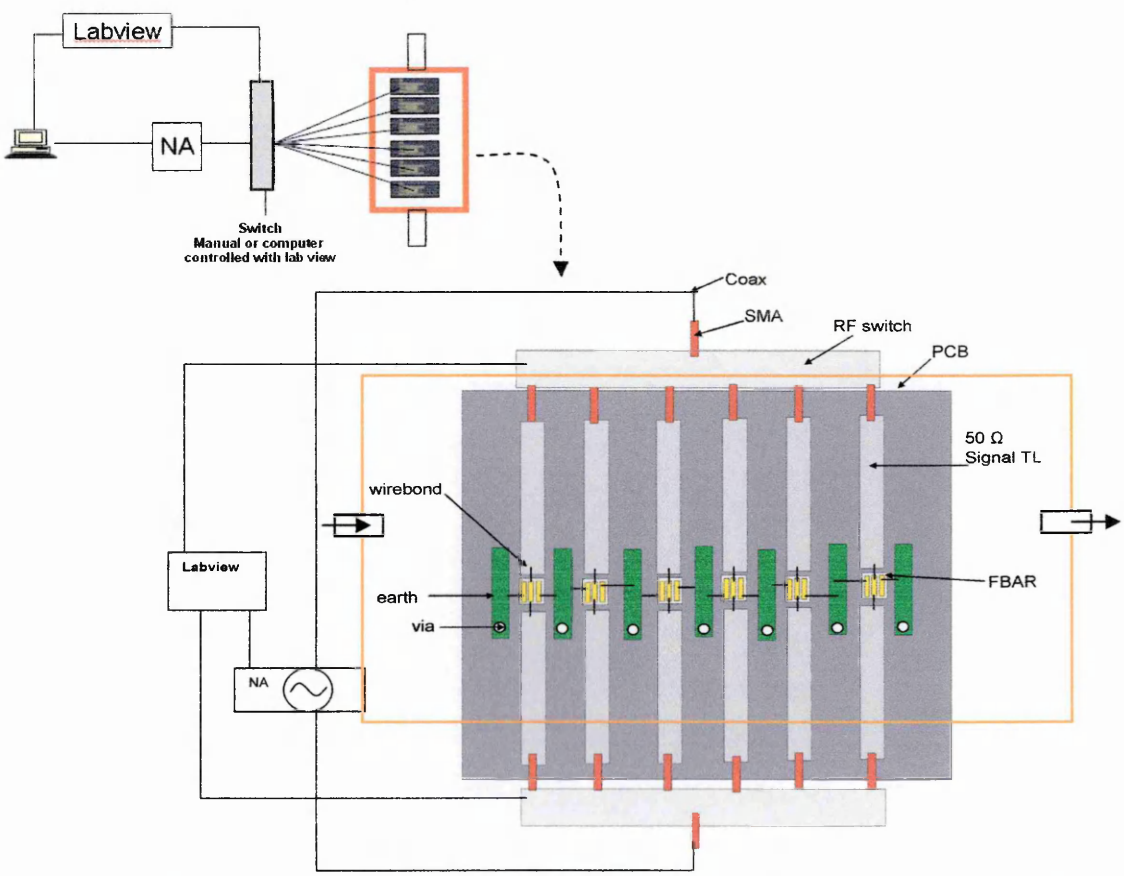

Figure 6.10 (B) As above but shows arrangement where each individual transducer module is interrogated sequentially by means of a switching mechanism capable of handling RF frequencies, but not necessarily switching at that speed.

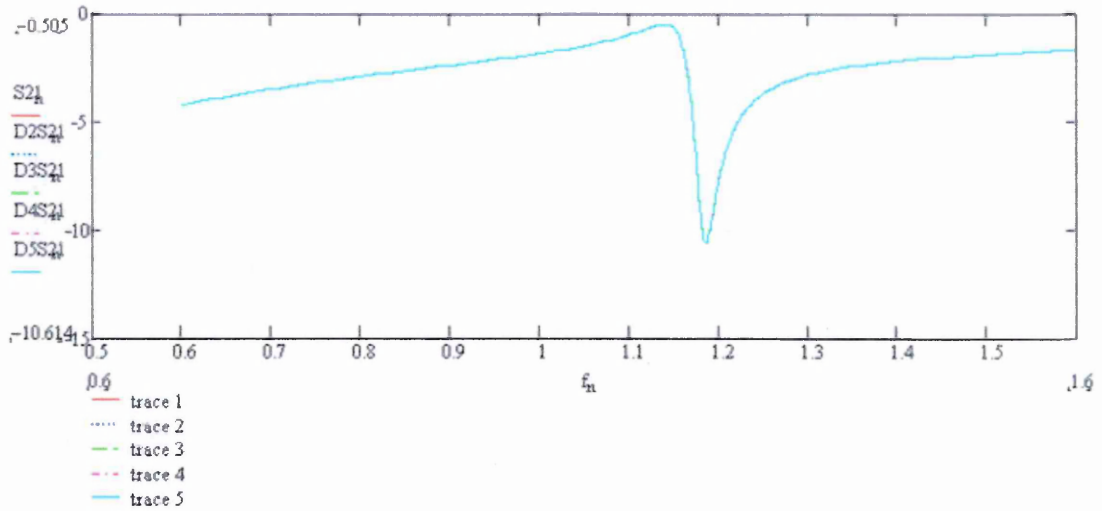

Figure 6.11 (A) Shows S_{21} modelling data for 5 individual resonators operating at identical frequencies The individual traces are not visible since they are on top of each other. i.e. Trace 1 to Trace 5 = 0 nm additional thickness.

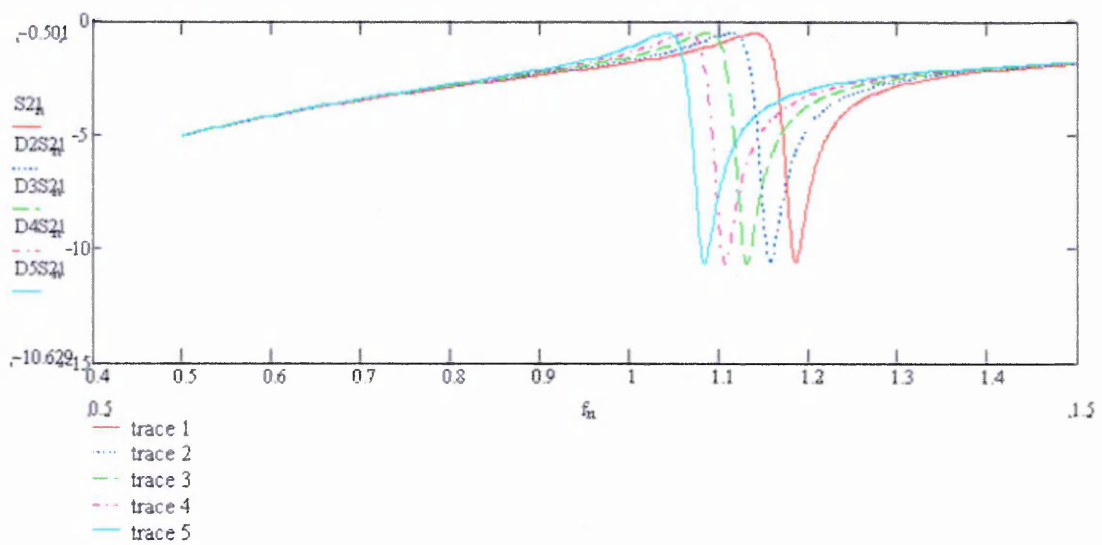

Figure 6.11 (B) Shows S_{21} modelling data resolving out of individual resonators frequency fine-tuned by means of modelling additional gold top electrode thicknesses in increments of 50 nm. i.e., Trace 1 = 0 additional thickness, Trace 5 = 200 nm additional thickness.

6.2.3.2 Modelling of series and parallel FBAR arrays.

The MathCAD Mason model of the FBAR was configured by colleagues to give FBAR arrays that were electrically connected in both series and parallel. An additional "top loading" term was also written to serve as an additional mass loading layer beyond the additional gold thickness of the top electrode. This top loading layer was programmable with the various acoustic properties important to a sensing layer, namely acoustic velocity, acoustic attenuation, layer density and layer thickness Focussing arbitrarily on the third resonator in the array it will be shown how the loading of an additional surface layer can be modelled and that the transducer in question can be identified as the loaded sensor.

Additional interpretive considerations in this case are the ability to unambiguously identify the responses of each individual resonator unit in the array and the possibility of increased noise, perhaps loss of sensitivity and a potential plethora of other problematic abstractions in both the fabrication, but more importantly in the interpretation of the response from the hypothetical series/parallel array. Potential advantages for this format are obvious, and include the fact that only a single NA or oscillator circuit is required, the reliance on a RF switching mechanism is removed and the size of the finished device is likely to be greatly reduced.

Here it will be shown that the models generated in MathCAD for the FBAR filter systems can be modified to handle a set of 5 (likely more) resonators operating simultaneously either in series or in parallel. (*See Figure* 6.12) The resonant frequencies of the devices are each altered slightly "tuned" by modelling the addition of thickness to the top gold electrode resolving closely spaced yet clearly separate resonant peaks with which to identify each module. An additional mass load, in this case with the acoustic properties of ZnO was modelled onto the third resonator in the chain for both series and parallel.

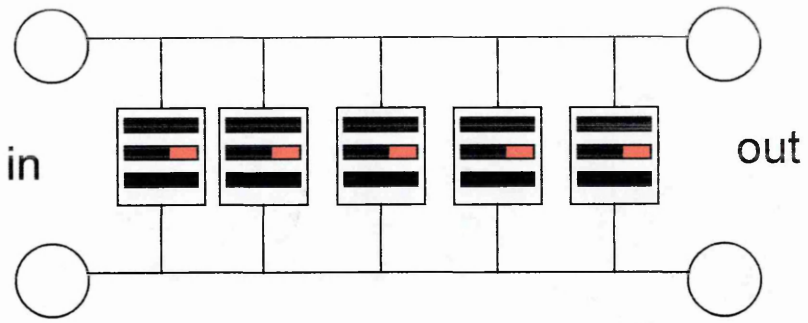

Figure 6.12 (A) Schematic of five FBAR transducers in linked in parallel.

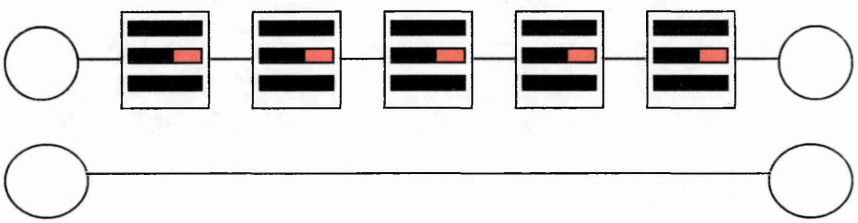

Figure 6.12 (B) As above in series.

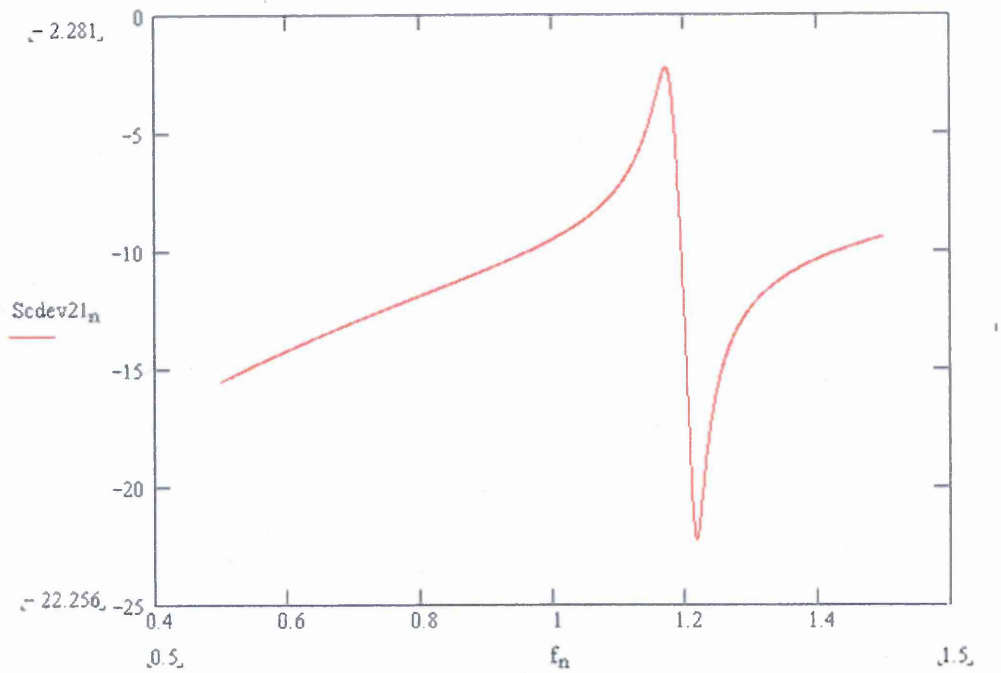

Figure 6.13 (A) Shows modelling data of 5 FBAR *Series* Chain of transducers each identical top electrode thickness and zero surface loading.

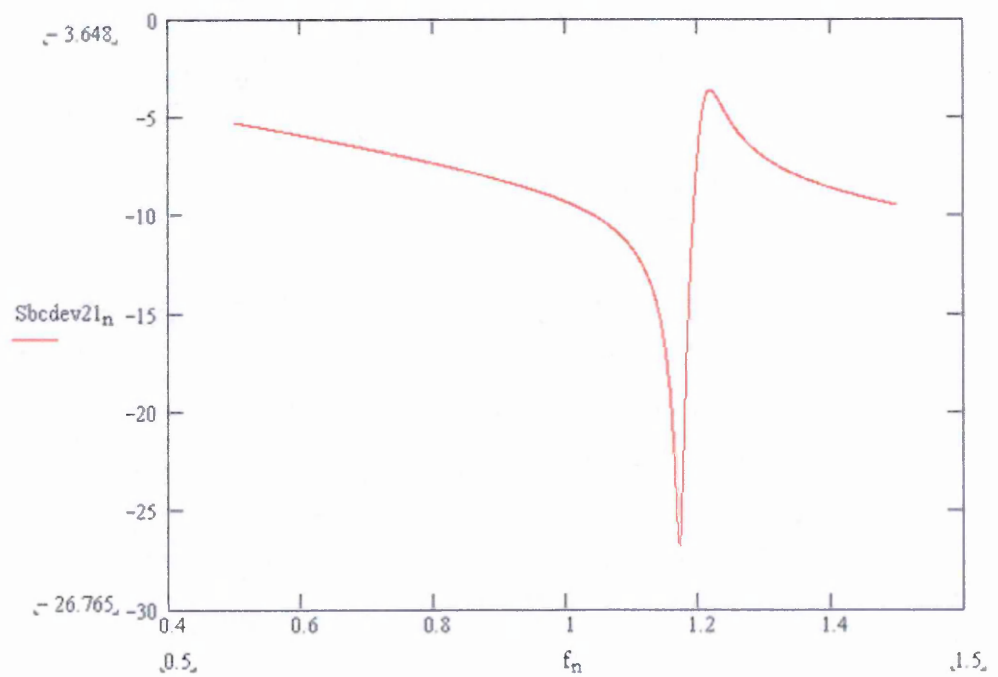

Figure 6.13 (B) Shows modelling data of 5 FBAR *Parallel* Chain of transducers each identical top electrode thickness and zero surface loading.

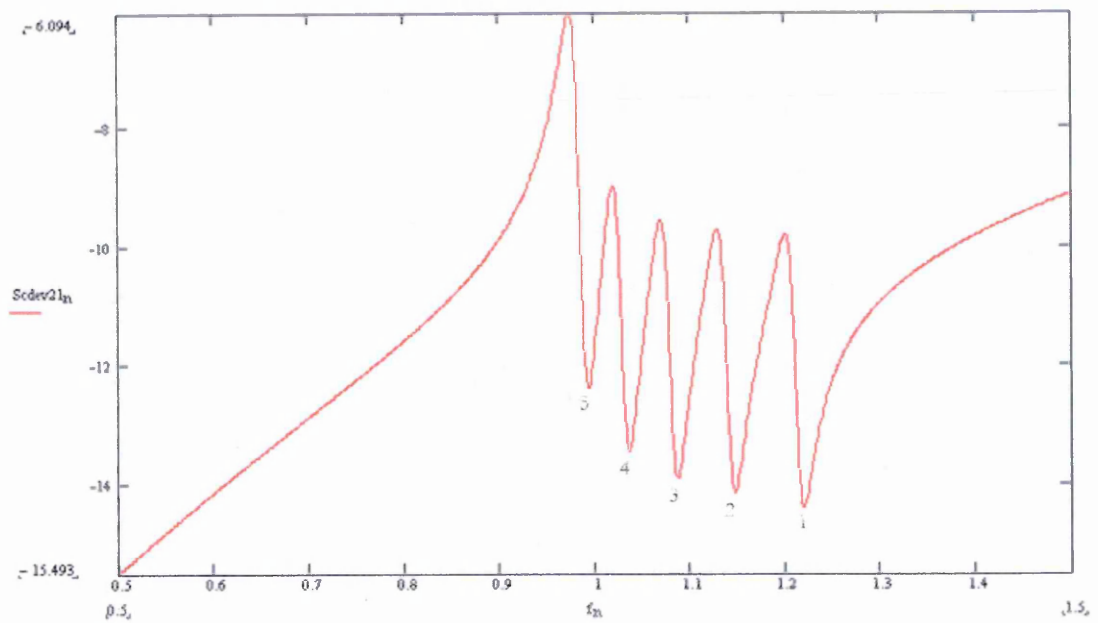

Figure 6.14 (A) Shows modelling data of FBAR *Series* Chain of transducers each "tuned" by the incremental addition of 50 nm gold top electrodes. Zero additional surface load.

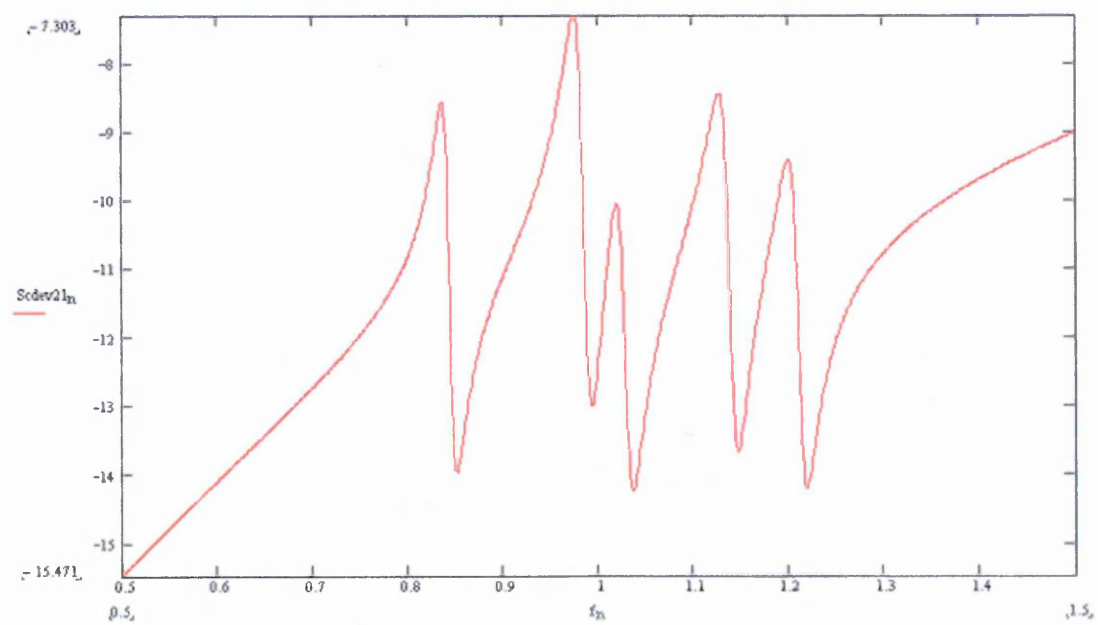

Figure 6.14 (B) As above but with addition of 1µm thickness mass (5.67 Kg M^{-3}) onto third resonator in the chain.

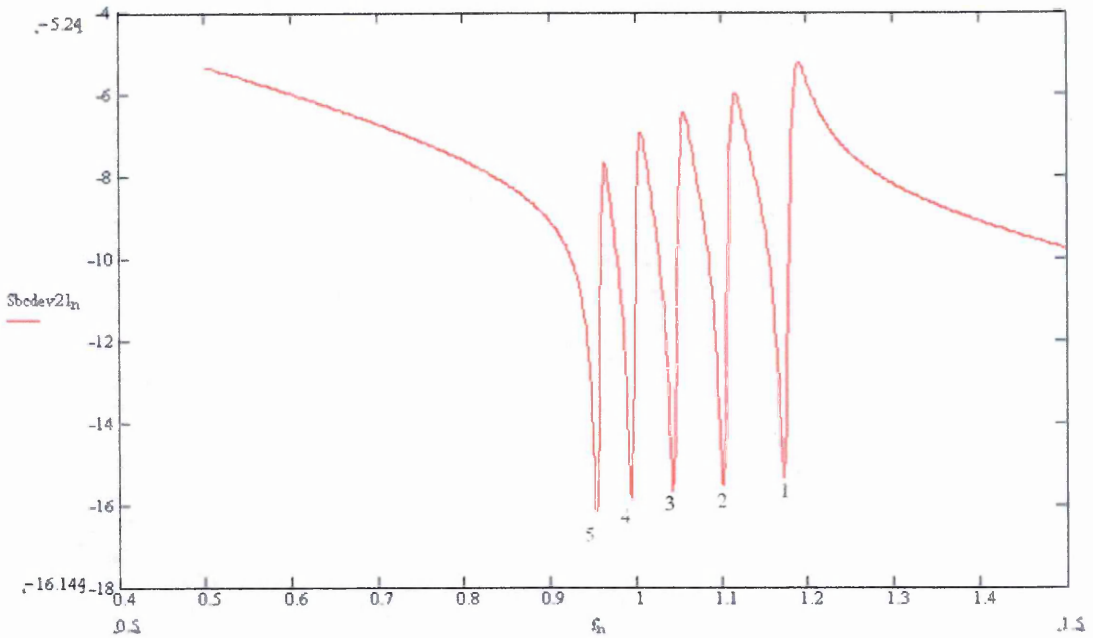

Figure 6.15 (A) Shows FBAR modelling data of *Parallel* Chain transducers each frequency fine-tuned" by the incremental addition of 50 nm gold top electrodes. Zero surface load.

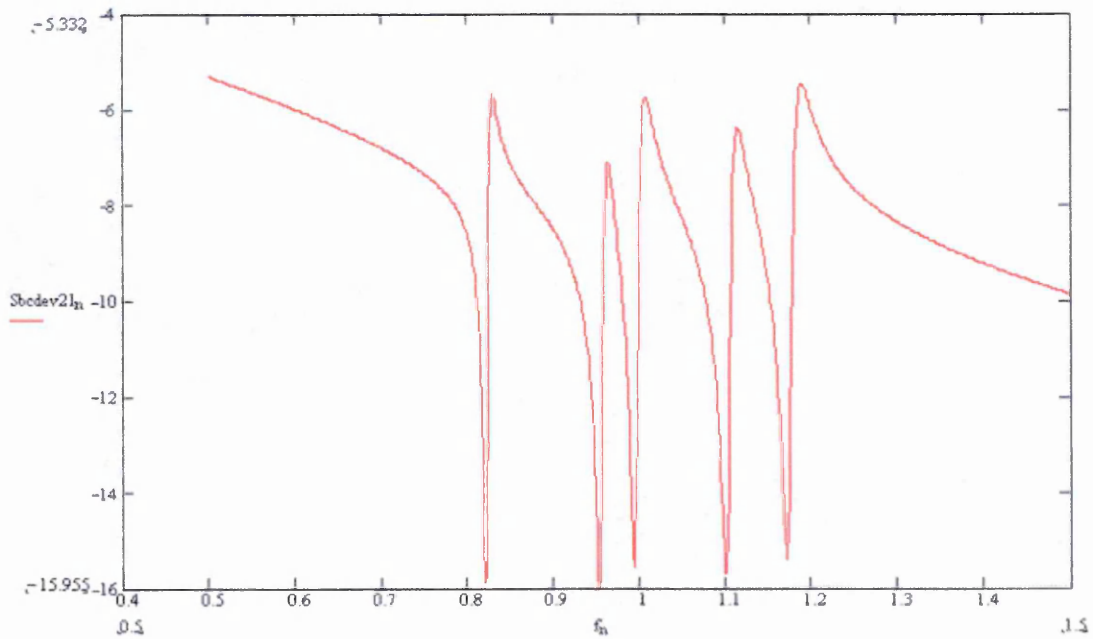

Figure 6.15(B) As above but with the addition of 1 μm thickness (5. 67 Kg M^2) on third FBAR in chain.

6.2.6.3 Linked Array Modelling Results and Discussion

Figure 6.13(A):- Shows modelling data from *series* linked chain of 5 FBARs with identical electrode thicknesses with working surface area of 250μm^2 and zero surface loads. Only one resonance curve is visible since the responses from the five resonators are identical [127]

Series resonant frequency = ~ 1.21 GHz.

Figure 6.13 (B):-Shows modelling data from *parallel* linked chain of 5 FBARs with identical electrode thicknesses and zero surface loads.

Parallel resonant frequency = ~ 1.91 GHz

Figure 6.14 (A) Shows the effect of the incremental increase in the top Au electrode thickness of 50 nm Range 0 nm 200 nm on each resonator in the series linked chain. Now 5 distinct peaks are visible. Each peak in the chain moves away from its preceding peak by about Δf = - 25 MHz. The insertion loss is less than 1 dB over the range, with device 5 the most loaded possessing the most signal attenuation @ ~ 12.8 dB. This result was more or less as anticipated.

Figure 6.14 (B):- Shows the model response when an arbitrary mass of 1μm with density (Kg M^3) 5.67x 10^3 is loaded onto the third resonator in the chain of the series frequency fine-tuned series array. Devices 1 and 2 resonance frequencies and power responses are relatively unaffected by this mass load. The loaded resonator (3) has decreased its resonance frequency by ~ 70 MHz, and its S_{21} power transmission value was improved by ~ 0.5 dB to ~14.2 dB. Devices 4 and 5 have been effected in a way that was not expected, since for device 4, a change in the characteristic resonance shape is seen, and Δf= ~ 20 MHz. Device 5 Δf = ~ 150 MHz, with a slight improvement in power transmission.

[127] **Note** that since this describes a chain array there is only a single trace, not one trace per resonator as was previously demonstrated in Figure 6.11.

These responses are not as the author had hoped for, because it was imagined that only resonator 3 in the chain would be effected by mass load, and clearly this must be a conceptual error due to oversimplification of the system.

Figure 6.15 (A):- Shows modelling data from a parallel chain of FBARs with working surface area of 250μm^2. Each device possesses incremental Au thickness of 50 nm Range 50 -250 nm. Spacing roughly equivalent to 20 MHz – 25 MHz per device can be seen, with less than a single decibel of difference over the parallel chain peaks. This result was as expected.

Figure 6.15 (B):- Shows the model response when an arbitrary mass of 1μm with density (Kg M^3) 5.67x 10^3 is loaded onto the third resonator in the parallel chain. The frequency of and characteristic responses of devices 1 and 2 are scant effected. The loaded resonator is effected by its mass load, $\Delta f = \sim$- 50 MHz but the shape of the curve is altered also and this may be indicative of an impedance change in the circuit. The resonance frequency of device 4 changed, Δf = - 25 MHz, and the shape of the curve has remained as it was originally. The final resonator in the chain has responded more strongly to the presence of a mass load on the 3rd resonator even though it was not directly loaded itself.

The most striking feature of the response is the shape change of the resonance curve in the mathematical Mason model representation of the array for the loaded device and adjacent devices, again this may be due a change in impedance in the line, and it is possible that the mass load in the centre of the chain is having inductive effects on the chain, it will be recalled that in the BVD circuits, the mass load is actually represented by an inductor.

6.3 Overall Conclusions

In essence, the overall experimental work gives a strong indication that the laboratory bound prototype FBAR sensor that was developed in this work is extremely viable as an analytical research tool and that it has the potential to act as a very sensitive universal platform for the selective, or in certain cases, ultra-specific detection of measurand.

FBAR in sensor format was shown to be responsive to physical changes such as temperature and lighting conditions, the temperature change was due to physical changes in the device, and the response to light was a purely electrical one, but both were independent of mass changes. Mass responses from the device were fairly straight forward, especially for the modelled gold layers, but also in the immuno-accumulation of proteins.

The isolation chamber and the associated microwave electronic components worked well as did the software that was developed, But why S_{11} (*See Figure* 3.2 (B)) failed to generate a resonance response is still not known because electrical continuity was established, and S_{22} to which the S_{11} was expected to be identical did show resonance. The response from the humidity sensor showed that the device was sensitised to the presence of moisture from the addition of the hygroscopic PVP polymer, and that the intensity of the FBAR frequency response was linked to the thickness and to the concentration of the polymer as well as the changes in the water vapour concentration which were independently monitored.

Looking at the shapes of the resonance curves showed that, independent of frequency changes, other changes in the characteristic responses, Q-factor, of the device could yield useful information about the rheology of the layer. The results were not always easy to interpret, but this may just mean that more detailed calibrations are needed. The presence of spurious modes of resonance on the resonance curve can cause instability in the sensor response. The addition of the PVP layer was found to suppress these spurious modes.

The FBAR remained a functional resonator when submerged in a semi-infinite water layer, but the behaviour of the device was drastically altered and the responses were interesting but also perplexing. It is not clear at this stage whether or not the FBAR in its present form could deliver meaningful information about changes in aqueous conditions. It may be necessary to change the electrode configuration, and piezoelectric deposition directions to create a lateral mode FBAR for it to behave in a more predictable manner in a liquid.

The increase in sensor sensitivity due to the increased frequencies of overmodes is linearly related to the fundamental frequency of the device, increases in the fundamental frequency give theoretical maximum increases in sensitivity to mass as f_o^2 but in practice figure is also influenced by the Q factor of the device.

As well as being able to accurately report changes in both the chemical and the biological micro-environments that were in close proximity to its resonating surface. The FBARs were physically robust, and the baseline responses that were generated from them were sensitive, accurate, and on the main reproducible and stable.

The theoretical modelling component of the work points the way toward integration of FBAR units into miniaturised array formats, this is useful because an array format linked to a data base can serve to act as an intelligent electronic nose. However, the chained series and parallel transducers did not behave as expected, and it is too early to say with any degree of certainty that this would be a viable sensing strategy. The responses from the independent resonator arrays worked in a much more predictable manner. It also very likely that the device planar working area may be considerably miniaturised and the advantages of this can not be overstated.

The robustness and low power requirements of the FBAR device present opportunities for sensing in hostile environments such as extra terrestrial environments, but the matter of developing oscillator circuitry to simultaneously excite and characterise the FBAR device is considered non-trivial at this stage. It is almost certain that continued research along this route will deliver the necessary microwave electronics required. Further research will also iron out the present difficulties involved in decreasing the thickness of the device to increase resonance frequency whilst maintaining reasonable Q values and efficient electro mechanical coupling values.

The emergence of a multi-analyte capable hand-held device based on this technology is possible, it may be that the sensing applications of this technology become additional functionalities in mobile telephones and PDA devices since FBAR technology is about to

become an intrinsic part of domestic mobile communications devices in the form of microwave duplexer filters.

Overall, the author considers that the work demonstrated in this thesis was successful, perhaps even exceeding the scope of the original work-plan since there is no doubt that not only have enhanced physical, chemical and biological sensing capabilities for BAW systems been confirmed through the exploitation of the high resonance frequencies typical of TFR technology, but also, new and potentially important discoveries about the behaviour of FBAR devices have been made during the course of this research.

REFERENCES
CHAPTER SIX

1. Shaoshan Li Markus Paulsson and Lars Olof Björn. (2002) Temperature-dependent formation and photorepair of DNA damage induced by UV-B radiation in suspension-cultured tobacco cells. *Journal of Photochemistry and Photobiology B: Biology.* **66**, Issue 1, pp 67-72
2. A.B. Britt, DNA damage and repair in plants. (1996), *Annu. Rev. Plant Physiol. Plant Mol. Biol.* **47** pp. 75–100
3. Hong Z., Huwei T., Ronghui W., Wanzhi W., Shouzhuo Y. (1998). Immobilization of DNA on silver surface of bulk acoustic wave sensor and its application to the study of UV-C damage. *Analytica Chimica Acta.* **374**. pp 31-38
4. Voinova . M. M., Jonson. M., Kasemo. B (2002) "Missing mass" effect in biosensor's QCM applications. *Biosensors and Bioelectronics.* 17 pp 835-841
5. Nomura, T., Minemura. A. (1980) *Nippon Kagaku Kaishi.* 1261
6. Bandey. H. L., Martin. S. J., Cernosek. R. W. (1999), Modelling the responses of thickness shear mode resonators under various loading conditions. *Anal Chem.* **71** pp 2205-214]
7. Liess. H. L., Knezevic. A., Rother. M., Muenz.J (1997) Acoustic waves at the solid /liquid interface. *Faraday Discuss.* **107**, pp 39-52
8. McHale. G., Newton. I.M., Banerjee. M, K., Cowen. J. (2000). Acoustic wave – liquid interactions. *Materials Science and Engineering C.* **12** 17-22]
9. Personal Communication with Professor Jens Hovem Acoustic Research Centre Norwegian University of Science and Technology.

Appendix (1)
A Supplemental Literature Review
Further Theoretical Considerations Regarding Additional Mass Loading on BAW Resonators.

1.1 Ideal cases of mass loading onto BAW devices

During the literature review, the particular form of the ideal mass loading equation was different in nearly every journal article encountered and this was initially a cause of some confusion, since it was not clear to the author which particular version of the classic Sauerbrey term was convenient to use for interpretation of the FBAR sensor responses.

The chief purpose of this supplemental review is to bring the core terms from a number of important research documents spanning five decades into a single document to assist acoustically orientated sensory researchers in the future.

The quartz plate resonant frequency can be given by; Cady (1946)[11]

$$f = \frac{m}{2d_F}\sqrt{\frac{\mu_F}{\rho_F}}, \qquad \text{(A1)}$$

Where m is the mode number of the vibration, μ_F is the shear modulus of the crystal, ρ_F its density and d_F is its thickness.

In quartz, the mechanical disturbances travel in a direction which is perpendicular to the plate surfaces. Particle displacements at these surfaces are parallel to the surface (shear) for AT cut crystals (+35° 15' angle from the *z*-axis). The plate thickness (d) determines the frequency (λ) of the fundamental (f_0) and harmonic (n = 3, 5,....) resonances according to λ=2d/n. So; Uttenthaler (2000) [14]

$$f_n = n.f_0 = \frac{n.v}{2d} \qquad \text{(A2)}$$

Where f_0 and f_n are the resonant frequency of the fundamental mode (n=1) and the nth harmonic overmode (n = 3, 5, 7,....) respectively, v velocity of sound (v = 3340m/s in AT quartz)

The historical origins of this microweighing with BAW systems can be traced back to the seminal paper written in *Z.* Physik (1959)[3] by G. Sauerbrey. This is such an important piece of work that it deserves further attention. Sauerbrey began by stating that "for the purposes of measuring the natural frequency of the oscillating quartz crystal, the crystal is used as the frequency determining component of the oscillator circuit."

The thickness shear oscillation of a quartz plate is a standing transverse wave. In the basic oscillation the plate thickness is equal to a half wavelength.

$$f = \frac{Vtr}{2.d} = \frac{N}{d} \qquad \text{(A3)}$$

where *Vtr* is the velocity of propagation of the elastic transverse wave in the direction of the plate thickness, d is the thickness of the plate and N=Vtr/2 is the frequency constant.

The frequency change $\Delta f / f$ is brought about when the thickness d of a plate is increased by Δd. The same change in frequency is brought about if a foreign layer of the same mass is deposited on the plate.

$$\frac{\Delta f}{f} = \frac{\Delta d}{d} = \frac{\Delta mQ}{\rho QFd} = -\frac{\Delta m}{\rho QFd} \qquad \text{(A4)}$$

where;

f=	natural frequency of the crystal
d	thickness of the crystal
ρQ	specific gravity of the crystal (sic *density*)
F	area of the plate surface
ΔmQ	mass of a layer of quartz with thickness Δd
Δm	mass of any foreign layer evenly covering the surface of the plate.

By introducing the mass coverage φ =Δm/F and the frequency constant N = *f*d, Sauerbrey deduced that the relationship between change in frequency (Δ*f*) and mass coverage (φ) as:

$$\Delta f = \frac{f\varphi}{d\rho Q} = -\frac{f^2}{N\rho Q}\varphi = -C_f^{\varphi} \qquad \text{(A5)}$$

This is the ORIGINAL Sauerbrey equation, where the "layer weighing sensitivity" is $C_f = f^2 / N\rho Q$.

Further to this, Sauerbrey went on to separate the responses of the oscillating crystal by using an equivalent LCR circuit[128] to deduce its susceptance as a function of the frequency.

ω_S series resonant frequency
ω_p parallel resonant frequency
Lq equivalent inductance
Cq equivalent capacity
Rsq series loss impendence
Cp capacity of the quartz plate and circuit capacitance.

The series resonant frequency ω_S is equal to the resonant frequency of the pure series LCR circuit and is equal to the required mechanical frequency ω_O:

$$\omega_s = \frac{1}{LqCq} = \omega_O \qquad \text{(A6)}$$

The S_{21} series resonant frequency was the exclusive frequency parameter used in this project to monitor the responses of FBAR devices.

Over time, modifications to the original Sauerbrey term have evolved in the literature and the most commonly presented forms are given below. But it should be remembered that the term was originally intended for thin metallic rigid films for microweighing in a vacuum, its application to thick or soft layers was never intended, and the term is not applicable when the QCM is interrogating aqueous solutions.

Lu and Lewis (1972) [4] State that mass loading onto QCM could be given as:

$$\Delta f_m = -f_0^2 \frac{2}{A\sqrt{\rho_q c_q}} \Delta m \qquad \text{(A7)}$$

where Δf_m is the measured frequency shift, f_0 is the resonant frequency of the crystal, Δm is the mass change, A is the piezoelectrically active area, and ρ_q and C_q are the density and piezoelectrically stiffened shear modulus respectively. This relation is valid of thin rigid films with uniform mass distribution

[128] Remarkably similar to the BVD model, but referenced by Sauerbrey as being developed by Cady[1]

Muramatsu *et al* (1990) [5] use a simplified form of the expression which relates the factional increase in mass with the unloaded mass of the resonators as;

$$\Delta F = -\Delta m / mF \qquad \text{(A8)}$$

where ΔF is the resonant frequency change, F is the basic resonant frequency m is the mass of the resonator and Λm is the surface mass change.

Barnes *et al* (1991)[7], Reason *et al* (2001) [10] and Kim *et al* (2003) [6] all use the following term to represent the mass loading of a an ideal thin film onto the surface of a BAW resonator.

$$\Delta f = -2.26X10^{-6} f_0^{\,2} \Delta m \qquad \text{(A9)}$$

where Λf is the frequency shift in Hz due to surface density Λm in g/ cm ^{2} and f is the resonance frequency in Hz, ρ_q is the density of quartz and v_q is the shear wave velocity in quartz.

Wong *et al* (2002)[11], who were using immunosensor modified QCM devices to differentiate between different subclasses of the *Salmonella* pathogen use the equation (A10) which has an additional term to define the area of the electrode and the surface coverage of the layer..

$$\Delta f = \frac{-2.3X10^{6} f_0^{2} \Delta m}{A} \qquad \text{(A10)}$$

Where ΔF is the change in the frequency (Hz), f_0 is the resonant frequency of the crystal in MHz, ΛM is the mass deposited and A is the area coated cm^2

The mass loading equation is given in three equivalent forms by O'Toole *et al* (1992)[8] in a single paper representing the three main variants of the *classic* equation. What is of particular interest in this case is that O'Toole *et al* identified each of the terms as being applicable for the purposes of microweighing on high frequency thin-film resonators, similar to the ones used in this project. O'Toole *et al* can be attributed as being the first researchers to demonstrate the application of TFR technology for sensing applications. The terms are given as :

$$\frac{\Delta F_S}{F_S^0} = \frac{-\rho_1 D_1}{\rho_s D_s} \qquad \text{(A10) (i)}$$

or

$$\frac{\Delta F_S}{F_S^0} = \frac{-2F_S^0 \rho_1 D_1}{(\rho_S C_S)^{1/2}} \qquad \text{(A10) (ii)}$$

or

$$\frac{\Delta F_S}{D_S^0} = \frac{-2F_S^0 \Delta M}{(\rho_S C_S)^{1/2}} \qquad \text{(A10) (iii)}$$

where ρ_1 is the density of the deposited layer, ρ_s is the density of the resonator material (substrate) D_1 is the thickness of the resonator, F_S^0 is the initial series resonance frequency, ΔF_s is the change in series resonance frequency after the deposition of the material, C_S is the stiffness constant of the substrate, and ΛM represents the change in mass per unit area. *Also See equations* (A10 (iv) and A 10(v))

It is noted here that the terms are only valid for mass depositions less than 2% of the actual mass of the resonator. More importantly, what is also noted is the fact that the three terms all neglect to take into consideration the effects of the differences in the elasticity and/or the viscosity of the sorped material with respect to the resonator material.

Ramsden (1993) [10] States that in many cases, it is knowledge of the average of the properties of foreign films (surface attached layers) that is sought. The primary quantity of interest is Γ, the mean mass of number of molecules per unit area. This is related to the fractional surface coverage Θ according to

$$\Gamma = \Theta m/a, \qquad \text{(A11)}$$

Where m is the mass per molecule (when Γ denotes the number of molecules per unit area, $m = 1$) and a the area per molecule.

For QCM with typical (mm) thicknesses f is typically a few MHz can be discovered to great accuracy by making the crystal part of resonant circuit. (Sauerbrey 1959). If materials are deposited at the antinode (surface displacement maxima) of the standing wave propagating across the thickness of the crystal, a frequency change Λf occurs as if the thickness of the crystal had increased by an amount $d_\Lambda = \Gamma/\rho_\Lambda \equiv = \Lambda d_F = \Gamma/\rho_F$, i.e.,

$$\frac{\Delta f}{f} = -\frac{d_A}{d_F} = -\frac{\Gamma}{\rho_F d_F} \qquad \text{(A12)}$$

This equation is considered to be exact for thin films with the same acoustic impedance as that of quartz. An accuracy of $\Delta f / f$ of $\sim 10^{-7}$ corresponds to a mass resolution of a few ng/cm^2 for a plate 0.1 mm thick.

Bandey *et al* (1997) [12] Use the following term to relate the mass load on a QCM to the change in resonant frequency.

$$\Delta f = -(2/\rho_q \upsilon_q)\Delta M f_0^2 \qquad \text{(A13)}$$

where ρ_q is the density of the crystal, υ_q is the wave velocity in the crystal, f_o is the fwhere ρ_q is the density of the crystal, υ_q is the wave velocity in the crystal, f_o is the

Bunde (1998) [13] Use the following term to relate the mass load on a QCM to the change in resonant frequency, but the equation uses an additional mass sensitivity parameter

$$\Delta f = \frac{-2 f_0^2 \Delta m}{A\sqrt{\mu_q \rho_q}} = -C\Delta m \qquad \text{(A14)}$$

Where Δf is the measured frequency shift, in Hz; f_o^2 is the fundamental resonant frequency squared in Hz; Δm is the mass change in grams, A is the piezoelectrically active area (area of electrode surface in cm^2) μ_q is the shear modulus of quartz, (2.947 X 10^{11} g cm^{-2}) and ρ_q is the density of quartz (2.648 g cm^{-3}). C is mass sensitivity constant (based on the cut of quartz used).

Uttenthaler *et al* (2001) [14] Use the following term to relate ideal mass loads to the responses of a QCM, the term shows the additional component of the overmode harmonic resonance (f_n) as well as the fundamental resonant frequency (f_0)

$$\Delta f_s = -\frac{2.f_0 \cdot f_n}{\sqrt{\rho_q \cdot \mu_q}} . \Delta m = -C_f . \Delta m \qquad \text{(A15)}$$

Where Δf_s is the change in the resonant frequency, ρ_q and μ_q are the density and shear modulus of the quartz crystal respectively, Δm is the mass per area and C_f is the sensitivity constant.

Voinova *at al* (2002) [15] Suggest that the simplified term below is quite adequate to describe the effect of an ideal mass load on a BAW. This term relates the fraction of the additional mass to the mass of the resonator at a given resonant frequency.

$$\Delta f = -f_0 \frac{M}{m_q} \qquad \text{(A16)}$$

Where Δf_0 is the fundamental frequency, M is the additional mass and m_q is the mass of the quartz resonator.

For quartz systems, another simple representation of the mass load is given by Hook *et al* (2002) [16] Hook's term uses the sensitivity constant instead of a direct fractional mass comparison.

$$\Delta m = -\frac{C}{n}\Delta f \qquad \text{(A17)}$$

Where C is a mass sensitivity constant (for quartz = 17 ng cm^2 Hz^{-1} at f = 5 MHz) and n (1, 3 ...) is the overmode or overtone number.

Hook *et al* also additionally state that the term is only valid for ideal loads, where they are distributed evenly, do not slip on the electrodes and are sufficiently thin or rigid to have negligible internal friction they also note that the term is not valid when attempting to measure mass loads from soft or dissipative load materials.

The frequency shift per mass attachment for a simple piezoelectric resonator can also be represented by the term given by: Gabl (2003). [17]

$$\frac{\partial f}{\partial m} = \frac{f_0}{M} \propto -f_0^2 \qquad \text{(A18)}$$

Where f_0 is the fundamental frequency, M is the mass of the oscillator.

In this recent paper, Gabl's term (A18) is used to describe the effects of ideal mass loading directly onto FBAR surfaces with similarities to the devices used in this project.

Lucklum (2002)[18] uses two equivalent simple equations to represent the mass load effect on a QCM operating in the gas-phase, relating the BAW responses to changes in coating density and /or coating thickness. But brings the concept of the mass load into the

electrical realm equating it with the purely mechanical[129] effects by considering the equivalent *transmission line model* (See Figure 1) for a QCM at resonance, stating that mass loads can represented by a surface acoustic impendence, or acoustic load. In this paper, Lucklum also goes on to show the derivations for the transformation of the acoustic load into electrical impedance. (*See Equation* (A22))

$$\Delta f_f = -\frac{2f_0^2}{Z_{cq}}\rho_s \qquad \text{(A19)(i)}$$

$$\Delta f_f = -f_0\frac{\rho_f h_f}{\rho_q h_q} \qquad \text{(A19)(ii)}$$

Where frequency change Δf_f is related to coating density and/or coating thickness. (equivalent to mass per area, $\rho_s = m_f / A = \rho f$) $Zcq = (\rho_q c_{66})^{1/2}$ is the characteristic quartz impedance, c_{66} is the piezoelectrically stiffened elastic constant, h, is the thickness. Indices q and f indicate the quartz crystal and the film, respectively. These equations are equivalent if f_0 is represented by the mechanical resonance frequency.

For completeness, it should be noted that the response of a resonator to an ideal mass load can also be solved analytically as a mechanical impedance (Z_1) which is useful when viewing the system as a transmission line model. (Bandy 1997)[12]

$$Z_1 = j\omega\rho_s \qquad \text{(A20)}$$

Where ρ_s is the mass per area contributed by the layer.

1.2 Non Ideal cases of Mass Loading on BAW resonators.

Pioneering studies to define what other parameters govern the change in frequency for a QCM have been investigated since about 1980. Film modulus can be related as a measure of the viscoelastic properties of the coating. Viscoelastic materials respond to external forces in a manner intermediate between the behaviour of an elastic solid and a viscous liquid.[19] Over a decade ago, Yamaguchi (1993)[20] demonstrated that as well as being employed as microbalances due to their resonant frequency responses to mass loading, the resonance was also sensitive to viscosity, elasticity, surface roughness and other

[129] It will be recalled from the original work of Sauerbrey that S_{21} series resonance of the LCR circuit is equivalent to the mechanical frequency of the piezoelectric device at resonance. See Equation (A6)

parameters of the sensing layers and in this particular case these effects have been seen as a form of *interference*, making the estimation of mass rather difficult. These workers have attempted circumvention by constructing equivalent circuits for the resonators and this is also the *first* study on the behaviour of DNA on solid surfaces based on *impedance measurements* of quartz crystal oscillators.

Nomura and Okuhara (1982)[22] were the first to relate the frequency change of a QCM to the square root of viscosity and density of a solution. Kanazawa and Gordon (1985) [23] reported the first rigorous theoretical model, noting the decay of the wavelength into the solution was a function of the square root of the viscosity of the contacting medium where pure water was taken as the reference. Similar relations were also described by Shay and Bruckenstein (1985) [24]. However the relations were found to not be applicable to solutions of very high viscosity.

Kanazawa and Gordon (1985)[23] derived an equation for the frequency shift from a shear/stress relationship in resonating quartz and liquid as;

$$\Delta F = -F^{\frac{2}{3}}\left(\frac{\eta\rho_L}{\pi\mu\rho_Q}\right)^{\frac{1}{2}} \qquad \text{(A21)(i)}$$

Where η is the viscosity of the liquid, μ is the shear modulus of quartz, ρ_Q is the density of the quartz, and ρ_L is the density of the liquid.

Muramatsu *et.al.*(1987)[26] monitored QCM frequency response in air, ethanol, sodium chloride solution, and purified water. In this case, the responses were evaluated in terms of the equations of Kanzawa and Gordon. They found that the oscillating frequency was effected by the density, viscosity, temperature, and conductivity due to ionic strength and pH of the liquid. However, they indicated that each of the Kanazawa equations were not accurate in predicting all of the experimental factors involved.

Muramatsu *et al* (1988) [27] then went on to derive an equation for electrical resistance of quartz in contact with liquids at their resonant frequencies considering energy loss on the surface of the quartz crystal as:

$$R = (2\pi F \rho_L \eta_L)^{\frac{1}{2}} A / k^2 \qquad \text{(A22)}$$

where R is the resistance (i.e., in BVD) A is the area of the quartz resonator and k is the electromechanical coupling factor of the quartz resonator. F is the frequency, ρ_L is the density of the liquid and η_L is its viscocity.

They demonstrated empirically that R shows excellent linearity in relation to the viscosity of the contacting solutions.

What this means in practice is that the surface bound elastic mass can be distinguished from the viscoelastic-density effects on the crystal frequency (f) and resistance (R) values. This knowledge has been used to monitor alterations in the cytoskeletal microtubules of living cells.[28] Another good example of a practical exploitative example of this knowledge is in the monitoring of the changes in the viscoelastic states caused by the gelation of a thrombin solution due to fibrinogen concentration .[21] A comprehensive survey of the responses obtained from TSM resonators under various loading conditions including rigid solids, viscoelastic media and Newtonian and Maxwellian liquids either singly or in any combination has been performed by Bandey *et al* (1999)[41]

Kurosawa. *et al* (1990) [25] Studied the effects of various types of solutions on QCM frequency and they found that the equations of Kanazawa and Gordon held true for all of the solutions tested except when there was the addition of an electrolyte into the solution or when a polymer layer was used. The reasons why the addition of electrolyte caused deviation from the Kanazawa term were not completely understood, the formation of an electrical double layer could not account wholly for the response. The reason why the use of polymers caused deviation from the Kanazawa term was only partially understood, but Kurosawa *et al* consider the fact that viscosity of the polymer layer is in some respects a frequency dependent function, this is in agreement with the conclusions of Ramsden (1993).[9]

When the QCM is immersed in a solution (as is a requirement for many biological sensing procedures) the elastic shear waves in the crystal couple with the viscous shear waves in the liquid and fade exponentially with characteristic length $\delta = \sqrt{[2\eta_C/(2\pi f \rho_C)}$. (

typically ~250 nm for aqueous solutions) The presence of liquid causes a shift δf in the resonant frequency of the crystal; if one side of the crystal is in contact with a liquid of absolute viscosity η_C and density ρ_C then by matching the shear waves in the two media at their interface then equation (A23) can be used given. Ramsden (1993) [9]

$$\delta f = -f_0^{\frac{2}{3}} \sqrt{[\rho_C \eta_C / (\pi \rho_F \mu_F)]} \qquad \text{(A23)}$$

Where f_0 is the frequency in the absence of a liquid.

The expression assumes that η_C is independent of frequency, but Ramsden concludes that this is not the case. This point should be kept in mind when considering the properties of the RF acoustic probe wave into proteins, DNA and soft polymer layers in the experimental sections of this thesis, since it is a parameter that was not considered whatsoever during the interpretation of the results.

Uttenthaler (2001)[14] represents the BAW viscosity-mass relationship as

$$\Delta f_K = -f_0 \cdot f_n^{1/2} \cdot \sqrt{\frac{\rho_l \cdot \eta_l}{\pi \cdot \rho_q \cdot \mu_q}} \qquad \text{(A21)(ii)}$$

Where Δf_k is the change in resonant frequency, ρ_l and η_l are the density and viscosity of the liquid in contact with the sensor surface respectively. Subscript q represents quartz

This is a modified term of the original Kanazawa law ($\Delta f_K \propto f_0^{3/2}$) (*See Equation* A21)(i)) but it includes the responses that can be obtained from monitoring overmode harmonics as well as the fundamental frequency. The term was used with some success when adapting thinned quartz plates to operate at high frequencies (up to 110 MHz) in a liquid environment to monitor the viscous effects of the addition of glycerol to a water loading layer, and also in the detection of M13-phages (viruses) by acoustic immunoassay.

Thompson and Yang (1993) [29] have concluded that the frequency response of a BAW is also dependent upon the hydrophobicity and hyrophilicity and pH of the liquid-to-metal interface due to variations interfacial slipping from changes in the interfacial viscosity. They relate the QCM response to kinetic energy transfer, acoustic energy dissipation and formation of interfacial structures. They also noticed some frequency rises on mass

loading with extremely hyrdophillic/hydrophobic interfaces on a QCM, running contrary to all previously published data. This fact is important in protein layering on the gold electrode of a QCM since Absolom (1987) showed adsorption on gold electrode surfaces decreases as protein hydrophobicity increases[30]

Voinova (1997) Worked on an extremely comprehensive approach to the relationship between the viscous loss of energy causing significant deviation from the Sauerbrey behaviour. This work has culminated in a successful prediction for the reduction in Δf in the special case of a pure viscous layer. This work takes into account proportionality in the linear viscoelastic regime between stored energy and strain and between strain rate and dissipated energy. The shift in resonant frequency Δf is calculated along with a so called dissipation factor ΔD due to the soft deposit and is calculated as the real and the imaginary part of the frequency shift of viscoelastically loaded resonators with non slip boundaries.[31]

Martin *et al* (2000)[32] state that the Sauerbrey model works well for acoustically thin films ($\varphi<\pi/4$) even if the film is not rigid (as is often stated in the literature), a viscoelastic layer can be treated as an ideal mass layer, with response dependent only upon its area mass density.

When the layer is thick in relation to the wavelength, then the displacement applied by the TSM quartz at the lower film surface can undergo significant phase shift, and attenuation in propagating across the layer. As this acoustic phase shift becomes significant, so do the interference effects. When the phase shift reaches $\pi/2$rad (or an odd multiple) interferences become constructive, resulting in enhanced absorption of acoustic energy by the film, this condition is known as *film resonance* which is dependent upon film thickness (h), modulus (G) and density (ρ). The detailed derivations dealing with this phenomenon and the construction of lumped element models where the quartz is represented by series LCR resonator and the film resonance by a parallel LCR component can be found in Martin (2000)[32]

Martin goes on to state that for excitation frequencies much greater than the film's resonant frequency,(ω / ω_f >> 1) large deviations occur between the predicted responses of the lumped element models and the transmission line models. Some of these differences being attributed to film harmonic resonances predicted by the general transmission line theory but not expressed adequately for the lumped element model. i.e., the BVD circuit. This observation may reveal a weakness in the QCM / FBAR analogy when considering it in terms of the BVD model, since the frequencies involved are likely to be much higher than the film resonances occurring on 5-10 MHz QCM. Indeed, if we consider the actual wavelengths involved with FBAR - then what is considered a thin film ($\phi<\pi/4$) on a 5-10 MHz QCM may be considered to be a rather thick layer ($\phi>\pi/4$) when used on FBAR.

Several other publications also show that mass loading is one, but not the only effect that influences QCM.. The second important factor influencing the results is from the film modulus on the QCM surface. Modulus and mass contributions can not be distinguished in a simple way. Lucklum (2000)[18] shows that the *transmission line model* based in a one dimensional solution of the wave equation which describes the propagation of acoustic waves in the system quartz-coating medium as an analogy to electrical waves significantly improved the modelling of the phenomenon.

An acoustic load can also be represented by its transformation into electrical impedance. Due to the piezoelectricity of the quartz crystal, the acoustic load impedance, Z_L can be determined from the electrical impedance, Z^e, or the electrical admittance $Y^e = 1/Z^e$. Lucklum *et al* (2000)[18]

$$Z^e = \frac{jx_1(\omega,q) + x_2(\omega,q)Z_L}{1 - jx_3(\omega,q)Z_L} \qquad \text{(A22)}$$

Where x is a parameter dependent only on the (angular) frequency, ω, and quartz constants q, not on the acoustic load.

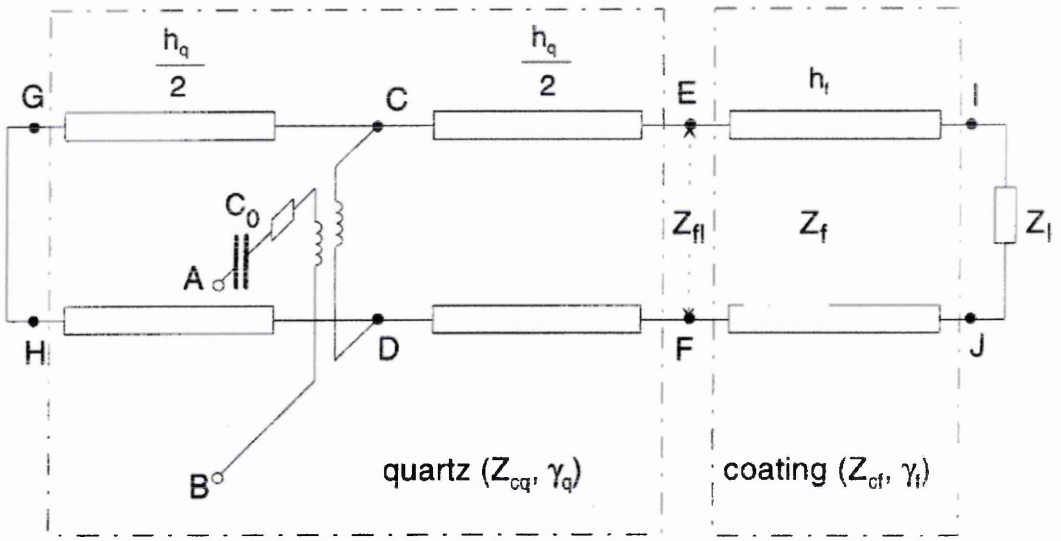

Figure . A1. Transmission line model of a quartz crystal with a single film coating, port EF, and liquid contact, port IJ. The other quartz crystal surface is unloaded, port GH. AB is the electrical port. From Lucklum [18]

The expression for admittance (Y) of the TSM is derived from the transmission line model. (Arnu 2002)[32]

$$Y = j\omega C_0^* + 1/Z_m \qquad \text{(A23)}$$

Where C_0^* is the static capacitance of the BVD circuit, Z_m is the impedance f_0 the motional arm. The static capacitance arises from the electrodes located on opposite sides of the dielectric resonator C_0 and from the parasitic capacitances external to the sensor. $C_p : C_0^* = C_0 + C_p$.

These workers (Arnu 2002) have isolated and separated the electrical responses from impedance analysis of the QCM using the transmission line model into the following components.

- Resonant frequency (f_o in Hz)
- Motional resistance (R in Ω)
- Motional capacitance (C in Farads - usually femto farads)
- Shunt capacitance (C_0 in Farads - usually pico farads)
- Motional inductance (L in mH)
- Quality factor

A similar method of approach of impedance characterisation for immunosensor piezoelectric systems has also been taken by (Kim 2003).[6]

Zhang *et al* (2002) [33]. have also used impedance analysis to examine the viscoelastic changes occurring during antibody/antigen interactions, relating the dissipation terms to changes in viscoelastic states. In this case, electrical equivalent parameters examined were motional resistance, shunt capacitance, and quality factors. Here, it is understood that the change in resonance frequency needs to be considered along with the damping behaviour of the crystal if the viscoelastic properties are to be measured. However in the work done in this thesis, it was concluded that the viscoelastic effects from thin antibody protein loading (~7 nm) were small enough to be ignored. (*See Figure* 5.6 (D) But it was shown that the relatively thick (~2 μm) PVP layers caused significant damping of the FBAR acoustic when they were hydrated (*See Figure* (4.13 (B))

To date, by far the most comprehensive derivations based on the transmission line model for the viscoelastic contribution to the responses of QCM are given by D. Johannsmann (2001). [35]

Mecea (1994) [34] has reviewed in detail the vibrating quartz resonator, and introduces a novel and sophisticated explanation of the mass loading effect in terms of an energy transfer model, but this model can not be given its deserved attention in this thesis. Suffice to note that it was developed in an attempt to explain that the ideal mass loading equations could not be used to calculate non-ideal or liquid loads and the converse was true where the equations used to describe the liquid loads fail to correctly interpret for ideal mass load.

Mecea also demonstrates that a relatively rare cut of quartz, the so called "X" cut will vibrate in a compressional mode, this more closely relates to the mode of the FBAR, albeit at only 1 MHz in the case in point. In his work, it is shown that the vibrational amplitude at every point in the X cut resonator can be described by an equation that is identical to that of the shear vibrating AT cut quartz resonator. Further, he has applied perfectly elastic films to the surface of the X cut compressional mode quartz and notes

that the experimental plots for frequency to mass relations follow the same equations as in the case of TSM vibrating quartz resonators. This information is useful in considering the analogies between the acoustic loading of FBARs operating in compressional mode and QCM in TSM.

Lucklum *et al* (2000)[18] has shown that the addition of a liquid load can be represented on TSM QCM by:

$$\Delta f_l = \frac{2f_0^2}{Z_{Cq}}\sqrt{\frac{\rho_l \eta_l}{4\pi f_0}} \qquad \text{(A19)(iii)}$$

and that the equations (A19(ii) and A19(iii)) can be added together to represent a loading film *and* the liquid layer as:

$$\Delta f = \Delta f_f + \Delta f_l = -\frac{2f_0^2}{Z_{cq}}\left(\rho_s + \sqrt{\frac{\rho_l \eta_l}{4\pi f_0}}.\right) \qquad \text{(A19)(iv)}$$

$Z_{cq} = (\rho_q c_{66})^{1/2}$ is the characteristic quartz impedance, c_{66} is the piezoelectrically stiffened elastic constant, *h,* is the thickness

Shchmitt et al (1997) [36] also show that shear acoustic impedance methods provide better insight into the changes of an antibody/antigen interaction taking the changes of viscoelasticity into account. In this case the real (R) and imaginary (X) components of the shear acoustic impedance are deduced respectively from the drop in quality factor ΔQ^{-1} and the resonant frequency shift. But again, they discovered that only small interfacial viscosity variations accompanied surface mass increases during immuno accumulation on QCM in the aqueous phase.

Impedance analysis on QCM has also been investigated by Wu *et al* (2000) [38] on denaturation in Herring DNA on the basis of the viscosity-density effect. Changes in both resonant frequency and the motional resistance of the motional arm of the BVD model gave linear results related to the DNA concentration in the range 210-5040 μg ml^{-1} These are the non-ideal mass loading equivalent impedance equations. They take into consideration the motional resistance R1 ($R1 = R_q + R_l$), motional inductance L1 ($L1 = L_q + L_L + L_M$) and motional capacitance C1 ($c1 = C_q$) and define the resonance frequency

of the motional arm as $f_0 = 1/2\pi(L_1C_1)^{1/2}$ They conclude that the equation below (A23) can accommodate the changes in resonant frequency and motional resistance in a QCM with one of its faces immersed in a viscous solution.

$$\Delta R_1 = -\frac{4\pi L_q \Delta f_0 \sqrt{f\mu_q}}{\sqrt{\bar{c}_{66} f_{0g}}} \qquad \text{(A23)}$$

Where Δf_0 and ΔR_1 are changes in the resonant frequency and the motional resistance of the QCM due to variations in the solution density and viscosity, L_q and f_{0g} are the motional inductance and resonant frequency of the QCM in air respectively, μ_q is the shear modulus of quartz, c_{66} is the piezoelectrically stiffened elastic constant.

Where Δf_0 and ΔR_1 are changes in the resonant frequency and the motional resistance of

There is no clear single format that provides universal applicability, Bunde *et al* (1998)[14] state that no unifying equations has been developed to fully describe all of the QCM responses in a liquid medium. While in their detailed work, Bandey *et al* (1999)[39] state that they have derived *"a unified treatment of the problem aiming to provide a framework capable of handling all physical circumstances likely to be encountered in acoustic wave / matter interactions"* .

Lucklum *et al* (2000)[18, 36] have discovered that by employing the Mason distributed model and using frequency change coupled to the change in motional resistance of the QCM response they can separate the viscous, elastic and mass components of non-ideal surface coating which is sufficiently accurate to model the complex shear modulus of the coating. However, Etchenique and Buhse (2000) [37] conclude that the presence of electrolyte in the mass load interferes with the accuracy of mass determinations in solution due to the formation of a Gouy-Chapman diffuse double layer and can result in errors as high as 70% and can not be excluded even by employing the most sophisticated QCM impedance methods. It will be recalled that Kurosawa. *et al* (1990) [25] stated that the formation of the electrical double layer could not wholly account for the deviations observed from the Kanazwa law. ($\Delta f_K \propto f_0^{3/2}$)

It will not be advantageous to cover all of the various forms of derivation that are available in the literature in this thesis, but suffice to understand that as the measurement parameter relations become more complicated as new components of it are discovered, so

the ways of interpreting them necessarily become more sophisticated. A unifying equation is still sought.

1.3 Mass to sensitivity relations and the concept of useable sensitivity.

Wensel and White (1989)[40] give the Mass sensitivity (S_m) of a piezoelectric mass sensor as :

$$S_m = \lim_{\Delta m \to o} \left(\frac{\Delta f_s}{f_s^0} \right) \left(\frac{1}{\Delta M} \right) \qquad \text{(A24)}$$

Where ΔM represents the change in mass per unit surface area arising from analyte sorption, f_s is the initial series resonance frequency. Δf_s is the change in series resonance frequency after the deposition of the material.

By applying this term to the classic Sauerbrey terms (See Equations A10 (i, ii, and iii), O'Toole *et al* (1992) developed two equivalent terms to calculate the mass sensitivity of high frequency TFR technologies.

$$S_m = \frac{-n}{\rho_s D_s} \qquad \text{(A10)(iv)}$$

where Ds is the thickness of the resonator, n is the integer designating the resonance mode.

The equivalent form relates S_m to n, f_s^0 , ρ_s and the velocity (V) of the acoustic wave as;

$$S_m = -\frac{2nf_s^0}{\rho_s V} \qquad \text{(A10)(v)}$$

where ρ_q is the shear modulus and the density of the quartz

But these terms do not take into consideration the Q factor of the device.
Gabl *et al* (2003)[17] state that the product of the Q factor *and* the sensitivity (S_m) are important in estimating the true limit of detection for an FBAR. They give the following term considering that the Q factor of an FBAR is important due to the fact that in a typical read-out circuit, the resonance frequency is determined by the phase detection.

$$m_r = \frac{2}{\pi} \cdot \frac{f_0}{sQ} \cdot \varphi_r \propto \frac{1}{f_0 Q} \cdot \varphi_r \qquad \text{(A25)}$$

Where m_r is *not stated but is assumed* to represent mass resolution, and φ_r is the phase resolution of the read out circuit. sQ i*s also not stated but is assumed* to represent series Q.

REFERENCES
APPENDIX (1)

1. .Cady, W. G. (1946) Piezoelectricity. New York : McGraw-Hill.).
2. .{error}
3. G. Sauerbrey, (1959) Verwndung von schwingquarzen zur wagung dunner schichten und zur mikrowagung (Use of oscillator quartz crystals for weighing thin layers and micro-weighing) Translated by technical information and library services. Ministry of Aviation in 1962 *Z. Physik.* **155** pp206-222
4. Lu, C., Lewis O. (1972) Investigation of film-thickness determination by oscillating quartz resonators with large mass load. J. *Appl. Phys.* **11**, 4385-4390.
5. Muramatsu. H., Suda. M., Ataka. T. (1990) Piezoelectric resonator as a chemical and biochemical sensing device. *Sensors and Actuators*, A21-A23 pp 362-368.
6. Gi-Ho Kim , A. Garth Rand , Stephen V. Letcher. (2003) Impedance characterization of a piezoelectric immunosensor Part I: Antibody coating and buffer solution Biosensors and Bioelectronics **18** 83-89]
7. Barnes. C., D'Silva. C., Jones. P., Lewis. T. (1991) A concanavalin A-coated piezoelectric crystal biosensor. *Sensors and Actuators B*, **3** 295-304.
8. O'Toole. R., Burns. S., Bastiaans., G., Porter. M. (1992) Thin aluminium nitride resonators: Miniaturised high sensitivity mass sensors. *Anal Chem.* 1289-1294.
9. Ramsden J. J. Investigating protein adsorption kinetics. (1993) Quarterly Reviews of Biophysics **27**, 1 pp 41-105]
10. Reason M, Teesdale-Spittle P. Latham R. Dawson G, Porteous P and Smith G. (2001) A TSM sensor investigation of low crystallinity cellulose films. *International Journal of Pharmaceutics* **222**. pp 121–128
11. Wong. Y., Ng. S., Ng. M., Si. S., Yao. S., Fung.Y. (2002) Immunosensor for the differentiation and detection of Salmonella species based on a quartz crystal microbalance. Biosensors and Bioelectronics **17** pp 676_ 684.
12. Bandey. H., Hillman., Brown M., Martin S. (1997) *Faraday Discussions* **107** 105.
13. Bunde. R., Jarvi. E., Rosentrter. J. (1988) Piezoelectric quartz crystal biosensors. *Tantala.* **46**. pp 1223-1236.

14. Uttenthaler. E., Schraml. M., Mandel. J., Drost. S. (2001) Ultrasensitive quartz crystal microbalance sensors for detection of M13-Phages in liquids *Biosensors & Bioelectronics* **16** pp 735–743
15. Voinova. M. V., Johnson. M., Kasemo. B. (2002) "Missing mass" effect in biosensor's QCM applications. Biosensors and electronics. **17** pp 835-841.]
16. Hook F., Voros. J., Rodhal M., Kurrat. R ., Boni. P., Ramsden. J., Textor. M., Spencer. N., Tengvall. P., Gold. J., Kasemo. B(2002). A comparative study of protein adsorption on titanium oxide surfaces using in situ ellipsometry, optical waveguide lightmode spectroscopy and quartz crystal microbalance/dissipation. *Colloids and surfaces B: Biointerfaces* **24** 155-170.]
17. Gable R., H.-D. Feucht, H. Zeininger, G. Eckstein, M. Schreiter, R. Primig, D. Pitzer, W. Wersing (2004) First results on label-free detection of DNA and protein molecules using a novel integrated sensor technology based on gravimetric detection principles. *Biosensors and Bioelectronics* **19** 615–620
18. Lucklum. R., Hauptmann. P. (2000) The quartz crystal microbalance: mass sensitivity, viscoelastic and acoustic amplification. *Sensors and Actuators B* **70** pp 30-36.
19. Ferry. J.D. Viscoelastic properties of polymers. Wiley. New York. (1980)
20. Yamaguchi S, Shimomura T. (1993) Adsorption, Immobilisation, and Hybridisation of DNA Studied by the Use of Quartz Crystal Oscillators. *Anal Chem* **65**, pp 1925-1927.
21. Maramatsu. H. (1989) Quartz-crystal gelation detector for the determination of fibrinogen concentration. *Anal. Chim. Acta.* **217**. pp 321-326.]
22. Nomura. T., Okuhara. M. (1982) Frequency shifts of piezoelectric quartz crystals immersed in organic liquids. *Anal Chim Acta.* **142** p281.
23. Kanazawa. K., Gordon. J. (1985) Frequency of a quartz microbalance in contact with a liquid. *Anal Chem* **57** pp 1771-1772
24. Bruckenstein, S., Shay, M., (1985). Experimental aspects of use of the quartz crystal microbalance in solution. *Electrochim. Acta 30*, pp 1295–1300.
25. Kurosawa. S., Tawara. N., Kobatake. (1990) Oscillating frequency of piezoelectric quartz crystal in solutions *Anal Chimica Acta.* **230** pp 41-49

26. Muramatsu. H., Dicks. J. M., Tamiya. E., Karube. I. (1987) *Anal. Chem* **59** 2760.
27. Muramatsu. H., Tamiya. E., Karube. I. (1988) Computation of equivalent circuit parameters of quartz crystals in contact with liquids and study of liquid properties. *Anal Chem.* **60** p2142.
28. Marx. K., Zhou. T., Montrone. A., Schulze. H., Braunhut. S. (2001) A quartz crystal microbalance cell biosensor: detection of microtubule alterations in living cells at nM nocodazole concentrations *Biosensors & Bioelectronics* **16** pp 773–782
29. Yang. Y., Thompson. M. (1993) Multiple chemical information from the thickness shear mode acoustic wave sensor in the liquid phase. *Anal. Chem.* **65** pp 1158-1168.
30. D. Absolom, W. Zingg, A.W. Neumann (1987) *J. Biomed.Mater. Res.* **21** 161
31. Voinova. M.V., Jonson. M., Kasemo. B. (1997) Dynamics of viscous amphiphilic films supported by elastic solid substrates. J. *phys. Condens Matter.* **9.** pp 7799-7808
32. Arnau. A., Sigorb. T. (2002) Circuit for continuous motional series resonant frequency and motional resistance monitoring of quartz crystal resonators by parallel capacitance compensation. *Review of Scientific Instruments.* **73** 7 pp 2724-2737
33. Zhang. J., Su. X., O'Shea. S. (2002) Antibody/antigen affinity behaviour in liquid environment with electrical impedance analysis of quartz crystal microbalances. *Biophysical Chemistry.* **99.** pp 31-41
34. Mecea. V. M. (1994) Loaded vibrating quartz sensors. Review paper. *Sensors and Actuators A.* **40.** 1-27.
35. Johannsmann. D (2001) Derivation of the shear compliance of thin films on quartz resonators from comparison of the frequency shifts on different harmonics: A perturbation analysis. *J. App Phys.* **89** 11 pp 6356-6364
36. Lucklum. R., Hauptmann. P. (2000) The Δf-ΔR QCM technique: an approach to an advanced sensor signal interpretation *Electrochimica Acta,* **45** pp 3907-3916.
37. Etchenique. R., Buhse. T. (2000) Anomolous behaviours of the quartz crystal microbalance in the presence of electrolytes. *Analyst,* **125** 785-787

38. Wu. Y., Zhou. A., Xie. Q., Cai. Y., Yao. S. (2000) A piezoelectric quartz crystal impedance study on denaturation of DNA. *Microchemical Journal.* **65** pp 67-74
39. Bandey. H. L., Martin. S. J., Cernosek. R. W (1999). Modelling the responses of thickness shear mode resonators under various loading conditions. *Anal Chem.* **71** pp 2205-2149
40. Wensel, S., White, R. (1989), *Appl. Phys Lett.* 54. 1976-1978.
41. Bandey H., Martin. S., Cernosek. R., Hillman. R. (1999) Modeling the Responses of Thickness Shear Mode Resonators Under Various Loading Conditions. *Anal Chem* **71**. 2205-2214

Appendix (2)
Materials Lists

CHAPTER 3

FHA. PCB's (FR4 2.4 mm and 3.2 mm)
100 cm flexible coaxial cables. (R1-T32 T1P1) (50Ω).
SMA connectors and neutral N type connectors.
50Ω signal terminators.
RF signal attenuator. (R411810 Radial -10 dB)
Various PCB test structures.
Peltier Heater.
RS thermocouple
NA 8753D
PCB wb FBAR die samples. (Pre-characterised on Summit 9000)
GPIB enabled computer running R.01 FBAR interrogation software on Lab View 6

Dr. DAQ environmental data acquisition board integrated thermocouple and light sensor

Table A2.1 DAQ ranges and resolutions

	RANGE	RESOLUTION	ACCURACY
TEMPERTURE (^{O}C)	-10 TO 150^{O}C	0.1@25^{O}C	0.3^{O}C @ 25%
HUMIDITY (%RH)	20 TO 90%	0.2%	$\pm$ 10%

FBAR on PCB in housing chamber

Dr.DAQ data acquisition board.

Dr.DAQ humidity Meter Range = minimum %RH20 to maximum %RH70

Dr.DAQ thermocouple.

Hanna Instruments humidity meter Range = minimum %RH20 to maximum %RH90

Hanna Instruments thermocouple.

Nitrogen supply

Rotamer gas flow controllers.

5 mm PTFE tubing.

Water bath.

Peltier heating system and heat transfer block.

Poly(vinyl pyrrolidone) (Sigma)

Methanol (Sigma)

Artists Airbrush, droplet size control nozzle, and propellant.

Ruler.

Retort stand.

Thickness profiler (Dektak)

Drying crystals.

Silica Gel granulated. (O_2 Si x $_{(n)}H_20$) were supplied by BDH.,VWR international, Hunter Boulevard, Magna Park, LE17 4XN

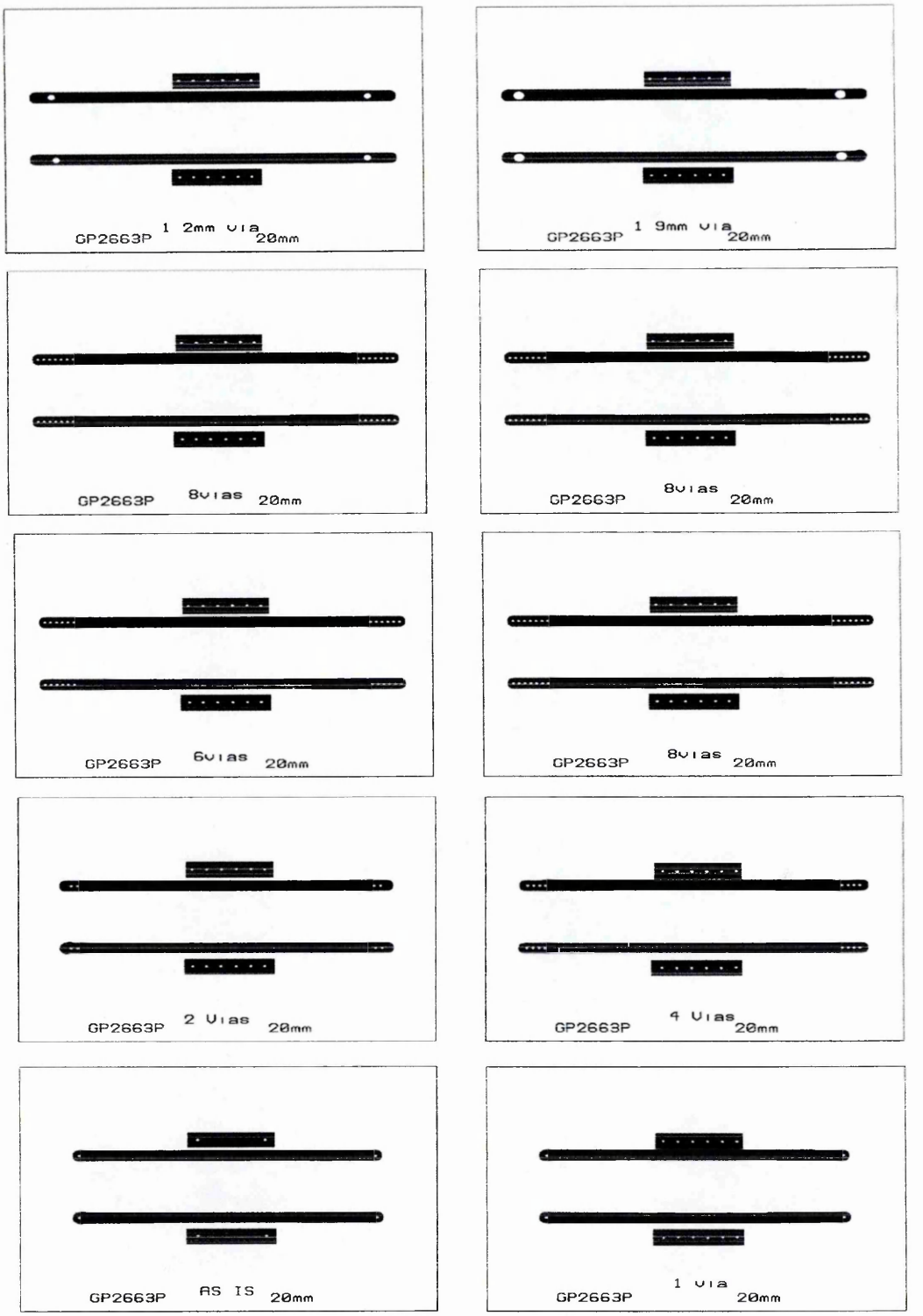

Appendix Figure 2.1. Board maker images of the via design for the PCBs. Via number or via size did not seem to have any significant effect on the S_{21} traces.

Appendix Table 2.2 Parts list of the SPR system – all parts were obtained from Melles Groit (Cambridge, UK).

PART	CODE
optical rail (50 x 500 mm)	007RN003
optical rail carrier	07CN501
post holder (80 mm)	07PHS006
laser holder	07HLC003
gimbal mirror mount	07RES004
pyrex mirror W/011 25 mm dia	02MFG015
lens holder	07LHF007
polariser holder	07HPR001
iris diaphragm holder	07HID001
pin actuated diaphragms	04IDC005
kinimatic prism table 25 mm	07MHT045
translation stage	07TMSC504
X-Y-Z translation stage	07TMC521
mounting post	07RMS003

Appendix 3

Important network analyser RF measurement parameter definitions

Data point definition:

A "data point" is a single piece of data at a single frequency representing a measurement at a single stimulus value

Sweep definition:

A "sweep" is a series of consecutive data point measurements, taken over a range of stimulus values. A sweep is performed over a given bandwidth and a given number of iterations.(*see iteration definition*) All sweeps without exception were S_{21}.

Bandwidth definition:

The frequency gap[130] between f_1 (start/first frequency) and f_2 (stop /end frequency) is the defined "bandwidth" of the sweep. The minimum bandwidth was 1 MHz, the maximum bandwidth was 3 GHz.

Resonance Frequency definition:

The data point within the bandwidth of the sweep with the least (most negative) S_{21} power transmission[131] (-dB) was denoted as (f_0) in Hz and this is defined as the series "resonance frequency" of the FBAR. This value (f_0) is important in this case because sensing analysis was based mainly on changes in f_0 (Δf). This was reported as both the real measured value directly from the network analyser, and also as the second order polynomial fitted value produced automatically in by the computer running the VI software, so two resonance frequencies could be reported.

[130] Frequency gap (Hz) was usually made by setting a centre frequency f_c, with f_1 START and f_2 STOP frequencies being equidistant from f_c It is very important to note that the centre frequency f_c is NOT the resonance frequency f_0. Although in some cases $f_c \equiv f_0$

[131] This occurred because "at resonance" the capacitate properties of the FBAR were transformed into a pure resistance.

Iteration definition.

During a single frequency sweep (one "iteration"), the software would report the data point with the most negative S_{21} power transmission (dB) over the range of stimulus values i.e., the bandwidth (f_1 to f_2) as the resonance frequency (f_0) in Hz. If the software was programmed to run say, 100 iterations, then 100 individual frequency sweeps over the fixed specified bandwidth would be performed by the network analyser and a graph of 100 (f_0) points over either iteration number or time (seconds)[132] would be produced as the final output chart used in the analysis. Once the measurement parameters were programmed, it was not possible to make any alterations to them during the entirety of the iteration set.

Baseline definition.

The "baseline" in this case is defined as the graphical representation of the output trace of iterative or repetitious f_0 values when conditions of the FBAR in the FHA were stabilised. For linguistic convenience, when conditions were changed to cause change in f_0, then this is called a change in the baseline response.

[132] Time was used exclusively to generate the charts of multiple f_0 single data points, but iteration number was also recorded.